University of Nottingham
UK | CHINA | MALAYSIA

Design, Synthesis, and Development of Novel Intracellular Allosteric Modulators of CXC Chemokine Receptor 1 and 2

Rhys Francis, MSc

Thesis submitted to the University of Nottingham for the degree of Doctor of Philosophy

March 2024

Abstract

Chemokine receptors, CXC chemokine receptor 1 (CXCR1) and CXC chemokine receptor 2 (CXCR2) play pivotal roles in various neutrophil-mediated inflammatory diseases, including COPD, asthma, and psoriasis. Additionally, evidence is mounting for the involvement of neutrophils and the CXCL8-CXCR1/2 axis in the progression and metastasis in multiple cancers. Their role in multiple disease states has made them an appealing candidate for therapeutic intervention for over a decade.

Much of the existing research of CXCR1 and CXCR2 has centred on their interaction with the endogenous chemokine CXCL8 and the ensuing CXCL8-CXCR1/2 axis in disease pathogenesis. However, despite promising preclinical evidence, challenges persist in translating these findings into effective therapies, particularly with intracellular allosteric binding site antagonists such as navarixin (**2**) and AZD5069 (**3**). The recent setbacks faced by these small molecules in phase II trials underscore the need for a comprehensive evaluation of the clinical effectiveness of CXCR1 and CXCR2 antagonists in inflammatory diseases. Additionally, emerging evidence points to distinct roles played by CXCR1 and CXCR2 in disease progression, particularly in cancer. To further evaluate the therapeutic potential of antagonists targeting CXCR1 and CXCR2, the use of pharmacological tool compounds is proposed to elucidate the intricate signalling pathways leading to their effects.

The recent publication of the CXCR2 crystal structure bound to NAM 00767013 (**1**) provides a promising foundation for the computer-aided design of intracellular allosteric antagonists. Leveraging this structural insight offers a valuable opportunity to develop novel therapeutics targeting CXCR2 and the closely related CXCR1.

This thesis reports the design, synthesis and pharmacological characterisation of a series of novel compounds belonging to the 3,4-diamino-3-cyclobutene-1,2-dione class of NAMs as part of an structure activity relationship study to further explore the chemical space around lead compound, navarixin (**2**) and providing evidence for modifications towards achieving dual CXCR1/CXCR2 activity, and potentially leading to CXCR1 selectivity over CXCR2, which could be prove useful in further studies of these receptors.

List of abbreviations

ADME	Absorption, distribution, metabolism, and excretion
ALDH	Aldehyde dehydrogenases
AMP	Adenosine monophosphate
ANC	absolute neutrophil count
AUC	Area under-curve
AZ	AstraZeneca
β1AR	β1-adrenergic receptor
β2AR	β2-adrenergic receptor
BLAST	Basic local alignment search tool
BRET	Bioluminescence resonance energy transfer
BSA	Bovine serum albumin
CADD	Computer-aided drug design
CCR	CC chemokine receptor
CHO	Chinese hamster ovary cells
COBALT	constraint-based alignment tool
COPD	Chronic obstructive pulmonary disorder
COSY	Homonuclear correlation spectroscopy
COX	Cyclooxygenase
CRPC	castration-resistant prostate cancer
CRS1	Chemokine recognition site 1
CRS2	Chemokine recognition site 2
cryo-EM	Cryo-electron microscopy
CSC	Cancer stem cell
CXCL	CXC chemokine ligand
CXCR1	CXC chemokine receptor 1
DCC	*N,N*′-Dicyclohexylcarbodiimide
DCM	Dichloromethane
DCU	1,3-Dicyclohexyl urea
DEE	Diethyl ether
DIBAL-H	Diisobutylaluminum hydride
DIPEA	*N,N*-Diisopropylethylamine
DMAP	4-Dimethylaminopyridine
DMEM	Dulbecco's modified eagle medium
DMF	Dimethylformamide
DMSO	Dimethylsulphoxide
DOPE	Discrete optimized protein energy
DUD-E	Directory of useful decoys, enhanced
ECL	Extracellular loop
EDC	1-Ethyl-3-(3-dimethylaminopropyl)carbodiimide
ELR	Glu-Leu-Arg

ESI	Electrospray ionisation
FBS	Fetal bovine serum
FCC	Flash column chromatography
FDA	Food and drug administration
FEV	Forced expiratory volume
FLIPR	Fluorometric imaging plate reader
FPR1	Formyl peptide receptor 1
FRET	Fluorescence resonance energy transfer
GBM	Glioblastoma multiforme
GDP	Guanosine diphosphate
GLASS	GPCR-ligand association
GPCR	G protein coupled receptor
GPT	Alanine aminotransferase
GRAFS	Glutamate, rhodopsin, adhesion, frizzled/taste2, secretin
GRK	G protein coupled receptor kinases
GSK	GlaxoSmithKline
GTP	Guanosine triphosphate
HBSS	Hanks' balanced salt solution
HBTU	Hexafluorophosphate benzotriazole tetramethyl uronium
HEK	Human embryonic kidney
HMBC	Heteronuclear multiple bond correlation spectroscopy
HOBt	1-hydroxybenzotriazole
HPLC	High performance liquid chromatography
HSQC	Heteronuclear single quantum coherence spectroscopy
HTS	High-throughput screening
IAM	Intracellular allosteric modulator
ICL	Intracellular loop
IL8	Interleukin-8
IP_3	Inositol 1, 4, 5-triphosphate
LC	Liquid chromatography
LCMS	Liquid chromatography-mass spectrometry
LgBiT	LargeBiT
LPC	Liquid-phase crystallization
LPS	Lipopolysaccharide
m/z	Observed ion
MAPK	Mitogen-activated protein kinases
MeCN	Acetonitrile
MEM	Minimal essential medium
MS	Mass spectrometry
MSS CRC	microsatellite-stable colorectal cancer
MVD	Micro vessel density
MW	Microwave
NADPH	Nicotinamide adenine dinucleotide phosphate hydrogen

NAM	Negative allosteric modulator
NanoBiT	NanoLuc binary technology
NanoLuc	Nanoluciferase
NET	Neutrophil extracellular traps
NMR	Nuclear magnetic resonance
NSB	Non-specific binding
NSCLC	Non-small cell lung cancer
OPLS4	Optimized potential for liquid simulations 4 force field
PAM	Positive allosteric modulator
PCA	Protein-fragment complementation assay
PDB	Protein databank
PFS	Progression-free survival
PI3K	Phosphoinositide 3-kinases
PIP_2	Phosphatidylinositol 4,5-bisphosphate
PIP_3	Phosphatidylinositol (3,4,5)-trisphosphate
PKA	Protein kinase A
PLC	Phospholipase C
PLD	Phospholipase D
PMN	Polymorphonuclear neutrophils
PROTAC	Proteolysis-targeting chimera
RMSD	Root mean square deviation
RNA	Ribonucleic acid
ROC	Receiver operating characteristic curve
ROS	Reactive oxygen species
SAM	Silent allosteric modulator
SAR	Structure-activity relationship
SBDD	Structure-based drug design
SBVS	Structure-based virtual screening
SEM	Standard error of the mean
SP	Standard precision
TEA	Triethylamine
THF	Tetrahydrofuran
TLC	Thin-layer chromatography
TM	Transmembrane
TME	Tumour microenvironment
TNF-α	Tumour necrosis factor-α
TOF	Time of flight
TOFMS	Time of flight mass spectrometry
TPR	True positive rate
VT NMR	Variable temperature nuclear magnetic resonance
WM	Wistar melanoma
XP	Extra precision

Table of Contents

Chapter 1 - General introduction

1.1 Chemokines

Chemokines are a family of signalling proteins belonging to the larger family of cytokines and govern a wide range of biological functions, including the innate immune res ponse of cells.[1,2] Chemokines are small 8-12 kDa proteins with variable sequence identity (20-90 %), however their sequences and tertiary structure are highly conserved.[2,3] Chemokines are produced by various cell types, including neutrophils (alternatively named polymorphonuclear leukocytes (PMNs)), macrophages, endothelial cells, and fibroblasts.[1,4,5] Chemokines are categorized based on the configuration of the first two cysteine residues (starting from the *N*-terminus), which form disulphide bridges.[3] These categories are C, CC, CXC, and CX_3C, with the CC and CXC families containing the most members. Representations of the various types of chemokines are depicted in **Figure 1-1**. In the CC chemokines, the cysteines are positioned adjacent to one another. In the C-X-C motif, the two cysteine residues are separated by a single amino acid, while in the C-X_3-C family, the cysteines are separated by three amino acids. The C chemokine subfamily is unique as its members only contains two cysteines across the sequence, forming a disulphide bridge.[2,3] CXC chemokines are further distinguished by the presence or absence of the ELR (glutamic acid-leucine-arginine) motif near the *N*-terminus. The presence of the ELR motif specifically correlates with potent neutrophil chemoattraction, crucial for early host defence response to inflammation. Additionally, ELR^+ chemokines play a role in angiogenesis, which is important for tissue repair.[5-7] The ELR^+ sub-family consists of CXC chemokine ligand (CXCL)1-3, and CXCL5-8.[4,7] ELR^- chemokines, such as CXCL4, CXCL9 and CXCL10, lack the ELR motif, and are generally considered angiostatic. They are responsible for facilitating lymphocyte and monocyte recruitment, but typically not neutrophils.

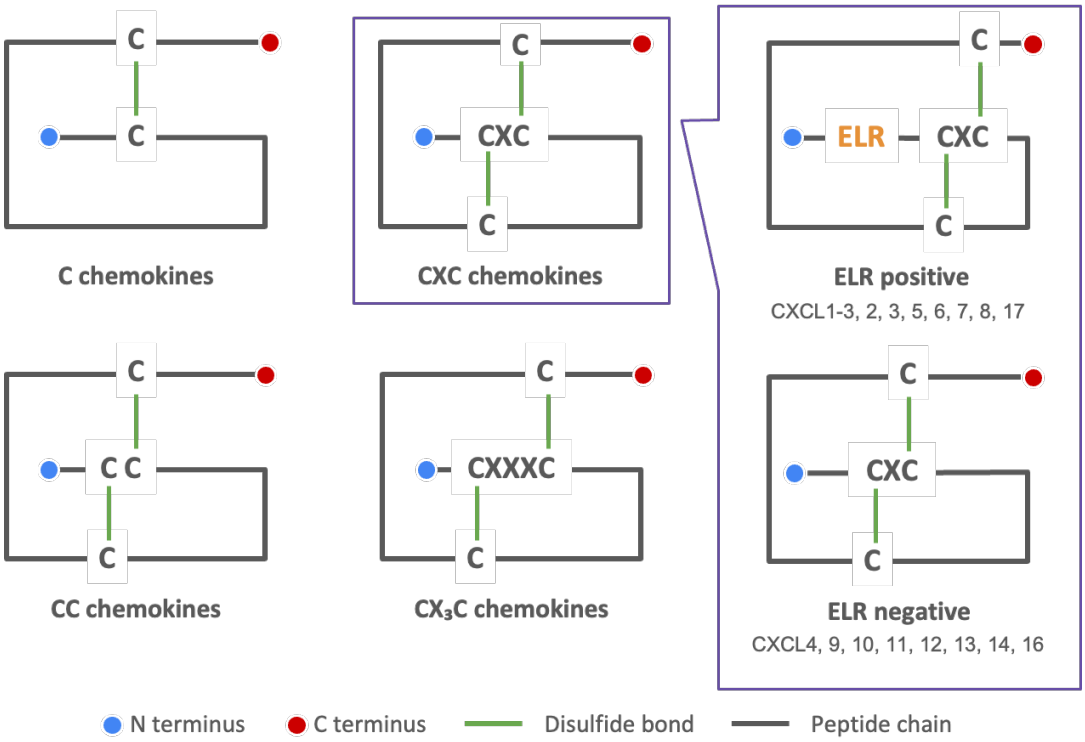

Figure 1-1 Depiction of the different classifications of chemokine ligands, C, CC, CXC, CX_3C. Classification based on the motif between two cysteines that form disulphide bonds The CXC chemokines can be further categorised in to ELR^+ or ELR^+, depending on the presence of an ELR motif at the *N*-terminus (purple box).

The first chemokine discovered by Oppenheim *et al.*[8] was CXCL8, also known as interleukin-8 (IL-8), belonging to the ELR^+ CXC chemokine ligand family. These are Secreted by various cell types, including macrophages, endothelial cells, and epithelial cells, CXCL8 is a key component of the inflammatory response. As a typical ELR+ chemokine, CXCL8 plays a pivotal role in recruiting and activating neutrophils during the early stages of inflammation.[6,9] It is a proinflammatory chemokine and is typically undetectable in non-stimulated cells. Expression of CXCL8 is stimulated by cytokines like interleukin-1 and interleukin-6, as well as other environmental stresses such as hypoxia, inflammatory signals, tumour necrosis factor (TNFα), or the presence of bacterial species. The combination of these stimuli and signalling pathways leading to CXCL8 transcription results in its upregulation in the extracellular space.[10]

1.1.1 The role of chemokines in inflammation

Inflammation is a critical component of the immune response and begins with the recruitment and activation of neutrophils, which are the most abundant type of white blood cells, typically constituting of 50-70% of all leukocytes in humans.[11,12] Neutrophils play a pivotal role in the innate immune system, the body's first line of defence against pathogens (**Figure 1-2**). At the forefront of this response is CXCL8 and its cognate receptors, CXCR1 and CXCR2. Neutrophils express high levels of CXCR1 and CXCR2, enabling them to respond to inflammatory signals such as infection or tissue damage.[1,4,5] CXCL8 is predominantly expressed at sites of infection or inflammation, acting as a potent chemoattractant for neutrophils. Upon encountering CXCL8, neutrophils undergo chemotaxis, directed migration towards the source of the chemokine.[10,13-15] Moreover, CXCL8 serves as a critical mediator in the activation of neutrophils. Binding of CXCL8 to CXCR1 and CXCR2 triggers intracellular signalling cascades that lead to the release of stored granules containing antimicrobial peptides and enzymes, as well as the formation of neutrophil extracellular traps (NETs). These NETs consist of chromatin and proteases that trap and neutralize pathogens, contributing to the host's defence against infection.[16,17]

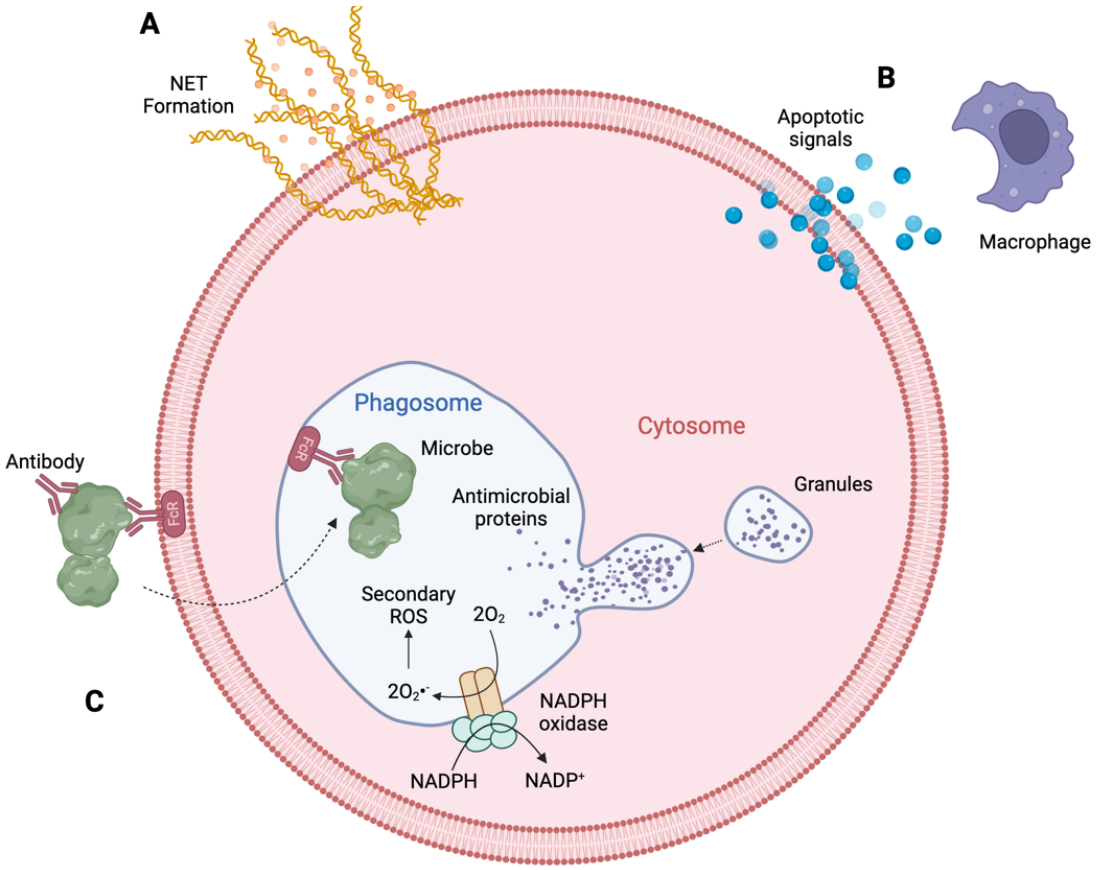

Figure 1-2 Roles of neutrophils during inflammation. (A) NET formation which can trap and kill pathogens extracellularly, preventing their spread. (B) Degranulation. Neutrophils release chemotactic species such as chemokine CXCL8, which can attract immune cells such as macrophages to the site of inflammation. Additionally, the release of chemotactic species can promote further amplification of the inflammatory signals. (C) Pathogen recognition and phagocytosis. Once engulfed, the production of ROS contributes to the destruction of the pathogen. Created with Biorender.

Under normal conditions, neutrophils are activated to perform phagocytosis in response to the detection of microbes and other immune signals. CXCL8 enhances this innate immune response by amplifying the neutrophils' phagocytic response. While phagocytosis can occur independently, CXCL8-induced activation amplifies this response. Additionally, CXCL8 boosts the production of reactive oxygen species (ROS) through oxidative burst, further strengthening the antimicrobial capacity of neutrophils.[18,19] This process involves the activation of NADPH oxidase, leading to the production of superoxide anions(O^{2-}), which play a crucial role in microbial killing within the cell.[10,20,21] The coordinated actions of CXCL8 and its receptors, CXCR1

and CXCR2, on neutrophils are vital for the initiation and regulation of the innate immune response against infections.

1.2 CXC chemokine receptors

1.2.1 Introduction to G protein-coupled receptors (GPCRs)

In 1994, Alfred Gilman and Martin Rodbell shared the Nobel prize in Physiology or Medicine for the discovery of G proteins and the role of these proteins in signal transduction in cells.[22] Rodbell and his team initially hypothesised the existence and role of guanine nucleotides for the activation of some proteins in 1971, followed by Gilman's work between 1778 and 1985, proving the existence of G proteins and their role in GPCR signalling. Their work revolutionised our understanding for the GPCR superfamily of proteins.[23-25]

Recent reviews have summarised the impact of GPCRs in modern drug discovery, with over 480 FDA-approved drugs that target GPCRs. This accounts for around 34% of all approved drugs and ~27% of the global pharmaceutical market.[26,27] A further 321 are currently in clinical trials and projections suggest that this research area is a still rapidly growing and shows no sign of slowing down.[26,27] GPCRs with FDA-approved drugs or have clinical trial candidates are summarised in **Figure 1-3**. Despite the number of drugs on the market, they target a minority of non-olfactory GPCRs in the genome (approximately 40 – 50 of 400 distinct receptor proteins). In addition, the function of ~140 GPCRs (often termed orphan GPCRs) is yet to be fully elucidated.[28] GPCR-targeted drugs on the market predominantly consist of traditional small molecule drugs (92%), although more recent advances in the area have shown that biological modalities such as monoclonal antibodies can be used to generate GPCR drugs.[28-31]

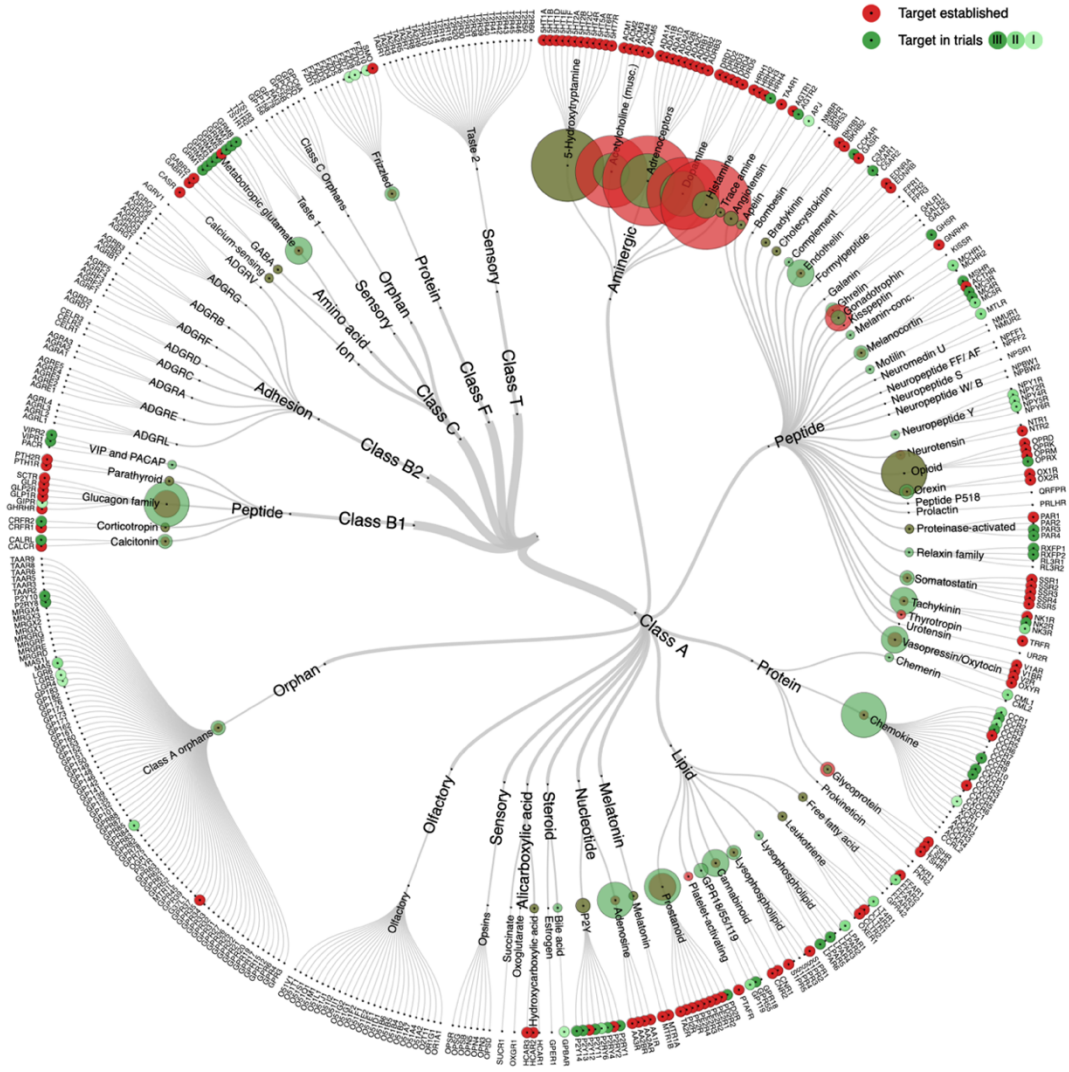

Figure 1-3 GPCR Class and Families Drug Target Map. Red circles indicate receptors with identified drugs on the market, while green circles denote receptors with drug compounds in clinical trials. Circle size correlates with the number of agents. Image generated using GPCRdb.[32]

A common method of GPCR classification was first introduced by Kolakowski *et al*.[33] and divides GPCRs into seven families (A,B,C,D,E,F and O), based on sequence similarity.[33] This system has been updated for the current G protein coupled receptor database (GPCRdb) website by Munk *et al*.[34] and, later, class T (Taste 2) receptors were added to the classification, which were previously classified along with the F class of GPCRs The GPCRdb classifications are summarised in **Table 1-1**. An alternative established classification is the GRAFS classification, which comprises of the five GPCR families found in humans Glutamate, Rhodopsin, Adhesion, Frizzled and Secretin.[35]

Table 1-1 Classification of GPCRs according to the GPCRdb. Included is the number of identified human members in each class and examples of drugged receptors for each class

GPCRdb Classification[34]	Note	Number of Human Members	Prominent Drugged Examples
A	Includes 390 olfactory and 5 vomeronasal receptors	689	CXCR4, CC chemokine receptor 5 (CCR5)
B	Further classified into B1 and B2	48	Glutamate receptor (GLR)
C	Includes 3 Taste 1 receptors	22	Neurotransmitter gamma-aminobutyric acid (GABA) receptors
D	Fungal mating pheromone receptors	0	-
E	cAMP receptors	0	-
F	None	11	Smoothed (SMO)
T	Previously grouped with Class F but later renamed	25	None
O	7TM receptors not belonging in any of the other defined families (orphan)	6	GPR35

1.2.2 Structure and function of CXC chemokine receptors

Figure 1-4 depicts the typical architecture of class-A Rhodopsin GPCRs, which includes CXCR1 and CXCR2. In this architecture, the membrane bound receptor consists of a single polypeptide chain folded into seven distinct transmembrane (TM) α-helices (referred to as TM1 to 7). The helices are connected by a series of intracellular loops (ICL1-3) and extracellular loops (ECL1-3), which can differ significantly in length and structure between receptors. Class A receptors also commonly contain an amphipathic 8th helix (H8) following the conserved NPxxY motif of TM7, towards the *C*-terminus.[36] Notably, whilst GPCRs share the highest structural homology in their transmembrane helical bundles, significant variations exist in their *N*/*C*-termini and loop regions.[37,38]

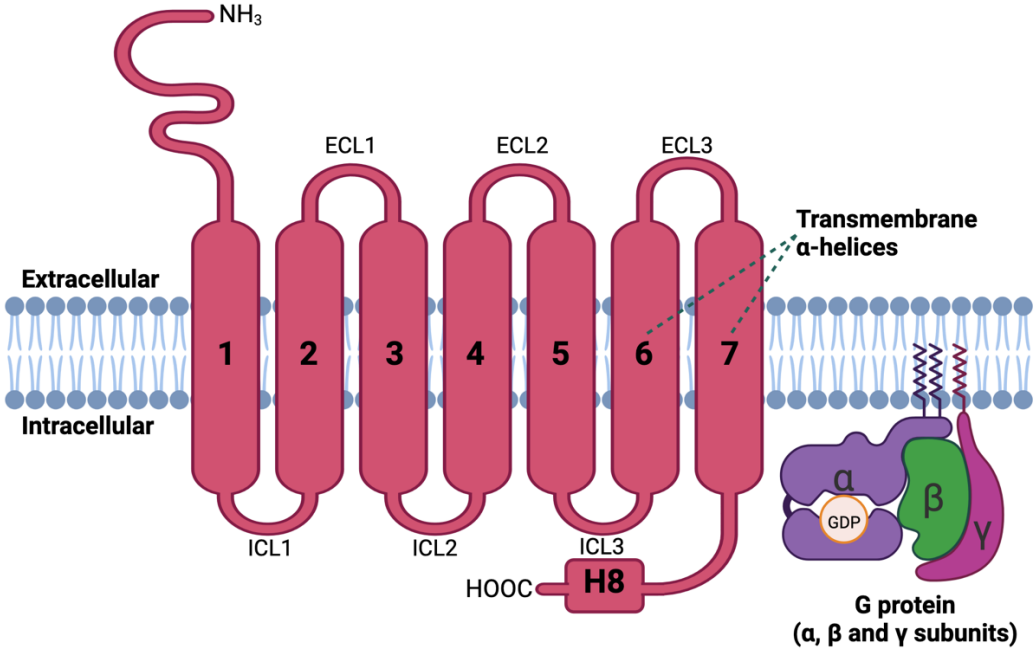

Figure 1-4 General structure of a GPCR showing the 7 transmembrane α-helices and the three subunits of the heterotrimeric G protein when bound to the *C*-terminus. Adapted from Tikhonova *et al*.[39] Created with BioRender.com

Class A GPCRs employ the Ballesteros-Weinstein numbering system, assigning two digits (in superscript) to each amino acid residue based on its position in the receptor.[40] The initial digit represents the helix number (1-8), while the subsequent digit denotes the residue's location relative to the most conserved residue, often identified as number 50. For example, 3.42 signifies a residue found in TM3, positioned eight residues

before the most conserved residue, Ala$^{3.50}$. This numbering convention extends to loop regions, where residues are numbered relative to the most conserved residues within those loops. However, variations may occur due to differences in conserved residues, especially in loop regions, potentially complicating the numbering process.[41]

In addition to the structural components of the receptor itself, signalling of CXC chemokine receptors involves interaction with an intracellular G protein partner/effector. Upon ligand binding, conformational changes in the receptor triggers the activation of G proteins, which are heterotrimeric complexes consisting of α, β, and γ subunits.[42] The four major classes of G proteins are categorized based on their α subunit: G_s (stimulatory), G_i (inhibitory), G_q (phospholipase C-activating), and $G_{12/13}$ (Rho-activating). These classes trigger specific downstream signalling pathways, including cAMP production, inhibition of cAMP production, activation of phospholipase C, and activation of Rho GTPases, respectively.[43,44] The Gα subunit contains a nucleotide-binding pocket between Ras-like and α-helical domains that, in the inactive state, are bound to guanosine diphosphate (GDP) and the Gβγ subunit.[45]

The ability of a GPCR to transduce signals from the extracellular to the intracellular region relies on its dynamic ability to undergo conformational changes. The conformations adopted by the receptor refer to the three-dimensional arrangement of atoms in the protein.[46] GPCRs can change their conformational state spontaneously, even in the absence of bound ligands or environmental changes.[46,47] Conformational changes are crucial for transitioning between conformational states such as unbound, active, and inactive. When bound to a diverse range of endogenous ligands, including ions, small molecules, peptides, and large proteins, can stabilize specific conformations thereby increasing the timescale which one conformational state is adopted. For example, the binding of CXCL8 to its native receptors CXCR1/2 will stabilise the active conformation increasing the population of active-state receptor.[44,46]

1.2.3 CXCR1/2 ligand binding and signal transduction

For Class A GPCRs, there exists a wide variety of orthosteric ligand binding sites in the TM bundle. These sites accommodate different types of ligands, including small molecules such as adrenaline, acetylcholine, dopamine, and prostaglandins, which bind within the TM bundle.[48-53] Peptides, on the other hand, engage extracellular loop

regions as well as TMs, while larger peptides like chemokines interact with both the N-terminus and extracellular loop regions.[2]

Chemokines binding to their receptors, such as CXCL8 binding to CXCR1 and CXCR2 can be described by two-step process (**Figure 1-5**). Initially, the chemokine interacts with the *N*-loop and nearby regions, termed chemokine site 1 (CS1), engaging with the *N*-terminal residues and ECLs of the receptor, defined as chemokine receptor site 1 (CRS1).[54-56] This interaction, dominated by ionic interactions, sets the stage for binding without triggering receptor activation. Following this, in the second step, the flexible *N*-terminal domain (including ELR motif for ELR^+ chemokines) and the 30s loops of the chemokine, known as chemokine site 2 (CS2), aligns with a second site on the receptor, chemokine receptor siter 2 (CRS2), which is located within TM bundle and ECL2 of the receptor.[56,57] This two-step model, proposed as a general mechanism for chemokine-receptor interactions, suggests that the initial interaction at CRS1 facilitates binding, while the subsequent interaction at CRS2 initiates receptor activation and signalling.[54,56,57] However, recent studies have shown that both CRS1 and CRS2 domains contribute to binding interactions, complicating the simplistic view of this two-step model.[54,55,57]

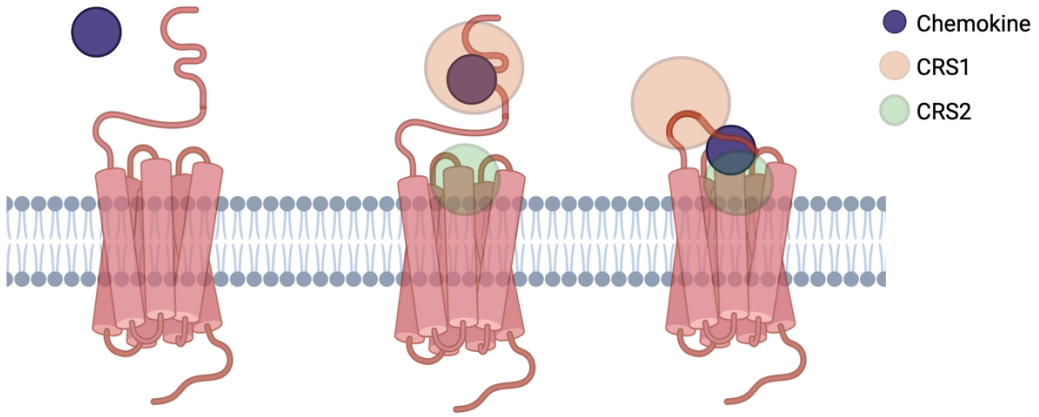

Figure 1-5 The two-step binding of a chemokine to its receptor. In the first step the chemokine interacts with its *N*-loop region to the *N*-terminal of the receptors (CRS1). Then, the *N*-terminal of the chemokine interacts with the TM bundle and ECL2 (CRS2). Created with BioRender.com.

Despite the diversity in orthosteric binding sites, class A GPCRs share a conserved mechanism of activation. Agonists binding to these receptors induce a 'rotational toggle switch' movement of the TM helices, particularly TM3 and TM6, resulting in

an outward movement and rotation of their cytoplasmic ends.[42,47,54,55] This conformational change alters the positions of the helices on the cytoplasmic face and affects the conformation of intracellular loops such as ICL3, exposing binding sites that can be recognized by G proteins.[58] Once a G protein binds to the activated receptor, the receptor acts as a guanine nucleotide exchange factor for the Gα subunit of the heterotrimeric G protein.[59,60] This promotes the release of GDP and the binding of GTP to the Gα subunit, initiating the G protein cycle and downstream signalling cascades.

Upon activation, the active state conformation of the receptor is stabilised, leading to the activation of the corresponding effector molecule.[2] The activation of GPCRs can mediate signalling *via* G proteins or G protein-independent pathways *via* arrestin recruitment.[38] Due to their importance, much interest has been given to the determination of GPCR-G protein complexes, and several have been determined since Rasmussen *et al*.[61] in 2011, including recent examples of utilising time resolved cryo-EM techniques for visualising the dynamic events driving G protein activation following GTP binding.[60]

1.2.4 G protein signalling pathway

Activation of the G protein proceeds through a nucleotide exchange on the surface of the G protein, replacing the bound GDP with guanosine triphosphate (GTP) on the α-subunit. The G protein then dissociates into the monomeric α-subunit and the dimeric βγ complex. These effectors then activate further secondary messenger pathways.

Figure 1-6 depicts the general activation of the G protein pathway. *C*-terminal conformational changes in the Gα subunit follow its binding to an activated receptor protein (R^*), facilitating GDP release and GTP interchange.[62] Specifically, this rearrangement occurs in the α-5 helix, which is the interface site of G protein-GPCR interactions in CXCR1/2.[54,55] Further related studies into G protein structural and mechanistic relationships have painted a more representative view of the activation and deactivation.[42,63] Gα undergoes a conformational exchange between three distinct states: GDP-bound (inactive), GTP-bound (active) and nucleotide-free (receptor coupled).[42] These states change from one to another *via* a conformational change at structurally distinct sites linked by weak allosteric coupling.[64] This includes the motion

of the α5 helix, nucleotide binding site opening, and changes in the Gβ/effector binding loop.[42,59] Activation of the G protein is terminated by the hydrolysis of GTP back to GDP on the α-subunit surface, followed by subsequent reassociation with the βγ complex allowing reassociation with the inactive GPCR.

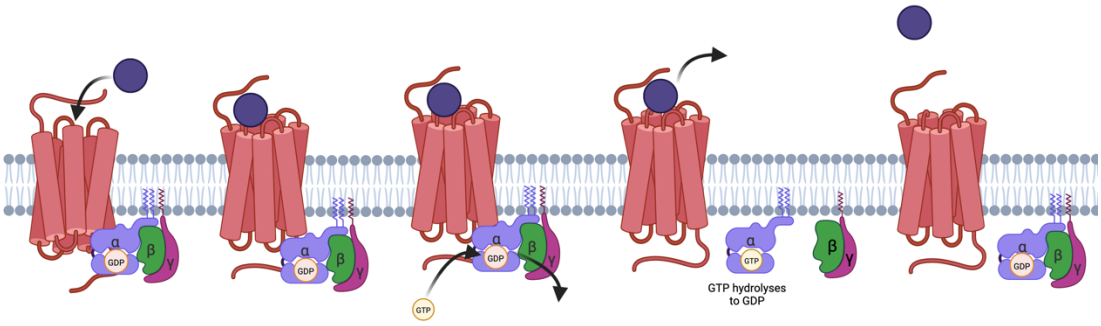

Figure 1-6 Activation of the G protein signalling pathway. From left to right: Ligand interacts through two step binding mode, stabilising the active, G protein conformation and mediating interactions with the G protein. Once bound, the G protein acts as a guanine nucleotide exchange factor allowing the exchange of GDP for GTP on the G protein α-subunit. This is followed by dissociation of the G protein into two species, the α and βγ subunits. Following activation, each subunit of the G protein proceeds to mediate various downstream signalling pathways. The Gα subunit, upon hydrolysing GTP to GDP through its intrinsic GTPase activity, facilitates the reassembly of the Gα-GDP complex with the βγ subunit. Subsequently, the dissociation of the ligand from the G protein-coupled receptor (GPCR) triggers a conformational change, returning both the GPCR and the G protein to their inactive states. This process effectively terminates the signal transduction initiated by the activated receptor. Created with BioRender.com

CXCR1 and 2 predominantly act through the G_i class of G proteins, which govern the pro-inflammatory effects of chemoattractant effectors and being of most importance to neutrophils.[65] Neutrophil activation through CXCR1/2 initiates a cascade of events crucial for the immune response. This activation triggers essential processes such as chemotaxis, adhesion, and transmigration, which direct neutrophils to the site of inflammation. Moreover, G protein signalling stimulates an increase in ROS production *via* the PI3K-Rac pathway and upregulates Ca^{2+} *via* PLC-β, contributing to the immune response.[15,66-69] ROS serve as potent antimicrobial agents, aiding in the destruction of invading pathogens.[68,69] By generating ROS, neutrophils enhance their

ability to neutralize pathogens and contribute to the clearance of infections.[15,68] Elevated intracellular Ca^{2+} levels play multifaceted roles in the immune response.[10,15] Ca^{2+} signalling facilitates processes such as phagocytosis, degranulation, and cytokine production in neutrophils. It regulates the cytoskeletal rearrangements necessary for migration and phagocytosis, ensuring efficient pathogen engulfment and destruction. Furthermore, Ca^{2+} influx triggers the activation of various signalling pathways involved in the release of inflammatory mediators, amplifying the immune response.[10,15,70]

Whilst CXCR1/2 are mainly associated with CXCL8 binding, other chemokines are known to interact with these receptors. While both CXCR1 and CXCR2 primarily bind to CXCL8, they also bind to other ELR^+ chemokines. CXCR1 exhibits a more limited binding profile, interacting primarily with CXCL8 and, to a lesser degree, CXCL6. In contrast, CXCR2 interacts with a broader range of chemokines, including CXCL1-3 and CXCL5-8 (**Figure 1-7**).[71-73] The differences in endogenous agonist binding can be attributed to variances in the amino acid sequence within the *N*-terminus of the receptors, which determines ligand binding specificity, despite their relatively high sequence similarity of 77%.[71] Variations in the binding affinity of agonists to receptors may result in biased agonism, wherein different ligands induce distinct conformational changes in the receptor.[74-77] These alterations can lead to the preferential activation of specific intracellular signalling pathways over others, ultimately resulting in diverse cellular responses. Boon *et al.*[74] demonstrated signalling bias upon CXCR2 stimulation by its chemokine ligands. Although no bias was identified within G protein or β-arrestin subtype activation, a distinct ligand bias favouring G protein activation over β-arrestin recruitment was associated with CXCL1-3 and CXCL5-7 activation.[74]

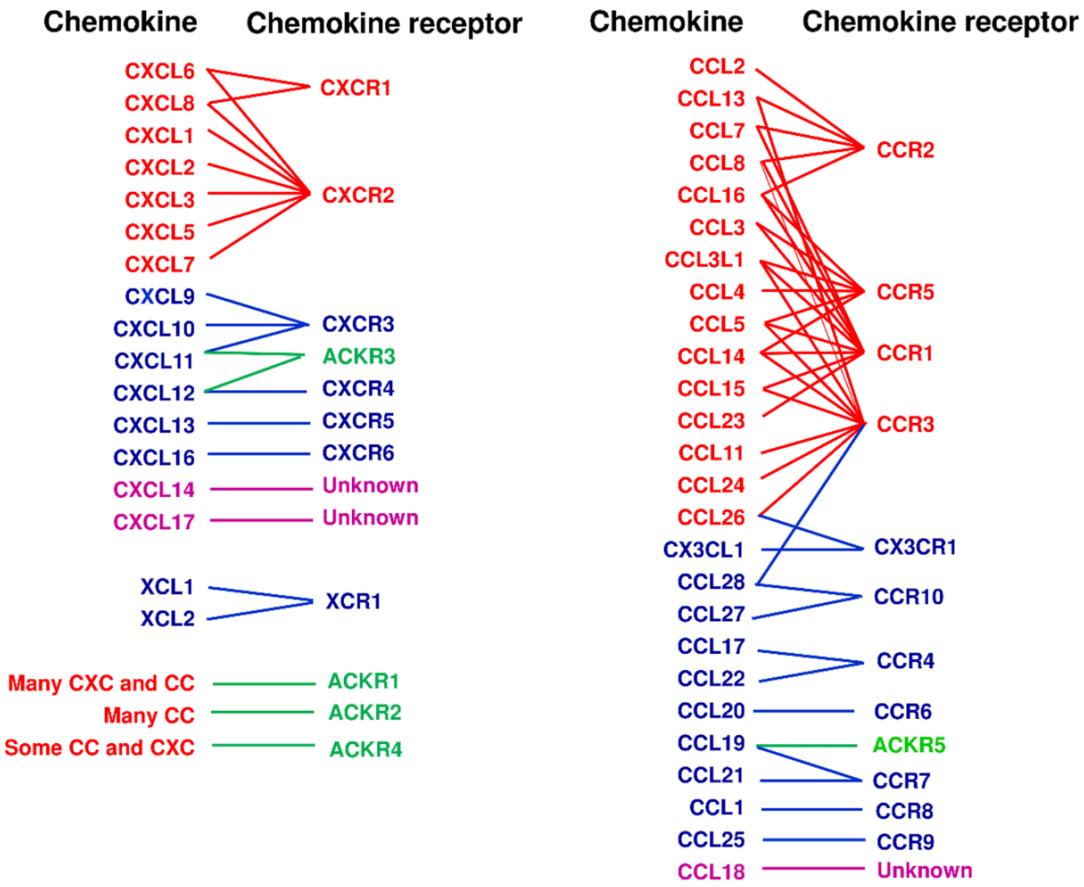

Figure 1-7 Overview of chemokines and their receptors. Inflammatory chemokines and their receptors are indicated in red. Immune chemokines (homeostatic/dual chemokines) are indicated in blue. Atypical chemokine receptors are indicated in green. Chemokines with unknown receptors are indicated in purple. Image taken from Yoshie *et al*.[78]

The signalling processes and secondary messengers associated with $G\alpha_i$ G proteins in neutrophils are depicted in **Figure 1-8**. The $G\alpha_i$ subunit is associated with inhibition of adenylyl cyclase activity, and consequently a decrease in cellular cAMP levels. This reduction in cAMP production leads to the attenuation of downstream signalling pathways, which are regulated by cAMP-dependent protein kinase A (PKA). In neutrophils, this attenuation of PKA activity is particularly crucial during the inflammatory response. Elevated cAMP and PKA activity serve to suppress key cellular processes involved in neutrophil activation, including chemotaxis, phagocytosis, and the release of inflammatory mediators.[79-81]

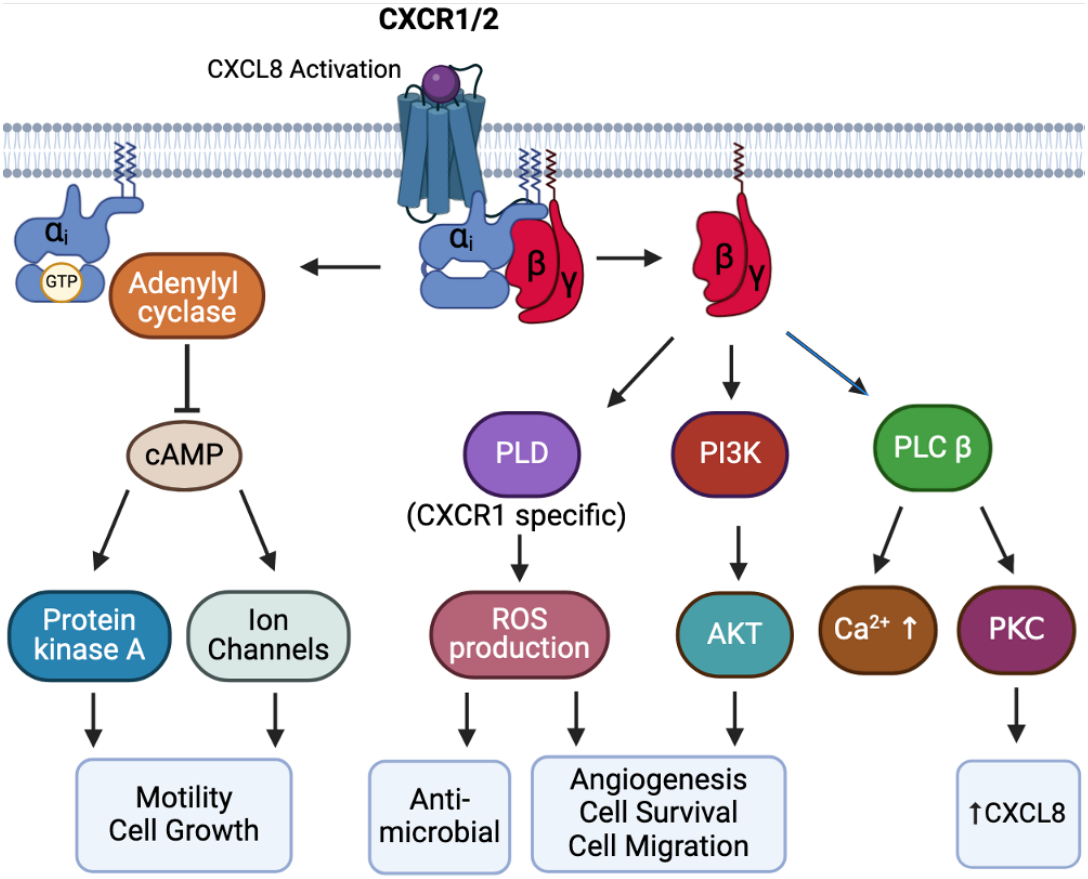

Figure 1-8 Overview of the signal transduction for G_i chemokine G protein coupled receptors. $G\alpha_i$ activation inhibits the adenylyl cyclase activity, reducing cyclic AMP (cAMP) production. The βγ-subunit independently activates the phosphoinositide 3-kinases (PI3K), phospholipase C (PLC) pathways in CXCR1 and CXCR2, along with *phospholipase D* (PLD) pathway in CXCR1. Created with BioRender.com

After dissociation from the $G\alpha_i$ subunit, Gβγ activates several pathways associated with neutrophil driven inflammatory response. The most notable pathways for neutrophil function are the Phospholipase C (PLC) and phosphoinositide 3-kinases (PI3Ks).[15,65] PI3K catalyses the conversion of phosphatidylinositol 4,5-bisphosphate (PIP_2) to phosphatidylinositol 3,4,5-trisphosphate (PIP_3), which leads to protein kinase B (AKT) activation.[82] The PLC pathway catalyses the conversion of PIP_2 to inositol triphosphate (IP_3) and diacylglycerol (DAG). This triggers Ca^{2+} release from endoplasmic reticulum (ER) stores and an increase in cytosolic Ca^{2+} levels. Ca^{2+} plays a vital role in neutrophil processes, including migration, neutrophil degranulation, and cytokine production.[79,82,83]

Despite CXCR1 and CXCR2 signalling through similar pathways for cell migration and granule release in neutrophils, CXCR1 is exclusively associated with phospholipase D (PLD) activation.[10] When activated, phospholipase D (PLD) triggers a cascade of events leading to the activation of nicotinamide adenine dinucleotide phosphate (NADPH) oxidase. This enzyme complex catalyses the conversion of molecular oxygen (O^2) into superoxide anions (O^{2-}) to produce ROS during a process known as the oxidative burst.[84] The oxidative burst is a vital antimicrobial mechanism utilized by neutrophils to combat pathogens.[10,85,86] In the context of CXCR1, it has been demonstrated that CXCL8-mediated signalling through CXCR1 is essential for initiating and sustaining the oxidative burst in neutrophils. This suggests that CXCR1 activation by CXCL8 is a key determinant in triggering the production of ROS and subsequent oxidative burst, thereby enhancing the antimicrobial activity of neutrophils.[10,84]

1.2.5 β-arrestin1/2 signalling pathway

Chemokine receptors, like other GPCRs, also activate G protein-independent pathways such as the arrestin pathway, important for receptor internalisation and desensitisation.[87-90] Receptors undergo a basal level of degradation and internalisation; however, binding of a ligand can enhance internalisation (ligand-induced internalisation). **Figure 1-9** depicts β-arrestin1/2-mediated internalisation of CXCR1 and 2. This mechanism begins with ligand binding that induces the phosphorylation of serine and threonine residues by GPCR kinases (GRKs).[10,89] There is currently no consensus on where phosphorylation occurs in CXCR1 and 2. Some papers describe phosphorylation occurring on the *C*-terminus and ICLs[91], whereas others describe only *C*-terminus phosphorylation.[89,92] Phosphorylation leads to β-arrestin1/2 recruitment to the agonist occupied and activated receptor, resulting in the uncoupling of the G protein and hindering further G protein interaction and subsequent G protein-mediated signalling. Arrestin acts as a scaffold for clathrin and β-2-adaptin-mediated endocytosis, leading to internalisation of the receptor.[86,89,93] It has been shown that CXCR2 also undergoes heterologous desensitisation *via* cross-phosphorylation, resulting in CXCL8 desensitisation by other chemoattractant receptors, such as formyl peptide receptor 1 (FPR1) and complement component 5a receptor (C5aR).[82] After

internalisation, receptor recycling can take place *via* mitogen-activated protein kinase (MAPK) pathways, which results in subsequent reintegration into the plasma membrane and resensitisation.[10,19,94] Alternatively, sorting of receptor containing endosomes to lysosomes can result in receptor protein degradation and long-term downregulation of signalling.

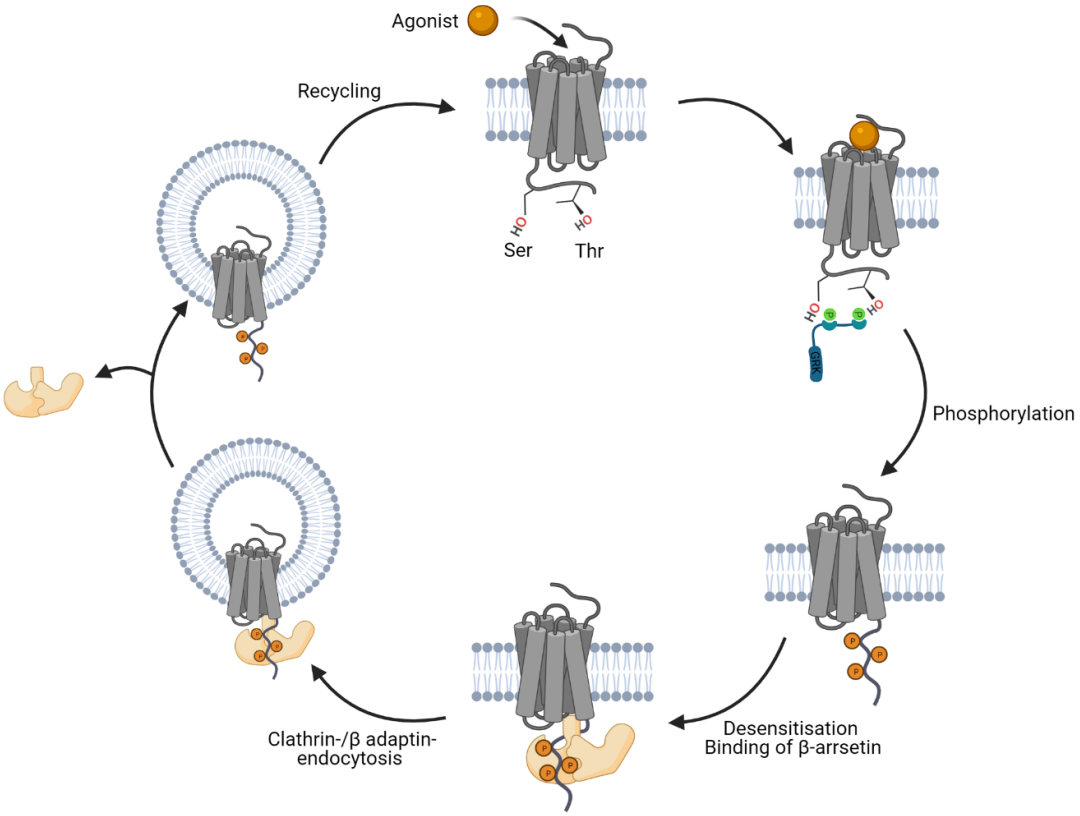

Figure 1-9 Arrestin-mediated desensitization and internalization of CXCR1 and CXCR2. Upon agonist binding, GPCR kinases (GRKs) phosphorylate specific serine and threonine residues on the receptor. These phosphorylated residues serve as binding sites for β-arrestin. Subsequently, β-arrestin facilitates the internalization of the receptor through endocytosis. Following internalization, the receptor undergoes dephosphorylation, leading to its recycling and resensitization, allowing it to respond to subsequent agonist binding events. Created with BioRender.com

The internalization dynamics of CXCR1 and CXCR2 present intriguing differences that may underscore their distinct regulatory mechanisms upon agonist binding. Internalisation of CXCR2 occurs at faster rates and at lower agonist concentrations

compared to CXCR1, suggesting that the regulation of the receptors differ in an agonist dependent fashion.[10,89,95]

1.3 Allosteric modulation of GPCRs

The conventional approach in targeting GPCRs therapeutically involves occupying and engaging the orthosteric binding site, which is where endogenous GPCR ligands naturally bind.[27,96] These drugs can either activate the receptor (agonists, partial agonists), inhibit its activation (antagonists), or induce an opposite functional response (inverse agonists). While a significant portion of marketed GPCR-targeted drugs operate through this mechanism, designing orthosteric ligands that are both safe and effective under diverse biological conditions presents notable challenges for chemokine receptors.[96,97] One of the challenges associated with targeting the endogenous binding sites for receptor activity modulation is the inherent competition with the endogenous ligand in physiological conditions.[98] For peptide receptors, such as CXCR1 and CXCR2, endogenous ligands exhibit high affinity for their respective receptors, posing a significant obstacle to the design of exogenous ligands that can effectively compete with them. This challenge is particularly pronounced in conditions characterized by elevated levels of endogenous ligands, such as chemokines during inflammation.[98,99] In these cases, designing ligands to achieve suitable efficacy for meaningful therapeutic outcomes is even more challenging.[99-101] Another challenge for designing ligands is target receptor specificity. Receptors across sub-family and classes of GPCRs often have highly conserved orthosteric binding sites.[98] Chemokine receptors, for example, exhibit highly conserved binding sites that allow promiscuous chemokines to bind. This is a key feature for chemoattractant receptors enabling the intricate relationship between chemokines and activation of differential downstream pathways (signal bias). The development of orthosteric ligands aimed at chemokine receptors frequently results in off-target side effects, often leading to undesired toxicity. These challenges stem from various factors, including the potential for inducible off-target effects and compromised receptor selectivity due to the high homology of orthosteric sites across the family. Additionally, targeting large and diffuse orthosteric sites activated by peptides or proteins poses inherent difficulties.[27,96,99] Allosteric ligands offer an alternative route for manipulation of GPCR response that attempts to address challenges with orthosteric ligands. Allosteric

ligands act through spatially and topographically distinct binding sites from the endogenous ligand(s) which offer potential subtype selectivity and tunability of receptor function (**Figure 1-10**).[96,102]

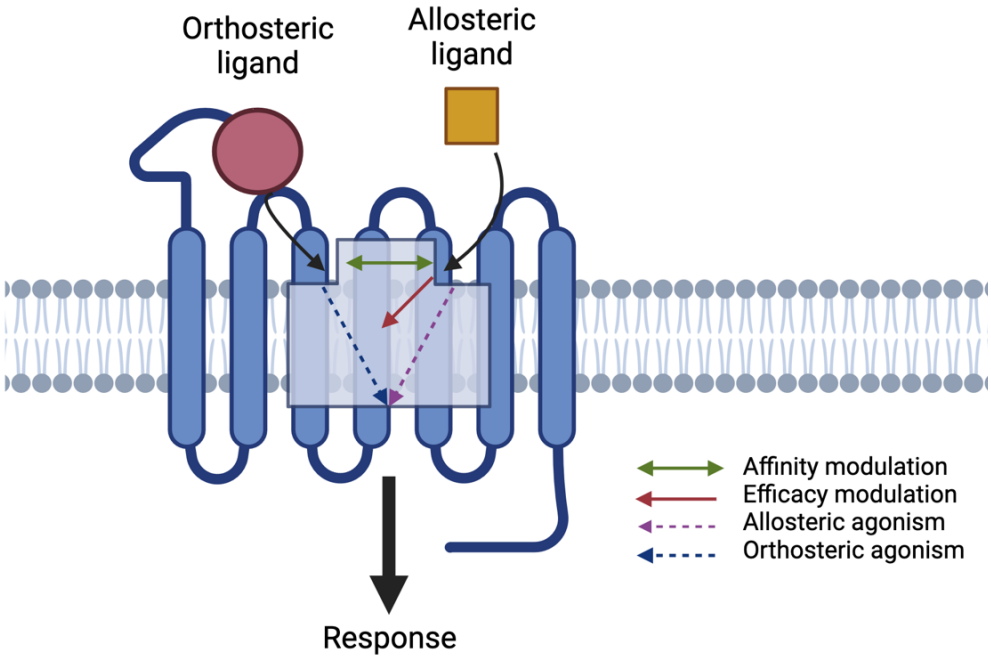

Figure 1-10 Allosteric modulation of class A GPCRs. Orthosteric and allosteric binding sites are topographically distinct sites within the receptor. Allosteric ligands have the potential to modulate the affinity of orthosteric ligand (and vice versa) (green arrow), the efficacy of the receptor (red arrow). Additionally, they may behave as direct agonists or reverse agonists (purple arrow) independently of the orthosteric ligand. Created in Biorender.

Allosteric ligands offer multiple modes of action that can modulate the innate activity of the receptor. Modulation of the receptor *via* an allosteric site, termed allosteric modulation, can occur *via* a conformational change of the protein, which can alter the affinity (and underlying association and/or dissociation rate) of endogenous ligands. This highlights the cooperativity of allosteric and orthosteric ligand binding that can occur, influencing the overall receptor activity in a dynamic and context-dependent manner.[77,103] Allosteric ligands can also affect the efficacy of the orthosteric ligand through modulation of the receptor's conformational response to their binding. The effect on the orthosteric agonist receptor response can be categorized as positive (PAM), negative (NAM), or silent allosteric modulation (SAM), depending on whether it enhances, diminishes, or leaves unchanged the orthosteric agonist

effect.[102,104] Direct effects on efficacy can also be exhibited by allosteric ligands, termed intrinsic efficacy, *via* the alteration of downstream signalling in either positive (agonism) or negative (inverse agonism) manner. Understanding of allosteric modulation offers promising avenues for designing therapeutics with enhanced specificity and efficacy in modulating therapeutically relevant GPCR signalling pathways.[27,103,104]

1.3.1 Allosteric modulators as therapeutics

Allosteric modulators offer several advantages as potential therapeutics for targeting GPCRs over orthosteric ligands.[105,106] The allosteric ligand's pharmacological effect, while potentially significant, can be constrained by the presence of the orthosteric ligand, thereby imposing a ceiling on the maximal allosteric effect. Unlike competitive antagonists, which exhibit increased inhibition with rising concentrations, allosteric modulation presents a ceiling to its influence on orthosteric responses. This enables precise adjustment of effects, allowing for desired modulation without triggering complete inhibition or activation of the orthosteric response. The degree of this ceiling effect varies depending on the co-operativity between allosteric and orthosteric ligands, as seen in cases like CXCR2 NAMs, which exhibit high negative co-operativity with chemokines, resembling antagonists.[107,108] This ceiling effect can be advantageous in designing therapeutics targeting GPCRs, particularly in contexts where overdose risks are prominent, such as opioid analgesics.[96,103,109]

Allosteric modulators offer the potential for sub-type selective ligands, presenting a distinct advantage over orthosteric ligands. Typically, GPCRs can be activated by multiple endogenous ligands, which can activate several receptors. An example of this is the previously stated shared binding of CXCL8 to CXCR1 and CXCR2, and other promiscuous chemokine ligands. Orthosteric binding sites must accommodate these diverse ligands, generally leading to highly conserved regions across receptor families.[2,10,73,110] In contrast, allosteric sites typically lack endogenous ligands or have only a few known ligands. Consequently, these sites may be less conserved, allowing for the design of ligands with desirable high selectivity.[106,109,111] Moreover, allosteric ligands can achieve high selectivity through their cooperative action with specific ligands.[109,112] This potential selectivity is particularly appealing to drug discovery

programs seeking highly specific therapeutic agents or modifications to ligands with undesirable off-target effects.

Another advantage is the ability of allosteric ligands to specifically "tune" the biological response of the receptors. By selectively modulating the receptor's response to endogenous ligands, allosteric ligands can adjust signalling pathways to achieve desired therapeutic outcomes.[105,106,113] This fine-tuning capability is particularly advantageous in complex diseases where dysregulated receptor signalling contributes to pathogenesis. Additionally, the ability to selectively target specific signalling pathways or cellular responses offers opportunities for therapeutic intervention with minimal disruption to normal physiological processes. The ability to modulate specific signalling pathways has been demonstrated in the CXC chemokine receptor, CXCR3. Bernat *et al.*[114] designed a series of boronic acid analogues acting on CXCR3 based on molecular docking into homology models. One of these derivatives was reported as the first reported biased NAM of CXCR3 displaying 24-fold selectivity acting upon recruitment of β-arrestin2 over the G protein activation upon CXCL11 stimulation.[105,114]

The cooperativity observed between allosteric and orthosteric ligands also raises specific considerations when attempting to characterise these ligands in biological assays. As the binding and efficacy of an allosteric ligand is dependent on the orthosteric ligand, careful consideration must be given to the choice of ligand.[111,115,116] This is highlighted in the case of chemokines like CXCR1 and CXCR2 where there is more than one endogenous agonist, and use of a single agonist does not always adequately represent the efficacy of the allosteric ligand. In such cases, utilizing multiple endogenous agonists becomes crucial for accurately characterizing the modulatory effects.[105,115] Another consideration when characterising allosteric ligands in different biological models is the potential for species variability in cooperativity between the allosteric and orthosteric ligands. This may be highlighted when transitioning between *in vitro* assays and animal models when the allosteric ligand is characterised in human GPCR and *in vivo* animal models where the pharmacological profile is not replicated due to the difference in cooperativity between the allosteric and orthosteric ligands between species.[105]

1.3.2 Rational design of allosteric ligands

The first GPCR allosteric modulator approved for use was cinacalcet, in 2004 (sold under Sensipar), for the treatment and management of secondary hyperparathyroidism by targeting the calcium-sensing receptor (CasR).[106,117] Following this, several other allosteric modulators targeting GPCRs have made it to market, including the selective CCR5 antagonist, maraviroc (sold under Selzentry), approved in 2007.[106,118] In a review of known allosteric ligands conducted by van Westen *et al*.[119] in 2014 it was noted that allosteric modulators tend to be more lipophilic and have more constrained structures compared to orthosteric ligands. Additionally, they exhibit relatively better adherence to desirable physicochemical properties from an oral-formulation perspective, which would allow for easier translation into a drug candidate. Their review also corroborated some of the potential advantages of allosteric modulators. They noted that allosteric ligands tend to be less promiscuous than orthosteric ligands, which was previously stated to be beneficial for reducing off-target effects.[119] The identification of the different physicochemical properties that exist between orthosteric and allosteric ligands could help identify candidates that exhibit desirable allosteric properties. Additionally, these properties could allow the creation of classification models and predicative models for further ligand design.

Despite the interest in allosteric modulators in drug discovery, the rational design of allosteric drugs has lagged, likely due to the incomplete understanding of the intricacies involved with allosteric binding and activity. Several databases currently exist that house data for allosteric ligands and allosteric binding pockets such as allosteric database (ASD)[120], ASBench[121], and Kinase Atlas.[122] Additionally several web server-based tools have been developed for rational allosteric ligand design, such as AlloSite[123] for prediction of allosteric binding sites and AlloFinder[124] for allosteric modulator discovery.[125] These computational tools are one of the ways in which rational allosteric ligand design have improved over the past decade however there are still substantial limitations, such as access to experimental data, and technical limitations. As previously described, the interplay between allosterism and receptor activity is extremely complex and dynamic which are difficult to capture and interpret in both experimental and in silico models.[119,125,126] The challenges faced in the rational design of allosteric ligands has been reviewed extensively. However, there is a clear

overlap is the need for higher quality protein receptor structures bound to ligands relevant to the allosteric site of interest, particularly with GPCRs as allosteric pockets can often be difficult to distinguish.[106,119,125-127]

1.3.3 Evidence for CXCR1 and CXCR2 allosterism

Several allosteric sites have been identified across GPCRs, with the majority close to the orthosteric site but are still able to manipulate GPCR function through conformational changes or assembly of the receptor complexes.[98,112,128] With the acceleration of GPCR elucidation several crystal structures have identified allosteric binding sites, such as for chemokine receptors CXCR2[54], CCR9[129], CCR2[130], CCR5[131] and CCR7.[132,133] These five structures exhibit a spatially overlapping intracellular binding site enclosed by TM1,TM2, TM3, TM7 and H8 (**Figure 1-11**). The crystal structure of CXCR2 in complex with diaryl squaramide NAM, 00767013 (**1**) supported previous biological reports by Salchow *et al.*[134] and Bertini *et al.*[135] describing a putative intracellular binding site identified in CXCR1 and CXCR2.[54,134-137] Comparisons between the active CXCL8-CXCR2-Gα_i with Cryo-EM CXCL8-CXCR2-00767013 (**1**) by Liu *et al.*[54] described the binding site of 00767013 (**1**) overlapping with the α-5 helix of the Gα_i suggesting a mode of action by which the IAM interferes with G α interacting with the receptor. The nature of this binding site along with comparisons of available structural data is further explored in **Chapter 2**.

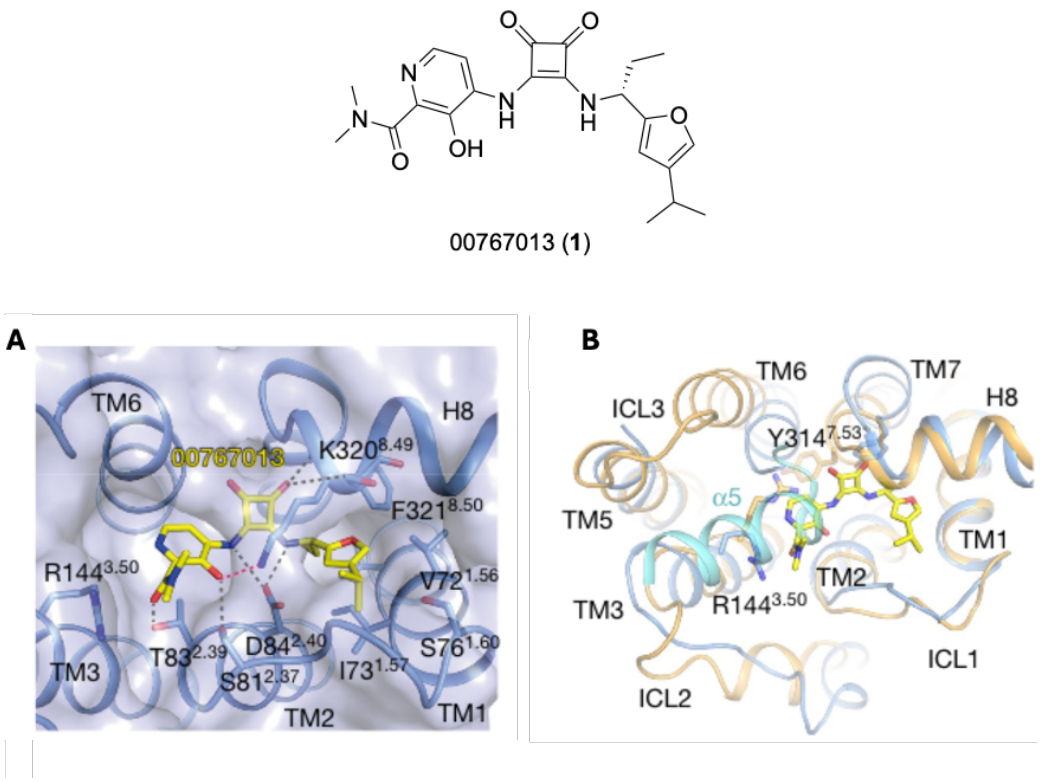

Figure 1-11 Allosteric antagonist 00767013 (**1**) binding interactions with CXCR2. (A) 3D view of 00767013–CXCR2 interactions from the intracellular side. CXCR2 is depicted as a blue cartoon and shaded surface representation. Ligand 00767013 (**1**) is shown as yellow sticks. (B) Structural comparison of active (orange) and inactive (blue) CXCR2, viewed from the cytoplasmic side. The 00767013 (**1**) (yellow sticks) overlaps with the binding of the α5 helix of Gαi (cyan cartoon) with CXCR2. Image taken from Liu *et al*.[54]

The biological reports by Salchow *et al*.[134] and Bertini *et al*.[135,137] show significant overlap in the important binding residues of the intracellular binding site of CXCR2 compared to the CXCR2-00767013 (**1**) crystal structure. The studies conducted by Salchow *et al*.[134] described site directed mutation experiments. In their findings D84N$^{2.40}$, T83A$^{2.39}$, A249L$^{6.33}$, and K320A$^{8.49}$ mutations were introduced and demonstrated 70, 40, 280, 30-fold reductions in affinity of navarixin (**2**), respectively, compared to wild type CXCR2 (determined by [^{35}S]GTPγS binding assays in Chinese hamster ovarian cell (CHO) membranes) (**Table 1-2**). The CXCR2-00767013 (**1**) crystal structures showed D84$^{2.40}$, T83$^{2.39}$, and K320$^{8.49}$ as important residues in proximity to the ligand to make hydrogen bonding and in the case of K320$^{8.49}$ ionic interactions with the ligand. Notably, in mutational studies, A249L$^{6.33}$ displayed the

largest reduction in binding affinity with a 280-fold reduction when mutated to L249$^{6.33}$. However, the crystal structure introduced a A249E$^{6.33}$ mutation, which did not appear to significantly alter the functional response of the receptor.[54,134]

Table 1-2 K_d values for [^{3}H]navarixin (**2**) determined from saturation binding experiments in CHO membranes expressing wild type and mutated CXCR2 receptor. Data shown are mean ± SEM. Data taken from Salchow *et al*.[134]

Mutation	**K_d (nM)**	**Fold-shift (mutant/wild-type)**
Wild type	0.059 ± 0.018	-
K320A$^{8.49}$	1.82 ± 0.39	30.8
Y314A$^{7.53}$	0.415 ± 0.097	7.0
A249L$^{6.33}$	16.52 ± 0.915	280.1
D84N$^{2.40}$	4.10 ± 2.23	69.5
T83A$^{2.39}$	0.694 ± 0.234	11.8
T83L$^{2.39}$	2.47 ± 0.78	41.9
D143R$^{3.49}$	0.804 ± 0.351	13.6

Whilst a crystal structure for CXCR1 in complex with an intracellular allosteric modulator is not currently available, biological data, along with amino acid homogeneity in the region supports the overlap of the binding site of diaryl squaramide ligands identified by Liu *et al*.[54,134,136,138]

1.4 CXCL8-CXCR1/2 axis in cancer and inflammatory diseases

As previously discussed, the CXCL8-CXCR1/2 axis plays a vital role in neutrophil homeostasis. The dysregulation of this axis or its downstream signalling pathways can lead to impaired immune function leading to the dysregulation of the inflammatory response, an important factor in many biological systems including, respiratory, digestive, cardiovascular, and nervous systems.[13,65,67] Therefore, there is great scope for diseases that CXCR1 and CXCR2 are implicated in as well as the need for biological modulators of these receptors for the treatment of inflammatory conditions is humans. The following summary of specific diseases in which targeting the CXCR1/2 axis could prove to be therapeutically beneficial.

1.4.1 Respiratory diseases

Respiratory diseases encompass diseases of the airways and other structures of the lung, and typically affect specific functions of the lung.[139,140] Among the most prevalent is chronic obstructive pulmonary disease (COPD), characterized by airflow limitation that primarily involve the airways and alveoli. In COPD, chronic inflammation damages the airway walls and leads to narrowing and destruction of alveoli.[140] The progression of COPD is associated with the recruitment and activation of immune cells such as macrophages and neutrophils to the affected areas of the lung, leading to chronic inflammation. Initial investigations into the role of chemokines in COPD progression found that increased levels of CXCL8 were identified in the sputum of COPD patients compared to healthy patients.[141] Studies have shown that increased CXCR1 and 2 expression along with associated chemokines, CXCL8 and CXCL5 (CXCR2 exclusive) have been observed in bronchial biopsies of COPD patients in a study by Qiu *et al.*[142] Additionally, CXCL1 expression has also been observed in the epithelial cells of COPD patients. CXCL1 binds to CXCR2 selectively over CXCR1 and is also associated with increased chemotaxis of neutrophils.[143] This study further concluded that during severe exacerbations of COPD, CXCL5-CXCR2 axis is preferentially stimulated and thus distinct from CXCR1 stimulation.[142,144] Exposure to environmental stimuli implicated in causing COPD, such as smoke and pollutants, has been shown to be a major trigger for the overexpression of CXCL8 and

its receptors CXCR1/2.[145,146] This leads to stimulation of epithelial cells in the airways by CXCL8, initiating a cascade of events that result in contraction and increased airway permeability to inflammatory cells.[10]

Investigations into the use of small molecule antagonists targeting CXCR2 are underway with promising clinical trial candidates in navarixin (**2**) developed by Schering-Plough (now under Merck) AZD5069 (**3**) developed by Astrazeneca (AZ), and danirixin (**4**) developed by GSK (**Figure 1-12**).[147-149] Early clinical data for danirixin (**4**) in COPD demonstrated promising target/receptor coverage in ex vivo studies, with significant reductions in blood neutrophils observed in patients with bronchiectasis. However, despite high receptor occupancy levels, it did not show efficacy in improving COPD outcomes, such as exacerbation rates or lung function.[15,149-151] GSK have since stopped the development of danirixin (**4**) as treatment for COPD.[15] Oral administration of navarixin (**2**) displayed ~50% reduction in sputum neutrophil counts whilst also showing an increase to forced expiratory volume (FEV1), a measure of breathing obstruction. Despite this, there was no improvement to COPD symptoms or a reduction in exacerbations.[14,15,147] Overall, whilst targeting CXCR2 presents a promising therapeutic approach for COPD by specifically addressing neutrophilic inflammation, efficacy of small molecules has yet to be demonstrated.

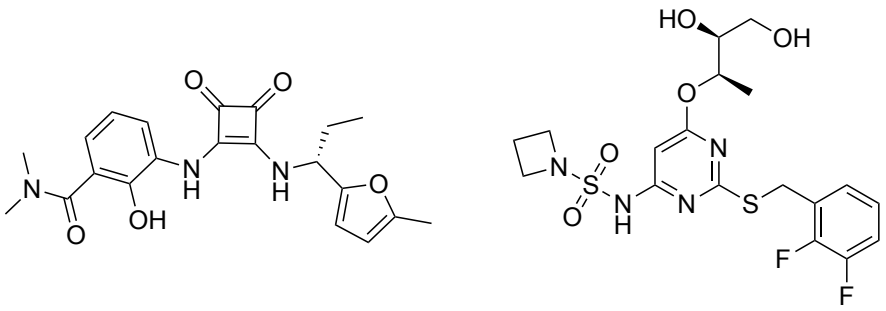

navarixin (**2**)

AZD5069 (**3**)

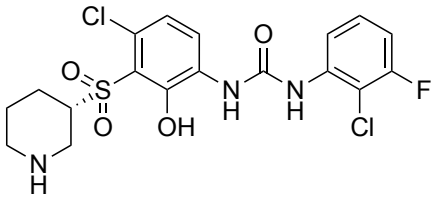

danirixin (**4**)

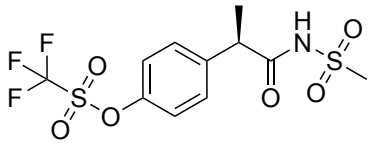

ladirixin (**5**)

Figure 1-12 Chemical structures of navarixin (**2**), AZD5069 (**3**) and danirixin (**4**)

Asthma, a chronic disorder, is marked by airway inflammation, increased mucus production, and constriction of the airways. Neutrophils have a multifaceted role in this condition, contributing to the complex inflammatory processes involved in asthma pathogenesis. While asthma is traditionally considered a disease primarily driven by eosinophilic inflammation, recent research has highlighted the involvement of neutrophils in various aspects of asthma pathophysiology. Studies into asthma pathology have shown that the expression of CXCL8 is markedly increased in lung epithelium, sputum, and peripheral blood in patients with asthma.[10,152-154] Experiments have found a direct relationship between the severity of asthma symptoms and the levels of CXCL8, along with other ELR$^+$ CXC chemokines, in lung tissue and bronchoalveolar cells.[144,155] Furthermore, the expression of the receptors for these chemokines, namely CXCR1 and CXCR2, has been observed to increase in response to elevated levels of CXCL8 and other ELR$^+$ CXC chemokines.[10,144,153,156-158] Additionally, stimulation of CXCR1/2 *via* CXCL8 on eosinophils induce further eosinophil chemotaxis that releases inflammatory mediators and toxic proteins, which further contributes to inflammatory symptoms in the airways.[10] It is estimated up to 300 million people worldwide are affected by some degree of asthma, and whilst patients with mild to moderate symptoms respond well to inhaled glucocorticoids, these therapies perform poorly in patients with severe forms of the disease.[158,159] The

use of small molecule treatments for targeting CXCR1 and CXCR2 stimulation are already underway. Ladirixin (**5**), acting at both CXCR1 and CXCR2, has shown to reduce the inflammatory effect in mice models induced with asthma and COPD. In the same study ladirixin (**5**) showed anti-inflammatory effects in steroid-refractory models compared to dexamethasone, a corticosteroid. This displays the ability of ladirixin (**5**) to address limitations of corticosteroid therapies in severe asthma and COPD cases.[158] With the crossover of molecular mechanisms between COPD and asthma, clinical candidates which have emerged as CXCR1/2 antagonists such as navarixin (**2**) and AZD5069 (**3**) have advanced to phase II trials as treatments for both COPD and severe neutrophilic asthma. Patients treated with oral AZD5069 (**3**) over a 6-month period showed no improvements in severe asthma symptoms or exacerbations.[160] Similarly, navarixin (**2**) failed to improve asthma control and lung function in asthma patients after oral administration over a 4-week period (NCT00688467).[161,162] Additionally, notable reduction in neutrophil count led to the discontinuation of clinical trials. Despite the promising *in vivo* studies into the use of CXCR1/2 antagonists, these therapeutics, thus far, share the same fate as the treatment of COPD, where their efficacy concerns have hampered their development for severe asthma treatment.[14,15]

1.4.2 Psoriasis

Psoriasis is a persistent inflammatory disease caused by an accumulation and infiltration of neutrophils, T lymphocytes, keratinocytes, and macrophage in the dermal and epidermal areas of skin. The production of neutrophils in the affected area are regulated *via* chemotactic factors, such as the large influx of CXCL8 and CXCL1, the latter only binding to CXCR2.[163] Studies conducted on the contents of psoriatic scales have also shown that both CXCR1 and CXCR2 receptor expression are upregulated in affected cells from various areas of the body.[164] Further studies have shown similar upregulation of CXCR1 and CXCR2 receptors, with more emphasis on CXCR2 in many cases.[163,165,166] Sumida *et al*.[167] showed that CXCL ligands activating CXCR2 facilitate disease progression and early-stage inflammation through the enhancement of the LTB_4-BLT1 axis in keratinocytes.[167] Targeting the chemokine pathway presents a promising therapeutic approach to ameliorating the condition of psoriatic cells.[168] Nevertheless, there has been a lack of recent updates assessing CXCR1/2 antagonists for the treatment of psoriasis, with the most recent being a phase

II clinical trials investigating the oral administration of navarixin (**2**) for treating psoriasis (NCT00684593), last updated in 2008. Further research and updates are necessary to assess the efficacy and potential of this intervention in managing psoriasis effectively.

1.4.3 Cancer

There is a complex relationship between inflammation and cancer that significantly influences tumour development and disease progression. Chronic inflammation, whether initiated by infectious agents, autoimmune diseases, or environmental factors, creates a microenvironment that promotes tumorigenesis. The role of chemokines and cancer progression has been explored extensively in previous reviews.[10,13,15,73,169,170] The CXCL8-CXCR1/2 axis is one of many chemokine mediated pathways that have been implicated with the proliferation and migration of tumour cell. CXCL8 directed neutrophil recruitment to the extracellular space surrounding cancer tissue is a major contributor to tumorigenesis and negatively corelates to patient prognosis.[15,171] The increased secretion of CXCL8 has been observed in the tumour microenvironment (TME) of multiple types of cancer including non-small cell lung cancer (NSCLC)[172,173], melanoma[174-176], prostate[177,178], pancreatic[179,180], breast[181,182] and lung.[183-185] Due to its involvement in tumour progression and metastasis, CXCL8 levels in the tumour microenvironment (TME) or in plasma levels have been proposed as biomarkers for assessing disease severity and predicting patient outcomes.[10,170,183] Moreover, the presence of neutrophils within the TME has been linked to immune suppression and resistance to treatments such as chemotherapy, molecular targeted therapy, and immune checkpoint inhibitors (ICI).[10,177,183,186] One of the limitations ICI therapies is therapeutic resistance observed in some patients resulting in poor therapeutic response. Recent studies have suggested that CXCL8 expression in plasma corelates to patient response to ICI therapies in NSCLC.[177,187] Therefore, the identification of patients with ICI resistance could improve the clinical outcomes. Furthermore, understanding the mechanisms underlying CXCL8-mediated resistance to ICIs and other cancer therapeutics could provide valuable insights into tumour immune evasion mechanisms and facilitate the development of novel therapeutic approaches to overcome resistance.[183,188] Targeting the CXCL8-CXCR1/2 axis or modulating neutrophil recruitment and function within the tumour microenvironment

are potential strategies to enhance the efficacy of ICIs and overcome resistance in cancer patients.[10,184,189 75,198,205]

1.5 Rationale for targeting CXCR1, as well as CXCR2 for therapeutics

The CXCR1/2 receptors have been identified as playing a key role in multiple neutrophil-mediated inflammatory diseases, such as COPD, asthma, and psoriasis, which have been discussed.[14,155,190] Whilst preclinical evidence has been promising for small molecules targeting these diseases, there has been a clear trend of the efficacy challenges faced by CXCR1 and CXCR2 antagonists, particularly those targeting the intracellular allosteric binding site such as navarixin (**2**) and AZD5069 (**3**). Further clinical studies are necessary to elucidate the potential for CXCR1 and CXCR2 therapeutics in the treatment of inflammatory diseases. Recent evidence has detailed the importance of neutrophils in the development and progression of cancer, with studies showing promising results in targeting the CXCL8-CXCR1/CXCR2 axis. The roles of CXCR1 and CXCR2 in multiple human cancers have been discussed in reviews.[10,13,15,175,191] There are several studies that have detailed the differential roles that CXCR1 and CXCR2 may play in tumorigenesis. Following is evidence for the potential of selectively targeting the CXCR1-CXCL8 axis in cancer.

Cancer stem cells (CSC) make up a small proportion of cancer cell populations in solid tumours, but they are thought to be crucial in the tumorigenesis as they exhibit stem cell-like properties that allow self-renewal and chemoresistance.[10,84,192] Studies have highlighted the CXCL8-CXCR1 axis for its role in CSC proliferation in multiple human cancers. Chen *et al*.[193] observed an upregulation of the expression of CSC markers. CD44 and CD133 were associated with CXCR1 expression, as well as an increase in the proportion of CSC observed in tumour formations taken from pancreatic cancer samples of patients. Additionally, they investigated the growth of tumour spheres in the presence of an anti-CXCR1 antibody compared to the absence of the CXCR1 antibody. They observed a reduction in tumour sphere size along with reduced CXCL8 induced expression of CSC biomarkers, CD22 and CD44.[193] CXCR2 has also been associated with pancreatic cancer and dual CXCR1/2 antagonist ladarixin (**4**) has been investigated in mouse models for its ability to improve the efficacy of immune checkpoint inhibitors. Ladarixin (**4**) showed promising results in

reducing tumour growth and metastases in mouse models by targeting both CXCR1 and CXCR2 signalling pathways. This dual inhibition approach holds potential for overcoming resistance to current chemotherapy regimens, although the understanding of how each of these pathways contribute to reducing chemoresistance is still unclear. In this context it is possible that selective CXCR2 or CXCR1 targeting would not be as effective.

In breast cancer, CXCR1 has been identified as a target for CSC with expression of CXCR1 mRNA observed in *in vitro* breast cancer cell lines.[194,195] Studies conducted on biopsies taken from breast cancer patients observed a corelation between the progression and severity of breast cancer and the increased expression of CXCR1. The study found that, after neo-adjuvant chemotherapy treatment, CXCR1 expression decreased. Additionally, the degree of reduced expression correlated with increased pathological response to treatment and increased efficacy of neo-adjuvant chemotherapy.[185] This increased expression was observed in $ALDH^+$ cell populations, which are associated with the maintenance and differentiation of CSCs. Additionally, this expression of CXCR1 was exclusive to $ALDH^+$ cell populations, suggesting that CXCR1 plays a vital role in CSC proliferation and self-renewal.[194] Tumorigenicity of $ALDH^+$-$CXCR1^+$ and ALDH-$CXCR1^-$ cells were assessed after transplantation in mice models. Whilst $ALDH^+$-$CXCR1^+$ cell populations regenerated expected cell compositions, $ALDH^+$-$CXCR1^-$ showed restricted differentiation suggesting that cellular differentiation and hierarchy is driven by CXCR1 expression.[194] The same study also assessed the use of CXCR1-antibody and 400-fold CXCR1 (vs CXCR2) antagonist reparixin (**6**) (**Figure 1-13**). They observed a dose dependent response to decreased $ALDH^+$-cell viability within 3 days of incubation and in turn induced cell death, despite $CXCR1^+$ populations representing less than 2% of the tumour cell population.[194] Clinical trials are currently underway for the use of the CXCR1 selective allosteric antagonist reparixin (**6**). Phase 2 trials conducted by Goldstein *et al.*[196] on twenty patients with operable HER-2-negative breast cancer showed promising results regarding the tolerability and safety of reparixin (**6**). The oral administration of reparixin (**6**) every 6-8 hours over a 21-day period was deemed tolerable and no adverse reactions were observed. Absolute neutrophil counts (ANC) were also recorded in patients with no sustained decrease. This contrasted with observations in phase I trials where patients treated with selective CXCR2 antagonists,

AZD5069 (**3**) and navarixin (**2**) displayed reversible neutropenia.[170,196-198] Additionally, it was noted that reductions in $CXCR1^+$ cells were observed in most patients suggesting a reduced recruitment of $CXCR1^+$ cells. Whilst this study does present promising results for the therapeutic targeting of CXCR1 in breast cancer, the clinical relevance is still in question due to the short window of the study, which is not likely to demonstrate the ability for reparixin (**6**) to reduce tumour proliferation or survival.[196] Following phase II clinical trials in patients with metastatic triple-negative breast cancer, reparixin (**6**) failed to show beneficial therapeutic efficacy for progression-free survival (PFS) after administering reparixin (**6**) in combination with paclitaxel over a 21-day period.[199] The negative results of this trial do question the use of CSC targeted therapies in late-stage cancer, but may still be beneficial for early stage and metastatic prevention treatment.[15,196,199]

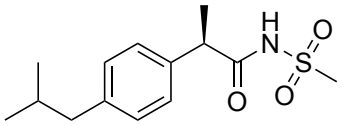

reparixin (**6**)

Figure 1-13 Chemical structure of reparixin (**6**)

Glioblastoma multiforme (GBM) is a fast-growing and aggressive brain tumour which has poor prognosis due to no treatments available with clinical efficacy. Sharma *et al*.[200] investigated the role of CXCL8 in the TME of tissue samples from patients. They noted that the CXCL8-CXCR1/2 axis was directly associated with the growth of GBM by promotion of cell proliferation an invasion in the TME. The study employed a lysine salt of allosteric antagonist reparixin (**6**), which is 400-fold selective for CXCR1, and demonstrated significant reduction in tumour cell proliferation. Furthermore, the researchers observed that CXCL8 promoted neovascularization by binding to CXCR1, as evidenced by increased CXCR1 expression in tumour vasculature.[200] Comparisons to the expression of CXCR2 showed that, whilst CXCR1 was upregulated in the tumour cells and tumour-associated vessels, CXCR2 expression was only observed in the tumour cells.[84,200] Further, whilst dual anti-CXCR1 and anti-CXCR2 antibodies had an additive effect on reducing tumour cell proliferations, disruption to the angiogenesis was observed when CXCR1 was neutralised alone.[200] Another study conducted by Zhang *et al*.[201] also noted the

difference in expression between CXCR1 and CXCR2 in glioma samples taken from patients. This study agreed that glioma cells upregulate CXCR1 however in contrary to Sharma *et al.*[200], they observed no increased CXCR2 expression. This led them to the conclusion that CXCL8 acts mainly with CXCR1 in the progression of glioma.[201]

Extensive research has focused on understanding the roles of CXCR1 and CXCR2 in breast cancer. Studies investigating the chemotactic effects of the CXCL8-CXCR1/2 axes have indicated that CXCR1 alone mediates CXCL8 chemotaxis in metastatic melanoma cell lines.[202] After the mixing of metastatic melanoma cells with CXCR1 and CXCR2 antibodies, it was observed that, whilst CXCR1 displayed a dose dependant reduction in chemotaxis of Wistar melanoma (WM)239 metastatic melanoma cells, CXCR2 didn't exert any significant effects on the chemotactic response.[202] This study also noted the differential expression of CXCR1 and CXCR2 in metastatic and non-metastatic melanoma cells. Whilst CXCR2 expression was similar in non-metastatic (WM35, derived from the radial growth phase) and metastatic (WM239 derived from secondary metastases) cells, CXCR1 expression was increased 20-fold in WM239 cells compared to the WM35. This suggests that CXCR1 plays a specific role in the spread of melanoma cells.[202]

Research on CXCR1 and CXCR2 as therapeutic targets is still evolving, particularly in their application for cancer treatment. It is currently unknown whether targeted therapies for selective CXCR1 or CXCR2 would be clinically beneficial compared to dual inhibitors. However, dual targeting may lead to increased toxicity and off-target effects, which needs to be considered. There is a clear need to investigate the individual roles of CXCR1 and CXCR2 in the progression of inflammatory diseases and cancer. Developing small molecule tools that selectively bind to either receptor would progress our understanding of these receptors and delineate their individual modes of action regarding progression *in vitro* and *in vivo* models. This, in turn, would allow for the development of therapies that may hold the key to overcoming the current efficacy issues faced with CXCR1/2 therapeutics currently under investigation. Additionally, the selective targeting of CXCR1 may be beneficial as this receptor is less promiscuous than CXCR2, only strongly binding to CXCL6 and CXCL8, whereas CXCR2 binds to CXCL1-3 and 5-8.[2,169] Consequently, one could envisage a scenario where a CXCR1 selective antagonist could mitigate the adverse effects on regular

inflammatory control compared to a dual CXCR1/2 antagonist or selective CXCR2 antagonist.

1.6 Medicinal agents targeting CXCR1/2

The development of chemical compounds aiming to target CXCR1/2 has been an active area of research since 1996, and several patents have been filed claiming additional series of compounds. With the expanding understanding of chemokine receptors and their potential therapeutic effects, there is a growing financial interest in this field. Most of the CXCR1/2 targeting ligands developed follow from the early work conducted by GlaxoSmithKline (GSK), with a urea or urea-like core being present. An exception to this is the work conducted by Dompé SPA, however evidence would suggest that their series of compounds act on a different allosteric binding site to the urea class of compounds.[134,135] The following is a record of the efforts made by some of the major pharmaceutical companies with a publicised interest into the drug development of this CXCR1/2 targeting small molecules, including the patents filed and the following pharmacological analysis that has been conducted on hit compounds.

1.6.1 Early work conducted by GlaxoSmithKline (GSK)

GSK were the first large pharmaceutical company to take an interest in CXCR1/2 modulators. Their work describes novel *N*-*N'*-diaryl urea compounds with the general structure shown in **Figure 1-14**. The general pharmacophore describes a urea core between two ring systems (ring A and ring B) which were subsequently used for CXCR1/2 antagonist design.[203-210] The first lead compound, SK&F83589 (**7**), identified through high throughput screening methods of [^{125}I]-CXCL8 binding assays in Chinese hamster ovary cells (CHO)-CXCR2 cells displayed IC_{50} of 500 nM.[211] Chemical modification of SK&F83589 (**7**) *via* combinatorial techniques led to introduction of an *ortho*-bromophenyl group, SB225002 (**8**). This compound marked the successful structure activity relationship (SAR) studies to selectively inhibit CXCL8 binding to CXCR2. SB225002 (**8**) displayed IC_{50} values of 22 nM against CHO-CXCR2 and no significant inhibition in CHO-CXCR1 up to 3.3μM concentration determined by [^{125}I]-CXCL8 binding assays. This marked a breakthrough in the group with a lead compound observing >150 – fold selectivity for

CXCR2 vs CXCR1.[211] Further SAR studies into the *N,N'*-diaryl urea scaffold resulted in several compounds developed by GSK being patented as potent and selective CXCR2 antagonists, containing the *ortho*-Br on ring B containing a phenyl moiety (**Figure 1-4**).[203,204,206,207,209,211] While SB225002 (**8**) exhibited selectivity for CXCR2 over CXCR1 and good potency in CXCL8-chemotaxis assays, it demonstrated inadequate oral bioavailability and unfavourable pharmacokinetic properties in animal models, (clearance rate 60 - 120 mL kg^{-1} min^{-1}).[211] Whilst SB225002 (**8**) was entered into clinical trials, further *N,N'*-diaryl urea analogues were identified and investigated in parallel. SAR studies sought to improve the biological activity of their lead compound, and they identified the hydroxy group of ring A to be important for retaining binding affinity towards CXCR2 and displayed improved biological stability.

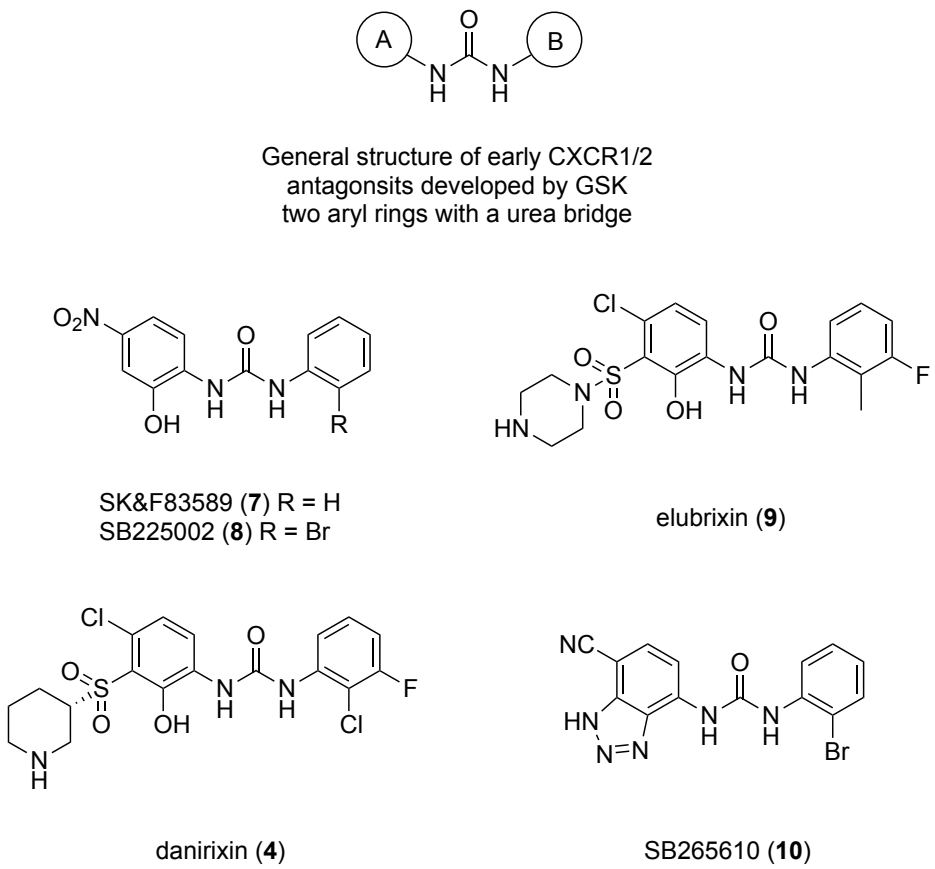

Figure 1-14 Representation of CXCR1/2 drug discovery efforts conducted by of GlaxoSmithKline (GSK) identifying key scaffolds and preclinical/clinical candidates. GSK identified the urea core, which became a strong scaffold in the future work towards CXCR1/2 antagonists.

Their analogues following this discovery led to breakthroughs with two compounds, elubrixin (**9**) (SB656933) and danirixin (**4**) (SB332235 or GSK1325756).[212,213] Initially disclosed in a patent filed in 2000, these two compounds featured a *meta*-substituted sulphonamide/sulphone moiety. This modification seemed to enhance biological stability by mitigating glucuronidation of the phenolic group. This could be rationalised by the introduction of steric hindrance and reducing the pKa of the phenolic group, consequently diminishing its nucleophilic reactivity.[212,213] A 2009 patent claimed the use of elubrixin (**9**) for the treatment of cystic fibrosis.[214] Preclinical studies of elubrixin (**9**) showed that the compound was well tolerated and decreased *ex vivo* CXCL1-mediated neutrophil activation and recruitment.[212] It was later entered into clinical trials for therapeutic use against COPD, colitis and cystic fibrosis but was discontinued due to efficacy and focus turned to the development of danirixin (**4**). Danirixin (**4**) was entered into phase II clinical trials for the treatment of COPD but subsequently terminated due to lack of efficacy and observations of increased exacerbations of symptoms in patients.[149,212,215,216]

In a subsequent SAR study, a triazole was employed instead of the *ortho*-hydroxy and *meta*-sulphone groups found in danirixin (**4**), while a cyano group replaced the *para*-nitro substituent. Among these compounds, SB265610 (**10**) emerged as the most promising candidate, featuring an additional *para*-cyano group in lieu of the nitro group present in danirixin (**4**). Although still potent, SB265610 (**10**) had a reduced potency with IC_{50} = 10 nM but improved pharmacokinetic and ADME properties in rabbit models.[217,218] Despite the continued development of *N,N'*-diarylurea analogues, danirixin (**4**) remained the most advanced small molecule for selective CXCR2, but no update has been issued since the discontinued phase II trials for the treatment of COPD in 2020.[219]

1.6.2 AstraZeneca (AZ)

AstraZeneca's early efforts in the early 2000s for CXCR1/2 antagonists focused on bicyclic purine and thiazolopyrimidine scaffolds.[220,221] AZD8309 (**12**), a potent 2-aminothiazolo[4,5-*d*]pyrimidine derivative is as a potent and selective CXCR2 antagonist. It is derived from SAR studies into the three thiazolopyrimidine substituents of hit compound **11**, discovered in a HTS process (**Figure 1-15**).[222,223] Whilst AZD8309 (**12**) possessed greatly improved potency towards CXCR2

([^{125}I]CXCL8 binding assay, IC_{50} = 4 nM), it still suffered from bioavailability concerns in rat models (F = 9%). In phase I clinical trials, AZD8309 (**12**) demonstrated promising indications. Evaluation of lipopolysaccharide (LPS)-induced airway inflammation in healthy volunteers revealed noteworthy reductions in neutrophil count in sputum, decreased activity of neutrophil elastase, and diminished expression of CXCL1.[224] In the same studies, AZD8309 (**12**) was described as a potential treatment pathway for COPD, severe asthma, and cystic fibrosis.[224,225] Despite the promising phase I clinical data, AZD8309 (**12**) is no longer being pursued by AstraZeneca in favour of AZD5069 (**3**).[222,223,226] AZD5069 (**3**) was the result of SAR around the ring opening of the bicyclic core in favour of a sulphonamide substituted pyridine. This compound was among the first series of compounds described in a 2010 patent, showing favourability of a monocyclic core.[227] AZD5069 (**3**) has been featured in various patent claims by the company, including an updated version in 2012 detailing the formulation of crystalline forms of the compound.[227] This patent, while referencing several other crystalline compounds previously mentioned in a 2006 patent, focuses on a more refined compound library. AZD5069 (**3**) is a highly selective CXCR2 antagonist, demonstrating a 150-fold difference in activity compared to its inhibitory effect on CXCR1, determined by [^{125}I]-CXCL8 binding assays. The pIC_{50} values were measured at 9.1 and 6.9 for CXCR2 and CXCR1, respectively.[228] Additionally, preclinical *in vitro* studies found that it was a potent antagonist for CXCL1-mediated neutrophil chemotaxis.[136] As the most advanced pyridine based CXCR2 antagonist, AZD5069 (**3**) was entered into clinical trials. Phase I trials were conducted on AZD5069 (**3**) to assess its safety and tolerability in healthy patients. Promising indications demonstrated reduced airway inflammation indicators, including neutrophil counts in the sputum. Subsequently, AZD5069 (**3**) advanced to phase II trials, where it is currently under investigation for the treatment of respiratory diseases, COPD[148,216], asthma[160,229], bronchiectasis[230].[15] Whilst being well tolerated, indications from patients with severe asthma showed a lack of efficacy after a 6-month period.[160] AZD5069 (**3**) has recently advanced to phase II trials for the treatment of cancers, including advanced hepatocellular carcinoma (currently recruiting) and metastatic castration-resistant prostate cancer (NCT03177187). These trials involve combinations with durvalumab and enzalutamide, respectively.

RIST4721 (**13**) (AZD4721) is another pyridine-based drug that was originally developed by AstraZeneca, but not developed past phase I trials in favour of AZD5069 (**3**). It was subsequently bought out by Aristea and renamed RIST4721 (**13**). It was entered into phase II clinical trials for the treatment of several neutrophil mediated inflammatory disorders including, hidradenitis suppurativa (NCT05348681); palmoplantar pustulosis[231], and familiar Mediterranean fever (FMF) (NCT05448391) but has been withdrawn from studies.[232]

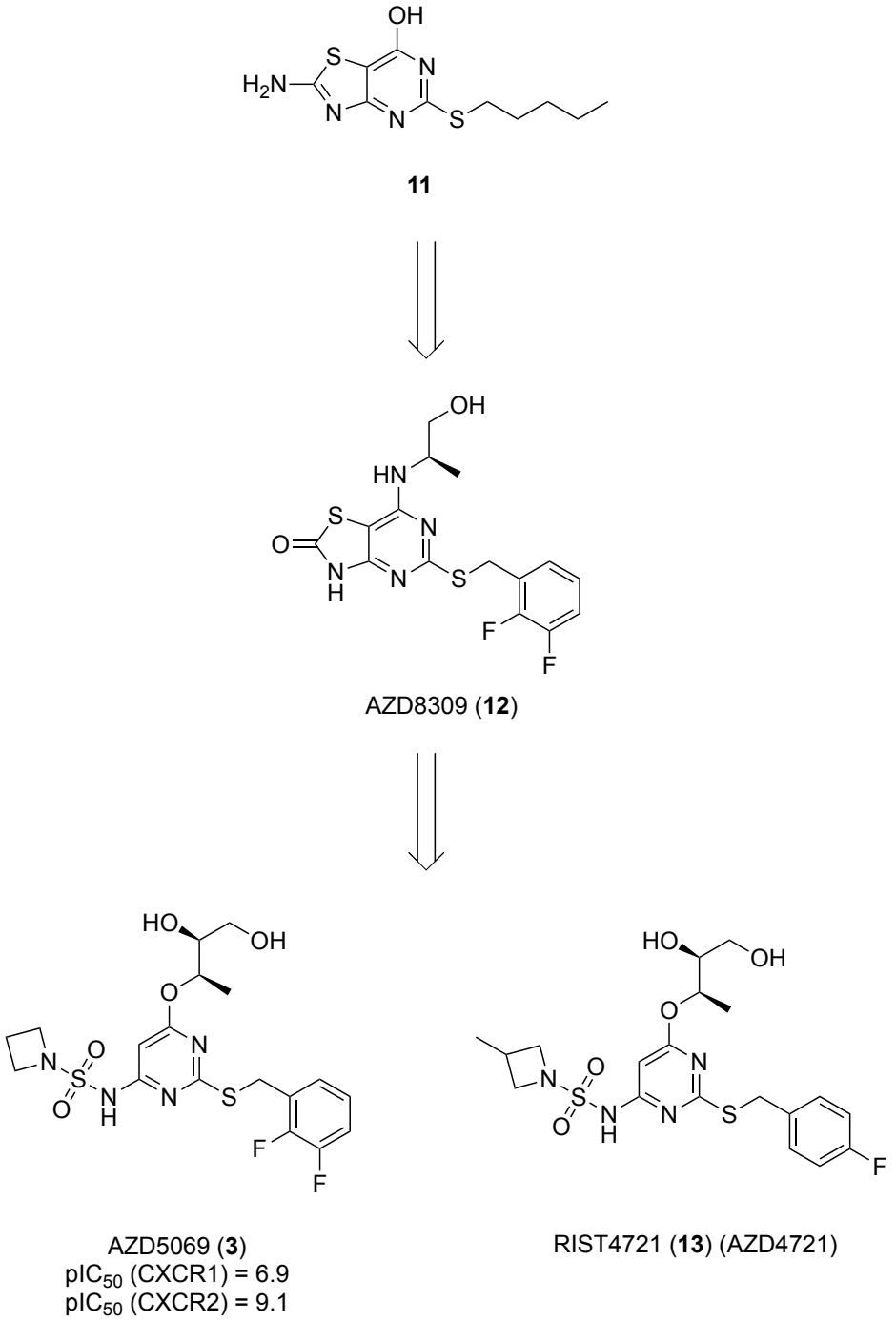

Figure 1-15 Medicinal chemistry efforts conducted by AstraZeneca (AZ).

1.6.3 Dompé S.P.A

Medicinal chemistry efforts conducted by Dompé in the area of CXCR1/2 antagonism are currently focused on the use of 2-arylproprionic acids as a core (**Figure 1-16**).[233] This was the culmination of early SAR work done on a series of 2-aryl-acetic acids derived from ketoprofen (**14**) and ibuprofen (**15**), for which a patent was filed in

2004.[234] Ketoprofen (**14**) and ibuprofen (**15**) are commonly associated with the non-selective inhibition of the cyclo-oxygenase-1 and 2 (COX-1 and 2) enzymes.[235,236] However, it was also shown to be associated with CXCL8-mediated neutrophil chemotaxis, not associated with the COX pathways. This unusual activity led to the finding of an allosteric interaction site between ketoprofen (**14**) and CXCR1 through molecular modelling and subsequent mutagenic studies. The allosteric binding site described by Allegreti *et al*.[237] is topographically distinct from the intracellular binding site which the intracellular NAMs, such as the *N,N'*-diarylurea/urea like and pyridine compounds, act. The binding site of ketoprofen (**14**) in CXCR1 lies in a cavity on the extracellular side of the receptor between TM1, 2, 3, 6 and 7. SAR studies conducted on ibuprofen (**15**) derivatives led to the development of reparixin (**6**) and ladirixin (**5**) as CXCR1/2 antagonists.[237] Reparixin (**6**) stands out compared to the urea mimetic compounds as acting selectively on CXCR1 (hPMN chemotaxis IC_{50} = 1 nM) compared to CXCR2 (hPMN chemotaxis IC_{50} = 400 nM). To date, it appears that reparixin (**6**) is the only compound entered into clinical trials with high selectivity towards CXCR1 over CXCR2. Later characterisation of the binding pocket using reparixin (**6**) and ladirixin (**5**) corroborated the proposed binding mode. Bertini *et al*.[135] suggested that the activity was driven by a strong network of hydrogen bonding and ionic interactions between the ligand and polar residues in the pocket ($K48^{1.32}$, $Y55^{1.39}$, $E300^{7.39}$, $K108^{2.64}$, $N129^{3.35}$).[135,237-239] Preclinical data showed reparixin (**6**) inhibited neutrophil chemotaxis, whilst not affecting radiolabelled CXCL8 binding.[135] Phase II and III clinical trials are ongoing on the use of reparixin (**6**) in treating early graft rejection of pancreatic islet transplants in type I diabetic patients.[240-242] They found that there was a desirable downregulation of neutrophil recruitment, along with reduced expression of CXCR1 and CXCR2 cell types.[242] Despite promising indications to reduced inflammation, no improvements were observed with islet graft acceptance despite improved islet graft survival in mice models, pointing towards an efficacy concern with treatment.[240-242]

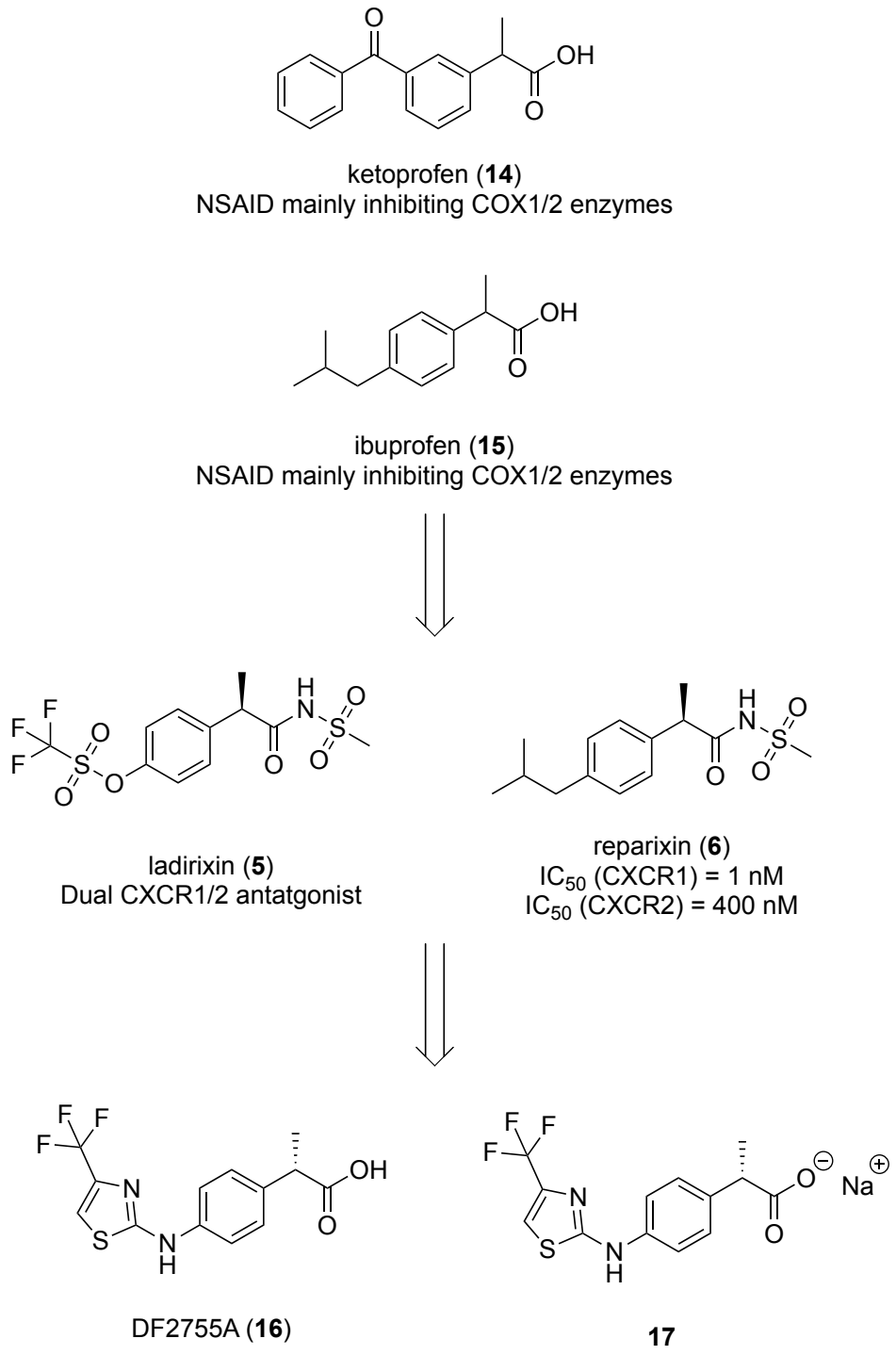

Figure 1-16 Representation of the medicinal chemistry efforts made by Dompé S.P.A in CXCR2 modulators. Their early work was based on the common scaffold derived from the ibuprofen (**15**) scaffold. Their efforts resulted in the discovery of reparixin (**6**), a promising lead compound. Addition of a second cyclic ring in the form of a thiazole gave DF2755A (**16**) and its sodium salt **17**.

Phase I reports suggest that reparixin (**6**) is well tolerated at a therapeutic dose with a reduction in cancer stem cells in breast cancer patients.[199] Pharmacological studies conducted suggest the use of reparixin (**6**) in combination with 5-fluorouracil for the treatment of gastric cancer, showed a 50% reduction in micro vessel density (MVD).[189] More recently, oral administration of reparixin (**6**), was evaluated in patients with HER-2-negative breast cancer, where it was well tolerated and reduced CSCs following 21-day treatment. This study suggested that the inhibition of CXCR1 may be beneficial to targeting CSCs in the tumour environment, following a CXCL8-CXCR1 axis in breast cancer being reported by other studies.[84,196,243] Subsequently, reparixin (**6**) was used in combination with paclitaxel in phase II trials, but failed to show improved progression-free survival in patients compared to the control group.

Dompé have also continued to develop their other 2-arylproprionic derivative, ladarixin (**5**). Characterisation of ladarixin (**5**) describes it as a dual CXCR1/2 antagonist with the ability to decrease PMN infiltration and angiogenesis in mice models. In the same study, they exemplified the ability of ladarixin (**5**) to reduce the CXCL1-mediated angiogenesis. This pathway is CXCR2 specific and pointed towards a dual inhibitory effect of ladarixin on CXCR1 and CXCR2.[135] Ladarixin has undergone phase I and phase II clinical trials for the treatment of onset type-I diabetes (NCT02814838).[244] Whilst >10 % of patients exhibited adverse reactions to the treatment (including dyspepsia and headaches), patients displayed reduced beta cell loss and warranted further progression to phase III trials which are currently ongoing (NCT04628481).[158,244]

A patent filed by Dompé in 2010 details the introduction of a second aryl ring in the form of a trifluoromethyl substituted thiazol ring.[227] 25 compounds were detailed and of these the most promising was DF2755A (**16**) and the corresponding sodium salt **17**, which showed 66% CXCL8 inhibition at 1 nM in chemotaxis of human monocytes with a high degree of selectivity for inhibiting CXCL8 chemotaxis versus C5a or f-MLP receptor chemotaxis. Recent *ex vivo* and *in vivo* studies have shown that DF2755A (**16**) is effective as a preventive or therapeutic against CYP-induced peripheral neuropathy by inhibiting chemokine-induced excitation of sensory neurons and therefore a potential treatment for non-ulcerative interstitial cystitis.[245]

1.6.4 Schering-Plough (before acquisition by Merck & Co)

Before the acquisition by Merck & Co, Schering-Plough had a small but impactful presence in the field of CXCR1/2 antagonists, with 2 patents being filed before 2009 (when their acquisition acquired by Merck & Co).[246] The first of these patents in 2002 detailed the use of a 3,4-disubstituted diamiocyclobutene-1,2-diones bioisostere in place of the urea scaffolds used in earlier GSK examples of allosteric CXCR1/2 antagonists. The patents describe a general structure of two aryl rings (ring A and ring B) on either side of a 3,4-diaminocyclobut-3-ene-1,2-dione core (**Figure 1-17**). This was the first patent to suggest a departure from two phenyl rings described in GSK examples and, instead, favoured a heteroaryl ring B. Merritt *et al.*[246] and their team at Schering Plough published their SAR work conducted on the *N,N'*-diaryl 3,4-diamiocyclobutene-1,2-diones, 4 years after the patent was filed.[246] The SAR detailed the importance of the hydroxyl group in the same manner described in earlier GSK antagonists.[209,247] Replacement of the hydroxyl with hydrogen gave IC_{50} of 8.6 μM compared to 0.036 μM displayed by the hydroxy analogue in a CXCR2 chemotaxis assay.[246] Methylation of the NH group of the 3,4-diaminocyclobut-3-ene-1,2-dione core next to ring B was also shown to be detrimental to activity with 790-fold drop in potency towards CXCR2 reported, determined by [^{125}I]CXCL8 binding assay. This study reported some of the SAR conducted around ring B of the molecule.[246]

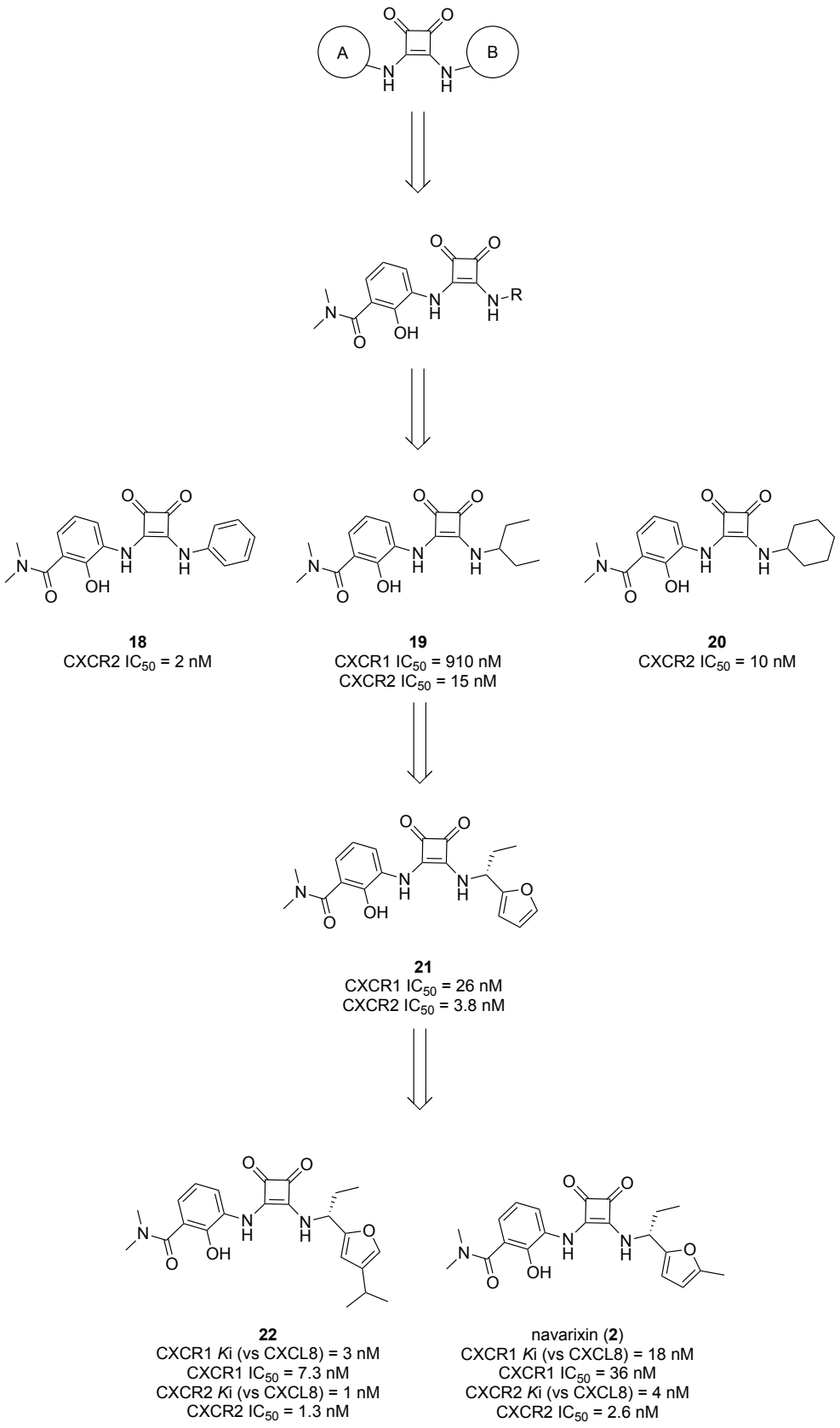

Figure 1-17 SAR studies conducted on the squaramide core by Schering-Plough up until their acquisition by Merck & Co in 2010. Compound **18**, **19** and **20**, potent

CXCR2 allosteric modulators identified by an SAR study conducted by Merritt *et al.*[246] at Schering-Plough. Later work led to the discovery of navarixin (**2**), a promising clinical candidate for the treatment of COPD, asthma, and psoriasis.

Work on the 3,4-diaminocyclobut-3-ene-1,2-dione scaffold continued, and several papers were published between 2006 and 2009 by Schering-Plough and their team detailing the SAR studies that were conducted on the squaramide core.[246,248-251] The next published work would be extensive SAR on ring B. Introduction of a chiral centre at the α-carbon to the amino group improved the potency with a preference for the *R*-enantiomer, whilst the *S*-conformation had an almost 15-fold reduction in potency (17 nM versus 244 nM). Additionally, simple alkyl substituents were surveyed and showed a preference for an ethyl group, with increasing length and branching having a negative effect on potency and bioavailability in rat models.[248] After identifying the preference for the *R*-ethyl substituent, they surveyed different substituted aromatic rings that could be incorporated to the ring B.[248] The addition of an electron-withdrawing atom into the aromatic ring in the form of heterocycles improved potency with furan and thiophene displaying CXCR2 (hPMN chemotaxis) IC_{50} = 3.8 nM and CXCR1 (hPMN chemotaxis) IC_{50} = 6 nM. It is evident at this time they shifted to developing CXCR2 selective compounds, with a preference for CXCR2 selective compounds. In some cases, CXCR1 chemotaxis assays were not conducted on compounds that showed no improved CXCR2 potency. A breakthrough compound from this SAR, first detailed in the original patent from 2002 was navarixin (**2**) (SCH527123 or MK7123 under Merck and Co) a highly potent compound showing 15-fold selective CXCR2 inhibition over CXCR1. Additionally, navarixin (**2**) exhibited a more desirable pharmacokinetic profile compared to **21**, with the C5 methyl substitution appearing to increase the bioavailability of the drug. Another compound detailed in a later SAR study conducted on substituted heterocycles describes a potent dual CXCR1 and CXCR2 inhibitor **22** that contains an isopropyl substitution at C4 with a K_i of 3 nM (IC_{50} = 7.3 nM) against the CXCR1 receptor and CXCR2 K_i of 1 nM (IC_{50} = 1.3 nM). Subsequent characterisation of **22** *in vitro* and *in vivo* demonstrated potent inhibition of CXCL8 and CXCL1 induced neutrophil chemotaxis and favourable oral pharmacokinetic profiles in rat, mouse, monkey, and dog models.[250] SAR studies conducted by Chao *et al*.[250] details CXCR2 having a

greater tolerance for larger C4 substituents with CXCR1 potency and points to a more restrictive binding pocket for CXCR1 in this region.

Preclinical assessment of navarixin (**2**) displayed its ability to supress [^{35}S]-GTPγS exchange of CXCR1 and CXCR2, when stimulated with CXCL8. Additionally, navarixin (**2**) decreased the efficacy of CXCL1. The chemokine potency did not increase in an expected linear fashion, as navarixin (**2**) concentration increased, implying that navarixin (**2**) displayed an insurmountable profile consistent with allosteric modulators.[252] The same study also described that the higher binding affinity towards CXCR1 and CXCR2 exhibited by navarixin (**2**) compared to earlier GSK compound SB225002 (**8**) translated to improved efficacy, inhibiting CXCL8-induced Ca^{2+} signalling. Navarixin (**2**) displayed the ability to suppress pulmonary neutrophilia (ED_{50} = 1.8 mg/kg) and reduced neutrophil counts in the sputum in rats supporting it as a potential treatment for neutrophil mediated airway inflammatory diseases, such as COPD.[253] Navarixin (**2**) was entered into a series of clinical trials starting in 2007 for the treatment of inflammatory based disorders, including COPD[147], asthma (NCT00688467) and psoriasis (NCT00684593).[15,162] After treatment of navarixin (**2**) lower neutrophil counts, CXCL8 counts, and myeloperoxidase were observed in the sputum of healthy patients, compared to a placebo, and warranted further investigation in patients with pulmonary disorders.[254] Comparable reduction in sputum neutrophil reductions were observed in patients with severe asthma, along with a notable reduction in mild exacerbation events. However, no statistically significant increase was observed in FEV1, sputum myeloperoxidase, or sputum CXCL8 levels.[162] Phase II trials have seemingly been terminated after long term studies where the drug failed to display suitable efficacy for continued treatment (NCT00441701).[15,147] *In vitro* studies showed navarixin (**2**) showed inhibition of melanoma cell growth, proliferation, chemotaxis, and invasiveness. Moreover, a notable decrease was observed in tumour micro vessel density and increased melanoma cell apoptosis.[255] Similar reductions in micro vessel density and apoptosis were observed against colon cancer including the reduction in metastasis.[256] The use of navarixin (**2**) in conjunction with pembrolizumab in phase II trials for the treatment of advanced/metastatic solid tumours has recently completed but the results have not yet been reported (NCT03473925).

Navarixin (**2**) and other 3,4-diaminocyclobut-3-ene-1,2-diones based NAMs act on CXCR1 and CXCR2 through an intracellular allosteric binding site which was originally delineated in 2010. During the work conducted in this project a crystal structure of CXCR2 bound with a 3,4-diamino-cyclobut-3-ene-1,2-dione based NAM 00767013 (**1**) was elucidated and confirmed the binding mode described in mutagenesis studies previously conducted by Salchow *et al.*[134] This binding mode is discussed further in **Chapter 2**.

1.6.5 Merck & Co

Merck & Co entered the area of CXCR1/2 modulators in 2010, following the acquisition of Schering-Plough, they continued the focus of the SAR on ring the B side of the 3,4-diamino-cyclobut-3-ene-1,2-diones based antagonists, with a patent detailing a series of novel hydrazino-cyclobut-3-ene-1,2-dione compounds (**Figure 1-18**).[257] Merck & Co continued from Schering-Plough's focus on the ring B of the molecule with the introduction of a hydrazine moiety. This publication included 224 compounds of which 9 were highlighted, however none of the compounds in this series displayed improved potency or pharmacokinetic profiles when compared to navarixin (**2**).[258] The most potent of the series were **23** and **24** displaying IC_{50} of 120 nM and 110 nM in CXCR2 and IC_{50} of 9.7 μM and 4.1 μM in CXCR1 determined by fluorometric imaging plate reader (FLIPR) assays.[258] Whilst navarixin (**2**) is currently under continued clinical evaluation, there has not been any additional compounds added to their pipeline of CXCR1/2 antagonists since 2010.

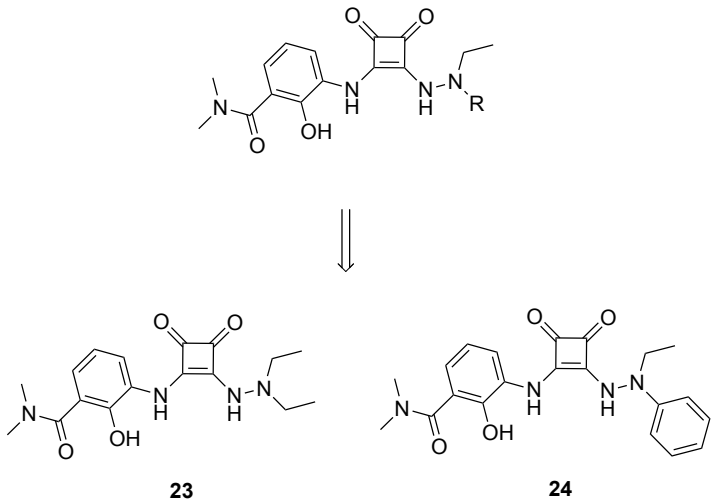

Figure 1-18 Work conducted by Merck & Co following the acquisition of Schering-Plough. ventures into the area saw the development of several hydrazino-cyclobut-1,3-ene-1,2-dione compounds, **23** and **24**.

1.6.6 Other Developments on Squaramide Analogues

Several other companies have developed 3,4-diamino-cyclobut-3-ene-1,2-diones based NAMs. Novartis have claimed a series of compounds with the general structure shown in **Figure 1-19** bearing a sulphonamide link in place of the amide in navarixin (**2**).[258] All except one of the published tested compounds shown displayed IC_{50} ([^{35}S]-GPTyS binding assay) > 0.1 μM with the best performing compounds showing IC_{50} ([^{35}S]-GPTyS binding assay) = 10 nM, although the identity of the compound was not disclosed. A subsequent patent was claimed for the choline salt **25** for the treatment of inflammatory disease, along with a promising pharmacokinetic profile in dog models, but further development has not been detailed.[259]

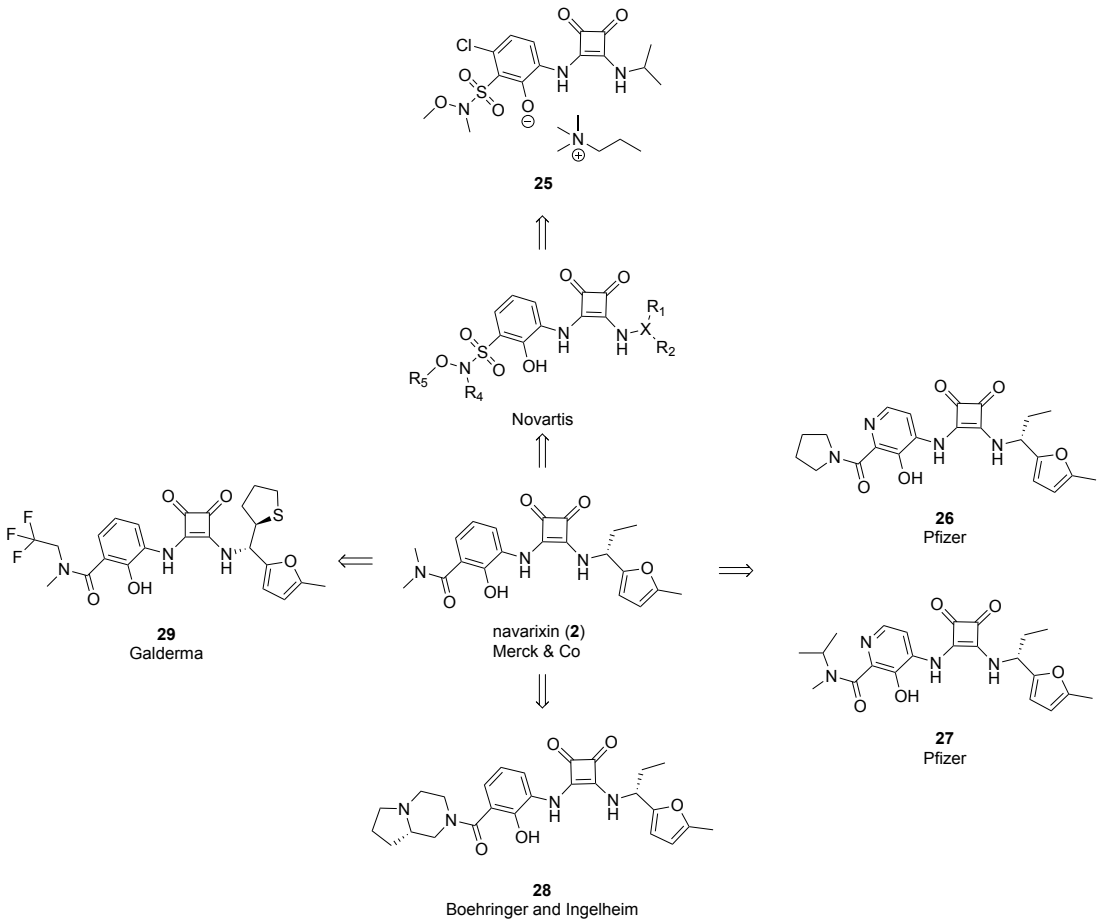

Figure 1-19 Other developments of 3,4-diaminocyclobut-3-ene-1,2-dione based NAMs by pharmaceutical/biotech companies.

Pfizer and Boehringer-Ingelheim focussed their development of modifying ring A of the squaramide core. Work by Pfizer demonstrated the use of a substituted hydroxy pyrimidine group in place of the phenol ring.[260] A total of 167 examples were given in the first of these patents published in 2010 and an SAR was conducted around the *ortho*-amide moiety. This included several bicyclic systems bound to the amide. Only a handful of compounds were tested in a neutrophil chemotaxis assay, due to poor binding affinity towards CXCR2. Potency dropped dramatically with the addition of cyclic groups, suggesting that large bulky substitutions are not tolerated in the CXCR2 cavity, and more linear substituents are necessary to retain binding affinity. Boehringer and Ingelheim's attempts included the use of "carbocycles" as an extension to the amide moiety on ring A of the molecule. Interestingly, their examples showed some promising data with **28** showing CXCR2 IC_{50} = 0.1 nM in a human PMN chemotaxis assay. The addition of a chiral centre in the bicyclic pyrazine moiety is preferred and may be the key to further developing tolerable amide group extensions.[260]

Galderma published three patents in 2013 detailing their efforts in developing squaramide based CXCR2 antagonists.[261-264] They focussed efforts on modification of the chiral ethyl moiety of Navarixin (**2)** and, to a lesser degree, modification of the aryl phenol group on ring A of the molecule. Several cyclic systems were tested in place of the ethyl group α to the 3,4-diaminocyclobut-3-ene-1,2-dione core.
In 2017 Galderma detailed the early development scale-up process for **29**, a potent CXCR1/2 antagonist.[265] The scale-up synthesis describes **29** as a clinical candidate with good solubility and penetrations properties and suggests that the published work provided evidence for its use as a topical treatments for acne to begin clinical trials. The compounds introduce a methyl tetrahydrothiophene ring in place of the ethyl group of the ring B, compared to navarixin (**2),** along with the addition of a 2,2,2-trifluoroethyl substitution to the amide of ring A. Literature related to this compound have discussed the scale up synthesis and suggests their efforts have been fruitful with a clinical candidate in the pipeline, although there have been no updated clinical indications since 2017.

1.7 Thesis aims

This chapter has highlighted the pivotal roles of CXCR1 and CXCR2 in various neutrophil-mediated diseases and their potential as therapeutic targets. Despite the challenges faced by current therapeutics in clinical trials, particularly concerning efficacy, there remains a pressing need for the development of novel treatments. Furthermore, the complexities of the CXCR1 and CXCR2 axis in disease states underscore the importance of ongoing research efforts aimed at unravelling the intricacies involved in their signalling and subsequent disease progression. A deeper understanding of the roles of these receptors in disease pathogenesis holds promise for informing future drug design strategies and advancing the development of more effective therapies. Such selective agents not only offer the potential for more targeted and effective treatments, but also facilitate in-depth investigations of each receptor's specific contributions to disease pathology, both *in vitro* and *in vivo*.

The recent publication of a CXCR2 crystal structure, bound to the intracellular allosteric modulator 00767013 (**1**), has contributed to the elucidation of the binding mode 3,4-diaminocyclobut-3-ene-1,2-dione class of NAMs, such as clinical candidate, navarixin (**2**). In the absence of a similarly suitable CXCR1 3D structure, this project

aims to use computational tools to build and refine an accurate and representative CXCR1 model. With the CXCR1 model in hand, the project aims to rationalize the preferential binding affinity towards CXCR2 observed for the 3,4-diamino-cyclobut-3-ene-1,2-dione class of NAMs, such as the clinical candidate navarixin (**2**). The project will involve exploring the two target receptors, CXCR1 and CXCR2, using *in silico* methods to investigate their binding sites and rationalize the molecular interactions that contribute to their demonstrated binding affinity. By rationalizing the selectivity profile through computational techniques, a series of ligands based on navarixin (**2**) will be designed and synthesised. This process will be followed by building a SAR to elucidate the structural features pertaining to the observed selectivity and affinity profiles of 3,4-diamiocyclobutene-1,2-dione based IAMs. The findings from the SAR will form the basis for further development of CXCR1 and CXCR2 ligands, with desirable receptor selectivity profiles, particularly towards achieving CXCR1 selectivity, which has been previously discussed as a potential adjunct therapeutic in several cancers. These compounds can potentially be advanced into therapeutic agents for various diseases where modulation of CXCR1 and CXCR2 pathways is beneficial. Additionally, the improved SAR resulting from these designed ligands may support the development of a diverse range of chemical biology tools. These tools could include fluorescent ligands, covalent ligands, and proteolysis-targeting chimeras (PROTAC). These tool compounds could assist in studying the roles of CXCR1 and CXCR2 in disease models to enhance our understanding of their involvement in various pathological conditions.

Chapter 2 – Development and validation of CXCR1 and CXCR2 models

2.1 Introduction

Rational drug design aims at identifying pharmaceutically relevant drug candidates based on the target of interest. The introduction of cheminformatics in drug discovery has vastly improved our ability to explore chemical space *via in silico* techniques, where previously medicinal chemistry, combinatorial chemistry and high throughput screening techniques were relied on. These techniques can be limiting due to time and cost factors.[313] Cheminformatics enables the efficient analysis of large chemical datasets, prediction of compound properties, and the design of novel molecules, thereby accelerating the drug discovery process and having a more targeted approach for the identification of drug candidates. Programs employing computer aided drug design (CADD) predominantly use two methods, structure-based virtual screening (SBVS) and de novo drug design both requiring three-dimensional structures of the target.[266-269]

3D Structural data available for biological macromolecules provide a wealth of insight into the function and druggability properties of proteins of therapeutic interest. Structural information can be used for understanding biological processes, target identification, rational drug design and lead optimisation in CADD. Specifically, advances in structural elucidation have revolutionised drug discovery by providing detailed information of ligand-binding pockets and conformational changes associated with activation and allosteric modulation. X-ray crystallography techniques were often considered the 'gold standard' of 3D structure determination however other techniques are commonly used such as nuclear magnetic resonance (NMR) and recently cryo-EM techniques. Historically, the determination of GPCRs have proven to be difficult owing to their innate complexity and dynamic/flexible nature, leading to a lack of stability required for crystallisation.[270,271] Early examples of GPCR structures, such as rhodopsin, were solved due to their natural stability and unique mechanism of action.[272,273] Breakthroughs in key crystallographic techniques, such as liquid-phase crystallization LPC crystallisation and fusion proteins, led to the structural

determination of β-2 adrenergic receptor (β-2AR) coupled to stimulatory G protein (G_s) in 2011 and paved way for a golden age for SBDD of GPCRs.[272-274]

The advances in crystallographic techniques have catalysed the deposition of GPCR crystal structures into the protein data bank (PDB[275]). There are 250 unique GPCR structures currently available, with a growing number of these deriving from cryo-EM techniques.[270,276] The introductions of cryo-EM techniques for GPCR structure determination in 2017 have improved the ability to determine GPCRs in their active states as complexes (GPCR-G protein and GPCR-arrestin).[270] Often, agonist-bound structures are in an intermediate state because the active state must be stabilised by an intracellular binding partner, such as a G protein. Until recently, only two examples of "true" active state GPCRs were determined from X-ray crystallography, whereas now 11 unique structures are available, which have been determined *via* cryo-EM.[271,277] Consequently, there is access to GPCR target structures in multiple states and in complex with multiple unique ligands, allowing understanding of the molecular basis for drug affinity. For SBDD, an attractive prospect is the elucidation of multiple structures of receptors bound to multiple unique ligands. This hope has been realised in the examples of β-1 adrenergic receptor (β-1AR), β-2AR and adenosine A2A receptor ($A_{2a}R$), which have been determined in complex with 14, 14, and 19 unique ligands respectively.[270]

The current state of GPCR determination after 20 years of revolutionary work have greatly improved our understanding of GPCR structure and function, excelling the field of SBDD.[278] As cryo-EM techniques continue to improve, the field is looking at a future where it will eventually rival X-ray crystallography in all aspects. However, its current limitations lie in determining smaller proteins such as those in inactive states bound to antagonists (generally in the 35-40 kDa range), which have yielded low resolution structures 3.0 - 3.5 Å, at best and often lower resolution.[279,280] With current limitations, the choice of crystallographic technique for determination of GPCRs lies in the desired outcome. However, there is little doubt that cryo-EM will continue to improve for smaller protein of higher resolution in the future.[279]

Despite the importance of chemokines and their receptors as therapeutic targets, so far only a few 3D structures have been made available for chemokine receptors. The advancement of crystallographic techniques led to the deposition of the first

chemokine class GPCR being deposited to the protein data bank (PDB) of five CXCR4 structures in complex with a small molecule and cyclic peptide antagonists.[281] To date, only 23 chemokine receptor structures have been determined through NMR, X-ray, or cryo-EM techniques being from seven unique receptors: CXCR4, CCR5, CXCR1, CXCR2, CCR9, CCR7, CX3CR1.[54,55,129,132,281-288]

As previously discussed in **Chapter 1**, a putative intracellular allosteric binding site has been reported for CXCR1 and CXCR2.[134,136] This binding site has been further evidenced in 2020 by the elucidation of the X-ray structure of CXCR2 in complex with a small molecule NAM, 00767013 (**1**), that has a resolution of 3.20 Å (PDB ID: 6LFL[54]) along with two cryo-EM structures (6LFM and 6LFO[54]) complexed with the downstream G protein and monomeric or dimeric CXCL8 (**Figure 2-1**).[54] 00767013 (**1**) is structurally similar to the high potency CXCR1/2 NAM, navarixin (**2**), containing a squaramide core, and differing by the introduction of a nitrogen into the salicylamide ring transforming it into a picolinamide. Additionally, an isopropyl moiety is substituted at the 4-position on the furyl ring and the methyl at the 5-position present in navarixin (**2**) is absent. 00767013 (**1**) occupies a binding pocket consisting of residues from TM1, TM2, TM3, TM6, as well as the turn between TM7 and H8. Superposition of the CXCR2 crystal structure (PDB ID: 6LFL[54]) with the two cryo-EM structures (**Figure 2-2**) shows that the NAM occupies a site overlapping with the Ga_i binding site. Additionally, it appears to restrict the conformational changes of TM6, TM3 and TM7 required for receptor activation. This evidence suggests the mechanism of action for receptor inhibition to be, at least partially, a competitive interaction with the G protein.[54] Inspection of the binding site (**Figure 2-3**) shows key hydrogen bond interactions between the carbonyl groups of the squaramide core and $D84^{2.40}$, which is key for the V-shaped pose adopted by the ligand. The carbonyl groups of the cyclobutene-dione core also have hydrogen bonding interactions with the backbone of $K320^{8.49}$ and $F321^{8.50}$ on the turn between TM7 and H8. Further hydrogen bonding is observed between $T83^{2.39}$ and the carbonyl of the picolinamide moiety. The ligand is shown to exist in its ionised phenolate form with a salt-bridge interaction with $K320^{8.49}$, and a hydrogen bond with $S81^{2.37}$. The isopropyl furan group occupy a hydrophobic pocket consisting of $V69^{1.53}$, $V72^{1.56}$, and $I73^{1.57}$.[54] Key motifs in the chemokine family of receptors are also present in the binding pockets, $R144^{3.50}$ of the DRY motif and $Y314^{7.53}$ of the NPxxY motif.[54]

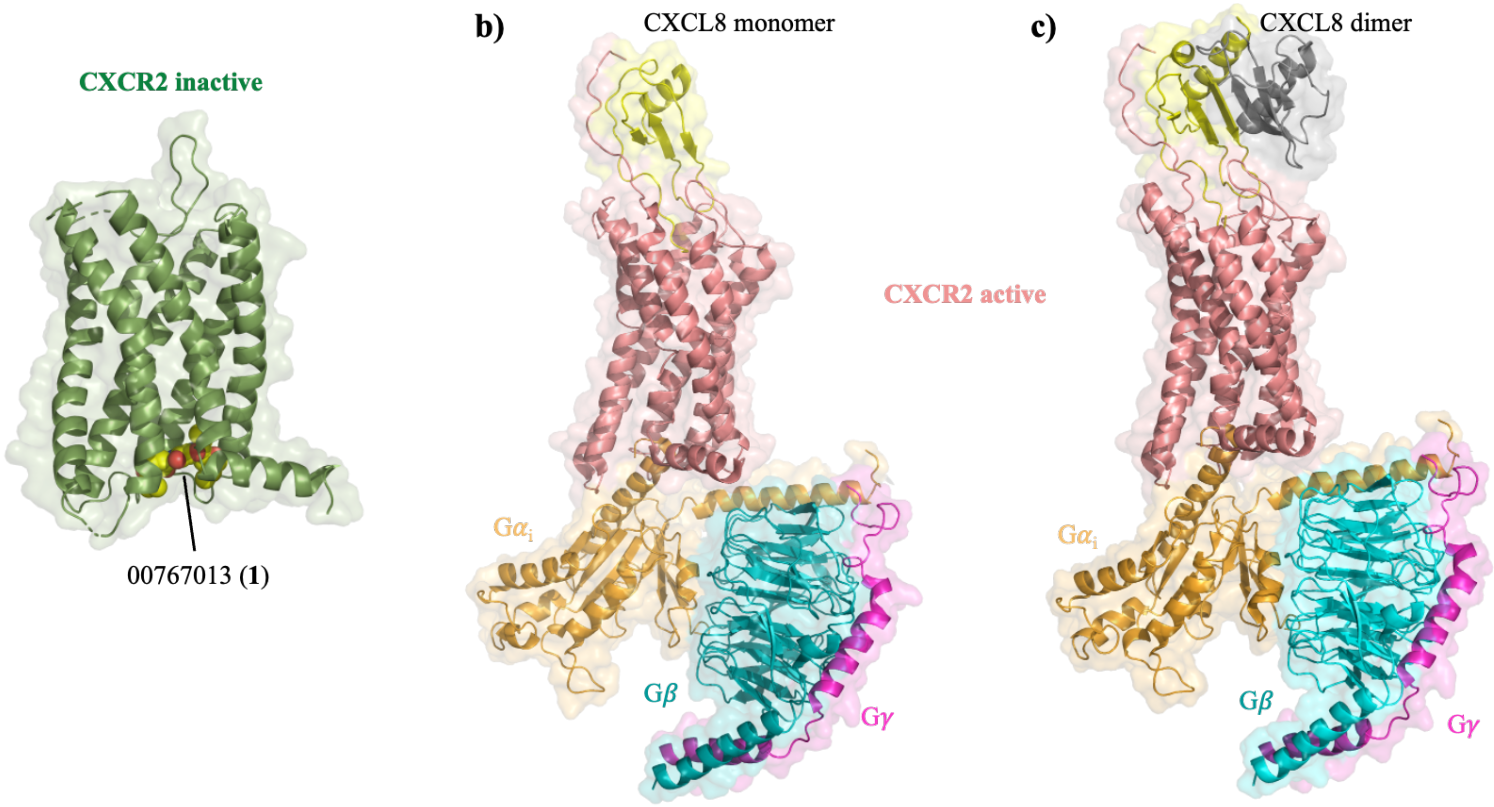

Figure 2-1 Structural compassion between inactive and active CXCR2.[54] (a) X-ray crystal structure of the intracellular NAM, 00767013 (**1**)-bound CXCR2 (PDB ID: 6LFL). The inactive state receptor and 00767013 (**1**) are depicted as green cartoon and yellow spheres respectively. (b) cryo-EM structure of active CXCL8 (monomer)-CXCR2-CXCL8-G_i complex (PDB ID: 6LFM). (c) cryo-EM structure of CXCL8 (dimer)-CXCR2-G_i complex (PDB ID: 6LFO). Cryo-EM structures are coloured using in the following order: CXCL8 (yellow and grey), receptor (pink), $G\alpha_i$ (orange), Gβ (blue), Gγ (pink).[54]

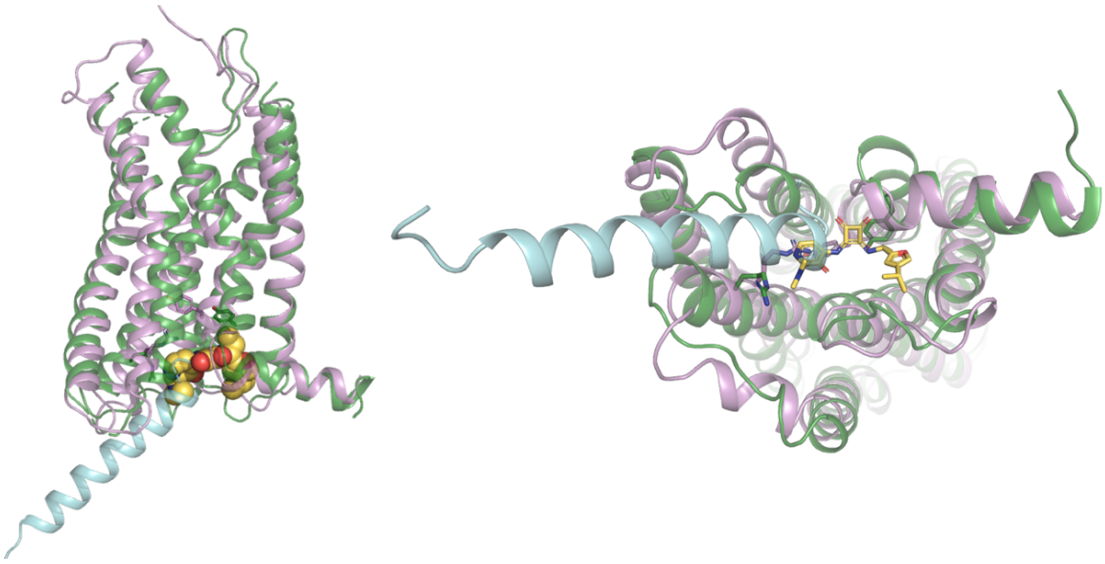

Figure 2-2 Overlay of inactive 00767013 (**1**)-bound CXCR2 (Green) (PDB ID: 6LFL[56]) and active G_i-bound CXCR2 (pink) displayed from a membrane cross section side (left) and the intracellular side (right). Depicted is the overlap of the $G\alpha_i$ α5 helix (blue) with the binding site of 00767013 (**1**) (yellow, red, and blue).[54]

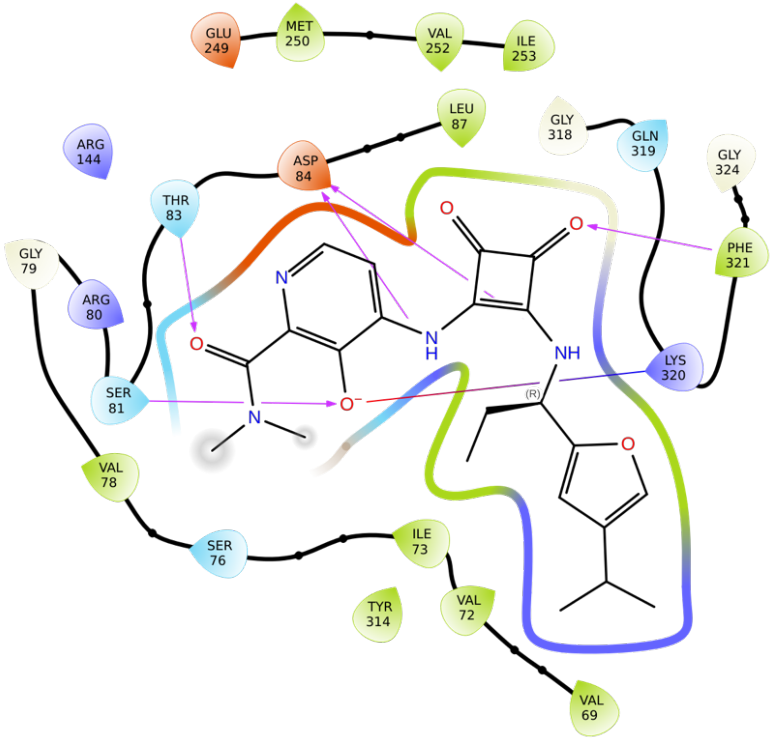

Figure 2-3 Residues contributing to the binding pocket of CXCR2 in complex with NAM 00767013 (**1**), three letter residue codes and numbers show residues contributing to the binding pocket to achieve the characteristic V-shaped binding mode. Purple arrows denote

hydrogen bonds and red/blue arrows denote ionic interactions. Image generated in Maestro (Schrödinger).[289]

With the addition of 6LFL, 6LF0 and 6LFM[54] to the PDB, there is now an ideal starting point for the CADD for small molecules targeting the NAM binding pocket described in 6LFL.[54] The inactive CXCR2 crystal structure contains stabilising modifications in the form of a scFv16 antibody fragment, along with multiple point mutation. In this case, modelling tools are often used to reverse engineer and refine the structure.[290-293]

Two unique CXCR1 structures currently available are an ensemble of 10 conformers in a phospholipid bilayer resolved *via* NMR (PDB ID: 2LNL[294]), and the other is a recent cryo-EM structure of CXCR1 in complex with CXCL8 and the G_i heterotrimer with a relatively low resolution of 3.41 Å (PDB ID: 8IC0[55]). In this latest example, the G protein binding pocket is discussed, which has previously shown to overlap with the cyclobutene-dione series of small molecules.[54] Hydrophobic $G\alpha_i$ $I344^{G.H5.16}$, $C351^{G.H5.23}$, $L353^{G.H5.25}$ and $Phe354^{G.H5.26}$ residues show hydrophobic interactions with TM6 and TM3 of CXCR1. Other interactions of note are observed between $D144^{34.52}$ and $D150^{34.58}$ in the ICL2 of CXCR1, as this region is conserved between CXCR1 and CXCR2. However, the interactions differ between resolved structures.[55,294] This more recent inclusion was not available for most of the research undertaken. However, efforts were undertaken to include any evidence that could be garnered from this structure.

Although two unique structures for CXCR1 (PDB ID: 2LNL[294] and 8IC0[55]) are available, there are problems for their use in a CADD program. It is widely understood that NMR structures, such as 2LNL[294], often do not possess high resolutions necessary for the accurate representation of side chains, which are crucial for binding pose and interaction prediction in molecular docking studies.[295-297] Additionally, docking ligands into an ensemble of NMR conformers can be challenging as it is difficult to determine which conformer is the most representative structure.[295] In addition, this structure is in an unliganded state, which has the disadvantage of the protein conformation not being in a representative position for the binding of IAMs. Such ligands have been suggested to have a negative binding cooperativity with the orthosteric agonist in CXCR2[107,138] and, therefore, a target CXCR1 structure in an CXCL8-CXCR1-NAM complex would be a better suited starting point for a SBDD project.

In the absence of a suitable CXCR1 crystal structure for an SBDD project the initial goal was to identify a suitable template for use in homology modelling techniques. It is assumed that the CXCR2 structure in complex with a NAM will provide an ideal starting point for homology modelling. However, other templates will be explored to confirm this hypothesis. This chapter will aim to model and validate CXCR1 and CXCR2 models. Upon the construction and validation of these models, molecular docking approaches will be employed on experimentally validated NAMs to investigate the mode of action for this class of compounds and attempt to rationalise CXCR2 selectivity over CXCR1 of ligands such as navarixin (**2**) described in literature SARs with the aim to use the models in a SBDD program.[134,298]

2.2 Methods

2.2.1 Choice of template

The first step in the construction of a CXCR1 model is the choice and analysis of a suitable template. As previously discussed, 6LFL[54], a crystal structure of CXCL8-CXCR2-NAM is closely related to CXCR1 with ~77% sequence homology may be an ideal starting point, but other templates were explored to confirm this. To accomplish this, the canonical human sequence for CXCR1 (UniProt[299] ascension code P25024) was obtained from the UniProt[299] server. This sequence was then truncated to remove residues 1-34 from the *C*-terminus and 326-250 of the *C*-terminus, as these are disordered regions that are difficult to model. Protein basic local alignment search tool (BLASTp[300]) was used to find non-redundant experimental structures in the PDB with a percentage sequence similarity of >40% (**Table 2-1**). This search found 9 templates belonging to the chemokine receptor family, CXCR1 (PDB ID: 8IC0[55] and 2LNL[294]), CXCR2 (PDB ID: 6LFL and 6LFM[54]), CCR6 (PDB ID: 6WWZ[286]), CXCR3 (PDB ID: 8HNK and 8HNN[282]) and CXCR4 (PDB ID: 3OE0[281] and 4RWS[283]). Sequence homology should not be the only factor considered for template choice, instead careful evaluation and inspection is required, guided by the question you wish to answer with your model. As previously stated, the goal is to develop a homology model that accurately predicts the intracellular binding pocket for designing novel small molecules targeting the binding pocket previously described.[54,134,298] Analysis of the available structures shows that only 3 structures (PDB ID: 6LFL[54], 8HNN[282] and 3OE0[281]) were available for structures with high enough sequence similarity for

comparative homology modelling and bound to an antagonist. Further inspection shows that only 6LFL[54] has a NAM bound to the intracellular binding region of interest, overlapping the interaction site of Gα of the G protein, as discussed in **Chapter 1**. In addition, whilst 6LFL[54] and 6LFM are similar in sequence homology, there is a relatively large difference when compared to the next highest structure being 6WWZ[286], which has a sequence identity of 45%.

Table 2-1 Summary of available structures in the PDB[299,301] with >40% sequence identity to canonical CXCR1 (UniProt[299] ascension code P25024). For each entry the PDB ID, receptor identity, experimental technique, & sequence identity and E value are shown.

PDB ID	Identity	Experimental technique	Sequence Identity (%)	E Value
8IC0_A	CXCR1 [Homo sapiens] active state in complex with agonist CXCL8 and Gai	cryo-EM	100	0
2LNL_A	CXCR1 [Homo sapiens] in phospholipid bilayer	NMR	100	0
6LFL_A	CXCR2 [Homo sapiens] in complex with CXCL8 and NAM 00767013 (**1**)	X-ray	84	$1.00E^{-95}$
6LFM_R	CXCR2 [Homo sapiens] in complex with CXCL8 and Gai	cryo-EM	87	$1.00E^{-167}$
6WWZ_R	CCR6 in complex with CCL20 and Go protein	cryo-EM	45	$2.00E^{-76}$
8HNK_R	CXCR3 in complex with DNGi and CXCL11	cryo-EM	43	$9.00E^{-58}$
8HNN_R	CXCR3 in complex with SCH546738	cryo-EM	42	$1.00E^{-54}$
3OE0_A	CXCR4 in complex with a cyclic peptide antagonist CVX15	X-ray	41	$4.00E^{-35}$
4RWS_R	CXCR4 in complex with chemokine antagonist vMIP-II complex	X-ray	41	$5.00E^{-35}$

2.2.2 Refinement and preparation of CXCR2 crystal structure (6LFL)

Refinement of the chosen template is crucial as the X-ray structure determination is based on electron density and atoms, such as oxygen and nitrogen, are indistinguishable at resolutions of 3.20 Å. This limitation holds significant implications, such as in residues containing Asn and Gln side chains. These side chains feature both oxygen and nitrogen atoms and accurately determining the positions of these atoms is crucial for understanding the local environment and interactions within the protein structure. For instance, in Asn, the side chain contains an amide group, where the oxygen is a hydrogen bond accepting species and the nitrogen is capable of hydrogen bond accepting and donating interactions.

An inherent concern with the use of bioengineered GPCRs to improve intractability for structure determination is the misrepresentation of the native receptor in its biological environment. In the aim to reverse-engineer the modifications made to 6LFL[54] for crystallisation, the antibody insertion on the ICL3 was removed (residues 1001 to 1196). Two ICL3 residues (H242 and M243) were absent in the crystal structure and were initially modelled using Prime Loop modelling in Maestro[289,302] and then refined using the loop refinement protocol. Additionally, mutations introduced to the crystal structure, W135$^{3.43}$, E249$^{6.33}$ and D303$^{7.42}$ were converted back to the canonical CXCR2 amino acids, L135$^{3.43}$, A249$^{6.33}$ and G303$^{7.42}$ respectively. The model was processed by the protein preparation workflow in Maestro[289] to correct common structural problems by adding missing hydrogen atoms, correcting bond orders to Hetero-containing groups (HET), determining optimal protonation states for histidine residues, optimising hydrogen bonds and, finally, performing a restrained energy minimization for the relaxation of bonds, angles, and clashes.

2.2.3 Sequence alignment and model building

The truncated amino acid sequence of the target, CXCR1 (UniProt ascension code P25024) was aligned to the chosen template, CXCR2 in inactive bound state (PDB ID: 6LFL[54]), and CXCR2 (UniProt ascension code P25025) using the constrained-based multiple alignment tool (COBALT)[303]. Initial alignment was refined using multiple sequence alignment of all available chemokine receptor structures available (**Section 2.1.1**) to identify key conserved residues across chemokine receptors and inform secondary

structure positioning. The auto model module in modeller was used to generate 100 knowledge-based homology models of CXCR1. The template, 6LFL contains a single protein chain (chain ID: A), along with the cyclobutene-dione small molecule, 00767013 (**1**). The query sequence of CXCR1 was aligned to the template and predictive models were generated using the automodel class in modeller.[304] Initially, models were built without a ligand in the template alignment, although these models performed poorly during docking. To combat this, the heteroatom-based function in automodel was utilised in the script to retain the binding pocket for later docking. Models were optimised for docking either by use of the protein preparation wizard in Schrödinger[289], or an in-house script for docking using autodock vina. The top model chosen after validation was further optimised by loop refinement and energy minimization using the OPLS4 forcefield in Schrödinger Prime.[289]

2.2.4 Model validation

Most homology modelling programs include an in-built scoring function to rank large numbers of generated homology models, including modeller, which includes discrete optimised protein energy (DOPE). As there are several methods to evaluate homology models, it is crucial to combine multiple methods for more reliable evaluation. A combination of knowledge-based, physics-based, and docking-based methods were used to assess models to generate a single model for further investigation.

Models were assessed using DOPE[304,305] and inverse docking using in-house scripts. The inverse docking script consists of the extraction of 00767013 (**1**) from the template crystal structure (PDB IDL: 6LFL[54]); preparation of the receptors for docking, using an in-house script; grid generation based on the position and size of 00767013 (**1**) and docking of the ligand into each receptor grid generating binding poses for each receptor. The docking score is reported and a final manual inspection of the pose to ensures it corresponds to known binding descriptors from the crystal structure and mutation studies from literature.[54,134] The model with the lowest docking score, whilst having an acceptably low global DOPE was carried forward. DOPE per residue plots were also inspected to assess any outlier regions in the predictive model. PROCHECK[306], Molprobity[307] and SwissModelAssess server[308] were used to assess the quality of models. The model was manually refined by rotamer and dihedral angle modification in Maestro to fix clashes,

high energy residues and Ramachandran outliers.[309,310] The RMSD between backbone atoms (C_α, C and N) of the target crystal structure and the models was calculated following least-squares-fit of the backbone implementing the Super command in PyMOL[311].

2.2.5 Ligand and decoy set selection

A set of 50 diverse high-affinity antagonists (Ki < 500 nM) reported at each target were obtained from the GPCR Ligand Association (GLASS) database[312] to be used as active ligands in a docking enrichment study. The active sets were converted to SDF format using an in-house script. Using the 50 known antagonists, a set of 1000 drug-like decoys were generated using the Directory of useful decoys, enhanced (DUD-E)[313] in the absence of verified decoys sets.[314,315] Decoys are generated with similar physical and chemical descriptors (molecular weight, number of hydrogen bond donors, number of hydrogen bond acceptors, rotatable bonds and calculated logP), whilst remaining chemically distinct using the Tanimoto coefficient between molecular characteristic fingerprints.[316-318] 3D conformations were generated, and the 1050 ligands were prepared based on physiological pH (pH 7.4) using LigPrep[289] in Maestro in preparation for docking.

2.2.6 Ligand enrichment and model benchmarking

The combined 1000 decoys and 50 active compounds were docked into each receptor using rigid protein docking using Glide with standard precision (SP) and extra precision (XP) protocols. Flexible sampling and rigid docking were also assessed for each SP and XP protocols. All other docking settings were set to default unless stated. Docking grid was defined as 20 x 20 x 20 Å with the binding site defined as the centre of 00767013 (**1**) in CXCR2 (PDB ID: 6LFL[54]). The performance of ligand enrichment docking was evaluated through the calculation of the area under the receiver operating characteristic (ROC) curves. These curves were generated by plotting the true positive rate (TPR) against the false positive rate (FPR) for each model, incorporating various docking protocols. The assessment was based on metrics such as the area under the curve (AUC) and logAUC.

2.3 Development of a CXCR1 homology model

2.3.1 Initial homology modelling

The multiple sequence alignment of CXCR1, CXCR2 and 6LFL (**Figure 2-4**) displays the high homology of canonical CXCR1 and CXCR2 corresponding to an identity matrix score of 76.6% in agreement with expected values, along with secondary structure positions from GPCRdb.[319,320] The sequence identity further improves when describing the truncated form of 6LFL and CXCR1, which have an identity matrix score of 85.8%. This is slightly lower than the truncated form of canonical CXCR2, due to missing residues in the crystal structure. This further enhances the evidence to use 6LFL as a singular template for the construction of a CXCR1 model. Residues are highly homogenous in the TM regions, with the differences mostly lying in the more disordered loop regions. The largest loop is ECL2 consisting of 17 residues in both receptors and only 3 conserved residues (C187, Y188, and Q189 in CXCR1 C196, Y197, and Q198 in CXCR2). As long loop regions such as ECL2 are notoriously difficult to model and this loop is not spatially close to the binding region of interest, no attempts to improve this loop were attempted. It is likely that the models poorly represent this loop which should be accounted for in further work which may implicate this region.

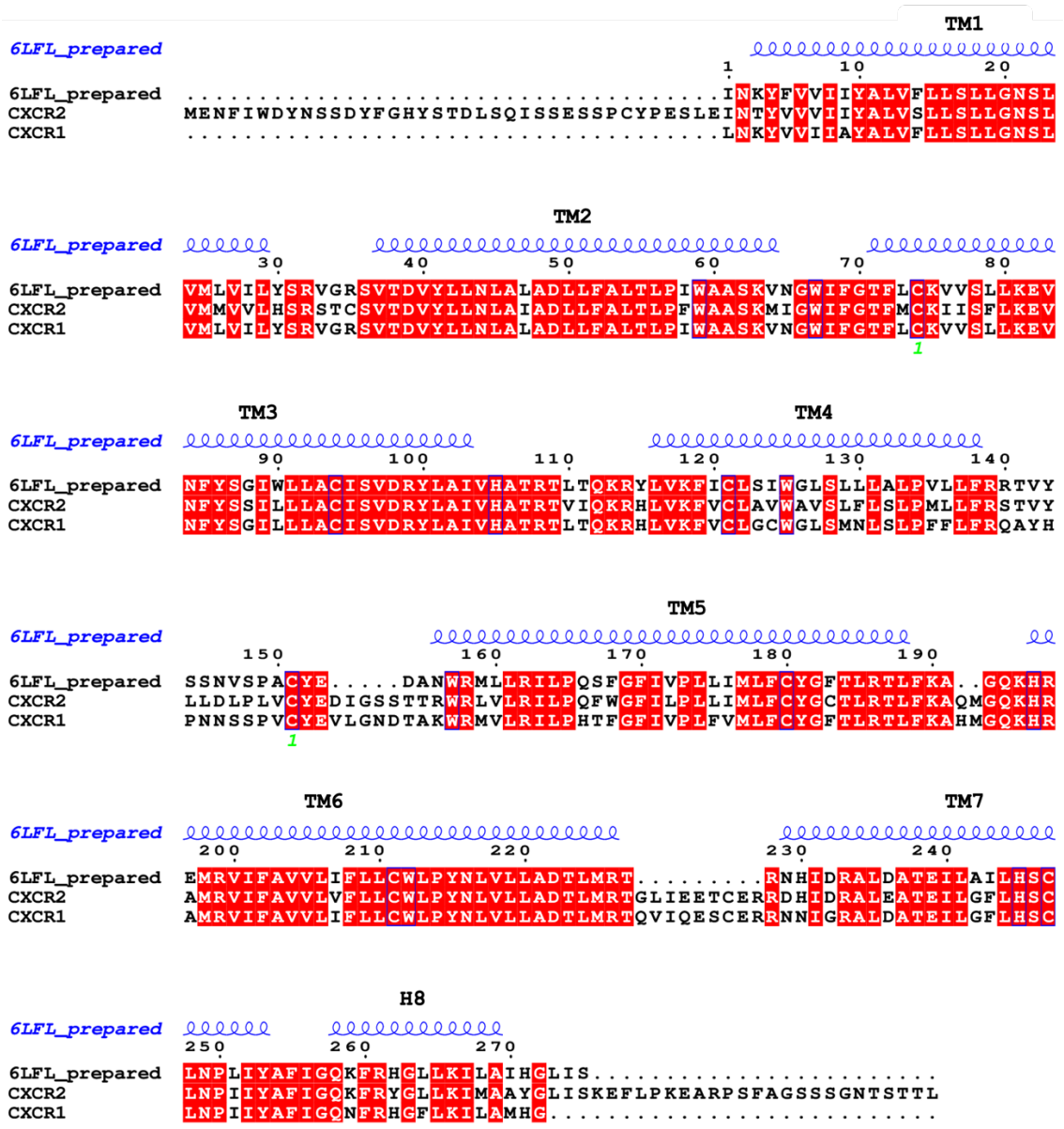

Figure 2-4 Sequence alignment of CXCR2 crystal structure (PDB ID 6LFL[54]) displayed as 6LFL_prepared, canonical CXCR2 (UniProt ascencion code P25025) and canonical CXCR1 (UniProt ascencion code P25025). Secondary structure is depicted as blue helices. Red highlighted regions depict residue identical in all 3 entries.

The models generated from the CXCR2 crystal structure (PDB ID: 6LFL[54]) are presumed to be representations of the inactive state, with CXCL8 and intracellular NAM bound. Initial modelling of 100 CXCR1 and CXCR2 models were built based on the CXCR2 template, 6LFL, without influence of the bound ligand (00767013 (**1**)) found in the crystal structure. However, initial docking of these unliganded structure with the 6LFL ligand, 00767013 (**1**), led to the problematic situation of poor or no binding poses being predicted

in both CXCR1 and CXCR2. Of the 200 docked proteins, only 8 led to successful docking. Of these, none produced the expected binding pose from the literature.[54,134] Further inspection of the binding pocket showed an occlusion to the binding site was introduced by the rotamer change of the I64$^{1.57}$ residue. To solve this problem, the models were built with the ligand as described in **Section 2.2.3,** allowing the binding cavity to be retained.

2.3.2 DOPE scoring to assess model quality

The modeller internal DOPE scoring function was used to determine the 10 lowest scoring CXCR1 truncated models (**Table 2-2**). The table includes the DOPE score of the template, allowing for the determination of the model that is most alike the template based on the distance-dependent statistical potential calculated by DOPE. The 10 models shown fluctuate from DOPE scores of -37736.46 to -37571.93, differing from the template model with a score of -38333.38. In this sample of models, comprising 10% of the total generated models, small differences are evident between the models, which is to be expected, given the high homology between the receptors.

Table 2-2 Top 10 truncated CXCR1 homology models based on global DOPE assessment compared to the template (PDB IDL: 6LFL[54]).

		DOPE scores
Template (PDB ID: 6LFL)		-38333.38
Models	1	-37736.46
	2	-37681.77
	3	-37638.45
	4	-37636.23
	5	-37627.07
	6	-37597.16
	7	-37578.44
	8	-37576.33
	9	-37572.48
	10	-37571.93

DOPE per-residue scores for the 10 best scoring models based on global DOPE are plotted in **Figure 2-5**, along with the template and the full-length CXCR1 model for reference. The *N*- and *C*-termini modelled in the CXCR1 full model displays residues without a reference template due to their omission from the crystal structure. As these regions (highlighted in blue) are highly disordered, it is unsurprising that the truncated models 1-10 show high variance as they approach these regions. This is most apparent close to the *N*-termini where the models not only vary significantly, but also are furthest from the reference template between residues 320-330. The *C*- and *N*- termini regions display no reasonable secondary structure and are unlikely to be implicated in ligand binding due to their distance from the binding site of interest. This strengthened the decision not to model these regions as they tend to be "noise" during investigation.

Poorly predicted loop regions (highlighted in pink) can be explained by the lack of template in these regions, ECL2 (residues 185-190) and ICL3 (residues 233-235). ECL2 presents a difficult challenge in GPCR modelling due its long loop (17 residues in CXCR1 and 2) and high diversity across the superfamily, exemplified even in two closely related proteins such as CXCR1 and 2.[321-323] ECL2 is functionally important for ligand recognition in the

endogenous binding region. It is expected to not be important for the investigation of ligands targeting an intracellular allosteric pocket. This is perhaps a key advantage, when attempting to model and investigate allosteric binding pockets, as ECL2 modelling is superfluous. ECL2 is frequently remodelled following comparative homology modelling using *de novo* techniques. However, it is in a distinct region from the IAM of interest and therefore it was assumed that the loop generated from Modeller[304] was sufficient.

The other poorly predicted region, ICL3, is likely to be important as it is spatially close to the binding site of interest and, subsequently, special consideration of these residues is required during refinement. The ICL3 corresponds to the residues removed for insertion of the stabilising antibody and consists of a small loop of 3 residues. These missing residues explain the high scores observed in this region. However, interestingly, models 1-8 have low variability in this region. It may be beneficial to investigate alternative stabilising techniques/insertions for the intracellular allosteric modulators. One could postulate that insertions into ECL may be beneficial. However, this may not yield the desired outcome due to the cooperativity that exists between the endogenous binding site and the allosteric binding site of interest therefore insertions in the ECL may potentially be unviable. An investigation into the effects of ICL insertions on ligand binding is required to further investigate and answer this hypothesis.

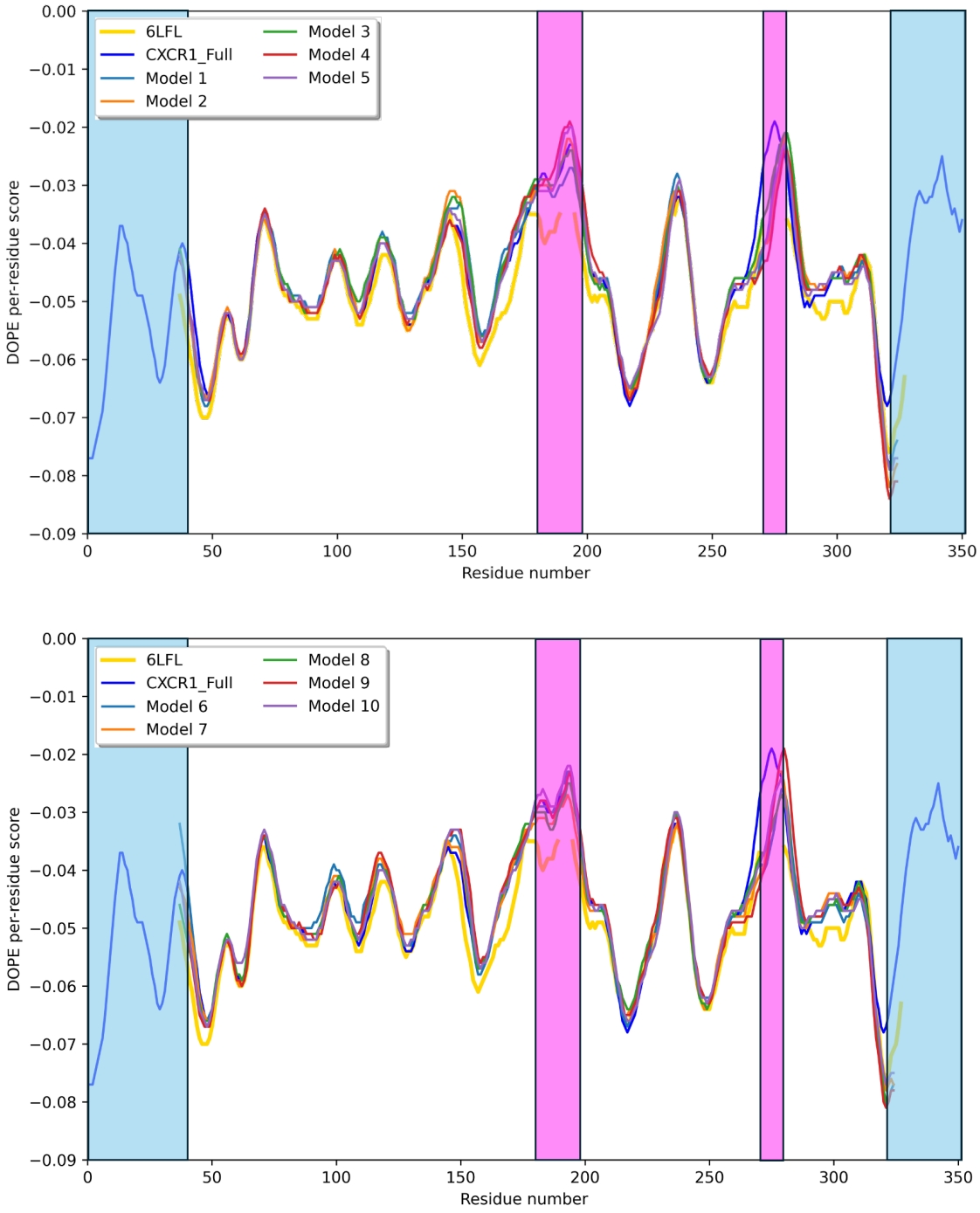

Figure 2-5 DOPE per residue comparison of truncated CXCR1 homology models 1-5 (top) and 6-10 (bottom), compared to the template CXCR2 structure (PDB ID: 6LFL[54]). Template is depicted as a yellow line and a full sequence CXCR1 model depicted as a blue line. Regions highlighted in blue are regions in the *C*- and *N*-terminus which are not present in the template. The region highlighted in pink are the missing loop regions of the template.

In general, the 10 truncated models closely resemble the template model, especially in TM regions, and there is low variability between models, which explains the small variations

in global DOPE scores in **Table 2-2**. Some modelling examples describe taking the model with the lowest DOPE score forward for further investigation.[324-327] The lowest DOPE model for CXCR1, model 1, performed poorly in subsequent docking, unable to generate a suitable docking pose. The poor docking into the "best" model assessed by DOPE and the indistinguishable DOPE per residue plots meant that an alternative approach to rank the models was required to distinguish the binding site residues.

2.3.3 Ranking by inverse docking

Inverse docking is a powerful and important technique that is often used for identifying new macromolecular targets for existing drugs or active molecules, which has been reported in literature reviews and case studies.[328-332] The principles used for inverse docking follow those of docking where sampling of ligand binding poses takes place in an active binding site, and through algorithmic calculations of the binding energies a docking score is generated. Unlike in traditional docking, where a set of ligands is docked into a single protein target, inverse docking takes a singular ligand and attempts to find an active binding site in a set of target proteins. This technique can be employed in this work, where often the "best" model based on an energetic profile does not generate a suitable binding pocket.

Inverse docking was conducted using the autodock vina docking algorithm opposed to Glide, because its ability to run docking protocols *via* scripts without licensing concerns, which occurred when attempting to dock parallel jobs using Glide in Maestro, resulting in failure to complete necessary docking jobs. This resulted in the discontinuation of Maestro for this portion of the investigation.[289,333] The inverse docking was completed *via* an in-house script for autodock vina that generated docking grids for the 100 CXCR1 models based on the position of 00767013 (**1**) in the CXCR2 crystal structure template (PDB ID: 6LFL[54]) after superimposing all receptors. Of the 5 poses generated, the top ranked pose was taken for inspection and the top 5 models were tabulated along with the DOPE scores (**Table 2-3**).

Table 2-3 CXCR1 homology models 11-15 that performed best in an inverse docking experiment into CXCR1. Models 11 and 12 performed equally giving a docking score of -9.9 kcal/mol. Models were compared with their global DOPE scores.

		DOPE scores	Autodock vina docking score (kcal/mol)
Template (6LFL[54])		-38333.38	
Models	11	-37336.26	-9.9
	12	-37182.73	-9.9
	13	-37235.01	-9.7
	14	-37364.54	-9.7
	15	-37470.24	-9.7

The top 2 models generated ligand poses with docking scores of -9.9 kcal/mol and 3 of the models shown generated docking scores of -9.7 kcal/mol. Four other models also gave docking scores of -9.7 kcal/mol, which are not shown. Inspection of these complexes showed that the top ranked model generated a binding pose correlating with the known binding mode of squaramide NAMs in CXCR2, used to determine an acceptable pose in the absence of evidence of a CXCR1 binding mode.[54,134]

DOPE per residue plots were then generated for the 5 models (**Figure 2-6**), displaying similar results to the 10 models in **Figure 2-5.** Again, the high variability regions are in unresolved or missing regions in the crystal structure. Of the top 2 models, model 11 displayed the closest DOPE score compared to the template (-37336.26) and an acceptable RSMD to the template of 0.143 Å. Model 11 was the determined to be the best candidate for further validation and is hereafter simply referred to as the CXCR1 model. The CXCR1 homology model along with the CXCR2 model resulting from modification and refinement of the CXCR2 crystal structure (**Section 2.2.2**) are displayed in **Figure 2-7.**

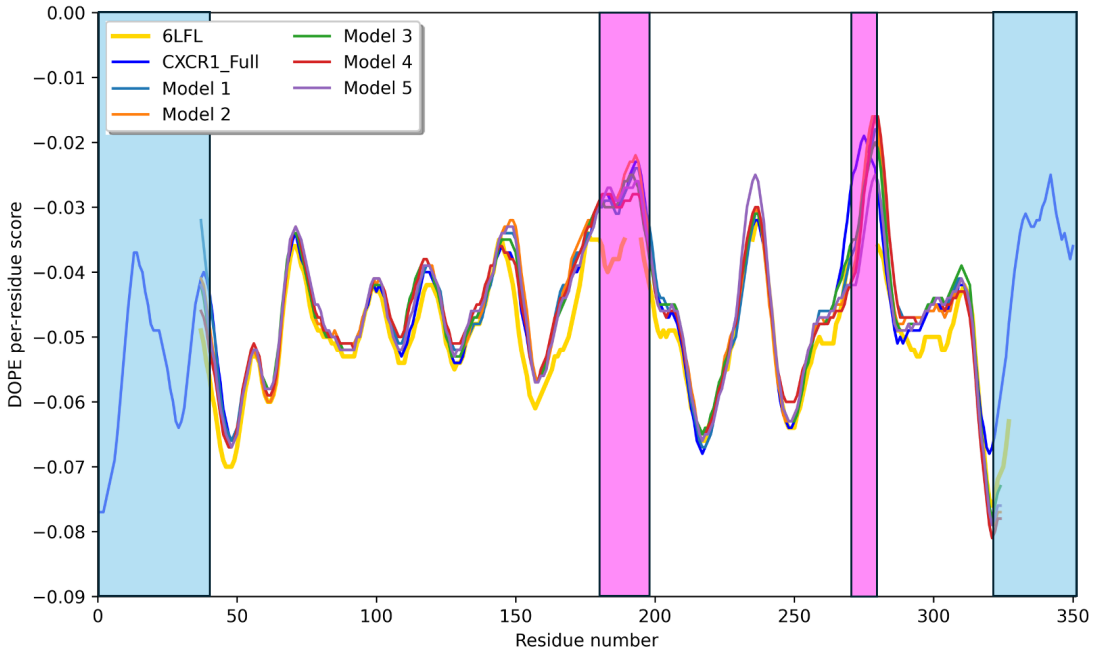

Figure 2-6 DOPE per residue plot of the top 5 inverse dope model 11-15 compared to the template structure (PDB ID: 6LFL[54]) depicted as a yellow line and a full sequence CXCR1 model depicted as a blue line. Regions highlighted in blue are regions in the *C* and *N*-terminus which are not present in the template. The region highlighted in pink are the missing loop regions of the template.

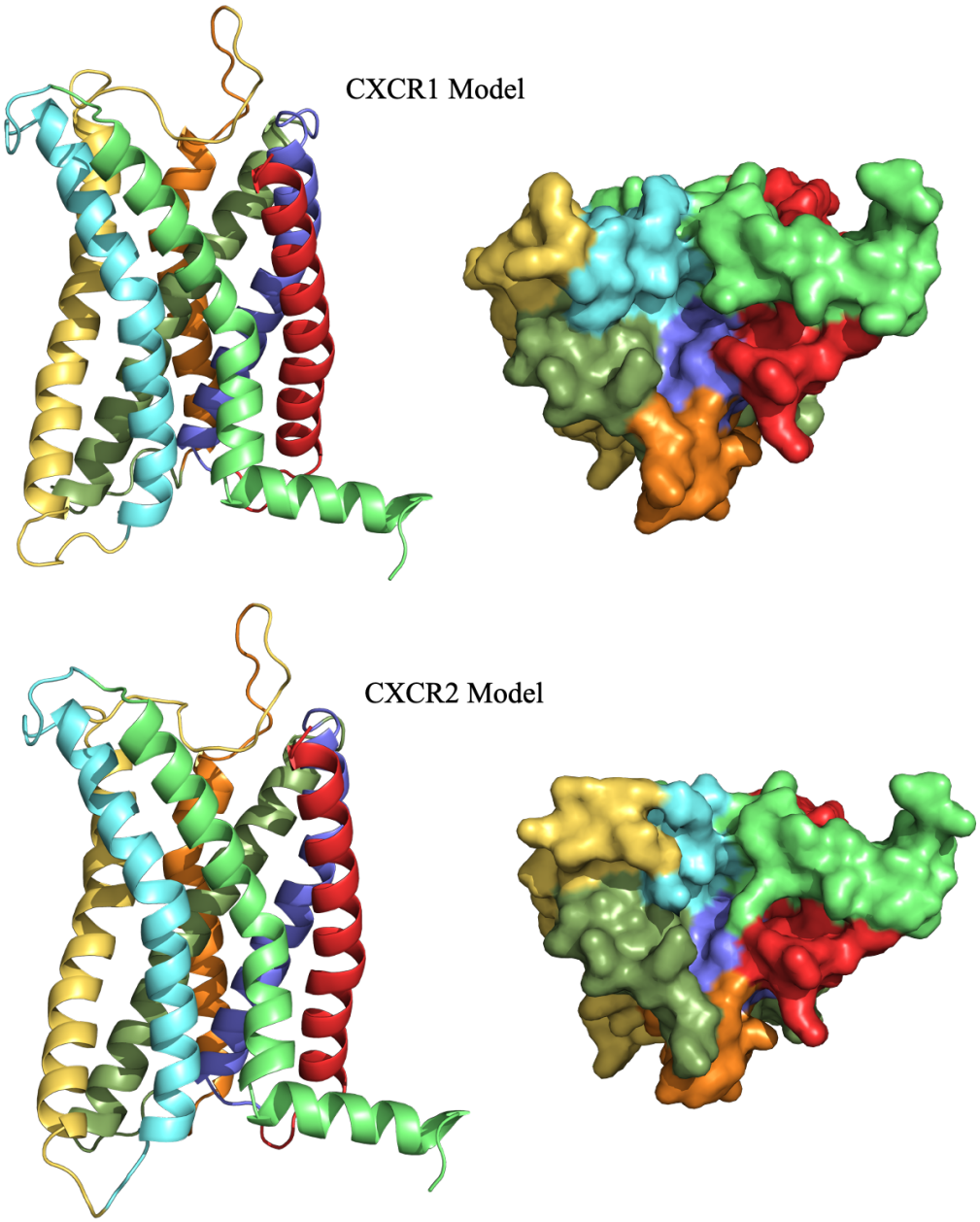

Figure 2-7 Proposed homology models taken forward for validation. (Top left) CXCR1 model displayed in cartoon representation. (top right) CXCR1 model depicted as protein surface. (bottom left) CXCR2 model displayed in cartoon representation. (bottom right) CXCR1 model depicted as protein surface. Transmembrane (TM) regions colour coded as followed: TM1 (Red); TM2 (purple); TM3 (dark green); TM4 (orange); TM5 (yellow); TM6 (blue); TM7 and H8 (Light green).

2.3.4 Server based Validation and model refinement

Models of CXCR1, CXCR2 crystal structure (PDB ID: 6LFL[54]) and the modelled CXCR2 structure were analysed using the web-based server Swiss-Assess[334] to generate Ramachandran plots (Appendix) along with physics and knowledge-based assessments in Molprobity[335] and qualitative model energy analysis (QMEAN) which are summarised in **Table 2-4**.

For the CXCR2 model, which had loops modelled in Prime[289] and mutated to rectify mutations and missing residues in the crystal structure (PDB ID: 6LFL[54]), it was determined that no further refinement was required, since the modifications did not introduce any substantial errors compared to the template. A relatively small increase in Molprobity scoring could be attributed to the newly introduced loop regions, which are disordered, and further inspection of the loops confirmed this. The concerned residues were introduced into ECL3, far from the ligand-binding site. Therefore, the model was not refined further beyond restrained minimization (over 130 steps).

Table 2-4 summary of Swissmodel assessment for CXCR2 crystal structure (PDB ID: 6LFL[54]), initial CXCR11 model, refined CXCR1 model and CXCR2 model. Ramachadran analyses along with Molprobity and QMean outputs are included.

Model	Number of residues							
	% Residues in Favoured regions	Additional allowed regions	Generously allowed regions	Outliers	Rotamer Outliers	Molprobity Score	Clash Score	QMEAN
CXCR2 (6LFL)	94	14	1	0	9	1.18	0	0.63
CXCR1 initial	93.2	14	2	2	16	2.72	20.91	0.67
CXCR1 post refinement	97.2	4	2	0	10	1.16	0	0.67
CXCR2-based on 6LFL	93.77	15	2	0	10	1.33	0	0.65

The initial CXCR1 model introduced 2 Ramachandran outliers of concern, along with 2 significant clashes between S114$^{3.29}$-R171$^{4.60}$ in TM3 and 4, respectively, and V49$^{1.42}$-F295$^{7.43}$ in TM1 and TM7, respectively. These clashes contributed to the high clash score and, consequently, a relatively poor Molprobity score. To solve this, these residues were iteratively refined by manual modification of rotamers, followed by energy minimisation (130 step default) and successfully removed steric clashes between the residues, whilst not introducing further conformational or geometric errors. Correction of rotamer outliers was achieved through manual correction in Maestro, ensuring no further clashes or Ramachandran outliers were introduced. The two Ramachandran outliers in the original structure D274$^{6.58}$ and I273$^{6.57}$ were in ECL3 and were quickly corrected *via* constrained minimisation (130 step default). Minimisation (130 step default) was also implemented on the 16 residues in generously allowed and additional allowed region of the Ramachandran plots, which resulted in all but 6 residues in favoured regions deemed acceptable and not requiring further refinement. Finally, loop modelling was implemented on the 7 residues (K231$^{5.67}$ -His238$^{6.31}$) making up ICL3, which was disrupted by the stabilising antibody in the template crystal structure. Ab initio loop refinement by LoopRefine in Prime[289] resulted in the blue structure displayed in **Figure 2-8.** An all-atom RMSD of 1.64 Å was calculated for the residues in ICL3 showing significant deviation from the original model, which is unsurprising as the template had missing residues in this region and along with the stabilising antibody introduced would likely lead to a high disruption in this region.[54] The final step of refinement was the optimisation of hydrogen bonds and restrained minimisation *via* the protein preparation wizard in Maestro, resulting in the refined CXCR1 model.

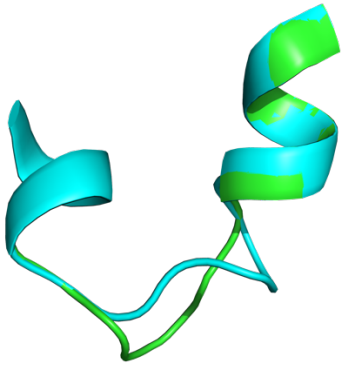

Figure 2-8 ab-initio prediction of CXCR1 ICL3 by RefineLoop in maestro for the loop region between K231$^{5.67}$ to H$^{6.31}$ amino acid sequence: KAHMGKH. the initial model displayed in green vs the refined loop displayed in blue. the bottoms of TM5 and 6 are displayed for reference. all atom RMSD calculated 1.64 Å.

2.3.5 Virtual screening and ligand enrichment for model benchmarking

After docking of the 50 diverse known high affinity ligands for each target along with decoys generated by DUD-E[313], the ligand enrichment was plotted as ROC curves for CXCR1 (**Figure 2-9**) and CXCR2 (**Figure 2-10**), along with calculations of AUC and logAUC values for both receptor models (**Table 2-5**). The ROC log AUC calculations provide a measure of general prioritisation of ligands vs decoys (true positive versus true negative). For docking protocols in CXCR1, rigid docking of ligands using standard precision (SP) Glide proved to perform poorly, unable to differentiate between the known ligands and decoys with linear AUC of 33.79 and logAUC of 10.94 and performed worse than expected than random ranking of ligands. Whilst there was some improvement observed in CXCR2 with AUC of 48.79 and logAUC of 18.69 this would still be concluded as a poor performing docking, with ROC plots displaying early and late enrichment but, overall, performed about the same as random. In contrast, flexible ligand sampling drastically improved logAUC values for the docked ligands, displaying logAUC of 48.47 and 49.195 in CXCR1 and logAUC of 46.66 and 47.39 for SP and XP, respectively. Although there was a minor improvement implementing the XP docking protocol in both receptors, the ROC curves show SP docking having better early enrichment displayed by all known ligands ranked in the top 25% of docked compounds, whereas this was not the case until the top 40% of compounds in XP.

The results from the enrichment study are conclusive that the theoretical model is well-suited to recognising and generating relatively low binding energy poses for known ligands versus predicted 'non-binders' when implementing the Glide SP and XP with flexible ligand docking. ROC logAUC were confidently above the expectation for random ranking for the tested models, and comparatively higher than other similar investigations of benchmarking GPCR homology models by de Graaf *et al*.[85] and Constanzi *et al*.[336,337] justifying the proposed models. In addition, the results suggest robust docking poses involving ligands with core structures akin to the squaramide NAMs such as navarixin (**2**) and 00767013 (**1**) which make up a large proportion of the known active compounds in this study.

Table 2-5 Summary of ligand enrichment study for CXCR1 conducted in Glide. Docking protocols assessed are rigid docking SP, flexible docking SP and flexible docking XP. Included are the enrichment factor (EF) at 1% (EF1) and 5% (EF5).

Receptor model	Sampling	Scoring function	AUC	LogaAUC	EF1	EF5
CXCR1	Rigid	SP	33.79	10.94	1.9	1.2
	Flexible	SP	93.42	48.47	19.1	16.6
	Flexible	XP	93.43	49.2	3.8	16.6
CXCR2	Rigid	SP	48.79	18.69	14.2	8.2
	Flexible	SP	86.67	46.66	19.0	17.2
	Flexible	XP	89.87	47.39	3.5	16.2

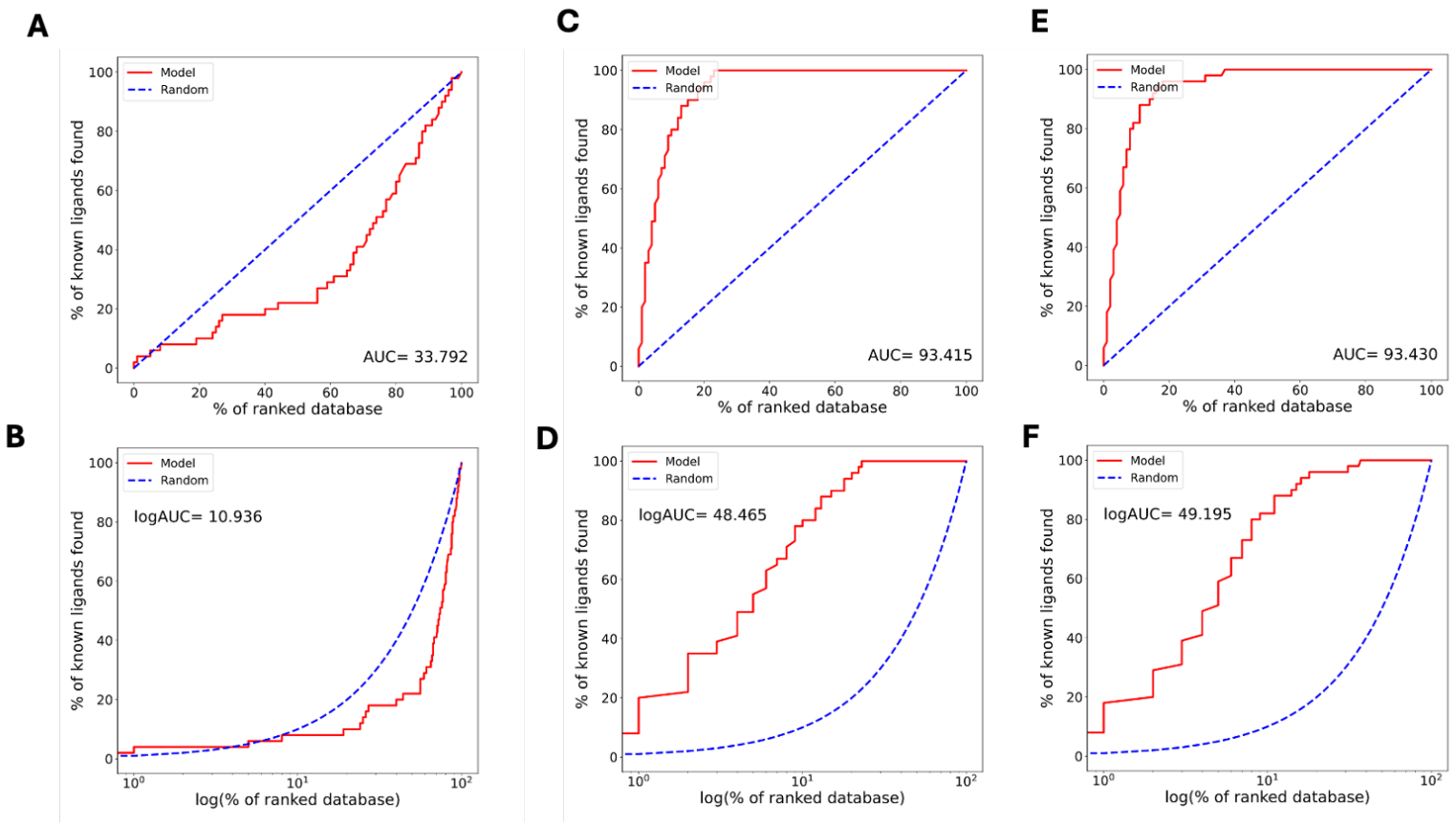

Figure 2-9 ROC plots for CXCR1. (A) and (B) ROC plots for ligand enrichment using rigid SP docking in Glide. (C) and (D) ROC plots for ligand enrichment using flexible SP docking in Glide. (E) and (F) ROC plots for ligand enrichment using flexible XP docking in Glide. Top plots are % known ligands found plotted against % ranked database with AUC displayed. Bottom plots are % known ligands found plotted against log(% ranked database) with logAUC calculated. The blue dotted lines represent the expected datapoints for "random" ranking of ligands. The red lines indicate the plotted values for the proposed CXCR1 homology model.

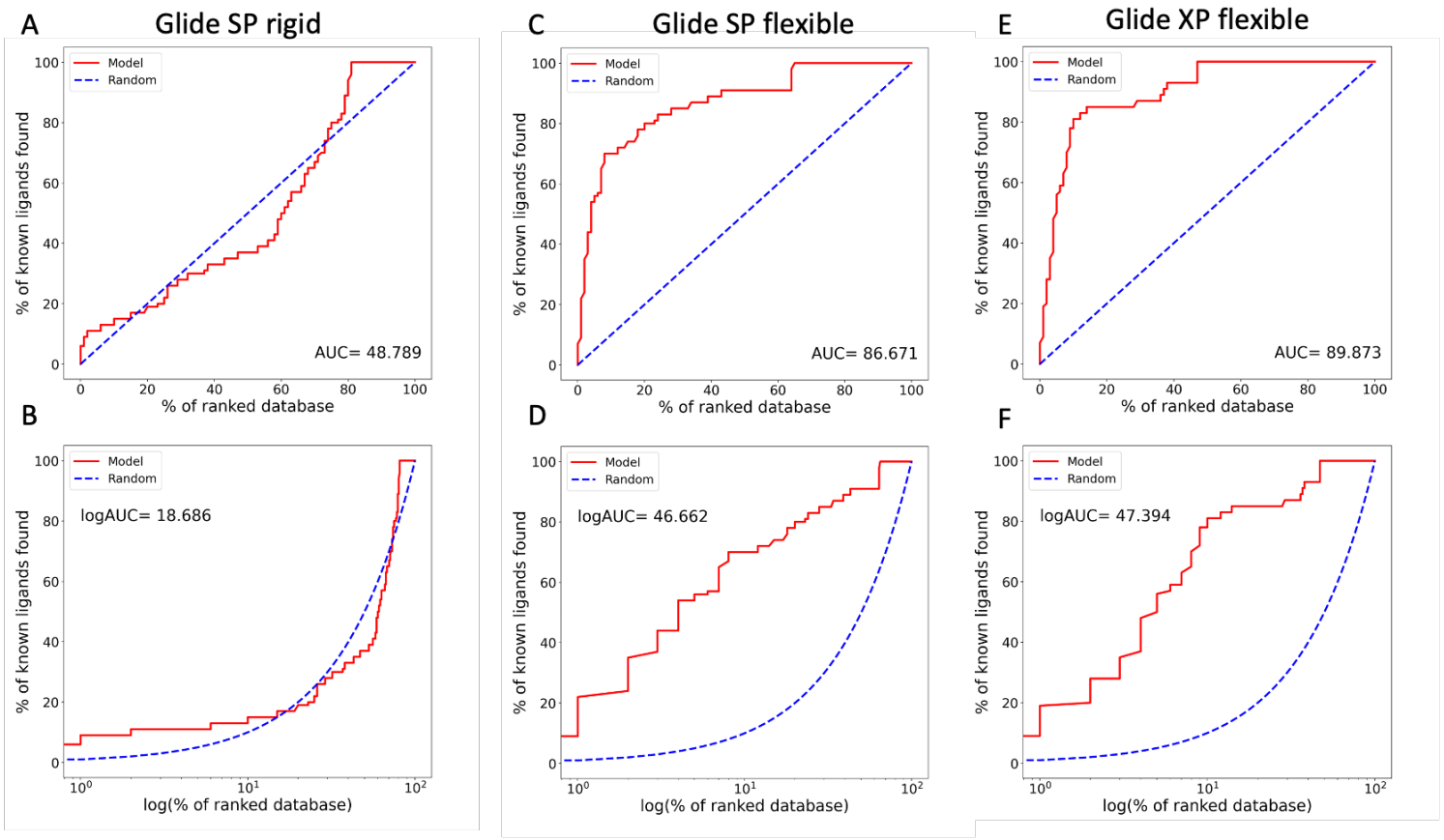

Figure 2-10 ROC plots for CXCR2. (A) and (B) ROC plots for ligand enrichment using rigid SP docking in Glide. (C) and (D) ROC plots for ligand enrichment using flexible SP docking in Glide. (E) and (F) ROC plots for ligand enrichment using flexible XP docking in Glide. Top plots are % known ligands found plotted against % ranked database with AUC displayed. Bottom plots are % known ligands found plotted against log(% ranked database) with logAUC calculated. The blue dotted lines represent the expected datapoints for "random" ranking of ligands. The red lines indicate the plotted values for the modified CXCR2 model.

2.4 Molecular docking of navarixin (2) and 00767013 (1) into CXCR1 and CXCR2

2.4.1 Redocking of the crystallised ligand 00767013 (1)

To examine whether the CXCR1 and CXCR2 models generated were accurate enough to conduct a docking investigation, the crystallised ligand 00767013 (**1**) was docked back into the model for each target. The RMSD of the of the ligands was then calculated and examination of the pocket was conducted. The overlay of the crystal structure-ligand binding mode, and the docked pose generated in CXCR1 and CXCR2 is displayed in **Figure 2-11**. In both targets, the crystal structure binding mode was accurately reproduced by the top scoring docking pose with excellent RMSDs of 0.203 Å and 0.195 Å for CXCR1 and CXCR2 respectively, compared to the crystal structure.

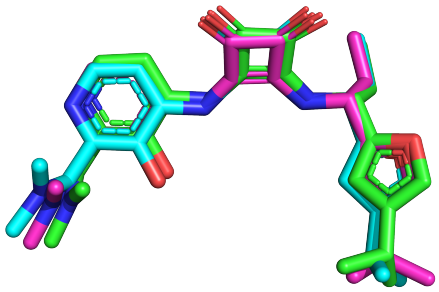

Figure 2-11 Overlay of crystal structure ligand 00767013 (**1**) (pink) with top ranking docking posed generated in CXCR1(blue) and CXCR2 (green) using Glide docking protocol.

Examination of the binding site, defined as residues within 4.0 Å of the docked ligand, displays the high conservation of the target binding pocket (**Figure 2-12**). Of the 17 residues, all but one residue is conserved between the two receptors being the mutation of K320$^{8.49}$ in CXCR2 to N311$^{8.49}$ in CXCR1 (**Table 2-6**). In the top predicted binding pose for each receptor, the hydrogen bond interactions between the squaramide NH and the side chain carbonyl of D75$^{2.40}$ in CXCR1 and D84$^{2.40}$ in CXCR2 were maintained. Furthermore, hydrogen bond interactions were preserved between the squaramide carbonyl and Phe312$^{8.50}$ in CXCR1 and Phe312$^{8.50}$ in CXCR2. Additionally, the unique ionic interaction in CXCR2 between the phenolate and K320$^{8.49}$ was also observed. Glide docking scores of -9.4 and -5.8 kcal/mol of 00767013 (**1**) into CXCR2 and CXCR1 respectively.

Inspection of the binding poses shows three residues contributing to the significantly lower docking score in CXCR1. The non-conserved residue K320$^{8.49}$ makes a salt bridge, with the phenolate along with a strong hydrogen bond with a length of 1.82 Å. The hydrophobic chain of the residue is also shown to help form the hydrophobic pocket which lines the isopropyl furan moiety and contributing to binding *via* van der Waals interactions. In contrast, the shorter N311$^{8.49}$ residue does not contribute any interactions from its side chain and the polar side chain is orientated away from ligand to allow the hydrophobic pocket to be formed for the isopropyl moiety of 00767013 (**1**). In the absence of the salt bridge interaction in CXCR1 the ligand docks preferentially in its protonated phenol state and allows it to form two further hydrogen bonds with D75$^{2.40}$ with lengths of 2.78 Å and 2.54 Å. Two additional interactions were absent in the CXCR1-00767013 (**1**), compared to the CXCR2-00767013 (**1**) complex, these being hydrogen bonds between Thr83$^{2.49}$ to the amide carbonyl and S81$^{2.37}$ to the phenolate in CXCR2. The missing equivalent S72$^{2.37}$ interaction can be rationalised by the bad hydrogen bonding angle introduced by the protonated phenol and conformation of the O-H bond allowing hydrogen bonding to D75$^{2.40}$. Comparison of the T$^{2.39}$ interaction shows that hydrogen bonding is not possible due to the increased distance between the carbonyl amide and the threonine residue, resulting from the phenol ring rotation and movement of the amide moiety moving to the exterior of the binding site.

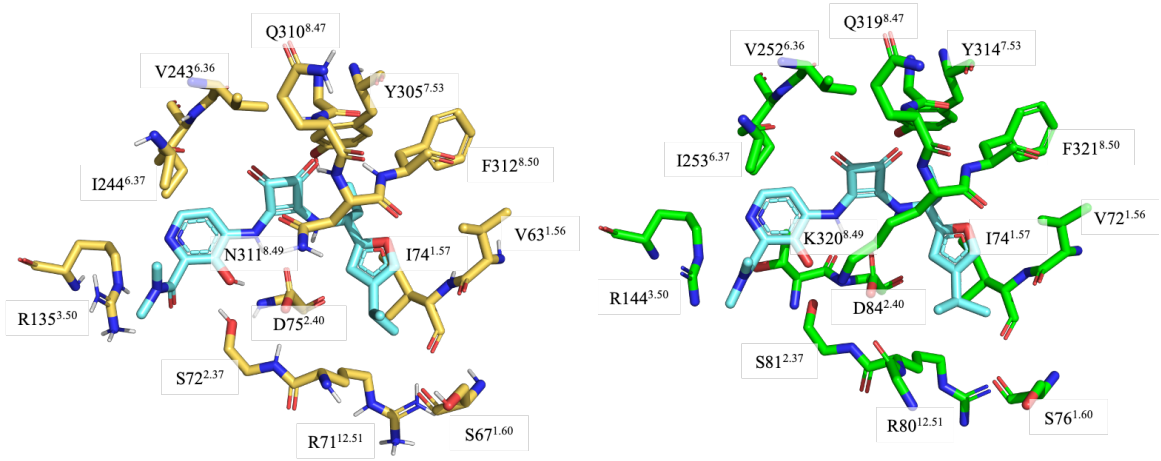

Figure 2-12 Representation of the binding pockets of CXCR1 (yellow) and CXCR2 (Green) when docked with 00767013 (**1**) (blue). Residues are shown as stick representations with single letter code, residue position and Ballesteros–Weinstein numbering (in superscript).[40]

Table 2-6 Summary of residues in the binding sites of CXCR1 and CXCR2 determined by residues within 5 Å of the 00767013 (**1**). Ballesteros–Weinstein numbering system for residue numbering is also displayed showing all residue positions are conserved in the binding pocket. The substitution of N311$^{8.49}$ in CXCR1 to K320$^{8.49}$ is the only modification observed in the binding site (highlighted in red).

Binding site residues		
CXCR1	**CXCR2**	**Ballesteros–Weinstein numbering**
V63	V72	1.56
I64	I73	1.57
S67	S76	1.60
G70	G79	12.50
R71	R80	12.51
S72	S81	2.37
T74	T83	2.39
D75	D84	2.40
R135	R144	3.50
A240	A249	6.33
V243	V252	6.36
I244	I253	6.37
Y305	Y314	7.53
G309	G318	8.47
Q310	Q319	8.48
N311	K320	8.49
F312	F321	8.50

The longer K320$^{8.49}$ residue in CXCR2 also forms hydrogen bond interactions with G79$^{12.39}$ (2.7 Å), S81$^{12.37}$ (1.9 Å) and D84$^{2.40}$ (2.1 Å) forming a polar "lock" at the entrance to the binding site (**Figure 2-13**). In its current conformation, N311$^{8.49}$ does not form any

intramolecular interactions with the side chain facing towards the exterior of the pocket. It would be expected that this "locking" mechanism in CXCR2 further stabilises the binding of diaryl squaramide class of antagonists, however further investigation is required to investigate the movement of these residues in a dynamic environment.

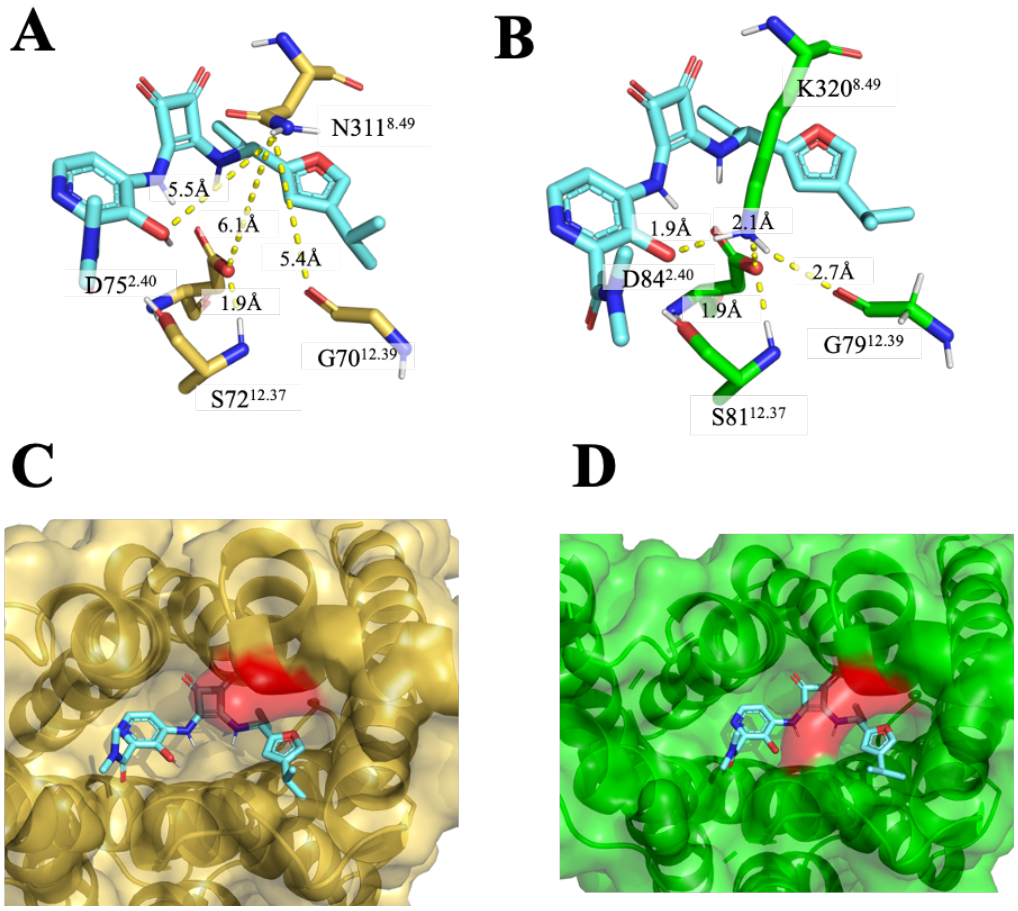

Figure 2-13 Differential binding pocket entrance between CXCR1 homology model and CXCR2 model based on CXCR2 crystal structure (PDB ID: 6LFL[54]). K320$^{8.49}$ (A) CXCR1-00767013 (**1**) complex with ligand represented by light blue sticks. G70$^{12.39}$, S72$^{12.37}$, D75$^{2.40}$ and N311$^{8.49}$ (represented by yellow sticks). (B) CXCR2-00767013 (**1**) complex with ligand represented by light blue sticks. G79$^{12.39}$, S81$^{12.37}$, D84$^{2.40}$ and K320$^{8.49}$ (represented by yellow sticks). (C) Depiction of the protein surface and cartoon ribbons orientated at the entrance to the binding site of CXCR1-00767013 (**1**) complex. N311$^{8.49}$ highlighted in red is shown to not interact with the residues at the bottom of the binding pocket. (D) Depiction of the protein surface and cartoon ribbons orientated at the entrance to the binding site of CXCR2-00767013 (**1**) complex. K320$^{8.49}$ highlighted in red is shown to interact with the residue surfaces at the bottom of the binding pocket.

2.4.2 Confirming the binding mode of 3,4-diaminocyclobut-3-ene-1,2-dione based antagonists using navarixin (2)

Later chemistry efforts will focus on the CXCR2 selective intracellular allosteric antagonist navarixin (**2**) as a basis for exploration of the targets, therefore it was pertinent that a suitable binding mode could be generated for the core structure, which could be used as a reference in future *in silico* studies. The docking of navarixin (**2**) was conducted in the same manner as previously described for 00767013 (**1**) and the crystal structure.[54] The top scoring predicted binding poses generated closely mimicked the V-shaped pose that overlapped well with 00767013 (**1**) in the respective receptors and retained all expected protein-ligand interactions.

A key difference observed in both receptors was the inversion of the furyl ring in both examples which is explained by the orientation of the methyl group into the hydrophobic bundle formed by the conserved residues between the two binding sites: $I253^{6.37}$ and the aliphatic chain of R80 (ICL1).

Docking scores of the top poses for the two ligands are displayed in **Table 2-7**. The results point towards a preference of the C-4 methyl group of navarixin (**2**) in CXCR1 improving the docking score from -7.7 to -8.2 kcal/mol. In contrast, the CXCR2 model displayed a relatively small increase in docking score from -9.4 to -9.0 kcal/mol, which appears to derive from a steric clash between the C-4 methyl with the $K320^{8.49}$ in CXCR2 that spans across the entrance to the binding pocket and isn't present in the CXCR1 model. It should be noted that these models are based on inactive structures bound to 00767013 (**1**). There is likely to be some bias of the binding pocket produced when using this "snapshot" of the receptor. It could be envisioned that the binding cavity around the furyl ring could reorientate to better accommodate the C-3 methyl moiety in an experiment exploring molecular dynamic simulations of the receptor. This work does not extend to additional dynamic experiments, and it was determined that the docking outcomes adequately demonstrate the approximation of the binding mode between 00767013 (**1**) and navarixin (**2**) to CXCR1 and CXCR2.

Table 2-7 Glide docking scores of 00767013 (**1**) and navarixin (**2**) into CXCR1 homology model and CXCR2 refined model based on CXCR2 crystal structure (PDB ID: 6LFL[54]).

Ligand	Glide docking score (kcal/mol)	
	CXCR1 model	CXCR2 model
00767013 (**1**)	-7.7	-9.4
navarixin (**2**)	-8.2	-9.0

2.5 Conclusion

Results suggest that the modified CXCR2 model approximates the binding mode of CXCR2 and squaramide-based antagonists accurately in comparison to crystallographic evidence.[54] The resolution of the CXCR2 crystal structure (PDB ID: 6LFL[54]) is not high enough to accurately detect all receptor-ligand interactions, however remodelling of CXCR2 and subsequent docking into the binding site corroborate what is known about the binding mode of 3,4-diaminocyclobut-3-ene-1,2-dione based antagonists. The modification of CXCR2 (PDB ID: 6LFL[54]) to represent its canonical amino acid sequence did not appear to disrupt the V-shaped binding mode and suggests that this proposed model would be adequate for further investigation for this class of compound.

This chapter has detailed the efforts to generate a high quality CXCR1 homology model. The described model, based on the inactive NAM bound state of CXCR2, could accurately reproduce the binding pose described in literature for CXCR2.[54,134] Ultimately, discriminating between binding of navarixin (**2**) to CXCR1 and CXCR2 is a difficult task without further high-resolution crystal structures of both receptors. Ideally, there would be access to an ensemble of structurally diverse ligands bound to the two receptors that would give us greater understanding of the binding site and the residues within it. In the absence of suitable experimental CXCR1 structures, efforts have been made to recreate the binding mode of the CXCR1-NAM bound inactive state. In principle, both receptors vary little in their immediate binding site (defined as 5 Å from the ligand), with the only differential residue being K320$^{8.49}$ in CXCR2 and N311$^{8.49}$ in CXCR1. The longer K320$^{8.49}$ residue is shown to move in close distance (1.9 Å) to the phenolate, generating a strong ionic interaction with the phenolate moiety present in navarixin (**2**) and 00767013 (**1**), compared to the N311$^{8.49}$ in CXCR1, which sits 5.4 Å away from the phenolate moiety in the two

ligands. In addition, the further reaching K320$^{8.49}$ in proximity to D84$^{2.40}$ and T83, which serves to "close" the binding pocket in the CXCR2 model. Investigation into the significance of the modification of K320$^{8.49}$ in CXCR2 to N311$^{8.49}$ in CXCR1 warrants further investigation which follows in **Chapter 4**.

It is unclear with the current limited evidence whether the binding mode described in this chapter accurately approximates that of CXCR1-IAM. However, given the substantial similarity between the binding regions of the two receptors, it is easy to envision that their binding modes are not significantly different. In comparing the two receptors, the main contributor to the differential binding of navarixin (**2**) and 00767013 (**1**) in the two receptors appears to be the mutation of K320$^{8.49}$ in CXCR2 to N311$^{8.49}$ in CXCR1. The residue seems to facilitate a strong ionic interaction between K320$^{8.49}$ and the phenolate in CXCR2 compared to in CXCR1, where N311$^{8.49}$ is distantly positioned from the phenolate, and similar interactions are absent. It is difficult to conclude whether this accounts for the 15-fold selectivity observed for navarixin (**2**) between the two receptors or, perhaps, a more nuanced relationship exists which cannot be distinguished from the current evidence that the CXCR1 and CXCR2 models present.

Chapter 3 - Design, Synthesis, and characterisation of amino acid ester functionalised analogues of navarixin (2)

3.1 Introduction

In the pursuit of allosteric modulators targeting the CXCR1 and CXCR2 receptors for therapeutic use, current efforts have yielded candidates with preferential activity against CXCR2 over CXCR1, aiming to address various inflammatory diseases (e.g., COPD, asthma, psoriasis) and cancer.[147,160,197,228-230,248] However, these efforts have faced challenges, with no successful drug reaching the market and encountering significant obstacles, notably in phase II clinical trials.[147,160,162,338] Navarixin (**2**), previously discussed in **Chapter 1**, is a highly potent clinical candidate for diseases including COPD[147] and an adjunct in advanced cancer treatment.[339] It predominately acts upon CXCR1/2 receptors and belongs to the 3,4-diamino-cyclobut-3-ene-1,2-dione series of compounds previously discussed in **Chapter 1**.[252] Navarixin (**2**) binds to both CXCR1 and CXCR2, but exhibits 15-fold selectivity towards CXCR2 over CXCR1.[134,252] Navarixin (**2**), as for other clinical candidate NAMs, such as AZD5069 (**3**) and danirixin (**4**), have failed to meet efficacy criteria for symptomatic relief and disease progression in phase II clinical trials for COPD[147-149], severe asthma[160] (NCT00688467), and other inflammation mediated diseases[10,15,191]. Navarixin (**2**) and AZD5069 (**3**) have now been retooled as adjunct cancer treatments and are under investigation for the treatment of cancers such as advanced or metastatic castration-resistant prostate cancer (CRPC), microsatellite-stable colorectal cancer (MSS CRC), or non-small-cell lung cancer (NSCLC) for navarixin[339] and advanced hepatocellular carcinoma (HCC) for AZD5069 (**3**).[340] Whilst preclinical evidence for the treatment of neutrophil-mediated diseases using intracellular allosteric modulators (IAMs) targeting the CXCR1/2 axis, are mounting, translation into clinical trials have, so far, been unsuccessful.[10,15,147,149,340] Consequently, there is a growing need for additional studies and clinical trials to evaluate the therapeutic potential of CXCR1/CXCR2 inhibitors against neutrophil-mediated diseases.[15]

In addition to IAMs there have also been compounds targeting CXCR1/2 developed that display CXCR1 selectivity over CXCR2, through an extracellularly accessible allosteric

binding pocket, such as reparixin (**6**), a clinical candidate for operable HER-2-negative breast cancer[196] and severe COVID-19 pneumonia.[341] There are currently no compounds of the intracellular allosteric mode of action, such as navarixin and AZD5069 (**3**), which display higher affinity for CXCR1 compared to CXCR2.[54,246,248] The development of high potency pharmacological tools that selectively bind to CXCR1 could be utilised in conjunction with those that selectively target CXCR2 to further understand the differential roles that CXCR1 and CXCR2 play during cellular signalling in neutrophil-mediated disease states such as COPD, asthma and cancer as previously discussed in **Chapter 1**.

The pursuit of selective CXCR1 therapeutics have also recently shown promise, especially in disease states that predominantly express CXCR1. For instance, preclinical evidence has highlighted the role of CXCR1 in driving proliferation and metastasis in human cancers, including melanoma[202], thyroid[342], and breast cancer.[13,84,196,343] The development of small molecule tools that selectively bind to either CXCR1 or CXCR2 could enhance our understanding of these receptors' individual roles in disease progression, paving the way for more effective therapies.[10,170,183]

With the majority of 3,4-diamino-cyclobut-3-ene-1,2-dione NAMs tooled to selectively target CXCR2 over CXCR1, there are often gaps in the SAR of CXCR1. An example of this is the clear preference for disubstituted salicylamides in CXCR2 affinity, although exploration of this region was lacking to determine activity towards CXCR1.[344] Efforts previously conducted on the SAR for CXCR2 and CXCR1 NAMS led to the currently established pharmacophore for targeting CXCR2 (**Figure 3-1**).[345-347] However, there are a lack of reports discussing an equivalent pharmacophore for CXCR1, or the structural characteristics leading to the selectivity of CXCR1. Addressing the gap in the literature may be crucial for the advancement of our understanding and application of therapeutic agents aiming to modulate the activity of CXCR1 and CXCR2.

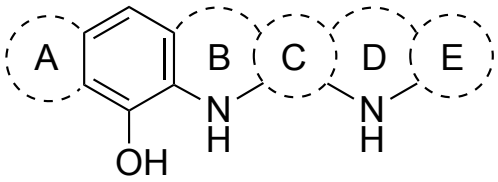

Figure 3-1 Proposed pharmacophore for negative allosteric modulators (NAMs) targeting CXCR2, situated within an intracellular pocket overlapping the $G\alpha_i$ binding site.[345-347] This pharmacophore is derived from SAR studies conducted on chemical scaffolds including diaryl ureas, such as danirixin (**4**), and 3,4-diamino-cyclobut-3-ene-1,2-diones, such as navarixin (**2**).[203,209,211,226,246,249,298,344,348]

With the CXCR1 and CXCR2 homology model previously developed in **Chapter 2**, a rational structure-based drug design (SBDD) strategy was envisioned to design and develop a series of squaramide based small molecules. Two compounds - navarixin (**2**) and compound **22** stood out as leads for further development. Navarixin (**2)** is a highly potent CXCR2/CXCR1 selective NAM with reported CXCR2 and CXCR1 potencies of IC_{50} = 2.6 nM and 36 nM respectively, derived from a functional human neutrophil chemotaxis assay. Compound **22** was later developed by the same group at Schering-Plough (now part of Merck & Co), with reported potencies against CXCR1 and CXCR2 of 7.3nM and 1.3 nM, respectively.[248] These two compounds differ by the removal of the furanyl C5-methyl moiety in navarixin (**2)**, and its replacement with an isopropyl group at C4 in **22**. Both compounds are derived from the same precursor; with the squaric acid monoamide monoester intermediate being subjected to an amidation with the corresponding chirally pure amine hydrochloride salt (**Figure 3-2**).[248,250] The synthesis detailed for the 4-isopropylfuran-2-yl amine (**22a**) involves an 8-step synthetic route, which presents several challenges in terms of time, labour, and cost. In contrast, the (*R*)-1-(5-methylfuran-2-yl)propan-1-amine derivative (**2a**) of navarixin (**2**) is available from commercial sources. The availability of this compound eliminates the need for an extended synthesis and allows immediate progression to subsequent stages of drug development around ring A, where efforts for this portion of work focussed. Therefore, navarixin (**2**) was chosen as the lead compound and benchmark for assessing pharmacological profiles.

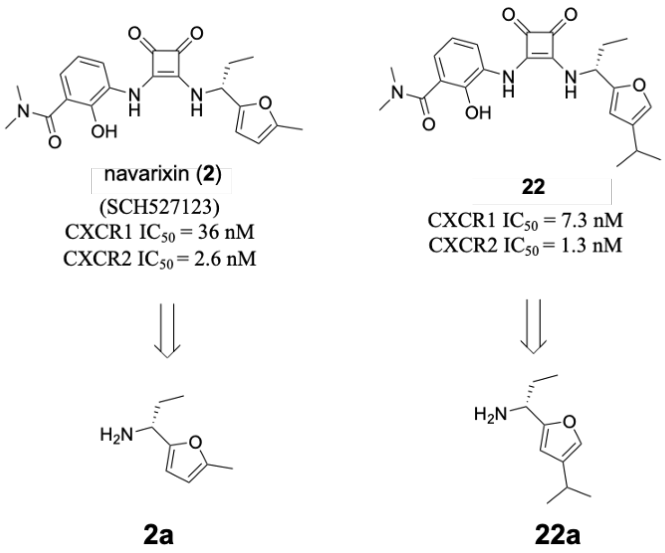

Figure 3-2 Navarixin (**2**) and **22**, reported NAMs targeting the intracellular binding site overlapping $G\alpha_I$, derived from substituted furanyl alkylamines, **2a** and **22a**, respectively. **2a** is commercially available, whilst **22a** involves an 8-step synthetic route.

3.2 *In silico* exploration of the intracellular binding pockets of CXCR1 and CXCR2

With the intracellular binding site of CXCR2 established in literature, **Chapter 2** showed that the binding mode displayed in the 00767013 (**1**)-CXCR2 bound pose, derived from crystal structure experiments, could be recreated in the presented CXCR1 homology model.[54,134] The key differences observed in binding modes between CXCR1 and CXCR2 were derived from hydrogen bonding and ionic interactions unique to CXCR2. Despite these differences, binding poses in both receptors were practically identical for 00767013 (**1**), with navarixin (**2**) adopting the characteristic V-shaped pose. Further inspection of the binding poses showed that, in all top-ranking poses, the methyl groups of the *N,N*-dimethyl amide moiety did not appear to make any crucial interactions with either receptor or was shown to protrude out of the binding pocket towards the cytoplasmic space (**Figure 3-3**). This provided evidence for this region as a potential site for tolerated modifications to navarixin (**2**). Recently, there have been examples presented by Casella *et al*.[138] and Huber *et al*.[349] that exploit this salicylamide moiety, through the attachment of a linker and fluorophore, allowing fluorescent probes that retain high CXCR2 affinity.[138,349] As previously discussed in **Chapter 1**, the SAR around the salicylamide region of navarixin (**2**) is not as well defined in the literature, compared to work that has been conducted around

the furan and squaramide core.[226,248-250,344,350] We hypothesised that a structure-based rational design program could be employed to investigate the CXCR1 and CXCR2 SAR surrounding the salicylamide.

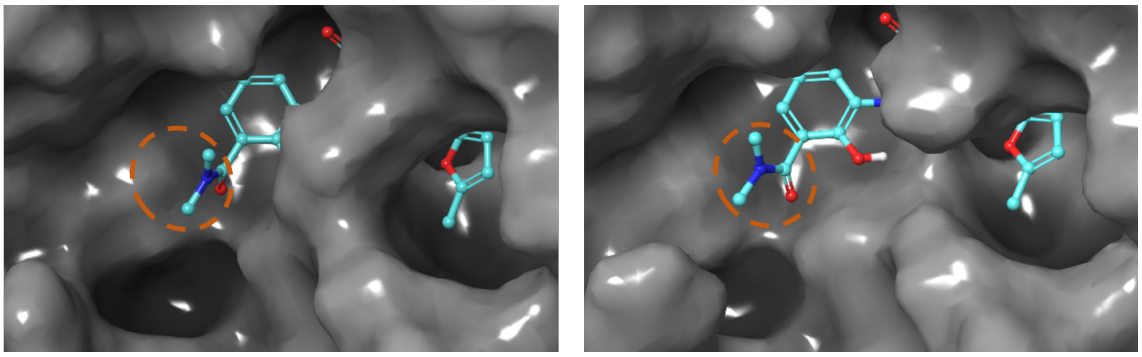

Figure 3-3 Binding surface depiction of navarixin (**2**) - CXCR1 complex (left) and navarixin (**2**)-CXCR2 (right) generated from docking studies in **Chapter 2**. Orange highlighted region shows the two methyl groups of the dimethylamide moiety protruding out of the binding pocket.

Observations of the ligand-receptor complexes for CXCR1 and CXCR2 identified some potential distinct cavities in proximity to the dimethyl amide moiety, which prompted the use of SiteMap in Schrödinger.[303,351] The aim of this investigation was to identify and characterise potential binding sites, which are not occupied by the docked ligands and could be exploited to facilitate modulation in the activity profiles of NAMs. This approach has been successfully employed to identify not only putative binding sites, but further active site cavities that could correlate to ligand-protein interactions.[351-356] From the SiteMap module, potential binding sites were analysed in regions up to 5 Å from navarixin (**2**) in the navarixin (**2**)-CXCR1/CXCR2 complexes to identify specific sites for potential small molecule interactions in both receptors.

SiteMap identified multiple regions for ligand binding around the dimethylamide moiety that may be exploited for drug modifications (**Figure 3-4**). A significant hydrogen bond donor region is observed, originating from a conserved Arginine residue shown to protrude from ICL2. A potential shallow binding cavity was observed in both receptors, but at different distances from navarixin (**2**) in CXCR1 (6.13 Å) and CXCR2 (5.18 Å), respectively (defined as the distance between the dimethyl amide moiety and $D^{3.49}$ in both receptors). This pocket comprises of multiple conserved residues between in the binding sites of CXCR1 and CXCR2 stemming from TM2, TM3, and ICL2. The residues

contributing this pocket are S72$^{2.37}$, V73$^{2.38}$, D134$^{3.49}$, T143 (ICL2) and T145 (ICL2) in CXCR1, and S81$^{2.37}$, V82$^{2.38}$, D143$^{3.49}$, T152 (ICL2) and T154 (ICL2) in CXCR2. The cavity appears to have a large cluster of hydrogen bonding residues from polar side chains, which contributes to a high potential for druggability in this region, and an aspartic acid residue at the back of the cavity. The potential binding regions identified warranted further investigation *via* molecular probes designed to probe this extended region of the receptor.

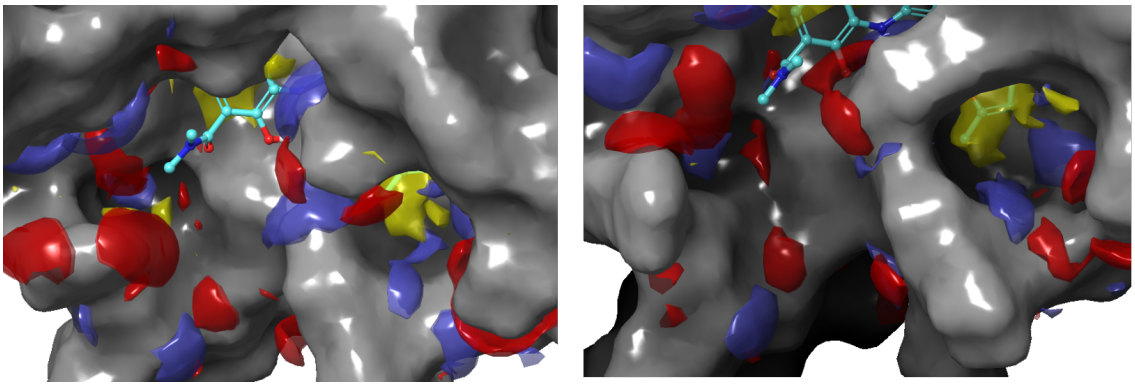

Figure 3-4 Results of Sitemap analysis in Schrödinger conducted on navarixin (**2**)-CXCR1 (left) and navarixin (**2**) – CXCR2 (right) generated from docking studies in **Chapter 2**. Coloured regions display potential binding interactions (hydrogen bond donating – red, hydrogen bond accepting – blue, hydrophobic surfaces – yellow).

3.3 Design of amino acid ester functionalised analogues of navarixin (2)

With several potential druggable binding cavities now identified in CXCR1 and CXCR2 to be exploited for protein-ligand interactions in proximity to the *N,N*-dimethylamide moiety, we then set about designing a series of small molecules with the aim to give insight into the CXCR1 and CXCR2 SAR around the salicylamide. Naturally occurring amino acids are simple and structurally diverse with extensive pharmacological activities.[357] These features make amino acids, or amino acid derivatives, appealing candidates for functionalising small molecules in medicinal chemistry when attempting to modulate the pharmacological activity of a lead compound.[357-359] Additionally, these modifications can often improve other therapeutically relevant properties, such as improved bioavailability, water solubility and reduced cytotoxicity.

It was envisaged that the lead compound, navarixin (**2**), would be an excellent candidate for the functionalisation *via* amino acid/amino acid-like moieties, owing to the presence of

the dimethylamide moiety. This feature does not appear to be vital for protein-ligand binding from our docking studies previously shown in **Section 3.2**. This is also supported in the literature, where the dimethylamide moiety has been utilised for the synthesis of fluorescent probes for CXCR1 and CXCR2.[138,349] By strategically incorporating amino acid ester moieties into the salicylamide region, we can visualise a platform for exploring diverse structural modifications, whilst requiring minimal modifications to the synthetic route.[360] This modification strategy not only enables the exploration of structural diversity, but also holds the promise of optimizing the lead compound's overall pharmacological and physicochemical properties. Moreover, this strategy could allow for further functionalisation of the lead compound. Specifically, the carboxylic acid/ester moiety, introduced through amino acid conjugation, provides a versatile handle for subsequent reactions. By exploiting the reactivity of the carboxylic acid/ester functionality, we can iteratively introduce tailored modifications to optimize various aspects of the lead compound, offering a powerful means to systematically exploring the chemical space. Ten amino methyl esters were selected based on their structural diversity (**Figure 3-5**) to incorporate into amino ester analogues of navarixin (**2**).

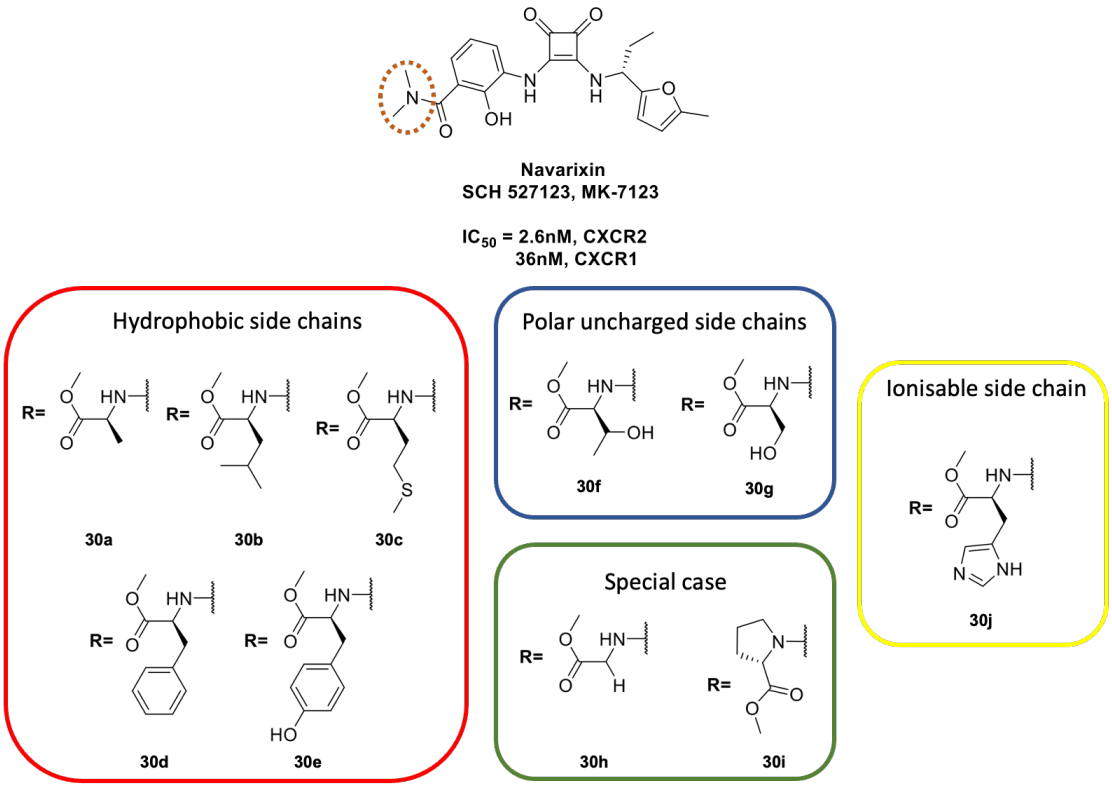

Figure 3-5 Proposed ligand design, functionalising lead compound, navarixin (**2**) with 10 structurally diverse amino esters in place of the *N,N*-dimethylamide moiety. Side chains

chosen are grouped into the type of substituent: hydrophobic side chains (red box), polar uncharged side chains (blue box), special cases (green box), and charged side chain (yellow box).

3.4 Molecular docking of amino ester functionalised navarixin (2) analogues

The proposed amino acid functionalised navarixin (**2**) analogues **30a-j** were docked into the intracellular binding site of CXCR1 and CXCR2 models using Glide in Maestro in a manner according to previous flexible ligand docking protocols in **Chapter 2**. Upon analysis, it was observed that the top scoring predicted binding modes for each of the proposed amino acid conjugate ligands (**30a-j**) exhibited similarities to the binding mode observed for navarixin (**2**), as determined in previous docking studies in **Chapter 2**. Additionally, these binding modes were consistent with the structural features observed in X-ray structures of CXCR2 bound to 00767013 (**1**).[54] Notable retained features of the binding poses include the positioning of the squaramide moiety, which allowed for hydrogen bond interactions with aspartic acid residue within the receptors. Specifically, the two nitrogen atoms of the squaramide core formed hydrogen bonds with conserved $D^{2.40}$ residue ($D75^{2.40}$ in CXCR1 and $D84^{2.40}$ in CXCR2), contributing to the stabilization of the ligand-receptor complex. Furthermore, the furan ring located on the ring B of the molecule was observed to occupy a hydrophobic pocket within both binding sites. This pocket was established by conserved residues $V60^{1.53}$, $V63^{1.56}$, and $I64^{1.57}$ in CXCR1 and $V69^{1.53}$, $V72^{1.56}$, and $I73^{1.57}$ CXCR2, which provide a favourable cavity for the accommodation of the furan ring. All ligands have the retained additional binding interactions in CXCR2, stemming from the $K320^{8.49}$ residue. This residue is shown to form ionic interactions with the phenolate, in addition to one, or both, carbonyls of the squaramide.[54] The preservation of these crucial binding mode features suggests that the proposed amino acid conjugates did not substantially interfere with the essential binding interactions demonstrated by the lead compound navarixin (**2**).

The Glide docking scores (kcal/mol) for each ligand with the squaramide and furan moieties, in agreement with previous docking poses, are reported in **Table 3-1**. In general, all proposed ligands (**30a**-**j**) exhibited lower docking scores in CXCR2, compared to CXCR1, indicating better predicted binding affinity.

Table 3-1 Glide docking scores of **30a-j** in CXCR1 and CXCR2 models generated in **Chapter 2**. Docking scores were calculated from the Glide docking protocol using flexible ligand docking. Displayed scores are from the top scoring pose for each ligand displaying binding poses correlating to validated poses in **Chapter 2** and crystal structure of CXCR2-00767013 (**1**) (PDB ID: 6LFL[54]). The side chain is given for structure reference.

Ligand		Glide docking score (kcal/mol)	
	Amino acid side chain	CXCR1 Model	CXCR2 Model
navarixin (**2**)	-	-8.6	-10.9
30j	*L*-His	-10.5	-11.0
30i	*L*-Pro	-10.1	-11.7
30e	*L*-Tyr	-9.8	-11.8
30f	*L*-Thr	-9.8	-11.2
30c	*L*-Met	-9.7	-11.2
30g	*L*-Ser	-9.5	-10.8
30h	Gly	-9.2	-10.8
30a	*L*-Ala	-9.2	-9.8
30b	*L*-Leu	-9.2	-10.9
30d	*L*-Phe	-9.2	-10.1

Ligands **30h** (Gly analogue), **30a** (*L*-Ala analogue), and **30b** (*L*-Leu analogue), correspond to increasing alkyl side chain lengths. In CXCR1, ligand **30h** displayed a distinct orientation where neither the methyl ester moiety nor the hydrogen side chain had favourable interactions in the binding cavity, and the glycine methyl ester modification of navarixin (**2**) orientated toward the intracellular space. This binding pose, showing no interactions with an extended binding pocket cavity was an outlier across predicted poses of **30a-j** in CXCR1. Ligands **30a** and **30b** demonstrated a common binding pose in CXCR1, with the methyl ester moiety buried into a binding cavity distinct from the potential druggable pocket previously described in **Section 3.2**. A representative binding pose of **30a**-CXCR1 is shown in **Figure 3-7a**. The methyl ester was shown to occupy a

relatively shallow binding cavity formed between I139$^{3.54}$ and the alkyl chain of K237$^{6.30}$ on TM3 and TM6, respectively. Additionally, this predicted binding pose was accompanied by a H-bond interaction between the ester carbonyl and R144$^{34.52}$ on ICL2.

In CXCR1, ligands **30a** (*L*-Ala analogue), **30b** (*L*-Leu analogue), **30d** (*L*-Phe analogue), **30f** (*L*-Thr analogue), and **30g** (*L*-Ser analogue) generated predicted binding poses, where the methyl ester consistently occupied the shallow binding cavity between TM3 and TM6. Ligands **30g** and **30f** displayed mildly improved binding energy, when compared to ligand **30h** (Gly analogue), evidenced from the docking scores (ligand **30g**: -9.5 kcal/mol, ligand **30f**: -9.8 kcal/mol, ligand **30h**: -9.2 kcal/mol). This improvement in docking score can be attributed to distinct hydrogen-bonding interactions within the ligand-receptor complex. Specifically, in ligand **30g**, an interaction between the hydroxyl group of the serinyl side chain and residue R135$^{3.50}$ was observed. Ligand **30f** demonstrated a hydrogen bond between the hydroxyl group of the threoninyl side chain and the carbonyl group of the backbone of residue A138$^{3.53}$.

In CXCR2, ligands **30h** (Gly analogue), **30a** (*L*-Ala analogue), **30b** (*L*-Leu analogue), **30d** (*L*-Phe analogue), and **30f** (*L*-Thr analogue) exhibited binding poses reminiscent of **30a** in CXCR1, with the methyl ester consistently occupying a hydrophobic pocket between transmembrane helices 3 and 6. The two residues forming this pocket are conserved between the two receptors, corresponding to I148$^{3.54}$ and K246$^{6.30}$ in CXCR2. This binding pose is represented by **Figure 3-7d**, illustrating the **30a**-CXCR2 predicted complex. While ligands **30a**, **30b**, **30d** and **30f** displayed similar binding poses in both CXCR1 and CXCR2, ligand **30h** exhibited the previously described hydrophobic cavity between TM3 and TM6 in CXCR2, in contrast to the binding pose observed in CXCR1. Additionally, analysis of the docking scores of **30a-j** in CXCR2 **30h**, **30b**, **30d**, **30f** and **30g** did not show significant improvement compared the reference, navarixin (**2**) (-10.9 kcal/mol) and **30a** and **30g** displayed poorer docking scores (-9.8 and -10.1 kcal/mol respectively).

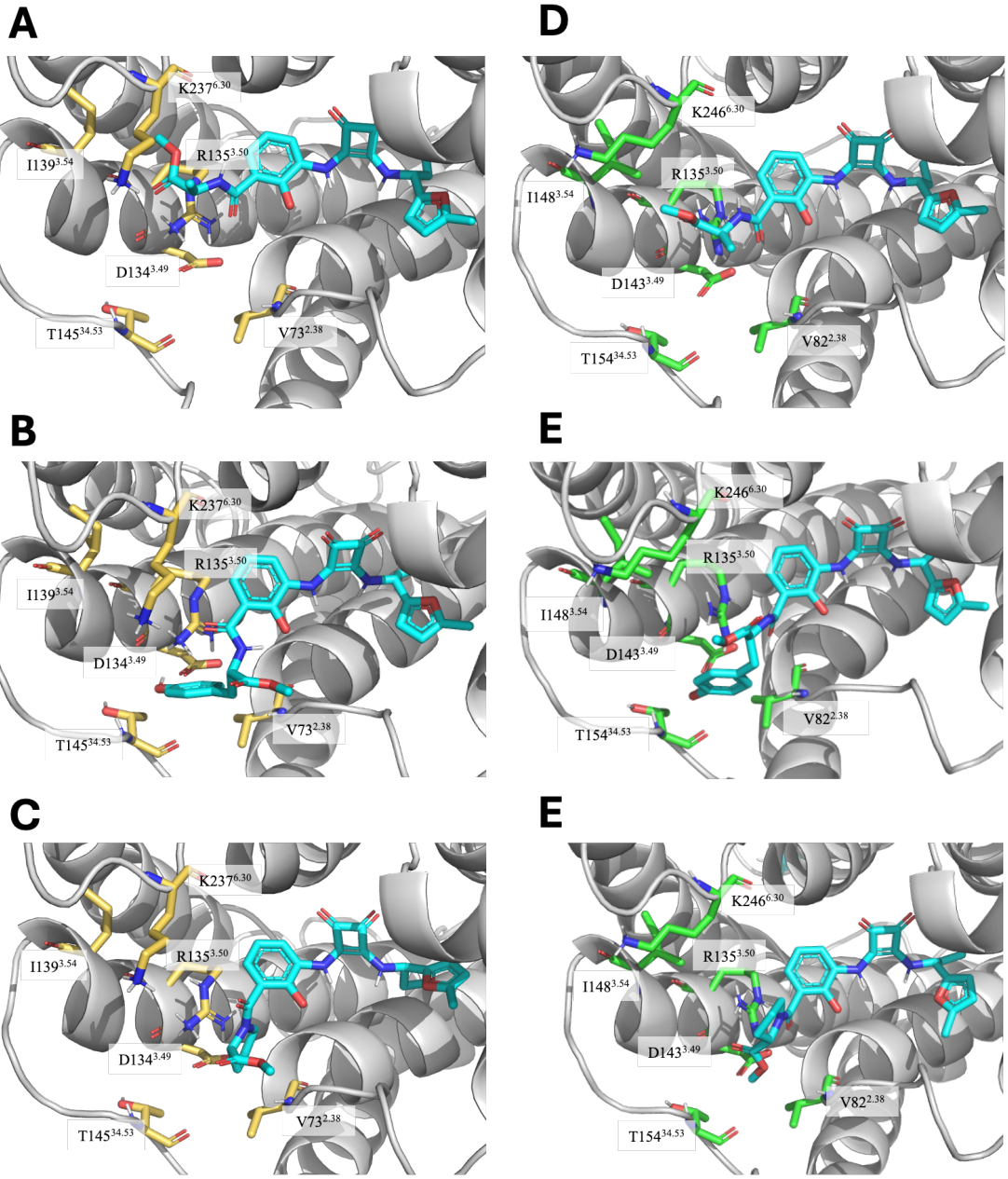

Figure 3-6 Predicted binding poses of the top scoring proposed ligands in CXCR1 and CXCR2 models generated from Glide docking in Schrödinger.[289] (A) CXCR1-**30a** (B) CXCR1-**30e** (C) CXCR1-**30i** (D) predicted CXCR2-**30a** (E) CXCR2-**30e** (F) CXCR2-**30i**. Depiction of receptors shown as grey cartoon with sticks representation of residues contributing to shallow binding pockets between TM2 and 3 and TM2, TM6 and ICL2 (yellow sticks in CXCR1 and green sticks in CXCR2).

Top ranking predicted binding poses were produced for **30e** (*L*-Tyr analogue) and **30c** (*L*-Met analogue) in both CXCR1 and CXCR2 in which the amino acid side chain occupied a binding cavity distinct from the conventional binding site of navarixin (**2**). This extended

binding cavity, previously identified from SiteMap analysis in **Section 3.2**, comprises of conserved residues S72$^{2.37}$, V73$^{2.38}$, D134$^{3.49}$, T143 (ICL2) and T145 (ICL2) in CXCR1 and S81$^{2.37}$, V82$^{2.38}$, D143$^{3.49}$, T152 (ICL2) and T154 (ICL2) in CXCR2. A representative docking pose is shown in **Figure 3-8**, which displays the predicted binding poses and interactions from molecular docking of **30e** into CXCR1 and CXCR2. Despite the binding pocket mainly consisting of mostly hydrophobic residues, the orientations of the residues in the proposed cavity are such that the pocket accommodates the methyl of the methionyl side chain of **30c,** and the 2-hydroxyphenyl ring of **30e** stemming from the hydrophobic alkyl chains of the residues in the binding cavity. This may also explain why no predicted binding poses were generated where the methyl ester moiety of ligands **30a-j** occupied the proposed binding cavity, as it contains significant polar characteristics from the ester functionality.

In both CXCR1 and CXCR2, compound **30e** (*L*-Tyr analogue) is shown to form H-bonding interactions between the hydroxyl of the phenol moiety and D134$^{3.49}$ in CXCR1 (D143$^{3.49}$ in CXCR2), located at the deepest point of the extended binding cavity (**Figure 3-7B** and **E)**. The presence of this hydrogen bond likely contributes to the stabilization of the ligand-receptor complex and may explain why a similar binding pose is not predicted for the *L*-Phe analogue, **30d**, as the phenyl moiety cannot form analogous polar interactions.

Predicted binding poses for **30g** (*L*-Ser analogue) in CXCR2 shows the ligand adopting a pose in which the hydroxyl of the serinyl side chain forms H-bond interactions with R144$^{3.50}$. In contrast, no such binding pose was predicted in the CXCR1 model in which the serinyl side chain occupied the proposed extended binding cavity. Whilst a favourable H-bond interaction was observed between **30g** and R144$^{3.50}$ in CXCR2, the interaction is observed at the shallowest point of the desired binding cavity and the side chain is unable to penetrate deeply into the cavity, likely due to the hydrophobic nature of the pocket, as previously discussed. Unfavourable contacts between the R144$^{3.50}$ and the methylene α to the OH of the serinyl functional group.

Compound **30i** (*L*-Pro analogue) demonstrated distinct binding behaviour in CXCR1 and CXCR2. In CXCR1, **30i** displayed an improved docking score -10.1 kcal/mol compared to navarixin (**2**) (-8.6 kcal/mol) and **30d** (*L*-Phe analogue) (-9.2 kcal/mol), and also displayed comparable docking scores to probes where the side chain deeply penetrated the S72$^{2.37}$, V73$^{2.38}$, D134$^{3.49}$, T145 (ICL2) and T147 (ICL2) binding cavity, such as **30e** (*L*-

Tyr analogue) and **30c** (*L*-Met analogue). The predicted binding pose CXCR1-**30i** displayed the proline ring occupying a hydrophobic region formed between V73$^{2.38}$ and the alkyl part of the side chain of S72$^{2.37}$, which resided in the shallow region of the binding cavity previously described in **Section 3.2**. In contrast, **30i** adopted a different predicted binding pose in CXCR2, with the proline ring orienting out of the bottom of the binding pocket towards the unoccupied space beneath the receptor. Despite this altered orientation, ligand **30i** exhibited a docking score of -11.7 kcal/mol comparable to **30e** (*L*-Tyr analogue) (-11.8 kcal/mol) in CXCR2. This positioning allowed the methyl ester moiety to occupy the previously described binding cavity formed by S81$^{2.37}$, V82$^{2.38}$, D143$^{3.49}$, T154 (ICL2), T156 (ICL2). This altered orientation resulted in additional interactions, including hydrogen bonding interactions between the carbonyl of the ester **30i** and residues R144$^{3.50}$ and R153 (ICL2) in CXCR2.

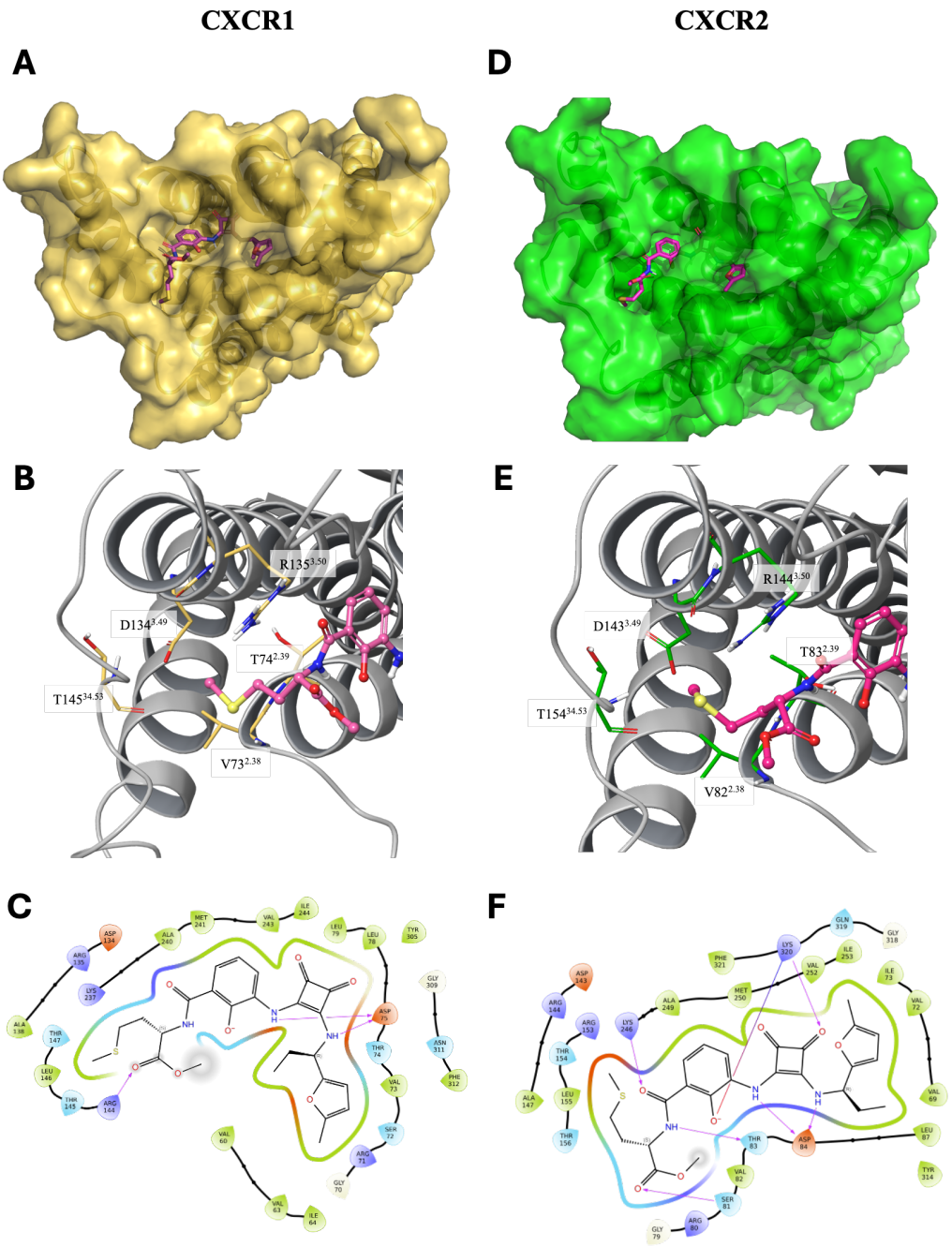

Figure 3-7 Predicted binding of **30c** in CXCR1 (A-C) and CXCR2 (D-F) generated using Glide flexible ligand docking protocol. The predicted binding pose displays methionyl side chain of **30c** orientated towards shallow binding pocket between TM2, TM3, and ICL2 in both receptors. Shallow binding cavity shown to comprise of conserved residues between receptors ($V73^{2.38}$, $D134^{3.49}$,$R135^{3.50}$, and T145 (ICL2) in CXCR1 model and $V82^{2.38}$, $D143^{3.49}$,$R135^{3.50}$, and T154 (ICL2) in CXCR2 model). (A) Bottom view of CXCR1 receptor model depicted as yellow cartoon and protein surface with **30c** depicted as pink sticks. (B) Magnification of the shallow binding region in predicted CXCR1-**30c** complex.

(C) Interaction map of CXCR1-**30c** in Maestro (Schrödinger[289]). (D) Bottom view of CXCR2 receptor model depicted as green cartoon and protein surface with **30c** depicted as pink sticks. (B) Magnification of the shallow binding region in predicted CXCR2-**30c** complex. (C) Interaction map of CXCR2-**30c** in Maestro (Schrödinger[289]). Predicted binding poses generated from flexible Glide docking in Schrödinger[289].

The molecular docking studies of compounds **30a-j**, analogues of lead compound navarixin (**2**), provide compelling evidence suggesting their potential to bind to an intracellular binding pocket of CXCR1 and CXCR2. These compounds, containing amino acid conjugates, introduce diverse potential binding interactions through their varied side chains. The predicted binding poses, particularly those of compounds **30e** (*L*-Tyr analogue) and **30c** (*L*-Met analogue), indicate interactions with a binding cavity distinct from the reported binding site of navarixin (**2**) from experimental X-ray crystal structures.[54] The extended binding region, hypothesized in **Section 3.2** is composed of conserved residues S72$^{2.37}$, V73$^{2.38}$, D134$^{3.49}$, T143 (ICL2) and T145 (ICL2) in CXCR1 and S81$^{2.37}$, V82$^{2.38}$, D143$^{3.49}$, T152 (ICL2) and T154 (ICL2) in CXCR2. This binding site has shown a propensity to accommodate side chains of the proposed ligands, **30e**, **30i**, **30c**, and **30j** in CXCR1 and **30e**, **30c**, and **30g** in CXCR2. While compounds **30e** and **30c** are shown to interact with the extended pocket in a similar manner in both CXCR1 and CXCR2, a difference in the binding mode is observed for **30j** and **30g**. This discrepancy may suggest that the extended pocket could serve as a route for modulating ligand selectivity between the receptors. Additionally, the distinct binding behaviour of **30i** (*L*-Pro) further underscores the potential modulation capabilities of these analogues.

3.5 Synthetic chemistry

3.5.1 Divergent synthesis towards amino ester functionalised analogues of navarixin (2)

The initial synthetic route designed to obtain compounds **30a, 30c, 30d, 30g, 30h,** and **i** was *via* a divergent synthesis in which (*R*)-2-hydroxy-3-((2-((1-(5-methylfuran-2-yl)propyl)amino)-3,4-dioxocyclobut-1-en-1-yl)amino)benzoic acid (**34**) would be obtained through a 3-step synthesis. The presence of an acid handle allows the attachment of the amine of the amino acid *via* an amide coupling. To achieve this, the commercially available starting material, 3-nitrosalicylic acid (**31**), was hydrogenated over Pd(0)/C to

obtain the corresponding aniline in a similar manner to the original synthesis of navarixin (**2**).[248] However, tetrahydrofuran (THF) was used as a solvent instead of EtOH, after some optimisation, to improve yields.[361] Early efforts using EtOH led to 2 unwanted products (*m/z* 304.1 and 160.0 by LCMS), with the 304 m/z corresponding to a hydrazobenzoic acid product, aniline dimer forming or similar adduct. The resulting mixture was also poorly soluble in the solvents used in the next step of synthesis and, without a reliable purification method, the solvent was swapped to the aprotic THF. This did not result in the unwanted side products and improved yields from 51% of a crude mixture to 65%. The resulting aniline was found to be poorly soluble in THF, and large volumes of methanol were required during celite filtration to remove the resulting aniline, which was not purified as in similar literature.[361] The aniline, **32**, is prone to oxidation, and exposure to air and moisture lead to the corresponding hydrazobenzoic acid or aniline dimer (determined by LCMS, *m/z* = 304.1). To combat this, the product remained *in situ* for the next step of synthesis by addition of dimethylformamide (DMF) and removal of THF to keep the Pd(0)/C catalyst wet, as a safety precaution.

Scheme 3-1: Synthetic route of α-substituted 2-(2-hydroxy-3-((2-(((*R*)-1-(5-methylfuran-2-yl)propyl)amino)-3,4-dioxocyclobut-1-en-1-yl-amino)benzamido) methyl esters (**30a, 30c, 30d, 30g, 30h, 30j**)

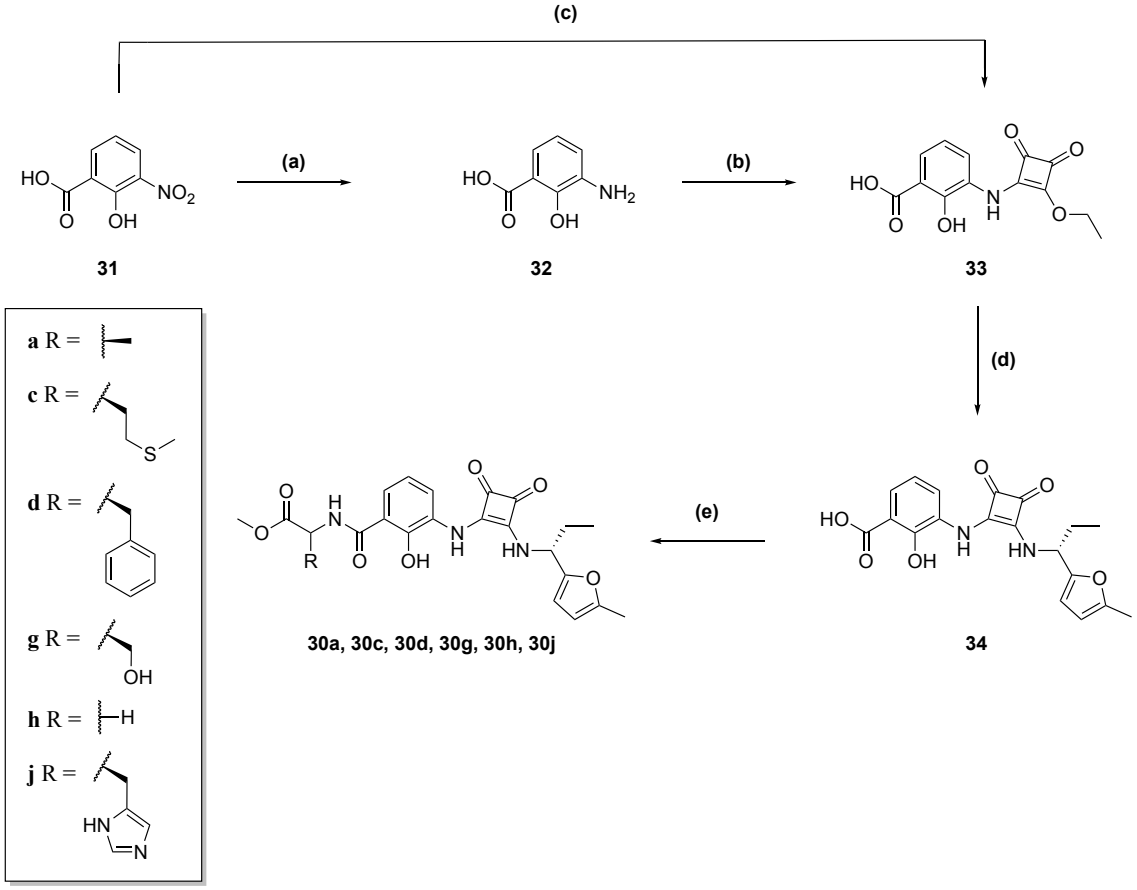

Reagents and conditions: (a) H_2, 10% Pd-C, THF, rt, 65%; (b) 3,4-diethoxycyclobut-3-ene-1,2-dione, triethylamine (TEA), dimethylformamide (DMF), 60 ˚C, 50%; (c) i) H_2, Pd-C, THF, rt; ii) 3,4-diethoxycyclobut-3-ene-1,2-dione, TEA, DMF, 60 ˚C 67%; (d) (*R*)-1-(5-methylfuran-2-yl)propan-1-amine, DIPEA, ethanol (EtOH), rt, 70%; (e) *S*-α-substituted amino acid methyl esters or *S*-α-substituted amino acid methyl ester hydrochlorides, 1-ethyl-3-(3'-dimethylaminopropyl)carbodiimide hydrochloride (EDC.HCl), 1-hydroxybenzotriazole (HOBt), triethylamine (TEA), DMF, microwave (MW) 90 ˚C 5-30%.

The resulting 3-amino-2-hydroxybenzoic acid was used in a base-mediated substitution of diethyl squarate to form **33** as a squaric acid monoester monoamide. No squaramide product was observed by LCMS during this reaction that would result from the double addition of aniline. The observed phenomenon arises from the deactivation occurring at

the carbon α-position, relative to the ethoxy moiety in the squaric acid monoester monoamide. This deactivation disrupts subsequent nucleophilic attack processes. The substitution was optimised using a variety of solvents, as initially 1,4-dioxane resulted in a low yield of 22%, this was changed to EtOH (as per literature examples) resulting in an improvement in yield to a moderate 34%.[210,362] Precipitate was observed in both cases, even when irradiated under MW conditions at 120 °C. Alternatively, DMF was used as an aprotic solvent and, in combination with heating at 50 °C, no precipitate was observed and yields improved to 67% (**Step c**, **scheme 3-1**).

Compound **33** was converted to the squaramide **34** using the amine salt (*R*)-1-(5-methylfuran-2-yl)propan-1-amine hydrochloride in the same manner as described in the synthesis of navarixin (**2**).[248] In this case EtOH, was sufficient to dissolve **33** and the primary amine is more nucleophilic than the aniline **32** and is able to replace the ethoxy group of the squaric acid monoester monoamide. After an acidic workup and extraction into EtOAc, the resulting squaramide was > 85% pure by NMR and carried forward to the final amide coupling step.

Various conditions were attempted to achieve the conversion of **34** to the desired compounds **30a**, **30c**, **30d**, **30g**, **30h**, and **30j**, which are summarised in **Table 3-2**. Pilot scale reactions focussed on methyl *L*-alanine hydrochloride as the amine of choice, towards **30a**. There are many amide coupling agents that could be suitable for investigation, however only (hexafluorophosphate benzotriazole tetramethyl uronium) HBTU, benzotriazolyloxy-tris[pyrrolidino]-phosphonium hexafluorophosphate (PyBOP) and 1-ethyl-3-(3-dimethylaminopropyl)carbodiimide (EDC) were evaluated in this work. The goal of this was to generate a suitable amount of compound for chemical and pharmacological evaluation. Therefore, extensive work into optimisation was not attempted. These coupling reactions were monitored by LCMS, after attempts to monitor *via* TLC were challenging as the resulting reaction mixture was complex. Even by LCMS, these spectra were not trivial to interpret, with overlapping LC traces. Therefore, in lieu of calculating conversion based on AUC calculations, what follows is a qualitative summary of the synthetic efforts towards **30a**.

In reactions in which HBTU was used, no reaction progression was observed at ambient temperatures, with the starting material still observed by LCMS. When microwave irradiation was used, the starting material was consumed but no mass corresponding to the

product, or the intermediate could be observed. Additionally multiple LC peaks were observed with *m/z* that could not be discerned. Use of PyBOP as a coupling agent was attempted, following literature examples of similar reactions between 3-amino-2-hydroxy benzoic acids and primary amines to form the corresponding secondary amide. In these attempts, small amounts of product were observed after 48 hr, but no further progression observed after an additional 24 hr. Additionally, several peaks were formed that did not correspond to expected intermediates or by-products. The combination of PyBOP and microwave irradiation improved starting material consumption, but also led to multiple new peaks being formed in the LC trace, which made interpreting conversion difficult. Further irradiation did not appear to further consume the starting material. Use of the carbodiimide coupling agent EDC.HCl was chosen in preference to a reagent such as DCC. This is because the resulting urea by-product in DCC reactions, dicyclohexylurea (DCU), can be difficult to remove during workup, compared to the byproduct of EDC, 1-(3-(dimethylamino)propyl)-3-ethylurea, which is readily water soluble and can be removed with an aqueous workup. Use of EDC.HCl with HOBt additive in ambient stirring was shown to give comparable product to starting material conversion as PyBOP. However, microwave irradiation led to full starting material consumption after 18 min. **30a**, **30c**, **30d**, **30g**, **30h**, and **30j** were generated using EDC.HCl and HOBt and, in all cases, the starting material was consumed as with observations towards **30a.** However, a difficult mixture resulted after workup and subsequent purification afforded **30a**, **30c**, **30d**, **30g**, **30h**, and **30j** in low yields (5-30%).

Table 3-2 Attempted coupling conditions of carboxylic handle (**34**) with alanine methyl ester hydrochloride to afford **30a**. Reaction conditions displayed, and results of reaction determined by LCMS comparing starting material peak (t_R = 3.4 min) and product peak (t_R = 2.8 min).

Coupling agent(s)	Solvent	Temperature	Time	Result
HBTU	1:1 DCM:DMF	25 ˚C	2 days	Starting material not consumed
	1:1 DCM:DMF	90 ˚C (MW)	46 min	Starting material not consumed
PyBOP	DMF	25 ˚C	2 days	Small amount of product with majority starting material
	DMF	90 ˚C (MW)	18 min	No starting material or product. Only by-products observed by LCMS
EDC and HOBt	DMF	25 ˚C	2 days	15% conversion
	DMF	90 ˚C (MW)	18 min	100% conversion

3.5.2 Alternative synthesis of amino acid ester functionalised analogues of navarixin (2)

Synthesis of compounds **30b**, **30e**, **30f**, and **30i** were also attempted using an EDC-HOBt amide coupling but yielded inadequate yields for characterisation or impurities that could not be separated from the desired compounds. After multiple attempts to generate **30b**, **30e**, **30f**, and **30i**, an alternative synthetic route was designed (**Scheme 3-2**). The alternative route devised closely resembles the synthesis of navarixin (**2**)[248] and other navarixin (**2**) analogues employed by the Schering-Plough group.[246,248,298,348] Instead of leveraging an acidic handle for divergent synthesis through amide coupling, the coupling is done first to give **35b**, **35e**, **35f**, and **35i** in high yields (77-90%). Initially, amide coupling agents were used for the synthesis of amino acid ester analogues in **Section 3.5.1**.

however, LCMS showed little product formed when using EDC-HOBt, PyBrOP or HBTU as reagents. Instead, an alternative amide coupling was employed by forming the reactive acyl chloride intermediate *via* a Vilsmeier-Haack reagent intermediate, using 3 equivalents of oxalyl chloride and a catalytic amount of DMF. Then, after removal of oxalyl chloride by evaporation, the amine could be added with an excess of DIPEA as an organic base. Literature for similar reactions uses sequential basic and acidic workups, although only an acidic workup was used for **35b**, **35e**, **35f**, and **35i**, due to the presence of the methyl ester group that would be hydrolysed upon exposure to strong base and the phenol which would be ionised to the corresponding phenolate and removed in the aqueous layer.

Scheme 3-2 Alternative synthetic route towards α-substituted 2-(2-hydroxy-3-((2-(((*R*)-1-(5-methylfuran-2-yl)propyl)amino)-3,4-dioxocyclobut-1-en-1-yl-amino)benzamido) methyl esters (**30b**, **35e**, **35f**, and **35i**)

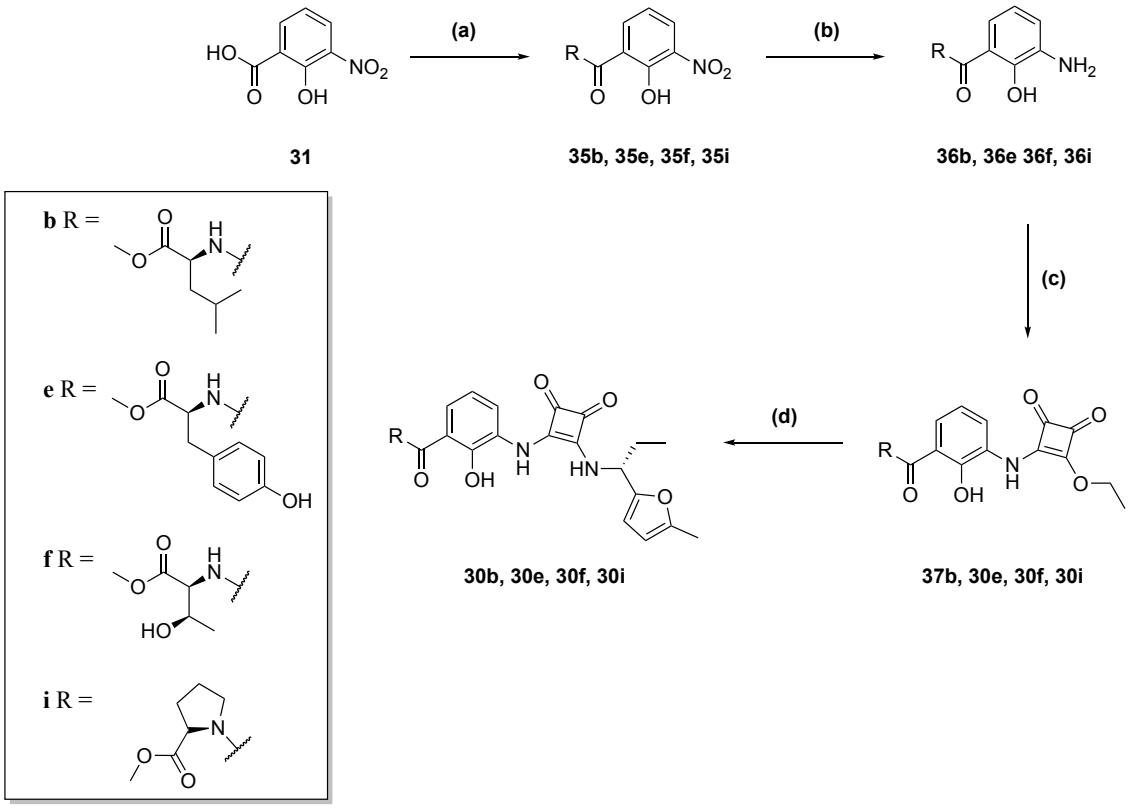

Reagents and conditions: (a) i) oxalyl chloride, DMF, dichloromethane (DCM) rt; ii) α *S*-α-substituted amino acid methyl esters or *S*-α-substituted amino acid methyl ester hydrochlorides, DIPEA, DCM, 0 ˚C – rt, , 77 - 90%; (b) H_2, 10% Pd/C, EtOH, rt, 88 –

96%; (c) 3,4-diethoxycyclobut-3-ene-1,2-dione, EtOH, 0 ˚C – rt; (d) (*R*)-1-(5-methylfuran-2-yl)propan-1-amine hydrochloride, DIPEA, EtOH, rt, 1 – 26%.

The resulting 2-hydroxy-3-nitro benzamides, **35b**, **35e**, **35f**, and **35i** were then be reduced in a similar fashion to **32** (**Section 3.5.1**, **Scheme 3-1**) to give anilines **36b**, **36e**, **36f**, and **36i**. However, EtOH was employed as the solvent as a replacement of 1,4-dioxane due to improved solubility of the reactants. This amine reduction was achieved in quantitative yields and required no further purification.

30b, **30f**, **30e**, and **30i** were synthesised in the same manner as **34** (**Section 3.5.1**, **Scheme 3-1**) and purification resulted in low yields of **30b**, **30f**, **30e**, and **30i** (2-20%). Initial purification of **30b**, **30f**, **30e**, and **30i** by preparative TLC were unfruitful and instead reverse phase flash chromatography was conducted, using water and acetonitrile as eluents. Yields were comparable to **30a**, **30c**, **30d**, **30g**, **30h**, and **30i** however final purification of **30b**, **30f**, **30e**, and **30i** was achievable using the alternative route (**Scheme 3-2**) in quantities necessary for characterisation.

3.5.3 Synthesis of *N*-methylated analogues

A similar synthetic route to that employed for the synthesis described in **Section 3.5.2** (**Scheme 3-2**) was utilised for the synthesis of *N*-methylated analogues of **43a**, **43d**, **43g**, **43h**, and **43k**. Whilst sarcosine methyl ester hydrochloride was cost-effective and commercially available, **39b**, **39d**, and **39g** were not and were synthesised from the corresponding *N*-methyl amino acids **38b**, **38d**, and **38g** *via* esterification. This transformation was achieved in high yields (84-94%) and did not require purification. After synthesizing **39b**, **39d**, **and 39g**, the synthesis of compounds **43a**, **43d**, **43g**, **43h**, and **43k** proceeded using established non-divergent methodology from 3-nitrosalicylic acid (**31**) described in **Section 3.5.2**.

Scheme 3-3 synthetic route towards **43a**, **d**, **g**, **h**, and **k**.

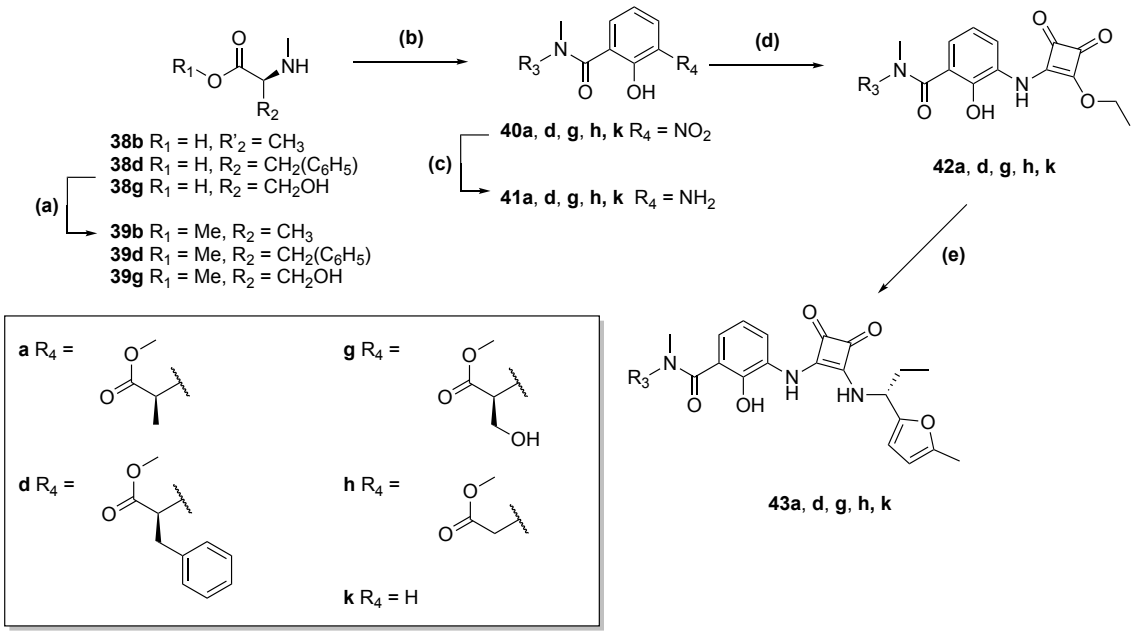

Reagents and conditions: (a) acetyl chloride, MeOH, 0 ˚C – 25 ˚C, 18 hr, 84 - 98%; (b) i) oxalyl chloride, DMF, DCM rt; ii) 3-nitrosalicylic acid, DIPEA, DCM, 0 ˚C – rt, 57 – 81%; (c) H_2, 10% Pd/C, EtOH, rt, 91 – 98%; (d) 3,4-diethoxycyclobut-3-ene-1,2-dione, EtOH, 0 ˚C – rt, 7 - 59%; (e) (*R*)-1-(5-methylfuran-2-yl)propan-1-amine hydrochloride, DIPEA, EtOH, rt 5- 29%.

3.5.4 Evidence of rotational isomerism introduced by *N*-methylation modifications

Rotational isomerism around the amide bond is a well-documented phenomenon in the literature, with examples of rotational isomers existing even in relatively small amide-containing molecules such as DMF.[363,364] Additionally the presence of rotational isomers has been shown in *ortho*-substituted benzamides, such as the functionality included in **40a**, **40d**, and **40g**.[365-368] The resonance stabilization across the amide functional group results in partial double-bond characteristics, which in turn restricts rotation around the bond. This introduces a relatively high energy barrier for the rotation around the bond compared to typical C-C bonds. Restricted rotation around the bond leads to non-equivalence of the *N*-substituents and, therefore, multiple populations of signals in the NMR spectra. Variable temperature NMR is a tool that has previously been used to investigate this phenomenon.[366-368] In VT NMR, the temperature at which the sample is analysed is

increased. The increase in temperature provides additional kinetic energy required to overcome the energy barrier associated with rotational isomerism. As a result, the interconversion of different conformer populations at a fast rate leads to the merging of signals into a single peak in the NMR spectrum.[365,367,369]

In the synthesis of compounds **40a**, **40d**, and **40g**, an interesting observation emerged wherein a single peak was obtained for the product by LCMS analysis, contrasting with the duplication of signals observed in the ^{1}H and ^{13}C NMR spectra taken at ambient temperatures (25 °C). This duplication of signals, visible in the ambient temperature NMR spectra (**Figure 3-8)**, prompted further investigation into their origin. It was hypothesized that this phenomenon could be attributed to rotational isomerism around the amide bond, particularly when a methyl substitution is introduced.

To investigate this, variable temperature NMR (VT NMR) experiments were conducted on the compounds **40a**, **40d**, and **40g**, with **40a** used to exemplify the finding from the experiments (**Figure 3-8**). The three aromatic signals observed at 8.05, 7.56, and 7.12 ppm, corresponding to proton environments 7, 5, and 6 respectively, exhibited broad signals with unresolved splitting at ambient temperatures. This contrasted with the expected splitting pattern typically observed for the aromatic protons of the phenol ring in the unmethylated analogue **40a**. Upon increasing the temperature, initial sharpening of the peaks was observed at 50°C, and coalescence of the peaks. At this temperature, the peaks began to display the anticipated splitting pattern (doublets for signals 5 and 7, and doublet of doublets for signal 6). Further improvement in peak resolution was observed at 70°C, with the peaks showing minimal chemical shift.

At ambient temperatures, signal doubling was more pronounced in the aliphatic region, particularly in the proton signals corresponding to environments 1, 2, and 4. Specifically, the α-proton adjacent to the methyl amide group (environment 2) exhibited splitting into two distinct peaks, labelled as 2_a and 2_b, with significantly different chemical shifts (5.07 and 4.52 ppm, respectively) and a relative proportion of 1.00:0.69. While signal 2_a displayed expected quartet splitting, the splitting of 2_b was not fully resolved. Upon heating to 50°C, the two signals became broad, but did not fully coalesce until heating to 70°C, where a single broad signal between 5.40 and 4.22 ppm was observed. Similarly, the coalescence of aliphatic signals 1 and 4 occurred at 70°C, appearing as singlets at chemical shifts of 3.68 and 2.50 ppm respectively. Confirmation that the observed signal doubling

in ambient temperature NMR spectra was likely due to rotational isomerism around the amide bond prompting the continuation of synthesis towards compounds **40a**, **40d**, and **40g**. The doubling of proton and carbon signals in the ^{1}H and ^{13}C spectra persisted in subsequent intermediates and the final product.

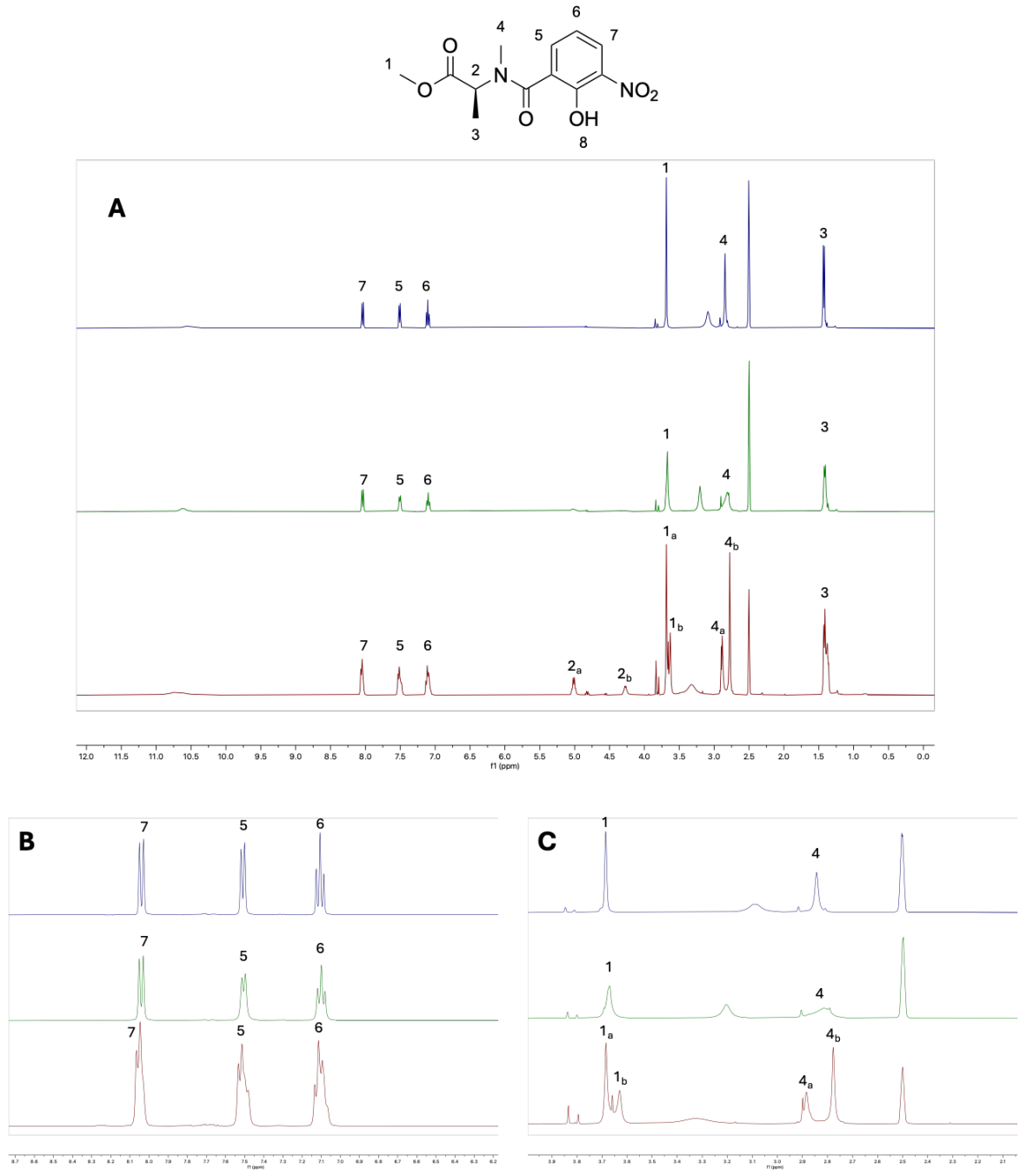

Figure 3-8 Variable temperature (VT) ^{1}H-NMR experiments of compound **40a** in DMSO-d_6. (A) whole spectra from 12.0 to 0 ppm (b) magnification of the aromatic region between 8.7 and 6.2 ppm (c) magnification of the region between 3.9 and 2.1 ppm. Red spectrum recorded at 25 ˚C, green spectrum recorded at 50 ˚C, and blue spectrum recorded at 70 ˚C.

3.6 Pharmacology

3.6.1 *In vitro* assessment of GPCR activation

Pharmacological investigations into agonist activation of GPCRs, and their inhibition by antagonists, can be determined using techniques that measure as a function of downstream effector signalling. Assays have been developed that exploit the changes in secondary messengers accompanying Gi coupled CXCR1 and CXCR2 activation (inhibition of cAMP, elevation of intracellular Ca^{2+} etc.), as well as further downstream biological functions (e.g. gene expression, cell proliferation and survival).[370-372] Although these techniques have been important in understanding the function of GPCRs, they measure receptor activation in processes downstream of receptor binding. For example, this can result in signal amplification, masking reductions in ligand efficacy (ability to activate the receptor) for agonists, or off-target effects of the ligands through other components of the signalling.

In addition, the characterisation of GPCR responses as a function of time is of importance in medicinal chemistry, as often the measured therapeutic effect of a drug can be dependent on the reported time point. Examples of this have been observed in dopamine D_2 receptor where drugs targeting the receptor exhibit narrow therapeutic window because of rapid dissociation from the target.[373,374]. Endpoint signalling assays can therefore mislead in characterising ligand pharmacology, unless binding and signalling kinetics are considered. With these factors in mind, the stoichiometric, real-time measurements of GPCR activation and signalling can be crucial for characterising the relationships of receptor-drug interactions.

3.6.2 *In vitro* assessment of CXCR1 and CXCR2 using the NanoBiT complementation assay

As previously discussed in **Chapter 1**, the activation of CXCR1 and CXCR2 by extracellular chemokines, such as CXCL8, triggers downstream signalling *via* a conformational change of the receptor. This process involves the recruitment of the heterotrimeric G_i protein to the intracellular surface of the receptor, and subsequently leading to G protein mediated signalling, including the inhibition of adenylyl cyclase and

a reduction in cAMP levels.[95] Separately, recruitment of β-arrestins to CXCR1 and CXCR2 after GRK-phosphorylation competes directly for the receptor G protein binding site, leading to desensitisation of the G protein response. β-arrestins also govern additional processes, such as receptor internalisation and independent signalling cascades (e.g. kinases, pERK and p-JNK).[88,90] Therefore, receptor β-arrestin recruitment direct to the receptor presents a point of monitoring to directly measure activation, without intervening with downstream signalling, and avoiding signal amplification. The position of arrestin binding to the receptor also overlaps with the G protein binding site and the proposed site of action of the NAMs in this study.[54] The ability for different newly synthesised squaramide based probes (**30a-j**) to inhibit CXCL8 mediated β-arrestin2 recruitment was assessed *in vitro* using HEK293 cells overexpressing CXCR1 and CXCR2 to develop an SAR.

The arrestin assay employs an example of the protein-fragment complementation assay (PCA) NanoBiT (NanoLuc Binary Technology) complementation technology developed by Dixon *et al*.[375] NanoBiT is an example of a split luciferase system, which uses an engineered luciferase enzyme derived from deep-sea luminous shrimp.[376,377] The engineered enzyme Nanoluciferase (Nluc) can be employed to report binary relationships of proteins by splitting the enzyme and tagging the two fragments (**Figure 3-9**). The enzyme is split such that, when in proximity, the two fragments will weakly interact in a robust, reversible manner. This allows the kinetics of the protein-protein interaction to be observed in real time and in physiologically relevant assays such as whole cell experiments.[378] Additionally, NLuc is small in comparison to other luciferase derived tags (e.g. RLuc and FLuc), making it less likely to sterically interfere with the proteins of interest, resulting in minimal perturbance to the activity of protein.[377] The NanoBiT assay utilised in this investigation consists of stably transfected HEK293 cells overexpressing CXCR1 or CXCR2, developed by D.Nesheva.[107] The receptor (CXCR1 or CXCR2) is *C*-terminally tagged with a 18 kDa large BiT (LgBiT) fragment of NLuc and β-arrestin2 *N*-terminally tagged with a 1.3 kDa small BiT (SmBiT) fragment of NLuc. Upon receptor activation and subsequent recruitment of β-arrestin2, the enzyme fragments are in proximity allowing reformation of an active luciferase allowing the conversion of the enzyme substrate, furimazine to furimamide generating luminescence.

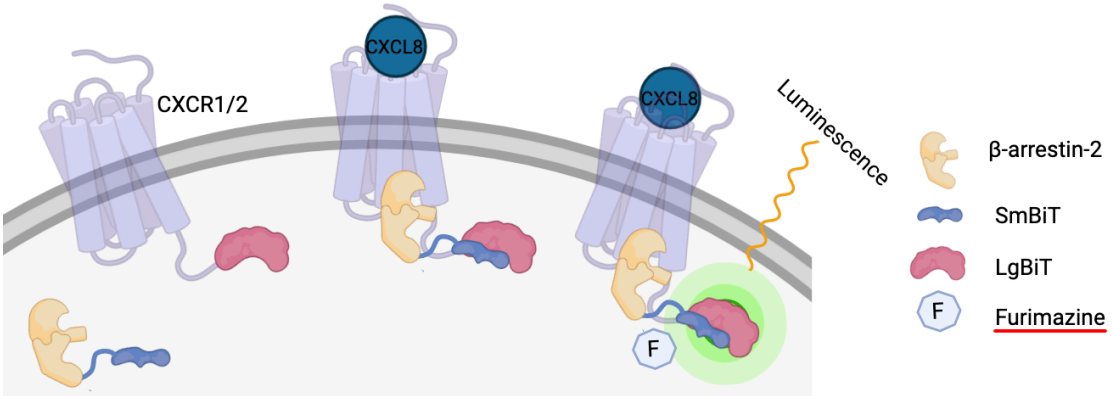

Figure 3-9 Representation of the NanoBiT complementation assay using β-arrestin recruitment as an example effector protein. Stimulation of the LgBiT tagged receptor (CXCR1/2) and subsequent SmBiT β-arrestin recruitment result in the complementation between the SmBiT and LgBiT allowing conversion of furimazine to furimamide resulting in luminescence. Image created in Biorender.

3.6.3 *In vitro* characterisation of navarixin (2) in CXCR1 and CXCR2

As navarixin (**2**) was the reference NAM to assess the functional effects of **30a-j** in an IC_{50} compound screen, it was important to characterise its potency in both CXCR1 and CXCR2 β-arrestin2 NanoBiT assays and identifying the appropriate agonist concentration in the IC_{50} assay. To achieve this, an agonist ($CXCL8_{28-99}$)-dependent study was conducted to produce concentration response curves (**Figure 3-10**), in which the inhibitory effect of navarixin (**2**) at different concentrations was measured as a function of the CXCL8 response. The CXCL8 S28-S99 fragment was chosen as the reference agonist based on its high potency and efficacy for CXCR1 and CXCR2 activation (based on intracellular Ca^{2+} signalling).[379] Data for the CXCR2 cell lines has been provided by Dr Bianca Casella (**Figure 3-10 D, E,** and **F**).

In these experiments, cells were pre-treated with varying navarixin (**2**) concentrations (or buffer for vehicle) for 1 hour at 37 °C to allow penetration of the cell and equilibration of receptor-modulator binding. The enzymatic substrate, furimazine was added post antagonist, incubation, followed by $CXCL8_{28-99}$. Stimulation of the receptor by the agonist was then measured as a function of luminescence generated over a 30-minute period, compared to a buffer control. As illustrated in the control CXCL8 time courses in **Figure 3-10A,** and **D**), CXCL8 stimulation led to a rapid (peaking at 5 – 10 min), predominantly

sustained level of arrestin recruitment over the 30 min incubation, with control pEC_{50} of 8.56 ± 0.18 in CXCR1 (concentration response curve at 30 min in **Figure 3-10C**) and 9.28 ± 0.16 in CXCR2 assay (**Figure 3-10F**). This difference in potency is consistent with the expected higher binding affinity of CXCL8 towards CXCR2.[93]

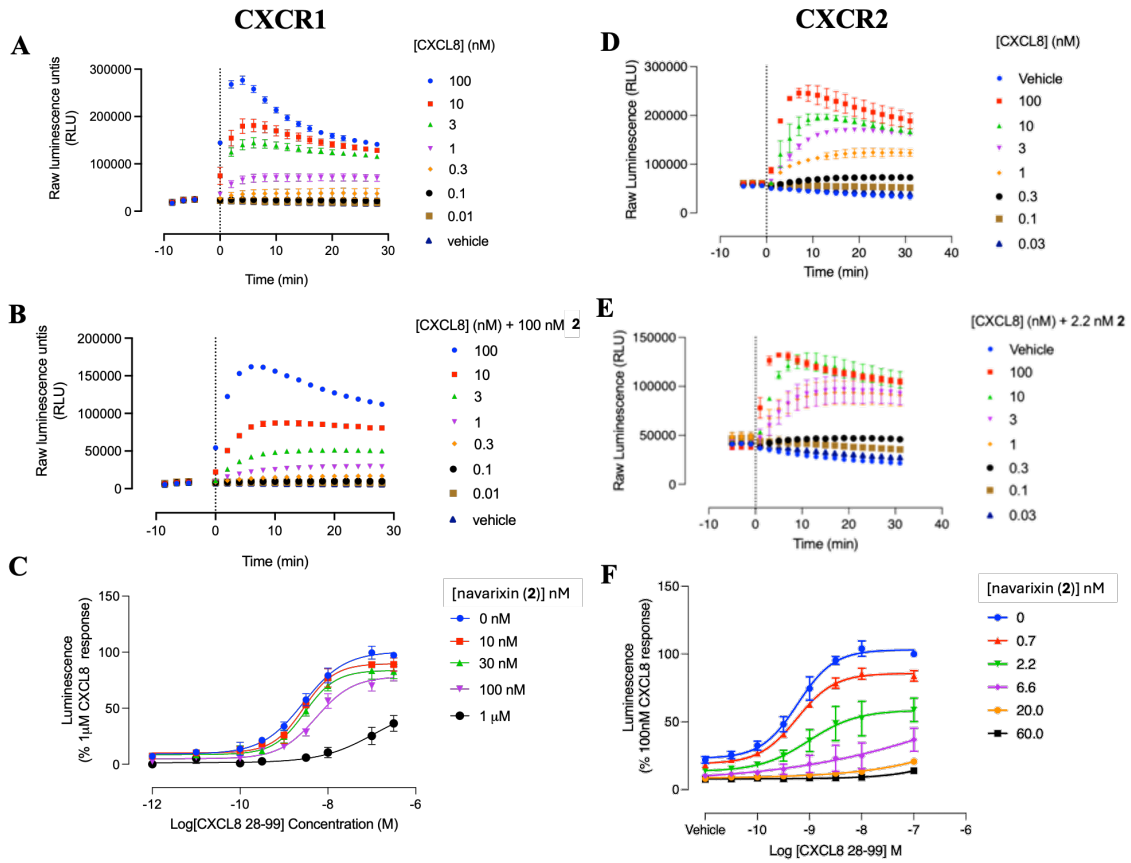

Figure 3-10 The antagonist effect of navarixin (2) measured in CXCR1 and CXCR2 β-arrestin2 NanoBiT recruitment assays. Cells were pre-treated with navarixin (**2**) (at the concentrations indicated) or vehicle for 1 h at 37 C, followed by the chemokine agonist $CXCL8_{28-99}$, and luminescence from the complemented nanoluciferase was measured after agonist addition for a 30 min period. (A) and (D) illustrate the control time courses (as raw luminescence using technical replicates from an example experiment) for $CXCL8_{28-99}$ dependent β-arrestin recruitment *via* CXCR1 and CXCR2, respectively, with the point of agonist addition indicated by the dotted line at t = 0. In the same manner, (B) and (E) illustrate the effect of 100 nM (CXCR1) or 2.2 nM (CXCR2) navarixin (**2**) treatment on the CXCL8 time course. Finally, $CXCL8_{28-99}$ concentration dependent response curves in the absence and presence of different navarixin (**2**) concentrations are indicated in (C) CXCR1 and (F) CXCR2. Data shown are from pooled individual experiments (mean ±

SEM) of n = 3 for CXCR1 and n = 5 for CXCR2, normalised to the maximal control $CXCL8_{28-99}$ response, with each experiment performed in duplicate. Data for CXCR2 (D), (E) and (F) NanoBiT assays provided by Bianca M. Casella using the same cell line used for subsequent IC_{50} experiments.

Navarixin (**2**) pre-treatment demonstrated antagonism of the CXCL8 response at both CXCR1 and CXCR2 receptors, as evidenced by a rightward shift of the concentration response curve and (particularly for CXCR2) a reduction in maximum response at high NAM concentrations. The selectivity of navarixin (**2**) for the CXCR2 receptor was demonstrated by the lower concentrations required for inhibition (2.2 – 60 nM), compared to the range over which CXCR1 antagonism was observed (30 – 1000 nM). Since navarixin (**2**) has a non-competitive allosteric mode of action, and insurmountability was observed, Schild analysis was not used to calculate a navarixin (**2**) K_D for each receptor. The insurmountable effect of navarixin (**2**) was more apparent in CXCR2, where navarixin (**2**) reduced the maximal response to 50-60% of the control at 2.2 nM, compared to CXCR1 where 100 nM was required to reduce maximal response to ~ 80%. This insurmountable antagonism of navarixin (**2**) towards CXCR2 has previously been reported[252], and may result from the non-competitive NAM mode, together with slow navarixin (**2**) binding kinetics resulting in non-equilibrium conditions in the assay.[252] It is also possible navarixin (**2**) acts through an insurmountable mode of action in CXCR1, but, to a lesser extent, considering 100 nM navarixin (**2**) addition displayed a less pronounced reduction in CXCL8 maximal response. Reduction of basal receptor activation was also observed in both assays, potentially through inhibition of constitutive activity; this is more substantial in CXCR2, which may indirectly result from high basal arrestin-recruitment activity in this cell line compared to that for CXCR1. The concentration of $CXCL8_{28-99}$ used in the IC_{50} screen of **30a-j** set was determined to be 10 nM from pEC_{80} 7.9 and 8.0 in CXCR1 and CXCR2, respectively.

3.6.4 Functional screening of compounds 30a-j *via* whole cell CXCR1 and CXCR2 NanoBiT complementation assays

Based on the CXCL8 potencies in the NanoBiT assays, a concentration of 10 nM, $CXCL8_{28-99}$ was selected as the stimulus for both CXCR1 and CXCR2 receptors in IC_{50} determination experiments. This concentration reflects approximately the pEC_{80} in CXCR1 (7.9) and CXCR2 (8.0) assays, against which the concentration inhibition of novel NAMs **30a-j** can be assessed against functional CXCL8 mediated β-arrestin2 recruitment. The interpretation of compound potency aims to develop an SAR for the amino acid ester conjugates of navarixin (**2**)**.** The analysis would elucidate the impact of structural variations around the salicylamide region on the compound's antagonist potency targeting CXCR1 and CXCR2.[210,298,344,380-383] In this format, the CXCR1/CXCR2 β-arrestin2 NanoBiT cell lines were treated with compounds **30a-j** at 37 ˚C for 30 minutes, followed 10 nM $CXCL8_{28-99}$ stimulation. The 30-minute end point for agonist stimulation was used to plot the concentration response curves in **Figure 3-11**, from which the calculated pIC_{50} values are presented in **Table 3-3**.

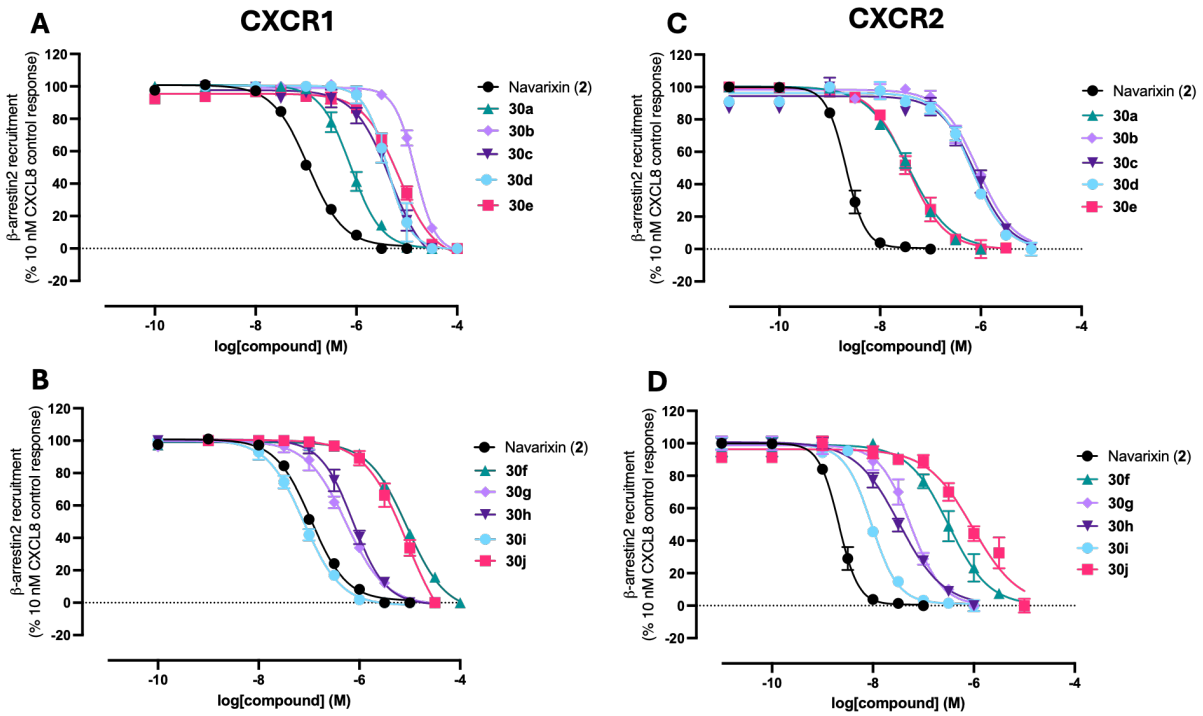

Figure 3-11 Concentration inhibition curves for navarixin (**2**)**, 30a-j** demonstrating the effect of NAMs on 10 nM $CXCL8_{28-99}$ stimulated β-arrestin2-SmBit recruitment towards CXCR1-LgBiT and CXCR2-LgBiT expressed HEK293 cell lines. (A) **30a-e** compared to

navarixin (**2**) (**2**) against CXCR1-LgBiT. (B) **30f-j** compared to navarixin (**2**) against CXCR1-LgBiT. (C) **30a-e** compared to navarixin (**2**) against CXCR2-LgBiT. (D) **30f-j** compared to navarixin (**2**) against CXCR2-LgBiT. Data represents pooled data (mean ± SEM), normalised to the control, $CXCL8_{28-99}$ response, from n = 3 individual experiments performed in triplicate.

Table 3-3 Functional inhibition of $CXCL8_{28-99}$ mediated β-arrestin2-SmBiT recruitment in CXCR1-LgBit and CXCR2-LgBiT for compounds **30a-j** compared to lead compound, navarixin (**2**). Data shown are mean ± SEM from n = 3 individual experiments.

Compound	Amino acid functionality	CXCR1 pIC_{50}	CXCR2 pIC_{50}	Selectivity IC_{50} (CXCR2/CXCR1)
navarixin (**2**)	-	6.96 ± 0.13	8.68 ± 0.13	53
30i	*L*-pro	7.10 ± 0.19	8.03 ± 0.14	9
30g	*L*-ser	6.26 ± 0.24	7.25 ± 0.18	10
30h	Gly	6.12 ± 0.21	7.48 ± 0.21	24
30a	*L*-ala	6.11 ± 0.21	7.44 ± 0.17	20
30j	*L*-his	5.06 ± 1.11	6.03 ± 0.38	10
30c	*L*-met	5.32 ± 0.55	6.11 ± 0.28	6
30d	*L*-phe	5.38 ± 0.27	6.16 ± 0.20	6
30e	*L*-tyr	5.16 ± 0.30	7.45 ± 0.22	184
30f	*L*-thr	5.06 ± 0.29	6.50 ± 0.33	25
30b	*L*-leu	4.84 ± 0.19	6.06 ± 0.23	15

Compounds **30a-j** represent amino acid methyl ester conjugates of navarixin (**2**), with variable side chains for comparing structural activity. Compounds **30a-j** all displayed reduced potency in CXCR2, compared to navarixin (**2**), displayed by the rightward shift in the IC_{50} curves. A similar trend was observed in CXCR1 with **30a-j** displaying reduced potency; however, compound **30i** displayed pIC_{50} 7.10 ± 0.19, which is comparable to navarixin (**2**) pIC_{50} = 6.96 ± 0.13. There was a general trend of retained selectivity for all compounds towards CXCR2 over CXCR1. This exemplifies the inability of the proposed compounds to fully overcome the selectivity towards CXCR2 over CXCR1 that the reference compound, navarixin (**2**), demonstrated, which has 50-fold selectivity in this whole cell assay. However, some examples demonstrated appreciably lower selectivity (6-

10-fold) by retaining higher CXCR1 potency, compared to the impact of the modification on CXCR2 potency (navarixin (**2**) as the reference compound).

Compound **30h** (Gly analogue) displayed a 10-fold reduction in potency compared to navarixin (**2**) at both receptors (**Table 3-3**). The introduction of a methyl group in **30a** (*L*-Ala analogue) did not further alter potency, showing there is some tolerance for the addition of alkyl substituents. However, further elongation and branching of the aliphatic side chain with the introduction of isobutyl side chain **30d** (*L*-Leu analogue) is poorly tolerated in both receptors with a significant drop in IC_{50} to > 1μM in CXCR2 and > 10 μM in CXCR1. Introduction of a thioether with **30c** (*L*-Met analogue) aimed to introduce a longer aliphatic chain to the molecule, along with a mildly electronegative sulphur that could contribute to hydrogen bonding whilst maintaining hydrophobicity. However, this displayed comparable poor potency to **30d** (*L*-Phe analogue), establishing the poor tolerance of hydrophobic alkyl of chain lengths 4 or more. Addition of alkyl hydroxy groups were explored with the introduction of an ethyl alcohol **30g** (*L*-Ser analogue), which displayed a moderate 5-fold reduction in potency in CXCR1, but a more pronounced 25-fold reduction in CXCR2. The hydroxy group did not significantly improve potency compared to **30h** (Gly analogue) and **30a**, indicating the hydroxy group has little effect in ligand potency, but was tolerated. Compound **30f** (*L*-Thr analogue), introduced a methyl group α to the hydroxy in the side chain compared to **30g** (*L*-Ser analogue), which was poorly tolerated in CXCR1 and CXCR2. This further evidenced an inability to tolerate additional hydrophobic substituents on the α-carbon. These findings suggest that, while the hydroxy group did not provide a significant improvement in potency, it was well-tolerated. Moreover, the introduction of bulkier hydrophobic substituents, such as the additional methyl group in **30f**, negatively impacted receptor inhibition, emphasizing the importance of maintaining an optimal balance of hydrophobicity introduced by alkyl substituents. Further investigation is required to bridge the gap in the current SAR to delineate the extent of hydrophobic substituents tolerable in this region of the binding pocket.

Compound **30i** (*L*-Pro analogue), a pyrrolidine with a 2-methyl ester group showed < 100 nM potency in both receptors with a 30-fold reduction in potency, compared to navarixin (**2**) towards CXCR2. Remarkably, **30i** displayed equipotency with navarixin (**2**) towards CXCR1, suggesting a potentially unique binding profile that could be further explored for

CXCR1 selectivity. Additionally, **30i** is unique in this SAR, as it is the only compound with a double substitution of the amide moiety. Similar SAR of pyrrolidine-based substitutions of the salicylamide moiety have been explored by Aki *et al*.[344] in a binding affinity experiment, which agrees with the improved selectivity towards CXCR1. Their SAR also suggests that CXCR1 selectivity could be further enhanced by the addition of a 3-hydroxy substituent in place of 2-carboxylic acid.[344] Further modifications to the pyrrolidine ring have been covered in patents from Galderma and Schering Plough (now Merck); however, limited biological data was available and are limited to introducing hydroxy or ester groups to the ring systems at either the 2- and 3- position.[362,384]

Introducing bulky aromatic groups was also explored in **30d** (*L*-Phe analogue), **30j** (*L*-His analogue) and **30e** (*L*-Tyr analogue). Compounds **30d** and **30j** exhibited notably lower potency in both receptors, demonstrating a 40 and 80-fold decrease in potency towards CXCR1, and a 300 and 400-fold decrease in potency towards CXCR2 compared to navarixin (**2**) respectively. However, introduction of a *para*-hydroxyl group to the benzyl moiety **30e** showed a remarkable improvement in inhibitory activity towards CXCR2 pIC_{50} = 7.45 ± 0.22 compared to **30d** and **30j** (pIC_{50} = 6.16 ± 0.20 and 6.03 ± 0.38 respectively), whilst showing similar micromolar potency for CXCR1 inhibition. This suggests the *para*-hydroxy substitution selectively enhanced selectivity (300-fold) towards CXCR2 over CXCR1, compared to **30d**, **30j** and navarixin (**2**). This also suggests that the CXCR2 extended binding site has a higher tolerance for bulky, polar aromatics and this may not solely be due to steric considerations. The difference in potency of **30e** towards CXCR1 and CXCR2 suggests a unique binding pocket or interaction site, which tolerates steric bulk when stabilised by a hydrogen bond interaction.

It's important to acknowledge that the whole-cell functional assay utilised necessitates the compounds to traverse the membrane and bind to the intracellular binding site. Consequently, it's challenging to separate the effects of amino acid functionalisation on membrane penetration from potency derived from direct receptor binding. Additionally, ligand inhibitory activity is measured as a function of CXCL8 mediated β-arrestin2 recruitment in this assay, and it is possible that antagonism of other coupling mechanisms (for instance G proteins) could differ, particularly given the location of the NAM binding site at the receptor-effector interface. As previously discussed, preferential CXCL8 mediated G protein activation in CXCR2 has been suggested previously by Boon *et al*.[74]

Past studies, however, have not suggested that navarixin (**2**) effects differ for G protein and β-arrestin2 recruitment at CXCR2 and CXCR1, including NanoBiT approaches measuring mini G_o as well as β-arrestin2 recruitment.[107,138,252] These factors collectively indicate that the observed ligand activity should be interpreted not only as a potency derived from the NAM binding affinity and allosteric effect on receptor conformation, but also based on the ligands' physicochemical properties that enable membrane penetration to access the binding site. Additionally, the nature of the CXCR1/2 coupling response being measured should be considered.

3.6.5 The use of NanoBRET assays for directly assessing compound binding affinity at CXCR1 / CXCR2

To address the limitations of whole cell functional assays in directly reporting the affinity of CXCR2 NAMs for SAR, a direct ligand binding assay in isolated membranes would be advantageous. To this end, several CXCR2 NAM investigations have used radiolabelled probe-based approaches. Several examples have examined the displacement of radiolabelled [^{125}I]CXCL8 chemokine probes, but this type of analysis relies on the allosteric effect of the NAM to prevent chemokine binding, rather than direct competition at the NAM binding site.[108,137] Alternatively, it has been feasible to generate tritiated NAMs as radiolabelled tracers for binding studies. For example, both Salchow *et al*.[134] and Gonsiorek *et al*.[252] utilised a [^{3}H]-navarixin ligand to characterise the pharmacology of unlabelled navarixin (**2**) in CXCR2. Tritium was introduced to the molecule in a synthetic route, akin to the original reported synthesis by Dwyer *et al*.[248] This enabled access to a molecular tool for the direct investigation of the intracellular NAM binding site without requiring significant synthetic redesign or development, often needed for molecular fluorescent probes.[138,385] Additionally, radioligands exhibit small differences to their derivative pharmacophore and thus, effects on modes of binding, and binding affinity, are minimised.[386] In contrast, the addition of fluorophores and the necessary ligands have been shown to alter the binding kinetics, making the choice of fluorophore and linker crucial to molecular probe design.[138,386,387] However, there are some distinct disadvantages to using radioligands, such as the innate radioactivity of labelled ligands. Assays requiring high concentrations of radioligands are costly and bring inherent safety concerns, which can be challenging to justify when compared to the use of non-radioactive fluorescent probes.[388]

Fluorescent probes, in combination with resonance energy transfer detection methods, can also exhibit a higher specific binding-to-non-specific binding ratio allowing for higher ligand concentrations to be used; this is advantageous with low binding affinity probes, and with lipophilic molecules such as CXCR2 NAMs that may exhibit a high degree of non-specific binding to membranes as radiolabelled tracers[389,390] Furthermore, fluorescence-based assays can be used to monitor binding affinity in real-time, making live cell real-time assays now a viable and advantageous technique for the measurement of binding affinity and the associated kinetics, a topic extensively explored in previous reviews.[388,390,391]

In **Section 3.6.3**, the NanoBiT assay was discussed, along with its advantages in use for functional screening of **30a-j**.This provided a measure of functional inhibitory potency as an IC_{50}, but in considering the resultant SAR, multiple factors could contribute to the effect of the NAM – including binding affinity, the degree of allosteric co-operativity in inhibiting receptor activation to different pathways, and the ability of the inhibitor to access the intracellular binding site through cell penetration. To complement these measurements, a direct binding assay was employed to determine affinity at the CXCR1 and CXCR2 binding site.

This assay makes use of the fluorescent navarixin (**2**) probes developed by Casella *et al.*[138], in conjunction with NanoBRET, to generate a competition binding protocol at CXCR1 and CXCR2 NAM sites. NanoBRET is based on bioluminescent resonance energy transfer (BRET) using full length nanoluciferase tagged to the intracellular domain (*C*-terminus) of the target receptor CXCR1 or CXCR2. In the presence of luciferase substrate furimazine, the luciferase emits light at the appropriate wavelength to act as an energy donor to a fluorescent acceptor species when in proximity (<10 nm, for example a bound fluorescent probe).[390,392] The measured BRET ratio of emissions at the acceptor versus donor wavelengths then provides a sensitive measure of probe specific binding. BRET techniques provide enhanced sensitivity for *in vitro* assays when compared to other Förster resonance energy transfer (FRET) techniques, such as fluorescent resonance energy transfer (FRET), due to the associated autofluorescence, fluorophore degradation and tissues attenuation with the excitation of fluorophores.[389,393]

3.6.6 CXCR1 NanoBRET competition binding assays of 30a-j

The fluorescent ligand **44** was used as the probe for the CXCR1 / CXCR2 binding assays. The fluorescent ligand has been shown to be a competitive ligand at the NAM binding site, whilst containing a BODIPY 630/650 fluorophore, allowing the measurement of activity in a BRET assay with the donor signal provided by CXCR1-Nluc or CXCR2-Nluc.[389,390,394] Due to the availability of the newly designed fluorescent ligand **44** during this study, the assay investigating **30a-j** was only conducted on CXCR1 expressing HEK293 membranes, with the receptor *C*-terminally tagged with NanoLuciferase (CXCR1-NLuc). Membranes were provided by James Farmer (University of Nottingham). When the probe binds to the CXCR1 intracellular binding site, there is co-localisation of the fluorophore with the tsNLuc tag. This allows energy transfer from the donor (tsNLuc) to the acceptor (fluorescent ligand **44**) in the presence of the furimazine substrate.[392,395] Specific probe ligand binding can then be measured through the BRET ratio (emission measured at 630 nm and 460 nm). Competition curve can then be constructed (**Figure 3-13**) to measure the concentration-dependent ability of unlabelled ligands to compete for fluorescent probe binding, from which their binding affinities (as K_i) can be determined.

In the NanoBRET competition assay, CXCR1-tsNLuc membranes were incubated with 100 nM fluorescent ligand **44** and varying concentrations of **30a-j** (100 μM – 0.1 nM) for 1 hour at 37 ˚C, to allow equilibration. Post incubation furimazine substrate was added to the assay plate and NanoBRET measurements were taken over 1 hour. Data at t = 1 hour was used to determine end point binding affinity.

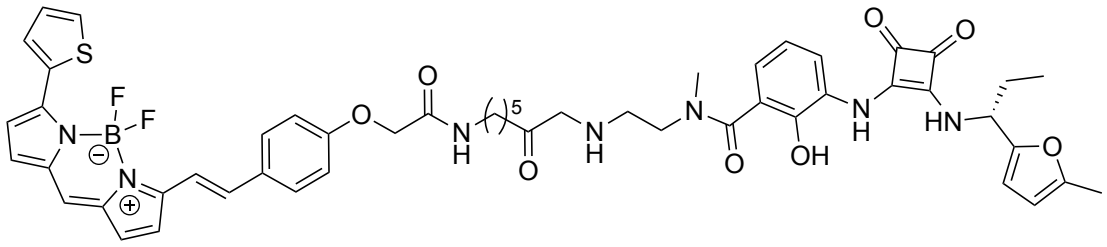

44

Figure 3-12 Fluorescent Ligand (**44**) developed by Casella *et al*.[138] **44** displays binding affinities of K_D = 101 ± 21 nM in CXCR1-NLuc membranes and K_D = 9.0 ± 4.9 nM in CXCR2-NLuc membranes determined by saturation binding assays.[138]

Navarixin (**2**) showed full displacement of the fluorescent ligand (**44**) allowing the calculation of pK_i through use of the Cheng-Prusoff equation as 7.42 ± 0.30 (**Table 3-4**). Of the 10 compounds tested, **30a-j** displayed sufficiently complete competition curves, with similar maximal displacement to navarixin (**2**), to allow calculation of pK_i. **30b**, **30f**, and **30e** caused ~ 80% displacement of the fluorescent ligand at 100 μM. Unfortunately, 100 μM was the highest concentration representing a 1000-fold dilution from the DMSO stock compound. Concentrations above 100 μM were not tested due to the cytotoxic effect that higher concentrations of DMSO can have on biological systems and assay readouts.[396-398] Reduced specific binding observed for all compounds provided further evidence that they compete with the same intracellular binding pocket which fluorescent ligand **44** targets, and, as described in previous reports for diaryl urea/urea-like NAMs targeting CXCR1 and CXCR2.[134,136,138]

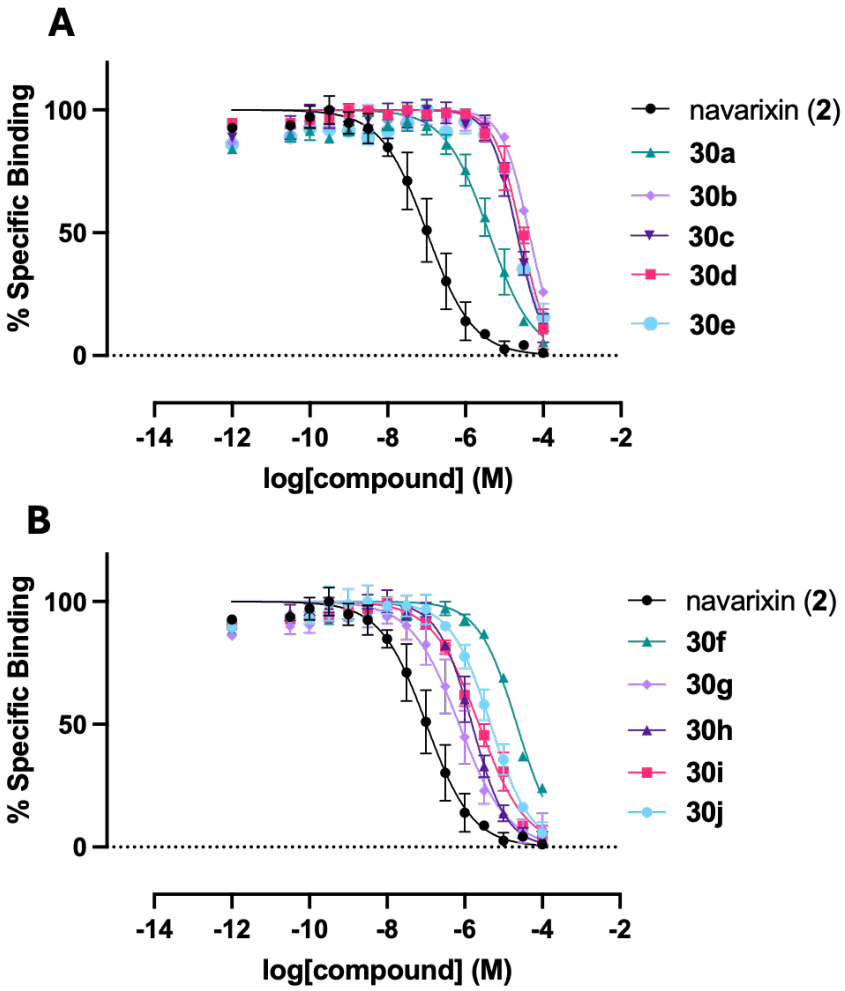

Figure 3-13 NanoBRET competition binding study of **30a-j** in CXCR1-NanoLuc membranes (provided by James Farmer). Membranes were incubated with 100 nM fluorescent ligand **44** (developed and provided by Bianca Casella)[138] and varying concentrations of **30a-j** for 1 hour at 37 ˚C in assay buffer (25 mM HEPES, 1% DMSO, 0.1 mg/ml saponin, 0.02 % pluronic acid, 1mM $MgCl_2$ and 0.1 % BSA). Data represents pooled mean ± SEM of n = 3 experiments with each experiment performed in duplicate. Specific binding was normalised from vehicle (100 %) and 10 μM navarixin (**2**) (0%) defining total and non-specific binding.

Table 3-4 pK_i ± SEM for compounds **30a-j** determined from NanoBRET competition binding assay. pK_i calculated from the Cheng-Prusoff equation using the fluorescent ligand (**44**) (K_D = 101 nM) and IC_{50} of compounds **30a-j** determined from **Figure 3-13**.

Compound	Amino acid functionality	CXCR1 pK_i ± SEM
navarixin (**2**)	-	7.42 ± 0.30
30g	*L*-Ser	6.56 ± 0.26
30h	Gly	6.21 ± 0.19
30i	*L*-Pro	6.01 ± 0.15
30j	*L*-His	5.76 ± 0.25
30a	*L*-Ala	5.71 ± 0.29
30f	*L*-Thr	5.33 ± 0.12
30d	*L*-Phe	4.83 ± 0.24
30c	*L*-Met	4.86 ± 0.20
30e	*L*-Tyr	4.73 ± 0.25
30b	*L*-Leu	4.26 ± 0.15

In a broad SAR assessment, all compounds demonstrated diminished binding affinities towards CXCR1 when contrasted with the reference compound, navarixin (**2**), as indicated by a discernible rightward shift in the concentration dependent binding competition (**Figure 3-5**). This was broadly consistent with the functional CXCR1 data for the compounds relative to navarixin (**2**). Compound **30h** (Gly analogue) showed a 10-fold drop-in binding affinity when compared to navarixin (**2**), with a further 3-fold reduction, compared to **30h**, with the addition of a methyl side chain on **30a** (*L*-Ala analogue). Both

alkyl elongation in **30b** (*L*-Leu analogue), and the integration of an electron-withdrawing sulphur moiety in **30c** (*L*-Met analogue) proved incompatible, showing low CXCR1 binding affinity consistent with low functional potency. **30g** displayed the highest binding affinity of the amino acid conjugates ($pK_i = 6.56 \pm 0.26$), with a comparable change in affinity to navarixin (**2**) displayed in the β-arrestin2 IC_{50} screen. Comparison of **30g** (*L*-Ser analogue) and **30f** (*L*-Thr analogue) shows a dramatic drop-in affinity associated with alkyl intolerance at the binding site, displaying over 100-fold drop in binding affinity with the addition of α-methyl group. Furthermore, introduction of steric bulk through phenyl **30d** (*L*-Phe analogue) and *para*-hydroxy phenyl **30e** (*L*-Tyr analogue), reduced binding affinity by 23 and 30-fold compared to **30h** (Gly analogue), respectively. This further confirms their low affinity towards CXCR1, corroborated in the functional screening. Compound **30j** (*L*-His analogue) exhibited a substantial 100-fold decrease in affinity, relative to navarixin (**2**), yet demonstrated enhanced affinity in comparison to analogues featuring phenyl ring containing side chains (**30d** and **30e**). This suggests some tolerance for the smaller imidazole ring present in **30j**. Additionally, the affinity of **30j** improved in the membrane competition binding assay compared to functional screening. This improvement could be attributed to the potential challenges posed by the imidazole ring. For example, its potentially charged nature under physiological conditions and high polarity, which could potentially lead to poor membrane permeability and access to the binding site in whole cell assays. Surprisingly the affinity of **30i** (*L*-Pro analogue) decreased in the binding assay, with a 50-fold reduction compared to navarixin (**2**), in contrast to the equipotency observed in the functional assay. The introduced pyrrolidine methyl ester is not expected to drastically change the $LogD_{7.4}$; however, this is only a based on predicted $LogD_{7.4}$ calculation and further experimental $LogD_{7.4}$ measurements would be required to discount a membrane permeability effect on ligand activity. A more nuanced explanation for the improved performance of **30i** in cellular based assays may be required. It is possible, for example, that the functional inhibition by this compound is improved due to its allosteric effect in inhibiting chemokine binding, or in preventing the activation of the effector measured β-arrestin2. These co-operative effects of the allosteric NAM may not be captured in the competition binding assay against the fluorescent probe labelling the same site, determining ligand affinity only.

3.6.7 Evaluation of *N*-methylated analogues

In the pharmacological assessment of amino ester functionalized analogues of navarixin (**2**), **30i** (*L*-Pro analogue) displayed the highest potency among tested ligands towards both CXCR1 and CXCR2 in the β-arrestin recruitment assay. (pIC_{50} = 7.10 ± 0.19 and 8.03 ± 0.14 respectively) (**Section 3.6.4**). Moreover, **30i** emerged as one of the most efficacious compounds in a CXCR1 membrane binding assay (Ki = 6.01 ± 0.15). Literature SAR around the salicylamide of 3,4-diaminocyclobut-3-ene-1,2-diones conducted by Aki *et al*.[344] showed that for CXCR2 a *N,N*-dimethylamide moiety displayed 6-fold increase in inhibitory activity (4.4 nM vs [^{125}I]-hIL-8), compared to the corresponding *N*-desmethylamide analogue (28 nM vs [^{125}I]-hIL-8).[344] Work conducted in our group for the generation of intracellular fluorescent probes based on the 3,4-diaminocyclobut-3-ene-1,2-dione scaffold also described enhanced binding affinities of *N*-methylated amide fluorescent ligands compared to their unmethylated analogues towards CXCR2.[138]

Considering these findings, we sought to expand upon existing knowledge by investigating the effect of *N*-methylation on a select number of amino ester analogues previously characterised in this work. Given the demonstrated potency of the prolyl-containing analogue **30i** towards both CXCR1 and CXCR2, we hypothesized that introducing *N*-methyl groups to these analogues could potentially enhance their potency profiles. The study focused on 3 methylated analogues **43a**, **43d**, and **43g** along with **43k** which represents the *N*-desmethylamide analogue of navarixin (**2**), which has previously been characterised in CXCR2.[344]

The compounds were subjected to analysis in a functional pIC_{50} screen, as previously described in **Section 3.6.3**, wherein the inhibitory activity was assessed based on the diminished recruitment of CXCL8-mediated β-arrestin2 to CXCR1 or CXCR2 expressing HEK293 cell lines.

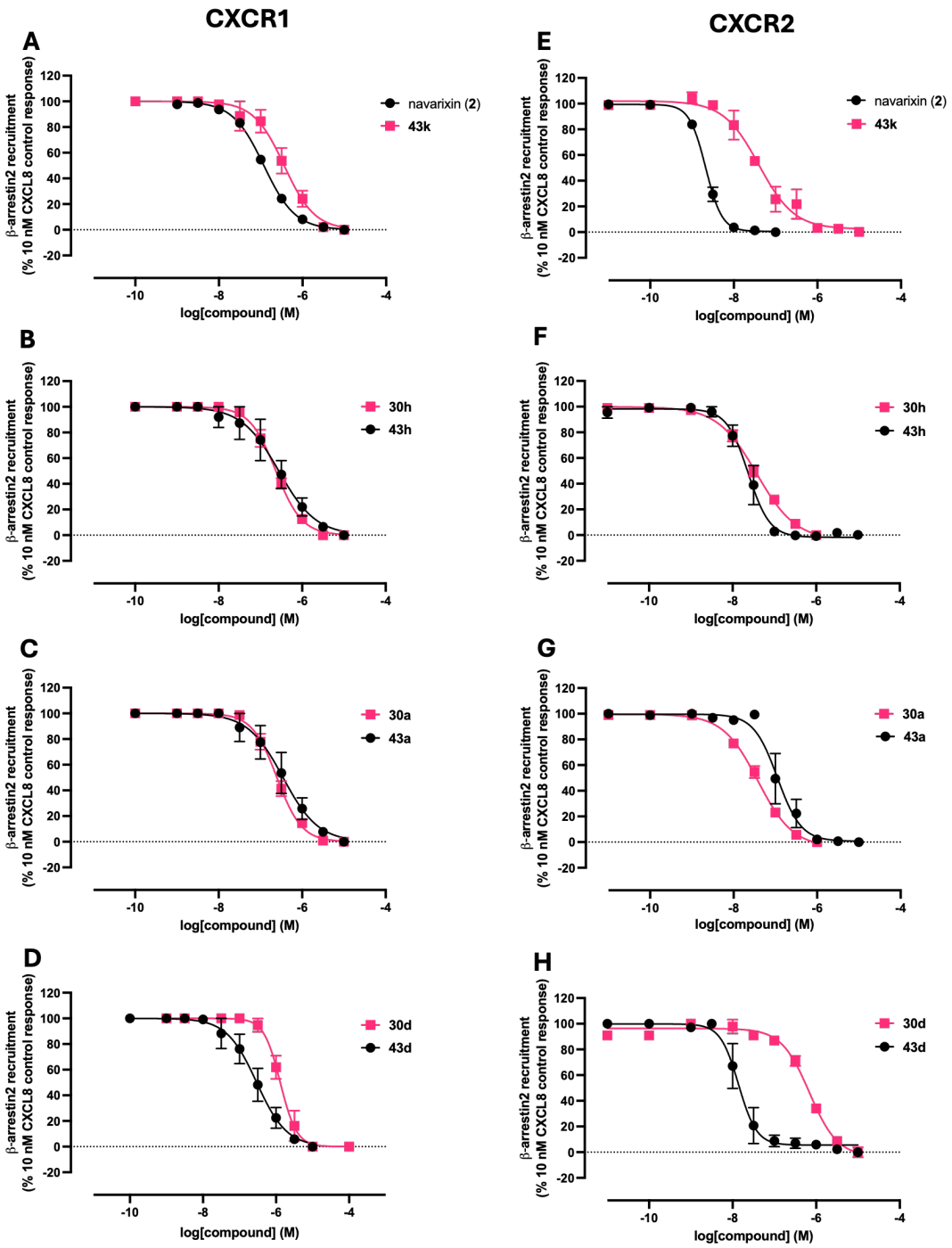

Figure 3-14 Concentration-response curves depicting the effects of *N*-methylation of 3,4-diaminocyclobut-3-ene-1,2-dione based NAMs on the inhibitory activity against CXCL8 mediated β-arrestin2 recruitment at CXCR1 (panels A to D) and CXCR2 (panels E to H). The curves were generated from inhibition assays of β-arrestin2-SmBit recruitment stimulated by 10 nM $CXCL8_{28-99}$. Data from unmethylated ligands represented in pink, and methylated ligands represented in black. The data represents pooled results (mean ±

SEM), normalized to the $CXCL8_{28-99}$ control response, obtained from at least three individual experiments conducted in duplicate (n = 3).

Table 3-5 Functional inhibition of $CXCL8_{28-99}$ mediated β-arrestin2-SmBiT recruitment in CXCR1 and CXCR2 demonstrating the effect of *N*-methylation modification. unmethylated compounds **30a**, **30d**, **30h**, and **43k** and methylated compounds navarixin (**2**), **43a**, **43d**, and **43h**. Data shown are mean ± SEM from n = 3 individual experiments.

Amino acid functionality	Compound	CXCR1 pIC_{50} ± SEM	CXCR2 pIC_{50} ± SEM	Selectivity IC_{50} (CXCR2/CXCR1)
-	**43k**	6.44 ± 0.23	7.40 ± 0.50	10
	navarixin (**2**)	6.96 ± 0.13	8.68 ± 0.13	52
***L*-Gly**	**30h**	6.12 ± 0.21	7.48 ± 0.21	24
	43h	6.56 ± 0.34	7.63 ± 0.25	12
***L*-Ala**	**30a**	6.11 ± 0.21	7.44 ± 0.17	20
	43a	6.46 ± 0.34	6.95 ± 0.47	3
***L*-Phe**	**30d**	5.38 ± 0.27	6.16 ± 0.20	6
	43d	6.53 ± 0.29	7.86 ± 0.33	20

Navarixin (**2**) remained the most potent among the ligands screened for CXCR1 and CXCR2 inhibition, with none surpassing its inhibitory activity towards either receptor. When comparing **43k**, the *N*-desmethylamide analogue of navarixin (**2**), it displayed a relatively mild reduction in potency (within 3-fold) to navarixin (**2**) in inhibiting β-arrestin2 recruitment towards CXCR1. Specifically, the pIC_{50} value of **43k** for CXCR1 inhibition (pIC_{50} = 7.40 ± 0.50) was moderately lower than that of navarixin (**2**) (pIC_{50} 6.96 ± 0.13), suggesting a comparable inhibitory effect against CXCR1. In contrast, the potency of **43k** decreased 20-fold in CXCR2 inhibition compared to navarixin (**2**). While navarixin (**2**) exhibited >10 nM potency in inhibiting CXCR2 (pIC_{50} = 8.68 ± 0.13),

compound **43k** displayed pIC_{50} 7.40 ± 0.50 towards CXCR2 inhibition (7.40 ± 0.50) was notably lower, indicating reduced inhibitory activity against CXCR2. This reduction corroborates literature findings on the *N*-desmethylamide analogue of navarixin (**2**).[344] This reduction in potency towards CXCR2 is further reflected in the CXCR2:CXCR1 selectivity, which decreased, from 52 for navarixin (**2**), to 10 for **43k**.

Compound **43h** (*N*-methyl-*L*-Gly analogue), featuring a glycine side chain, exhibited a pIC_{50} value of 6.56 ± 0.34 for CXCR1 inhibition. **43a** (*N*-methyl-*L*-Ala analogue) and **43d** (*N*-methyl-*L*-Phe analogue) displayed comparable pIC_{50} values of 6.46 ± 0.34 and 6.53 ± 0.29 for CXCR1 inhibition respectively. The relatively flat SAR observed among *N*-methylated analogues **43a**, and **43d**, and **43h** in CXCR1 inhibition suggest that the modifications in side-chain structure explored in this series do not exert a significant impact on their inhibitory activity against.

Comparing the methylated analogues (**43h** (*N*-methyl-*L*-Gly analogue), **43a** (*N*-methyl-*L*-Ala analogue), and **43d** (*N*-methyl-*L*-Phe analogue)) to their unmethylated counterparts, **30h** (*L*-Gly analogue), **30a** (*L*-Ala analogue), and **30d** (*L*-Phe analogue), reveals notable differences in potency towards CXCR1 and CXCR2. **43h** and **43a** demonstrated a mild increase in potency compared to their corresponding unmethylated counterparts, **30h** and **30a**, falling within the 3-fold increase threshold that may be considered equipotent. **43h** exhibited a pIC_{50} value of 6.56 ± 0.34 for CXCR1 inhibition, slightly higher than the pIC_{50} value of 6.12 ± 0.21 for its unmethylated counterpart **30h**. Similarly, **43a** displayed a pIC_{50} value of 6.46 ± 0.34 for CXCR1 inhibition, compared to the pIC_{50} value of 6.11 ± 0.21 for its unmethylated analogue **30a**. In contrast, **43d** exhibited a substantial increase in potency for both CXCR1 and CXCR2, compared to its unmethylated analogue **30d**. **43d** showed a pIC_{50} value of 6.53 ± 0.29 for CXCR1 inhibition, significantly higher than the pIC_{50} value of 5.38 ± 0.27 for **30d**. Similarly, for CXCR2 inhibition, **43d** displayed a pIC_{50} value of 7.86 ± 0.33, notably higher than the pIC_{50} value of 6.16 ± 0.20 for **30d**. The increase in potency for **43d** was more pronounced in CXCR2, compared to CXCR1. Specifically, the increase in potency from **30d** to **43d** was approximately 14-fold for CXCR1, whereas for CXCR2, the increase was approximately 50-fold, indicating a more significant enhancement in potency for CXCR2 inhibition compared to CXCR1 inhibition. These observations suggest that the impact of *N*-methylation on potency varies depending on the side chain functionality. While compounds with less bulky side chains showed only mild

increases in potency with *N*-methylation, the effect appears to be more pronounced for compounds with bulkier aromatic side chains such as **43d**.

3.7 Comparison of Molecular Docking and Pharmacology for ligands 30a-j

This chapter has identified key differences in the findings from molecular docking of proposed amino ester functionalised analogues of navarixin (**2**) compared to the experimentally derived functional activity. Initial docking studies were promising, with improved docking scores demonstrated for all ligands towards CXCR1 and most ligands showing improved docking scores towards CXCR2. Notably in both receptors ligands tended to adopt one of two predicted binding poses. The first of these poses predicted the methyl ester occupying shallow binding cavity between TM3 and TM6. The second type of binding pose involved the amino acid ester side chain moiety occupying a binding cavity between TM2 TM3 and ICL2.

To conduct a basic analysis of potential correlation between molecular docking scores and functional inhibitory activity derived from pharmacological characterization, docking scores were plotted against pIC_{50} values. Additionally, rank order docking scores were compared with rank order pIC_{50} values in **Figure 3-15** and **Figure 3-16**. The results of these plots yielded R^2 coefficients of less than 0.1, indicating a weak correlation between docking scores and pIC_{50} values. This suggests that the predicted binding affinities obtained from molecular docking simulations poorly predict the experimental inhibitory activity measured in functional assays. Despite efforts to model ligand-receptor interactions of NAMs accurately in **Chapter 2**, the complexities of protein-ligand binding and the limitations of current structures available for CXCR1 and CXCR2.

Although analysing docking score vs pIC_{50} can provide insights into the relationship between predicted binding affinity and experimental inhibitory activity, it should be noted of the limitations of this type of analysis. Firstly, functional screening to obtain pIC_{50} values are variable depending on the type of experiment used and can vary depending on factors such as assay conditions, cell types and assay sensitivity. Additionally, molecular docking protocols rely on simplified representations of ligand-receptor interactions that do not fully capture the complexities of binding in a biological system or the dynamic nature of the receptor.

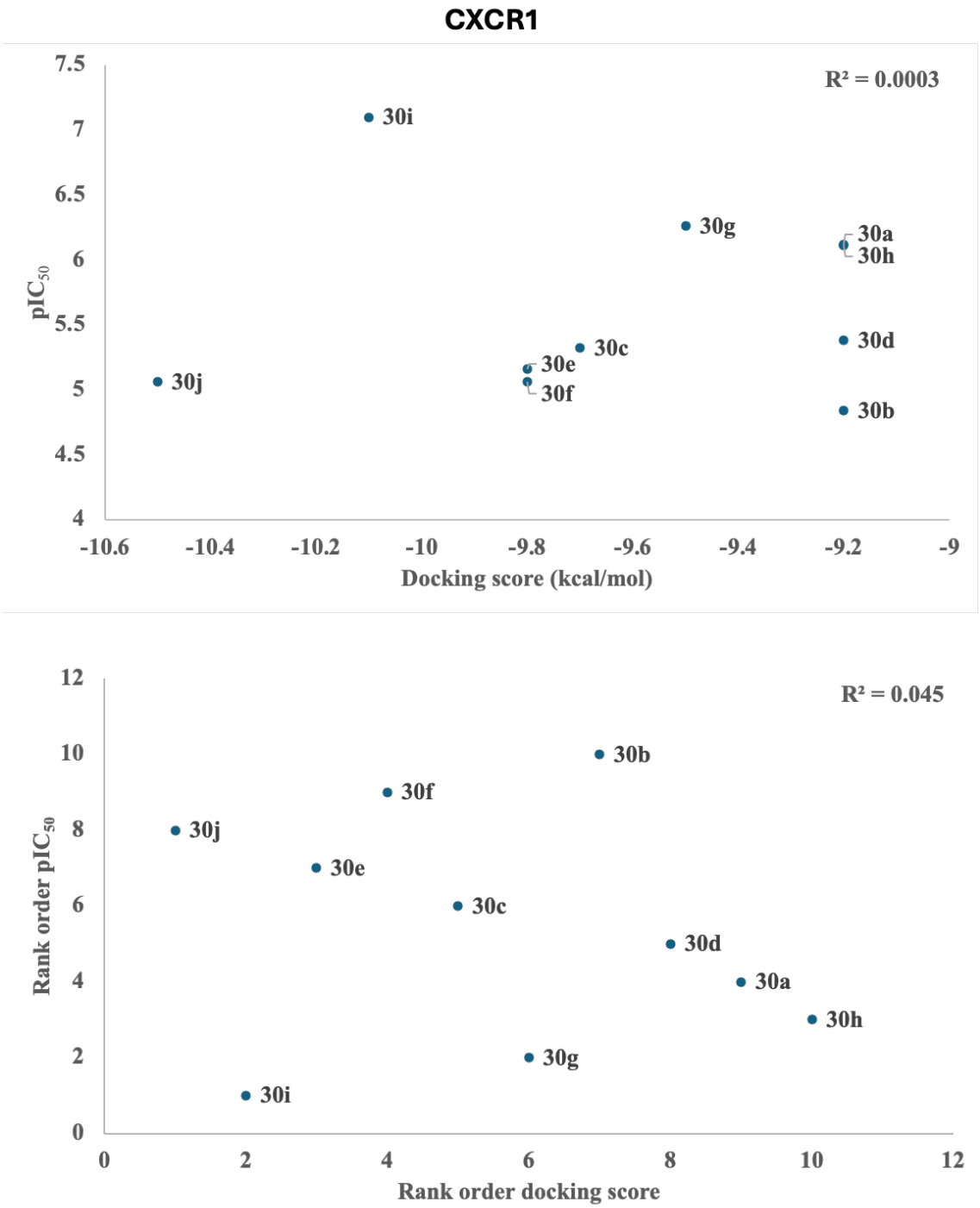

Figure 3-15 Experimental pIC_{50} vs docking score (top) and rank order experimental pIC_{50} vs rank order docking score (bottom) collected for compounds against CXCR1. Docking scores obtained for each compound using Glide in Schrödinger[289] suite. Experimental pIC_{50} values determined from inhibition of CXCL8 stimulated β-arrestin2 recruitment.

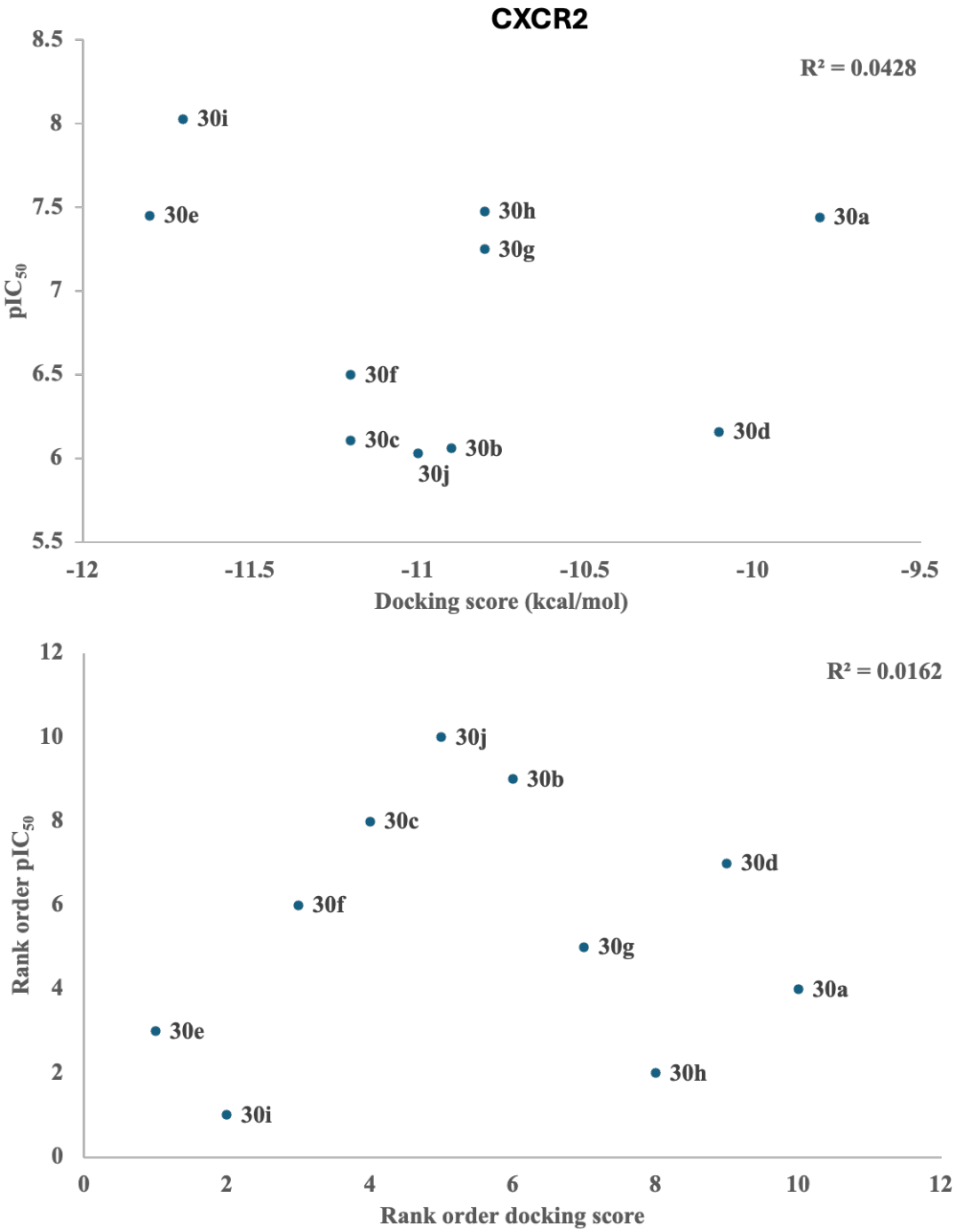

Figure 3-16 Experimental pIC_{50} vs docking score (top) and rank order experimental pIC_{50} vs rank order docking score (bottom) collected for compounds against CXCR1. Docking scores obtained for each compound using Glide in Schrödinger[289] suite. Experimental pIC_{50} values determined from inhibition of CXCL8 stimulated β-arrestin2 recruitment.

An additional note to emphasise from **Chapter 2** when discussing the correlation of experimental and *in silico* results is the origin of the homology models. These models are

based on the crystal structure of CXCR2 in complex with 00767013 (**1**) and included structural modifications, presumably to facilitate crystallisation.[54] Modifications included the mutation of A249$^{6.33}$ and an antibody insertion in ICL3. These modifications are in close proximity to the binding regions proposed for the functionality added in the proposed analogues, and with currently available structures it is unclear what disruptions these modifications could have introduced in the region.

3.8 Conclusion

To summarise, CXCR1 and CXCR2 models based on the CXCR2-00767013 (**1**) crystal structure from **Chapter 2** were utilised for the design of 3,4-diaminocyclobut-3-ene-1,2-dione-based NAMs. This work aimed at developing compounds serving as pharmacological tools for studying CXCR1/CXCR2 chemokine signalling pathways, potentially valuable for addressing CXCR1/CXCR2 related diseases. While compounds targeting the intracellular allosteric site typically exhibit CXCR2 selectivity over CXCR1, the feasibility of achieving CXCR1 selectivity through the intracellular allosteric binding site remains uncertain. Moreover, CXCR2 selective therapeutics have faced challenges in demonstrating efficacy in Phase II trials, underscoring the potential utility of dual CXCR1/CXCR2 antagonists or even selective CXCR1 antagonists.

To advance this objective, the CXCR1 and CXCR2 models, developed in **Chapter 2**, docked with lead compound, navarixin (**2**), were investigated for potential novel modifications of the chemical structure. Through systematic exploration using SiteMap in Schrödinger[289], druggable binding cavities in proximity to the *N*,*N*-dimethylamide moiety of navarixin (**2**) were identified as potential targets for modification. Interestingly, the *N,N*-dimethylamide moiety of navarixin (**2**) was identified as non-critical for receptor binding during docking studies, as it was consistently predicted to protrude from the bottom of the intracellular binding site or make favourable interactions in either CXCR1 or CXCR2 models. These observations guided the design of 10 amino ester functionalized analogues (**30a-j**) of navarixin (**2**) to exploit the identified druggable binding cavities.

Molecular docking of the proposed ligands revealed top-scoring binding poses, aligning with previous findings for navarixin (**2**) and 00767013 (**1**), as well as the crystal structure of CXCR2-00767013 (**1**). The predicted binding poses displayed the unmodified functionalities, furan, squaramide and phenol, of the ligands in agreement with previously generated binding poses of navarixin (**2**) and 00767013 (**1**) and crystal structure of

CXCR2-00767013 (**1**). Two predominant binding modes were identified for the proposed ligands. The first mode featured the methyl ester group occupying a hydrophobic binding cavity between TM3 and TM6, while the second mode showcased differential side chains occupying a binding cavity between TM2, TM3 and ICL2. This cavity was comprised conserved residues between CXCR1 and CXCR2 binding sites: $V73^{2.38}$, $T74^{2.39}$, $D134^{3.49}$,$R135^{3.50}$, and T145 (ICL2) in CXCR1 and $V82^{2.38}$, $T83^{2.39}$, $D143^{3.49}$,$R144^{3.50}$, and T154 (ICL2) in CXCR2. This region displayed the ability to accommodate the side chains of various ligands and exhibiting potential improved binding affinity through favourable binding interactions in both CXCR1 and CXCR2 models. Interestingly, while this binding site accommodated hydrophobic side chains such as Met in **30c** and Tyr in **30e** towards both CXCR1 and CXCR2 models, it also accommodated His of **30j** in CXCR1 only, although the rationale for this specificity remains unclear. Furthermore, improved docking scores were observed in all compounds (**30a-j**) when docking in CXCR1 compared to navarixin (**2**), ranging from -9.2 to -10.5 kcal/mol, compared to navarixin (**2**) (-8.6 kcal/mol). In CXCR2, **30e** and **30i** exhibited improved docking scores (-11.8 and -11.7 kcal/mol, respectively), while the remaining compounds showed comparable, or worse, docking scores (ranging from -9.8 to -11.2 kcal/mol) compared to navarixin (**2**) (-11.2 kcal/mol).

Initial attempts toward synthesizing compounds **30a-j** involved a divergent synthesis route utilizing 3-nitrosalicylic acid (**31**) as the starting material, followed by a series of transformations to obtain a common precursor (*R*)-2-hydroxy-3-((2-((1-(5-methylfuran-2-yl)propyl)amino)-3,4-dioxocyclobut-1-en-1-yl)amino)benzoic acid **34,** from which the desired compounds could be obtained. However, challenges arose during the final amide coupling reaction, including the formation of unwanted side products and difficulties in purification. Despite the challenges faced, adequate quantities of **30a**, **c**, **d**, **g**, **h**, and **j** were obtained for pharmacological characterisation. Subsequently, an alternative, non-divergent, synthetic route was devised, resembling the approach employed for the synthesis of navarixin (**2**) and its analogues by the Schering Plough group.[248]This alternative route circumvented the issues encountered in the amide coupling step by employing a strategy *via* the corresponding acyl chloride and subsequent transformations resulted in the desired products **30b**, **f**, **e**, and **i**.

Functional screening using NanoBiT complementation assays provided data on the inhibitory potency of compounds **30a-j** against CXCL8-mediated β-arrestin2 recruitment,

with the aims of generating an SAR around amino ester functionalisation, compared to the reference lead compound navarixin (**2**). The results indicated that the addition of amino ester functionalities could be tolerated in both CXCR1 and CXCR2. Additionally, modulated inhibitory activity was observed based on the differential side chain, suggesting the proposed hypothesis held merit. However, comparisons to the previously conducted molecular docking studies showed little correlation in the docking scores obtained *in silico* and the experimental functional data. This suggests there is a nuance to CXCR1/CXCR2-NAM interaction that was not captured in the molecular docking studies. Further investigations are required on the proposed models from **Chapter 2** to ascertain their viability in predicting binding in the region corresponding to the proposed functionality introduced to navarixin (**2**) in this work. This may include investigations using molecular dynamics, that could help to recapture some of the dynamic nature of the binding pocket. Another example could include further structural refinement based on the experimental data obtained in this work. The work exemplifies the difficulties that can be faced when attempting to rationalise experimental results from *in silico* experiments and whilst the models were useful to generate a hypothesis for the project, the results from molecular docking into CXCR1 and CXCR2 models were not representative of the potency observed from experimental functional screening of **30a-j**.

Although no ligand exhibited enhanced potency compared to navarixin (**2**), compound **30i** emerged as the most potent among the tested ligands. In CXCR1, it demonstrated equipotency with navarixin (**2**) (pIC_{50} = 7.10 ± 0.19 and 6.96 ± 0.13, respectively), while in CXCR2, it displayed a five-fold reduction in potency compared to navarixin (**2**) (pIC_{50} = 8.03 ± 0.14 and 8.68 ± 0.13, respectively).

From the observed potency from **30i,** along with observations in the group[138], *N*-methylation appears to be preferred in CXCR2; this prompted investigations into the effect of *N*-methylation on amino ester analogues.[138] The investigation focused on three methylated analogues, **43a**, **43d**, **and 43h**, along with **43k**, representing the *N*-desmethylamide analogue of navarixin (**2**). The compounds underwent analysis in a functional pIC_{50} screen. The results showed that *N*-methylation appeared to not significantly improve activity of Gly and *L*-Ala containing analogues towards either CXCR1 or CXCR2. Additionally, **43k**, the mono-methylated analogue of navarixin (**2**), exhibited similar potency towards CXCR1, but a significant 20-fold reduction in potency towards CXCR2, compared to navarixin (**2**). The *N*-methylated analogue **43d**, containing

a phenylalanine side chain, showed a 14-fold increase in potency towards CXCR1 and a remarkable 50-fold increase in potency towards CXCR2. These findings suggest that the impact of *N*-methylation depends on other modifications to the amide moiety, such as the amino ester functionality introduced in these studies. Moreover, the effect of *N*-methylation appears to be more substantial in CXCR2 compared to CXCR1.

Chapter 4 – Design, synthesis, and characterisation of navarixin (2) analogues with modifications to the phenol moiety

4.1 Introduction

Investigation using CXCR1 and CXCR2 models developed in **Chapter 2** demonstrated the high level of sequence homology between the two subtype receptor binding pockets. The only difference in amino acid sequences observed in the pocket is an amino acid modification of K320$^{8.49}$ in CXCR2 to N311$^{8.49}$ in CXCR1. This observation led to important questions regarding the shape of the binding pocket entrance, and the significance of this residue for the selectivity profile often exhibited by 3,4-diaminocyclobut-3-ene-1,2-dione CXCR1/CXCR2 antagonists such as the 15-fold selectivity observed by navarixin (**2**) towards CXCR2 over CXCR1. In comparing the CXCR1/2 receptor-navarixin (**2**) complexes in **Chapter 2**, molecular docking predicted K320$^{8.49}$ in CXCR2 forms an ionic interaction with the phenolate anion of navarixin (**2**). However, such interactions were absent in CXCR1, due to the increased distance between the phenolate moiety and N311$^{8.49}$, along with the non-ionizable nature of the Asn side chain. To delve into the structural aspects arising from the residue modification between the two receptors, *in silico* modelling and *in vitro* functional screening techniques (specifically monitoring CXCR1/2 activation through β-arrestin recruitment) were explored to investigate the effect of site-directed mutagenesis on ligand potency.

There was an absence of an SAR towards CXCR1 selectivity over CXCR2 identified in **Chapter 3**, which aimed at modulating CXCR1/CXCR2 selectivity through an extended binding cavity discovered *in silico.* Instead, efforts were redirected towards exploring alternative strategies for achieving the desired modulation of selectivity. Urea or urea-like antagonists, such as the 3,4-diaminocyclobut-3-ene-1,2-dione class of NAMs, that target an intracellular allosteric binding site of CXCR1 and CXCR2 share common structural features, including urea or urea-like cores and a phenol ring, as previously discussed in **Chapter 3**.[226,249,250,298,344,346,348,399] For squaramide containing antagonists, such as navarixin (**2**), the two NH groups and the phenolic OH group are deemed necessary for retaining binding affinity in CXCR2.[344] Justification for the presence of the phenol can be

rationalised due to its relatively low pKa, arising from the electron withdrawing effect of the *ortho*-amide substituents. This increased acidity provides stabilisation of the phenolate anion, improving the ionic interaction with K320$^{8.49}$ and stabilising the ligand-protein complex. From analysing the predicted binding modes of CXCR1-navarixin (**2**) and CXCR2-navarixin (**2**) in **Chapter 2**, such justification for the phenol is not as clear in CXCR1, where a corresponding ionic interaction cannot take place. Therefore, the importance of the phenol moiety in a CXCR1 pharmacophore was questioned. To investigate this further, a pilot SAR study around the phenol was proposed. This study could provide insights for further CXCR1 ligand development and assess whether modifications in this region could influence selectivity. Additionally, the SAR investigation aimed to enhance the understanding of ligand-receptor interactions of NAMs towards CXCR1, and potentially contribute to a divergent CXCR1 pharmacophore model.

4.2 *In silico* investigations into structural modifications around the phenol ring

4.2.1 Designing ligands for the docking study

A set of potential NAMs were designed for initial docking studies into the intracellular binding pocket of CXCR1 and CXCR2, which were grouped into 2 sets. Ligands in set A aimed to explore some simple functional group modifications of the hydroxy group. **45b** modifies the hydroxy of the phenol of navarixin (**2**) to a methoxy, in which it was envisaged that replacement of the polar OH with non-polar groups may remove favourable interactions associated with the phenolic OH moiety. Aki *et al*.[344] has previously described the effect of hydroxy to methoxy substitution for 3,4-diaminocyclobut-3-ene-1,2-dione NAMs in SAR studies. Their findings showed that this modification resulted in >60-fold reduction in binding affinity against CXCR2, K_i (vs ^{125}I- hCXCL8) = 4.4 nM for hydroxy and K_i (vs ^{125}I- hCXCL8) = >270 nM for methoxy.[344] Unfortunately, corresponding affinity data for CXCR1 was not provided in their study. **45c** introduces an acetate moiety which not only introduces steric bulk to the region, but also the potential for hydrogen bonding *via* the carbonyl. The general strategy of the rest of the ligands was to extend the chemical space around the OH moiety, whilst retaining polar functionality, allowing for hydrogen bonding interactions. It was postulated that the presence of steric bulk in the area corresponding to the phenol region might play a crucial role in conferring CXCR1/CXCR2

selectivity. This hypothesis suggests that the larger size of the K320$^{8.49}$ residue might not accommodate ligands with increased size as effectively, potentially influencing selectivity.

Set B aimed to explore the introduction of hydroxy-substituted phenyl ring systems to the region (in *ortho*, *meta* or *para* positions). These ligands extend the hydroxy moiety away from the di-ortho substituted ring and introducing a relatively larger amount of steric bulk. The hypothesis was formulated that the incorporation of hydroxy functionality could offer advantages, particularly considering the polar nature of the binding pocket entrance, as discussed in **Chapter 2**. The objective of set B was to evaluate the tolerability of CXCR1 and CXCR2 to the modified planar aromatic steric bulk and aromaticity. This investigation aimed to elucidate the structural requirements for ligand-receptor interactions, offering valuable insights for the rational design of CXCR1 and CXCR2 intracellular modulators based on navarixin (**2**) analogues with modified phenol moieties.

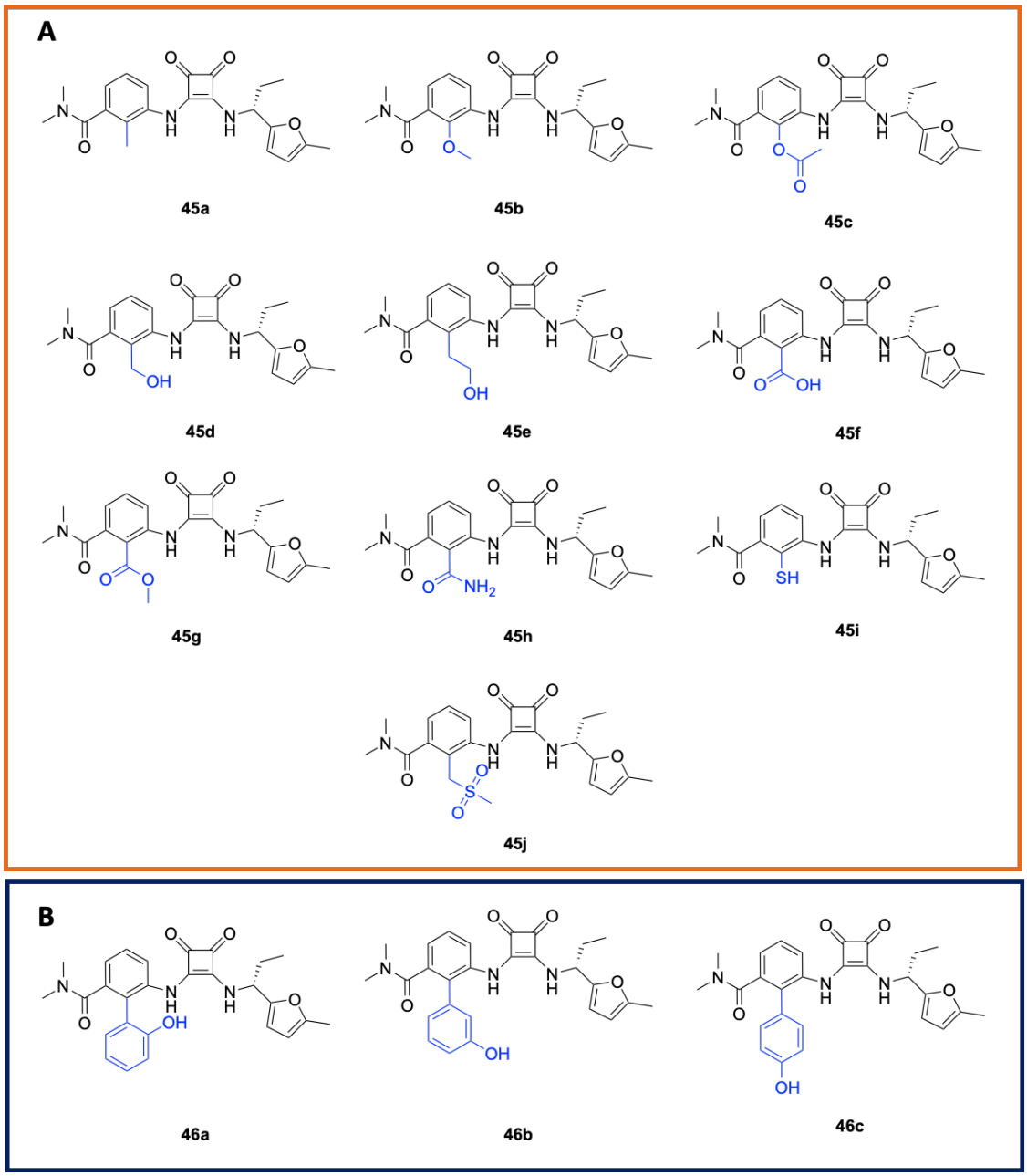

Figure 4-1 Proposed ligands to investigate modification in the phenol region of navarixin (**2**).

4.2.2 Glide docking of ligand set A

Ligand set A comprises analogues of navarixin (**2**) with modifications to the hydroxy moiety in the phenol core (**Figure 4-1**). Utilizing Glide SP flexible ligand docking, these ligands were docked into CXCR1 and CXCR2. The docking scores of the top poses for each ligand in set A, into each receptor model (CXCR1 and CXCR2), are presented in **Table 4-1**.

Table 4-3 Glide docking scores of **45a-j** into CXCR1 and CXCR2 models generated in **Chapter 2**. Docking scores were calculated from Glide docking protocol using flexible ligand docking. Displayed scores are from the top scoring pose for each ligand displaying binding poses corelating to validated poses in **Chapter 2** and crystal structure of CXCR2-00767013 (**1**) (PDB ID: 6LFL[54]).

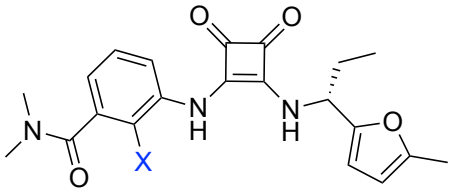

Ligand	X	Glide docking score (kcal/mol) CXCR1	CXCR2
navarixin (**2**)	OH	-8.2	-9.0
45a	Me	-8.0	-7.5
45b	OMe	-8.2	-7.6[A]
45c	OAc	-8.3	NP
45d	CH_2OH	-9.3	-7.9[A]
45e	CH_2CH_2OH	-8.5	-7.8[A]
45f	CO_2H	-9.3	-9.2
45g	CO_2Me	-9.2	-7.4[A]
45h	$CONH_2$	-9.2	-8.3
45i	SH	-8.6	-7.5
45j	CH_2SO_2Me	-8.7	NP

A – Binding poses generated displays rotation of the phenyl ring compared to experimental binding pose – quoted docking score is the most favourable observed

NP – No reasonable binding poses generated

In CXCR1, all proposed ligands exhibited top-scoring binding poses consistent with the poses adopted by navarixin (**2**) and 00767013 (**1**) previously described in **Chapter 2** and crystallographic experiments of CXCR2-00767013 (**1**).[54] However, in CXCR2, ligands **45c** and **45j** failed to produce adequate predicted binding poses. Ligands **45d**, **45e**, **45c**, and **45g** displayed significant variation in the position of the phenyl ring in CXCR2, whilst retaining expected positions of squaramide and furan moieties. Notably, ligands **45d** and

45e exhibited a 'twisted' phenyl ring conformation, with modified substituents directed towards the back of the pocket and the phenyl moiety moving towards the entrance, establishing pi-cation interactions with $K320^{8.49}$ (**Figure 4-2**). The dihedral angles provided in the **Table 4-2** represent torsion angles between specific bonds in the ligand molecules, namely the C=O amide bond and the phenyl ring, as well as the N-H squaramide bond and the phenyl ring. Compounds **45d** and **45e**, which exhibited a 'twisted' phenyl ring conformation, as described earlier, display significant deviations in dihedral angles, when compared to navarixin (**2**). While navarixin (**2**) and ligands **45d** and **45e** show similar torsion angles between the N-H and the phenyl ring, both compounds **45d** and **45e** exhibit negative values for the dihedral angle between the C=O amide bond and the phenyl ring (-114.6 ° and -112.2 °, respectively), whereas navarixin (**2**) displayed a torsion angle of 98.7 °. This indicates a torsion or “twisting” of the phenyl ring in the opposite direction in compounds **45d** and **45e** compared to navarixin (**2**).

This twisting phenomenon was absent in corresponding poses for CXCR1, suggesting potential challenges in accommodating hydroxy alkyl groups in CXCR2. Only four of the proposed ligands **45a**, **45f**, **45h** and **45i** exhibited predicted binding poses that aligned with the unaltered region of the ligands. This observation suggests that CXCR2 tends to be less tolerant of modifications to the phenol moiety of the lead compound navarixin (**2**).

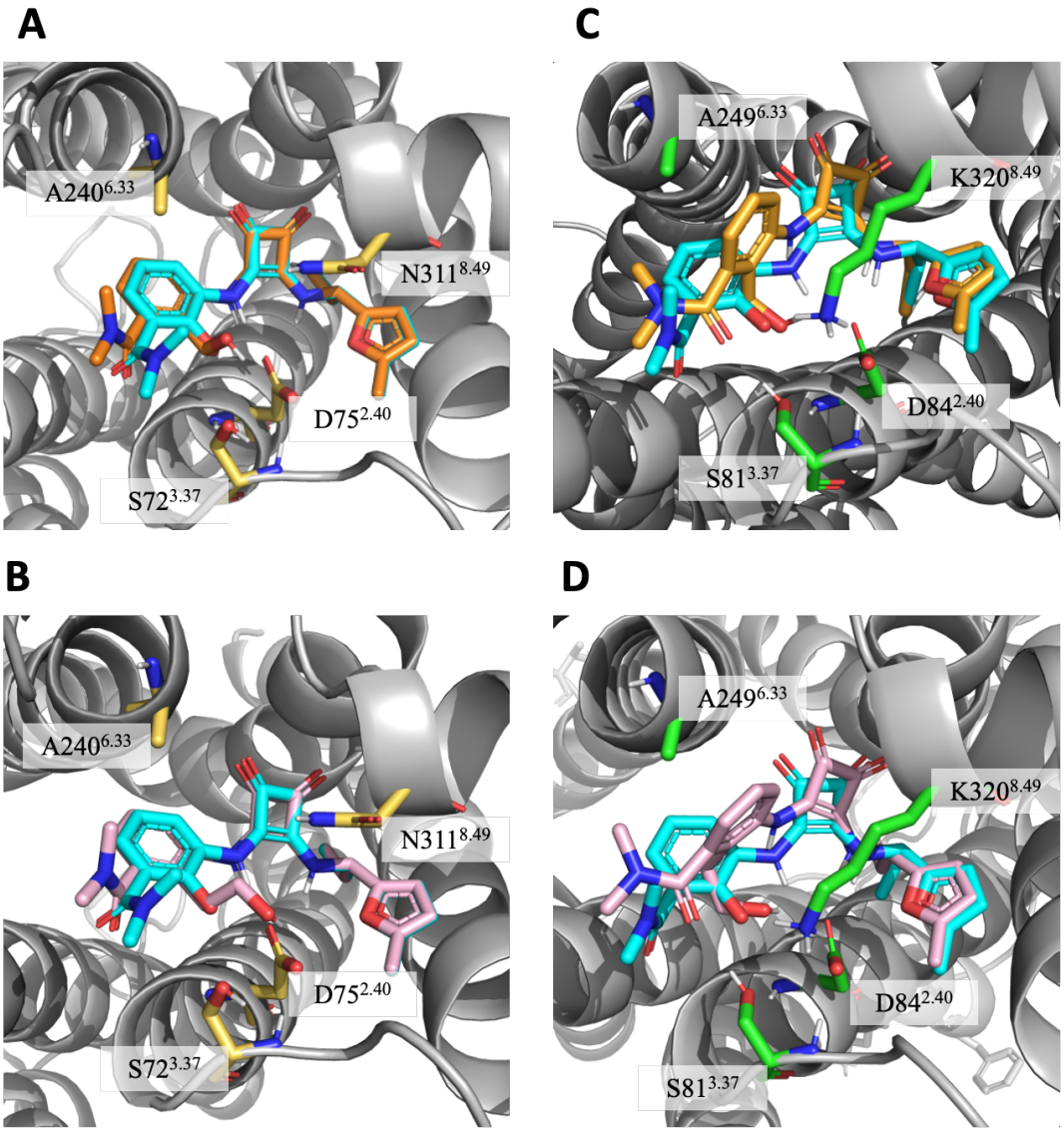

Figure 4-2 Top ranking predicted binding poses generated by Glide. (A) CXCR1-**45d** (B) CXCR1-**45e** (C) CXCR2-**45d** (D) CXCR2-**45e**. Protein represented as grey cartoon for both receptors. Binding site residues represented as sticks in yellow (CXCR1) and green (CXCR2). Navarixin (**2**) represented as blue sticks, compound **45d** represented as orange sticks and compound **45e** represented as pink sticks. Binding site residues labelled: S72$^{3.37}$, D75$^{2.50}$, A240$^{6.33}$ and N311$^{8.49}$ in CXCR1 and S81$^{3.37}$, D84$^{2.50}$, A249$^{6.33}$ and K320$^{8.49}$ in CXCR2.

Table 4-2 Dihedral angles of phenyl substituents in predicted docking poses of navarixin (**2**), compound **45d,** and compound **45e** in CXCR2.

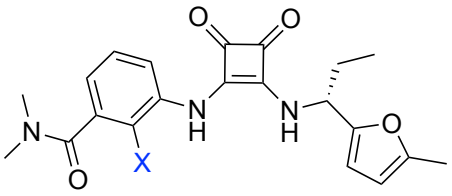

Ligand	X	Dihedral angle between C=O amide and phenyl ring	Dihedral angle between N-H squaramide and phenyl ring
navarixin (**2**)	OH	98.7°	-154.9°
45d	CH_2OH	-114.6°	-162.6°
45e	CH_2CH_2OH	-112.2°	-174.4°

Compound **45f**, a carboxylic acid analogue of navarixin (**2**), displayed the lowest docking score amongst docked ligands towards CXCR2 and CXCR1. When comparing compound **45f** with navarixin (**2**), compound **45f** showed improved docking scores in both CXCR1 and CXCR2. However, this improvement is more substantial in CXCR1. While navarixin (**2**) had docking scores of -8.2 kcal/mol for CXCR1 and -9.0 kcal/mol for CXCR2, compound **45f** demonstrated lower predicted binding energy with scores of -9.3 kcal/mol for CXCR1 and -9.2 kcal/mol for CXCR2. In both CXCR1-**45f** and CXCR2-**45f** complexes, the carboxylic acid facilitates two hydrogen bond interactions. The first interaction involves the carbonyl oxygen interacting with the conserved residue $S72^{2.37}$ in CXCR1 and $S81^{2.37}$ in CXCR2 of TM2. This residue forms interactions with the phenolate anion of navarixin (**2**) in both receptors. The second interaction observed is the carbonyl of the carboxylic acid forming a hydrogen bond with the non-conserved residues $K320^{8.49}$ in CXCR2 and $N311^{8.49}$ in CXCR1. Compound **45f** was the only example in set A that showed hydrogen bonding or ionic interactions towards $K320^{8.49}$ in CXCR2, and $N311^{8.49}$ in CXCR1 without introducing significant steric clashes in the receptor entrance.

Compound **45h** showed a propensity to form hydrogen bond interactions between the amide carbonyl and N311$^{8.49}$ in CXCR1 and K320$^{8.49}$ in CXCR2. However, significant clashes were observed in CXCR2 stemming from the introduced primary amide of **45h**. The observed clashes were between the carbonyl of the amide and S81$^{2.37}$ and clashes between K320$^{8.49}$ and the carbonyl, NH moiety and carbon of the amide moiety.

In the CXCR1 model, all ligands generated poses displaying retained hydrogen bond interactions in the squaramide region of the ligands, showing interactions between the carbonyl oxygen with F316$^{7.55}$ and both amide NH moieties and D75$^{2.40}$. The placement of the furan residue was also retained, suggesting that changes in the phenol moiety did not have any disruptive effect on the predicted binding mode adopted by the squaramide and the furanyl ring.

Except for **45a** and **45b**, all ligands containing *ortho*-modifications to the salicylamide moiety exhibited enhanced ligand binding in CXCR1, when compared to the lead compound, navarixin (**2**). **45b** displayed no markable change in calculated docking score, compared to navarixin (**2**) in CXCR1, with both displaying docking scores of -8.2 kcal/mol. Additionally, **45a** showed an increase in docking score to -8.0 kcal/mol in CXCR1. Upon inspection, it appears that there is a steric clash of the methyl group with the polar side chains, S72$^{2.37}$ and D75$^{2.40}$, lining the entrance to the binding pocket. Docking of **45a** into CXCR2 displayed a more pronounced reduction in binding from -9.04 in navarixin (**2**) to -7.50 displaying a further steric clashes in CXCR2, compared to CXCR1, with the non-conserved residue K320$^{8.49}$. The findings in CXCR2 corroborate the reduction in binding affinity observed in structural activity studies, where the hydroxy is substituted for a methyl.[383]

Ligands that exhibited enhanced predicted binding energies in CXCR1 were observed to contain groups that made hydrogen bonding interactions with S72$^{2.37}$, except for **45h**, which contained an amide adopting a conformation allowing for a hydrogen bond with the more deep lying D75$^{2.40}$ residue. The ligands containing modifications that extended the phenol region contained polar atoms that would facilitate hydrogen bonding with the highly polar residues at the entrance of the binding site. The docking of these ligands has shown that the interactions observed between the phenolate anion of navarixin (**2**) in CXCR1 can be mimicked by introduction of different polar functional groups such as amide, esters, and alcohols. In addition, the formation of new interactions can be

established by introducing extensions to the phenol, allowing the ligand to interact with residues that are too distant in navarixin (**2**)-CXCR1 binding modes.

4.2.3 Glide docking of Ligand set B

In the same fashion as ligand set A, ligand set B was docked into CXCR1 and CXCR2 models using Glide flexible docking protocol. The top-ranking binding poses of each ligand in CXCR1 and CXCR2 are displayed in **Figure 4-3,** and the docking scores calculated for the binding poses are summarised in **Table 4-3**. All ligands generated binding poses in the CXCR1 and CXCR2 models, however docking into CXCR2 generated poses that did not align with the canonical V-shaped pose observed by navarixin (**2**) and 00767013 (**1**) in **Chapter 2**. Consistently across the three analogues, there was a shift of the ligand binding pose away from the hydrophobic cavity formed between TM1, TM7 and ICL1 that typically accommodates the furan ring in CXCR1 and CXCR2. This shift in binding poses for **46a** and **46b** appears to allow the introduced hydroxy phenyl rings to occupy a region outside of the binding pocket, towards the cytosolic space beneath the receptor. Additionally, the positioning of the ring in **46a** and **46b** does not allow the hydroxy phenyl functionality to form notable beneficial interactions with the receptors contributing to ligand binding. **46c** adopts a binding pose which sees the hydroxy phenyl ring point towards the back of the binding in a region that is canonically occupied by the phenol ring of navarixin (**2**). As none of the binding poses of **46a**, **46b** and **46c** correlate to the binding mode of navarixin (**2**) and 0076713 (**1**), previously demonstrated in **Chapter 2**, or other NAMs in **Chapter 3**, it is difficult to reason the validity of the observed poses and their relevance to ligand binding in the CXCR2 binding site described in **Chapter 2**.

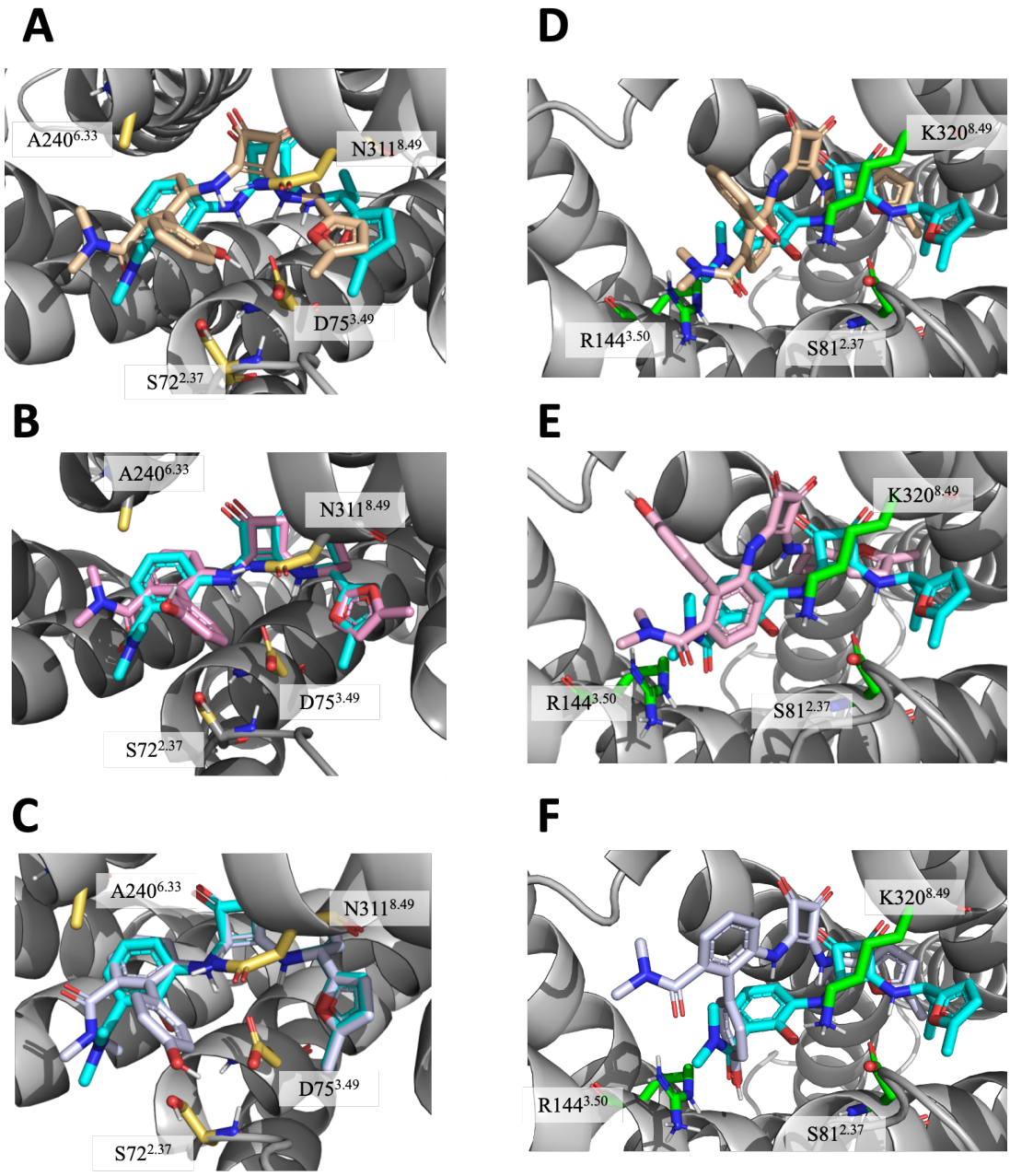

Figure 4-3 Predicted binding poses generated from Glide docking protocol of ligand set B. (A) CXCR1-**46a** (B) CXCR1-**46b** (C) CXCR1- **46c** (D) CXCR2- **46a** (E) CXCR2-**46b** (F) CXCR2-**46c**. Protein represented as grey cartoon for both receptors. Binding site residues represented as sticks in yellow (CXCR1) and green (CXCR2). Navarixin (**2**) represented as blue sticks, compound **46a** represented as cream sticks, compound **46b** represented as pink sticks and compound **46c** represented as light purple sticks. Binding site residues labelled: S72$^{3.37}$, D75$^{2.50}$, A240$^{6.33}$ and N311$^{8.49}$ in CXCR1 and S81$^{3.37}$, R144$^{3.50}$ and K320$^{8.49}$ in CXCR2.

In contrast to observed predicted binding poses in CXCR2, **46b** and **46c** generated reasonable binding poses when docked into CXCR1. This difference stems from the absence of K320$^{8.49}$ in CXCR1, allowing the hydroxyphenyl moiety to occupy a region at the entrance of the pocket. The *meta*- and *para* hydroxy analogues **46b** and **46c** does not appear to make a difference to the docking score or introduce beneficial interactions with the surrounding polar residues, S72$^{3.37}$, D75$^{2.50}$ and N311$^{8.49}$, at the entrance of the binding pocket. Whilst **46a** does show a slight shift in the squaramide and furan moieties, the hydroxy in the *ortho* position does form hydrogen bond interactions with D75$^{2.50}$ and S72$^{3.37}$. These residues are conserved between CXCR1 and CXCR2 and are shown to form hydrogen bond interactions towards the phenol in navarixin (**2**) and 00767013 (**1**). Despite the promising binding poses observed in CXCR1 for compounds **46a**, **46b**, and **46c**, there was a significant decrease in the docking score. This decrease is attributed to the introduction of the hydrophobic aryl ring into the hydrophilic binding region lining the entrance to the pocket, resulting in an energetic penalty for binding.

Table 4-3 Glide docking scores of **46a-c** into CXCR1 and CXCR2 models generated in **Chapter 2**. Docking scores were calculated from Glide docking protocol using flexible ligand docking. Displayed scores are from the top scoring pose for each ligand displaying binding poses corelating to validated poses in **Chapter 2** and crystal structure of CXCR2-00767013 (**1**) (PDB ID: 6LFL[54]).

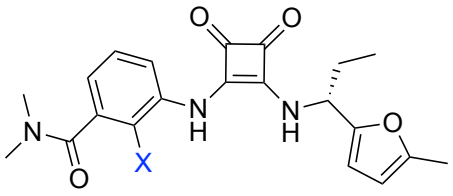

		Glide docking score (kcal/mol)	
Ligand	**X**	CXCR1	CXCR2
navarixin (**2**)	-	-8.21	-9.04
46a	2-hydroxyphenyl	-6.90	-5.39[A]
46b	3-hydroxyphenyl	-7.79	-5.26[A]
46c	4-hydroxyphenyl	-7.79	-6.03[A]

A – Binding pose generated did not correlate with canonical binding pose of NAMs at the intracellular allosteric binding site overlapping $G\alpha_i$.[54]

4.3 Synthetic chemistry

4.3.1 Synthetic strategy towards compounds containing phenol modification of navarixin (2)

Due to time constraints, the decision was made to pursue the synthesis of five selected ligands (**45b-d**, and **45f-g**). Among these, ligands **45b** and **45c** were prioritized due to their perceived ease of synthesis, representing straightforward modifications of the phenol moiety of lead, navarixin (**2**) - essentially entailing the introduction of a methyl group and an acetate protection, respectively.

In a similar fashion to the synthesis described in **Section 3.5.2**, the strategy was to obtain the final *ortho*-substituted benzamides *via* a 3-step synthetic route from the corresponding 3-nitro benzamides (**47a-d** and **47g**) (**Scheme 4-1**). This involves the palladium-catalysed nitro reduction of the *ortho*-substituted 3-nitro benzamide, to the corresponding aniline. Sequential nucleophilic substitution of diethyl squarate, first with the anilines **48a-d** and **48g** to form the corresponding squaric acid monoamide monoester, and then with the (*R*)-1-(5-methylfuran-2-yl)propan-1-amine to give the desired squaramide products **45b-d**, **45g** and **46a**.

Scheme 4-1 Proposed synthesis of intracellular antagonists with substituted benzamides from 3-nitro benzamide precursors **47a-c** and **47g.**

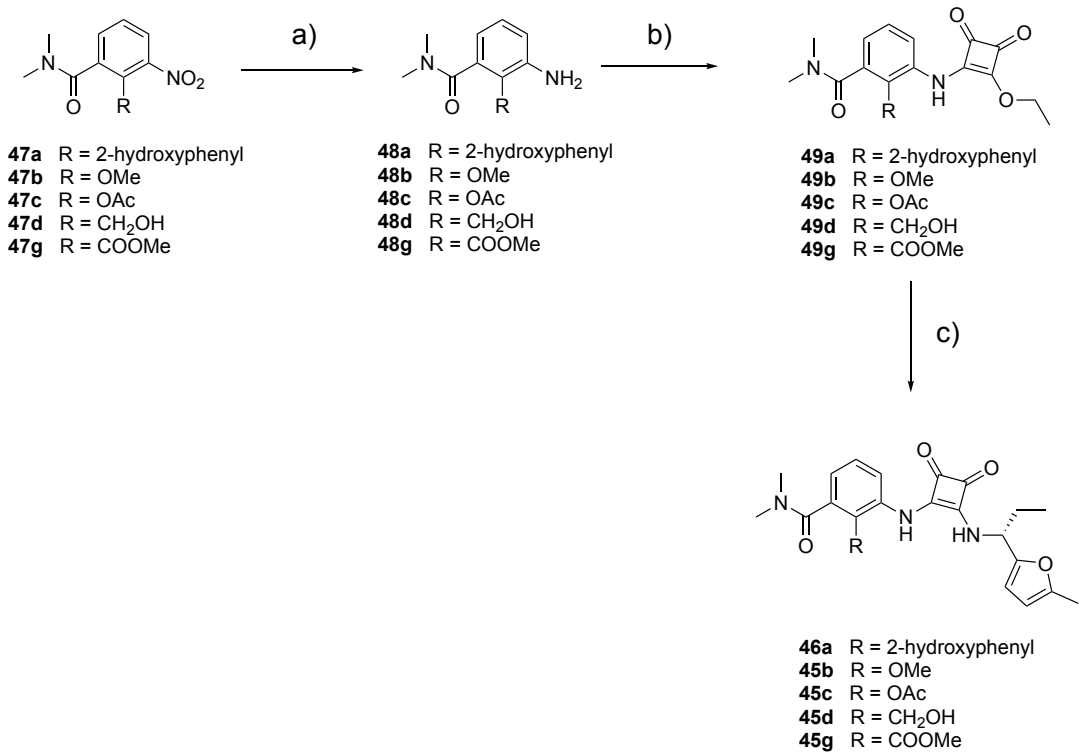

Reagents and conditions: (a) H_2, 10% Pd/C, EtOH, rt; (b) 3,4-diethoxycyclobut-3-ene-1,2-dione, EtOH, rt; (C) (*R*)-1-(5-methylfuran-2-yl)propan-1-amine hydrochloride, EtOH, DIPEA, rt.

4.3.2 Attempted synthesis towards 2'-hydroxy-*N*,*N*-dimethyl-6-nitro-[1,1'-biphenyl]-2-carboxamide (47a)

Efforts to synthesize 2'-hydroxy-*N,N*-dimethyl-6-nitro-[1,1'-biphenyl]-2-carboxamide (**47a**) initially involved utilizing commercially accessible aryl bromide (**50**) and (2-hydroxyphenyl)boronic acid in a Suzuki-Miyaura cross-coupling reaction. This reaction was anticipated to produce intermediate **51**, which could subsequently undergo amide coupling with dimethylamine to yield the desired product **47a** (**Scheme 4-2**). Several reaction conditions were attempted for the Suzuki-Miyaura cross-coupling, which are summarised in **Table 4-4**. Initially, a palladium on carbon catalyst was employed as an economical and readily removable option for the cross-coupling reaction. Solvent systems comprised of a 1:1 mixture of methanol and water, as well as ethanol and water, were

investigated. Furthermore, variations in temperature were explored, with experiments conducted both at room temperature and under reflux conditions. Despite these efforts, none of the tested conditions led to product formation. Analysis *via* TLC and LCMS revealed that the starting material remained unaltered throughout the reactions. This was recovered after filtration to remove the heterogenous catalyst. There are examples of Suzuki-Miyaura reactions demonstrating the use and potential benefits of palladium on carbon as a heterogenous catalysts.[400-403] However, the choice between homogeneous and heterogeneous catalysts for Suzuki-Miyaura reactions remains a topic of debate.[219,404,405] While heterogeneous catalysts, such as palladium on carbon, may offer certain practical advantages such as ease of catalyst recovery and recyclability, others argue that homogeneous catalysts are preferred for their potentially superior kinetics and selectivity in certain reaction conditions.[405]

Scheme 4-2 Attempted synthesis towards 2'-hydroxy-*N,N*-dimethyl-6-nitro-[1,1'-biphenyl]-2-carboxamide (**47a**)

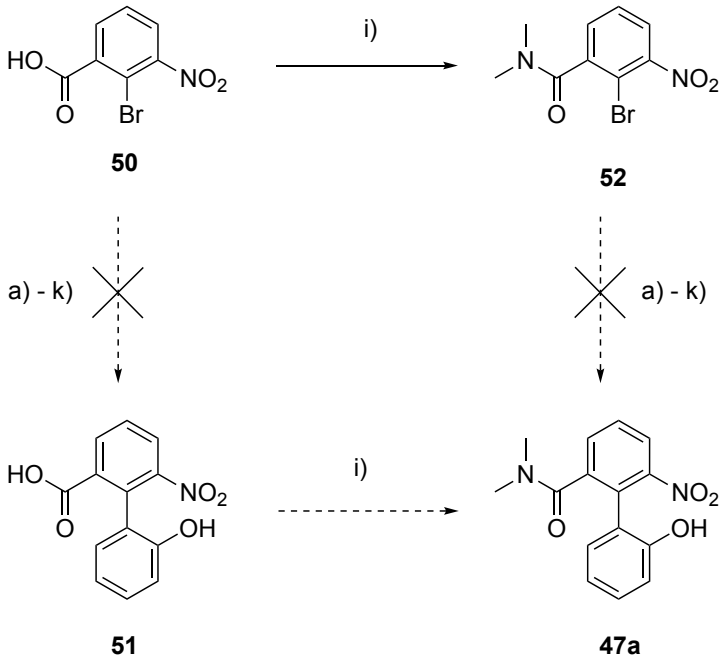

Reagents and conditions: (a) – (k) (2-hydroxyphenyl)boronic acid, conditions for catalyst, solvent, base(s), and temperature used are summarised in Table 4-4 (l) i) oxalyl chloride, DMF, dichloromethane (DCM) rt; ii) 2M dimethylamine in THF, DIPEA, DCM, 0 °C – rt, 85%.

Coupling of di-ortho-substituted aryl bromides using homogenous catalysts, tetrakis(triphenylphosphine)palladium(0) ($Pd(PPh_3)_4$) or

bis(triphenylphosphine)palladium(II) dichloride ($PdCl_2(PPh_3)_2$) have been demonstrated in moderate to high yielding reactions.[406-408] Several reaction conditions were attempted using these literature procedures. Unfortunately, application of these methods gave seemingly similar reaction profiles as those using Pd(0)/C catalyst with no reaction proceeding, confirmed by TLC and LCMS.

As examples of cross coupling have been demonstrated between sterically hindered di-*ortho*-substituted aryl halides and 2-substituted aryl boronic acids[409,410], It was suspected there may be a significant electronic effect on the C-Br bond hampering oxidative addition to the palladium catalyst.[402] To address this issue, efforts were undertaken to perform the cross coupling after the introduction of the dimethyl amide **52**. The expected lower-electron-withdrawing nature of the amide functionality would increase the electron density around the carbon atom of the C-Br bond. However, it should also be considered that the dimethyl amide may also impart a significant steric effect on the system. Unfortunately, reattempting the coupling conditions detailed in **Table 4-2** with benzamide **52** did not have the desired outcome, with no consumption of the starting material observed by TLC and LCMS in the same manner observed for the attempted cross-coupling of **50**.

Table 4-4 Conditions attempted for a) – k) in **Scheme 4-2** for the Suzuki Miyaura cross coupling of aryl bromides **50** and **52** using (2-hydroxyphenyl)boronic acid.

Method	Catalyst	Solvent	Base	Temperature
a	Pd/C	1:1 MeOH:water	4 eq K_2CO_3	25 °C
b	Pd/C	1:1 MeOH:water	4 eq K_2CO_3	reflux
c	Pd/C	1:1 EtOH:water	4 eq K_2CO_3	25 °C
d	Pd/C	1:1 EtOH:water	4 eq K_2CO_3	reflux
e	$Pd(PPh_3)_4$	1:1 MeOH:water	4 eq K_2CO_3	50 °C
f	$Pd(PPh_3)_4$	1:1 MeOH:water	4 eq K_2CO_3	reflux
g	$Pd(PPh_3)_4$	1:1 MeOH:water	4 eq K_2CO_3 + Et_3N	50 °C
h	$Pd(PPh_3)_4$	1:1 MeOH:water	4 eq K_2CO_3 + Et_3N	reflux
i	$Pd(PPh_3)_4$	EtOH	4 eq K_2CO_3	50 °C
j	$Pd(PPh_3)_4$	EtOH	4 eq K_2CO_3	reflux
k	$Pd(PPh_3)_4$	1,2-dimethoxyethane	4 eq K_2CO_3 + Et_3N	reflux

4.3.3 Route towards phenol protected aniline derivatives

2-Hydroxy-*N*,*N*-dimethyl-3-aminobenzamide **53** was synthesised from **31**, according to the method described in the synthesis of navarixin (**2**).[248] **53** was then methylated *via* base mediated alkylation using iodomethane affording 2-methoxy-*N*,*N*-dimethyl-3-nitrobenzamide (**47b**). This reaction proceeded quickly in high yields and did not require further purification.

Alternatively, **47c** was synthesised from **53** *via* a base-mediated acetylation using acetic anhydride. This reaction initially gave moderate yields of ~50 %, requiring purification to remove starting material, as no further reaction progression was observed after 24 hours. The reaction was improved with use of a catalytic amount of 4-dimethylaminopyridine

(DMAP), as per literature examples.[411-413] This led to full consumption of the starting material after 18 hr, observed by TLC giving higher yielding reactions (77%) with products that did not require purification after workup. Nitro reduction of **47b** and **47c** by methods previously described in **Section 3.5.2** gave the desired anilines **47b** and **47c**.

Scheme 4-3 Proposed synthesis of O-substituted 3-amino benzamides **48b** and **48c** as precursors towards **45b** and **45c**.

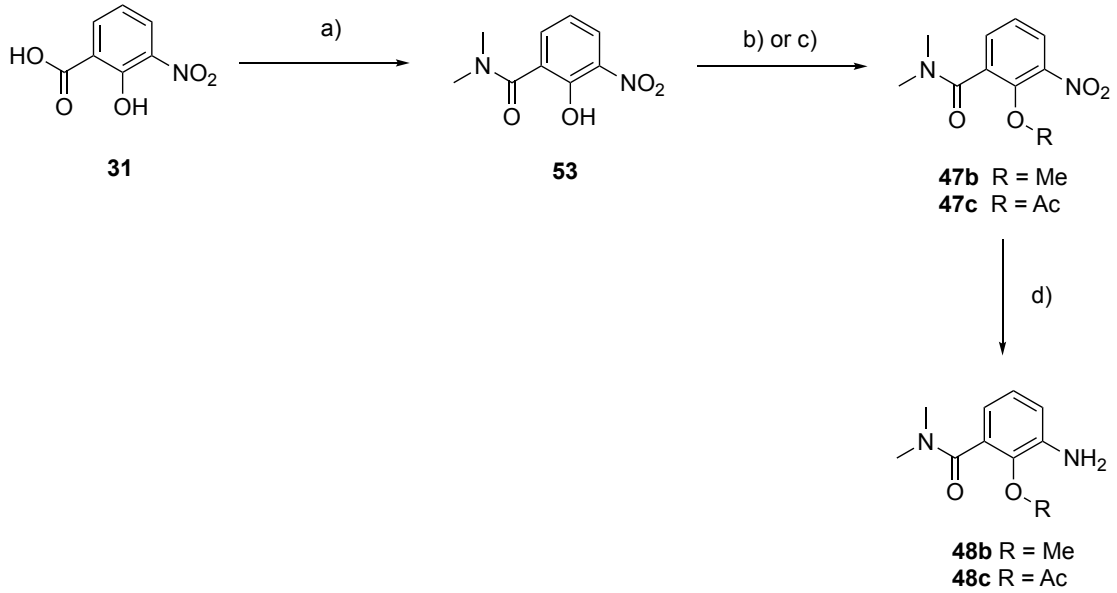

Reagents and conditions: (a) i) oxalyl chloride, DMF, dichloromethane (DCM) rt; ii) 2M dimethylamine in THF, DIPEA, DCM, 0 ˚C – rt, 81%; (b) K_2CO_3, iodomethane, acetone, 83%; (c) acetic anhydride, TEA, DMAP, DCM; rt, 77%; (d) H_2, 10% Pd/C, EtOH.

Attempts to synthesize squaric acid monoamide monoester **49b** using the conditions outlined in **Scheme 4-2** resulted in two products: a minor product **49b** and a major product **54**. While the minor product **49b** corresponds to the desired squaric acid monoamide monoester, the major product **54** arises from the double substitution of the aniline to the squarate, occurring in approximately a 3:1 ratio compared to the single substitution product. As previously reasoned in **Chapter 3**, the formation of the double substitution product in the reaction between *ortho*-hydroxy anilines and diethyl squarate is hindered, due to deactivation of the squaric acid monoester monoamide, which subsequently impedes secondary attack of the *ortho*-hydroxy aniline. This deactivation is attributed to the reduced electronegativity of the nitrogen of the amino benzamide moiety in the squaric acid monoester monoamide **49b**, compared to the oxygen of the ethoxy moiety of diethylsquarate. Additionally, there is increased steric bulk from the amino benzamide

which could contribute to hindering further nucleophilic attack of the aniline. Interestingly, the expected mild increase in nucleophilicity of the aniline **48b** containing an *ortho*-methoxy, compared to the *ortho*-hydroxy group, appears to overcome this deactivation. The difference in nucleophilicity appears to promote double substitution over single substitution in the reaction conditions, leading to the observed predominance of the major product . Major product was isolated through reverse phase flash column chromatography, for functional screening, as a compound of interest, due to it containing the diaryl squaramide pharmacophore described for CXCR2 IAMs.[346,347] Reaction of the minor squaric acid monoamide monoester product **49b** with (*R*)-1-(5-methylfuran-2-yl)propan-1-amine hydrochloride gave the desired squaramide **45b**.

Scheme 4-4 Synthesis of (R)-2-methoxy-*N,N*-dimethyl-3-((2-((1-(5-methylfuran-2-yl)propyl)amino)-3,4-dioxocyclobut-1-en-1-yl)amino)benzamide (**45b**).

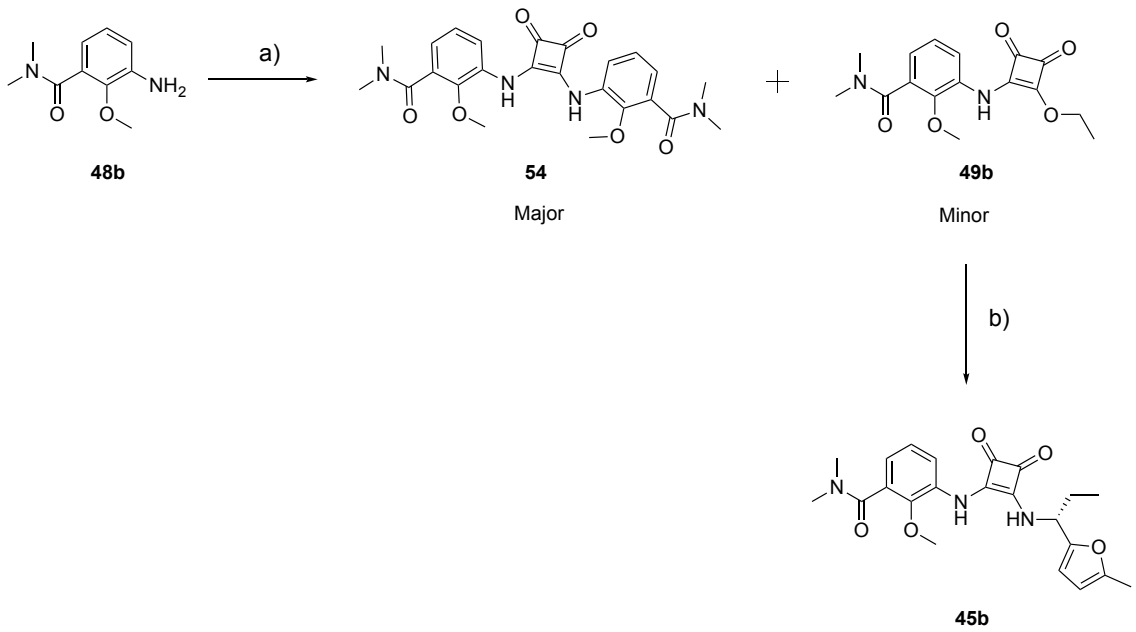

Reagents and conditions: (a) 3,4-diethoxycyclobut-3-ene-1,2-dione, EtOH, rt, 3%; (b) (*R*)-1-(5-methylfuran-2-yl)propan-1-amine hydrochloride, EtOH, DIPEA, rt, 14%.

Attempts to form squaric acid monoester monoamide **49c** from **48c** were unsuccessful when using the previously described method for **49b**, involving room temperature stirring in ethanol, which resulted in unchanged starting material (**Scheme 4-5**). Heating the reaction mixture to boiling point did not have any effect on the progression of the reaction, observed by TLC analysis.[414] The opposite electronic effect to the methoxy analogue is evident, whereby the electron-withdrawing effect of the acetate diminishes the reactivity

of the aniline towards the necessary nucleophilic attack for the reaction. The addition of zinc triflate ($Zn(OTf)_3$) as a catalyst aimed to enhance the reactivity of diethyl squarate. $Zn(OTf)_3$ is known to act as a Lewis acid catalyst, capable of coordinating with electron-rich species and facilitating bond formation.[415-417] By introducing $Zn(OTf)_3$ as a catalyst, it is anticipated that it could coordinate with the electron-rich carbonyls of diethyl squarate, thereby activating it towards nucleophilic attack. Previous examples have demonstrated the effectiveness of $Zn(OTf)_3$ in facilitating the formation of squaric acid monoamide monoesters from squarate and aniline species, providing support for this rationale.[418-420]

Addition of a catalytic amount of $Zn(OTf)_3$ and overnight room temperature stirring did not yield the desired product **49c**, but instead gave double substitution product **55** and **56**, corresponding to 3-amino-2-hydroxy-*N*,*N*-dimethylbenzamide (**Scheme 4-5**). Perhaps unsurprisingly, $Zn(OTf)_3$ appears to catalyse the hydrolysis of the phenyl acetate moiety present in aniline **48c**. The Lewis acidic nature of $Zn(OTf)_3$ likely promotes nucleophilic attack by water or ethanol on the acetate group, leading to its hydrolysis. Although the desired product **49c** was not obtained, the rationale for the addition of $Zn(OTf)_3$ did appear to be correct by activating nucleophilic attack towards diethyl squarate, evidenced by the formation of double substitution product **55**, confirmed by LCMS (*m/z* = 439.0, expected *m/z* = 439.2) and ^{1}H NMR. This was unprecedented in previously conducted additions of *ortho*-hydroxy anilines (**Scheme 3-1** and **Scheme 3-2**).

Scheme 4-5 Synthetic route towards (R)-2-(dimethylcarbamoyl)-6-((2-((1-(5-methylfuran-2-yl)propyl)amino)-3,4-dioxocyclobut-1-en-1-yl)amino)phenyl acetate (**45c**)

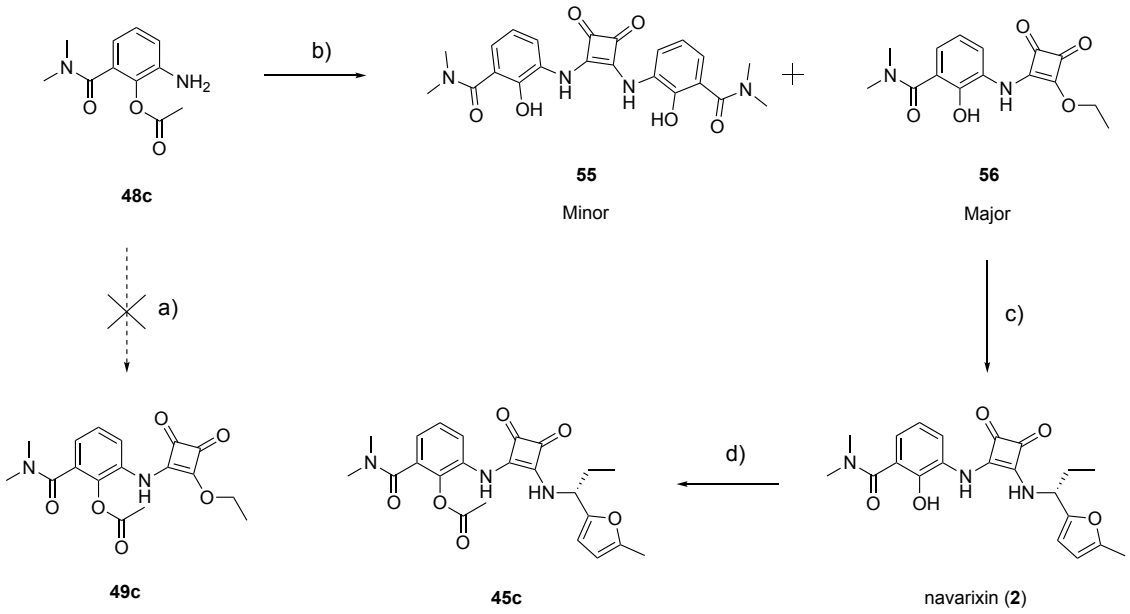

Reagents and conditions: (a) 3,4-diethoxycyclobut-3-ene-1,2-dione, EtOH, rt, 6 days (b) ,4-diethoxycyclobut-3-ene-1,2-dione, $Zn(OTf)_2$, EtOH, rt, 24 hr, 49%; (c) (*R*)-1-(5-methylfuran-2-yl)propan-1-amine hydrochloride, EtOH, DIPEA, rt, 48 hr, 18%; (d) acetic anhydride, DMAP, TEA, DCM, 16 hr, rt, 27%.

Due to time constraints, further optimization of the reaction was not feasible. Therefore, an alternative route was taken by which the squaric acid monoamide monoester **56** was taken forward in a reaction to yield navarixin (**2**).[248] Subsequent acetylation of navarixin (**2**), using organic base and DMAP catalysed esterification conditions described in **Scheme 4-5** afforded the desired squaramide **45c.**

4.3.4 Ring Opening of 4-Nitroisobenzofuran-1,3-dione

2-(Methoxycarbonyl)-3-nitrobenzoic acid (**58)** was produced through the reflux of commercially available 4-nitroisobenzofuran-1,3-dione (**57**) in methanol (**Scheme 4-6**). The reaction proceeds through regioselective nucleophilic attack on the carbonyl *ortho* to the nitro group.[421,422] This regioselectivity is driven through the strong electron-withdrawing effect of the nitro group on the *ortho*-carbon, creating a relatively larger partial positive charge compared to the *meta*-carbonyl. Initially, formation of the desired

regioisomer **58** occurred in 9:1 ratio compared to 2-(methoxycarbonyl)-6-nitrobenzoic acid **59** (**Figure 4-4**). However, subsequent recrystallisation from water removed **59** from the mixture and giving **58** in high yield as a pure white solid. Regioselectivity could not be confirmed through 2D NMR analysis, due to the distance of the methyl from relevant carbon or hydrogen atoms on the aromatic ring. Therefore, confirmation of the product was established with comparison to previous literature examples using ^{1}H and ^{13}C NMR spectra.[422]

Scheme 4-6 Ring opening of 4-nitroisobenzofuran-1,3-dione towards 2-(methoxycarbonyl)-3-nitrobenzoic acid (**58**)

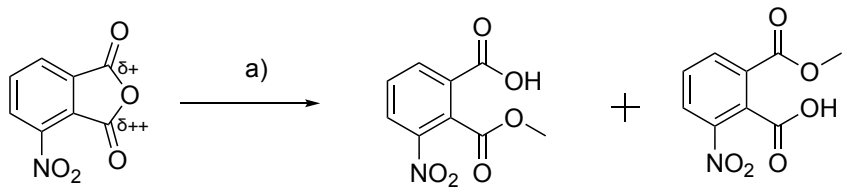

57 **58** **59**

Reagents and conditions: (a) MeOH, reflux, 18 hr, 78% (**58**).

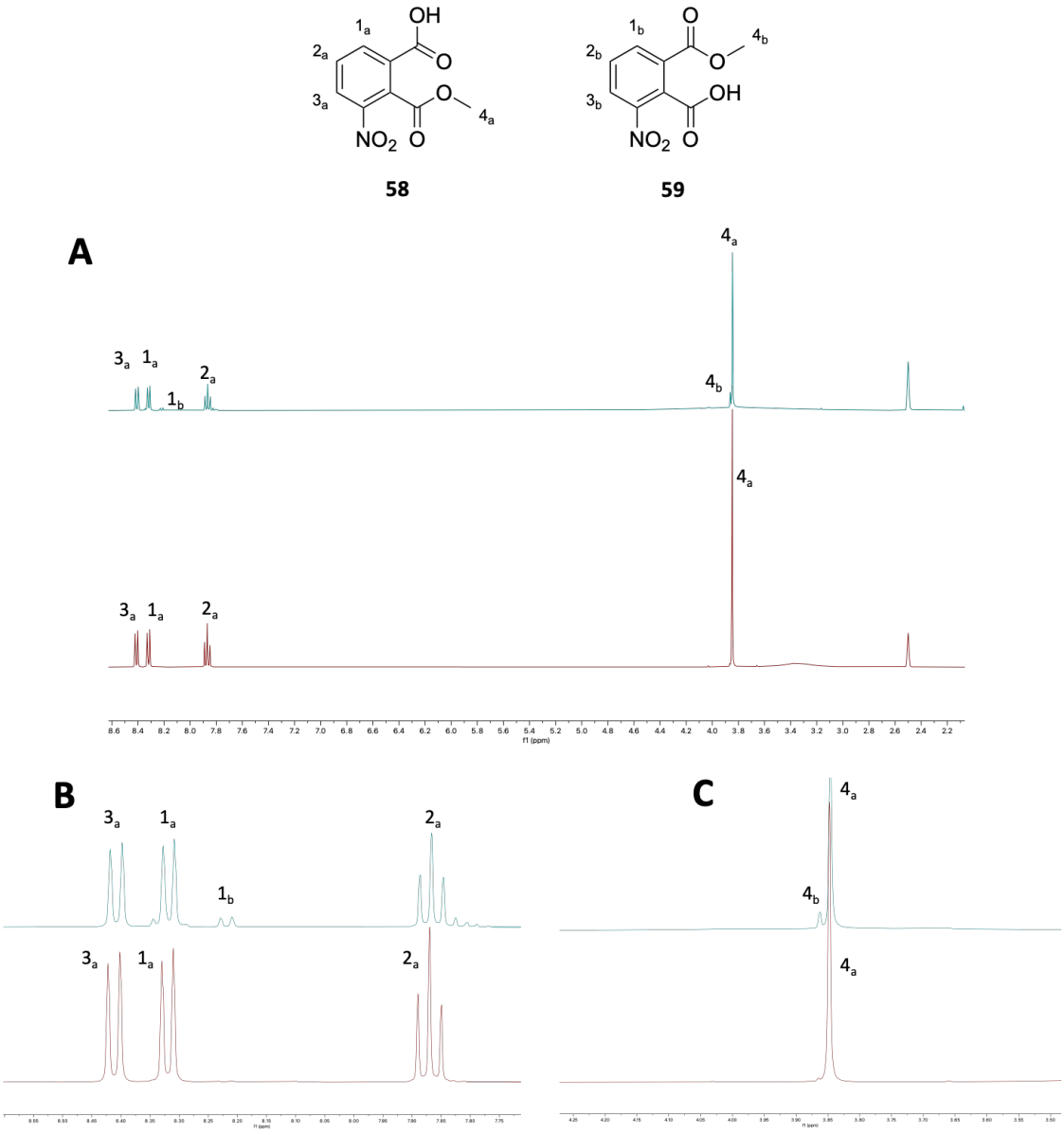

Figure 4-4 Stacked ^{1}H NMR of **58** pre (blue spectra) and post (red spectra) recrystallisation from water. (A) Full spectrum displayed from 8.6 ppm to 2.2 ppm. (B) Magnification of the aromatic region displayed from 8.6 ppm to 7.7 ppm. (C) Magnification of the aliphatic region displayed from 4.3 ppm to 3.5 ppm, showing the methyl peak originating from the methyl ester. The structure of the desired product **58** and regioisomer **59** are displayed for reference. Peaks labelled corresponding to the ^{1}H signals on **58** and **59**.

4.3.5 Problematic reduction towards 2-(hydroxymethyl)-*N*,*N*-dimethyl-3-nitrobenzamide (47d)

Initial pilot scale reduction of ester **47g** was attempted using $LiAlH_4$, according to the method described by Ho *et al*.[423] for the reduction of aryl ester in presence of an amide species (**Scheme 4-7**).[423] Unfortunately, attempts to reduce the aryl ester **47g** utilising this method were unsuccessful at 0 °C and 25 °C, showing no progress after 48 hours (**Table 4-4**). Various conditions were then attempted using 1M diisobutylaluminium hydride (DIBAL-H), summarised in **Table 4-4**.[424-426] In all cases, the starting material was consumed within the first hour of the rection with three main peaks observed by LCMS during this investigation (**Scheme 4-8**). A peak at ~ 2.1 min with *m/z* 223.0 corresponding to the mass of the aldehyde, 2-formyl-*N*,*N*-dimethyl-3-nitrobenzamide **61** (expected *m/z* = 223.0) was observed when using THF and DCM as a solvent. When using diethyl ether (DEE) and DCM, a peak at ~ 2.8 min was observed, however no discernible *m/z* could be distinguished for this peak. The *m/z* of 225.1 corresponding to the desired alcohol **47d** (expected m/z = 225.1) was observed as a broad peak with retention time ~ 0.5 min. The change in retention time between the aryl ester **47g** at ~2.5 min, and the presumed alcohol product **47d** is quite stark, speaking to the drastic increase in polarity of this molecule. Unfortunately, the product could not be isolated due to difficulties in extracting the presumed product from the aqueous phase after quenching the reaction with water. Attempts to extract the product into DCM, EtOAc, DEE, and *n*-octanol were unsuccessful. Concentration and drying of the crude mixture under reduced pressure gave a white solid, however subsequent ^{1}H NMR were inconclusive to confirm the formation of the desired alcohol **47d**, due to the presence of a substantial water peak and multiple impurities.

Scheme 4-7 Attempted synthetic route towards 2-(hydroxymethyl)-*N,N*-dimethyl-3-nitrobenzamide **47d**

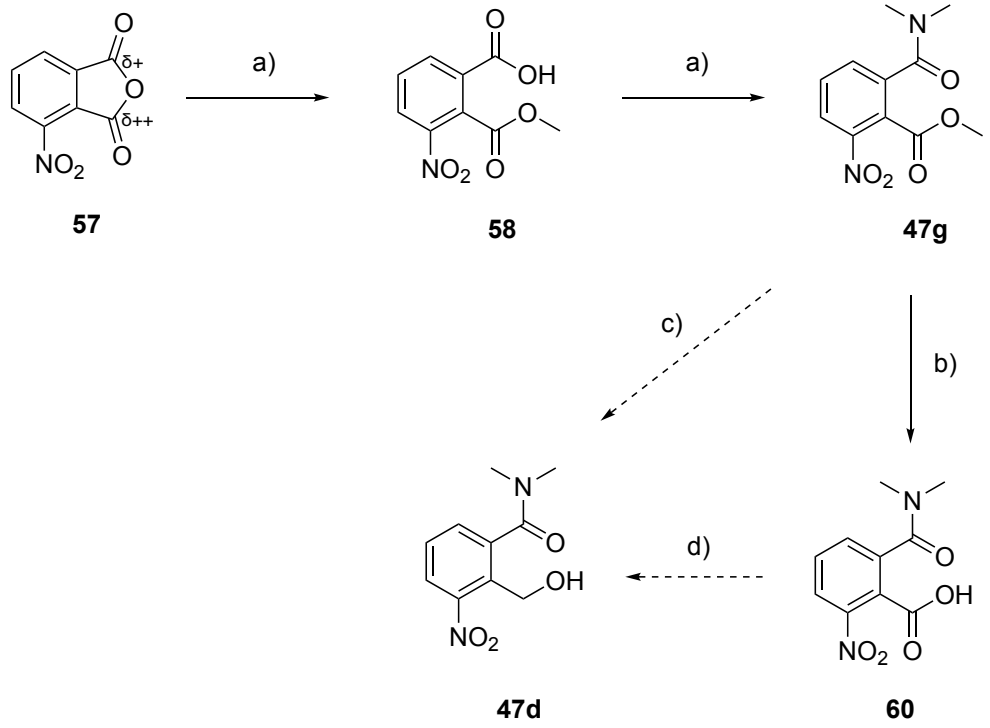

Reagents and conditions: (a) i) oxalyl chloride, DMF, DCM, rt, 18 hr, 66%; ii) 2M dimethylamine in THF, DCM, DIPEA, DCM, 0 ˚C, 2 hr; (b) 2M NaOH, rt, 3 hr, 84%; (c) conditions summarised in **Table 4-5**; d) 1M DIBAL-H, DCM, -40 ˚C, 2 hr.

As an alternative approach to obtaining the desired product **47d**, the ester **47g** was subjected to hydrolysis under basic conditions to yield the corresponding carboxylic acid **60**, which could subsequently be evaluated for potential reduction. This strategy aimed to explore the potential reactivity of the carboxylic acid functional group of **60** towards reduction, compared to the corresponding methyl ester **47g**, under similar reaction conditions. Additionally, reducing the carboxylic acid directly to the alcohol would bypass the formation of the aldehyde intermediate, which was observed in some cases during the ester reduction using 1M DIBAL-H as a reducing agent (**Table 4-5**). However, attempts to reduce the carboxylic acid with 1M DIBAL-H in DCM at -40 ˚C were also unsuccessful, yielding similar crude mixtures as the previous reduction of ester **47g**.

Table 4-5 Attempted conditions for the selective ester reduction of methyl 2-(dimethylcarbamoyl)-6-nitrobenzoate **47g**. Peak observed at t_R = 2.1 min with m/z = 223.0 corresponding to the aldehyde product, 2-formyl-*N,N*-dimethyl-3-nitrobenzamide **61** and Peak observed at t_R = 0.5 min with m/z = 225.1 corresponding to the desired alcohol **47d.**

Reducing agent	Equivalents of reducing agent	Solvent	Temperature (˚C)	Time (hours)	Result
2M $LiAlH_4$ in THF	3.0	THF	0	6	No progression
2M $LiAlH_4$ in THF	3.0	THF	25	48	No progression
1M DIBAL-H in toluene	2.4	THF	-78	2	*m/z* 223 peak at 2.1 min *m/z* 225 peak at 0.5 min
1M DIBAL-H in toluene	2.4	DEE	-78	1	Peak at 2.8 min *m/z* 225 peak at 0.4 min
1M DIBAL-H in toluene	2.4	DCM	-78	2	*m/z* 223 peak at 2.0 min peak at 2.8 min
1M DIBAL-H in toluene	2.4	DCM	-40	1	*m/z* 225 at 0.5 min

Scheme 4-8 DIBAL-H reduction of ester **47g** resulting in 2 discernible products by LCMS. Peak observed at t_R = 2.1 min with m/z = 223.0 corresponding to the aldehyde product, 2-formyl-*N,N*-dimethyl-3-nitrobenzamide **61** and peak observed at t_R = 0.5 min with m/z = 225.1 corresponding to the desired alcohol **47d**.

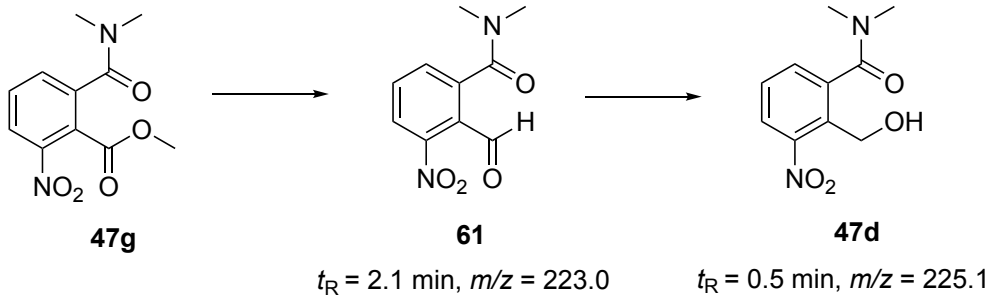

4.4 Pharmacology

4.4.1 Functional screening of modified phenol analogues *via* the whole cell CXCR1 and CXCR2 NanoBiT complementation assay

In a similar manner to **Section 3.6.4**, the NanoBiT complementation assay was used to determine NAM inhibition of 10 nM $CXCL8_{28-99}$ stimulated β-arrestin2 recruitment for **45g, 45b, 45c** and **54**, *via* activation of either CXCR1 or CXCR2 receptors. The data shown in **Figure 4-5** displays the concentration inhibition curves generated for end point luminescence when CXCR1 / CXCR2 β-arrestin2 NanoBiT cell lines were treated with **45b**, **45c**, **45g** and at 37 ˚C for 30 minutes, followed by 10 nM $CXCL8_{28-99}$ stimulation for 30 min. The pIC_{50} values calculated from the response curves are summarised in **Table 4-6**.

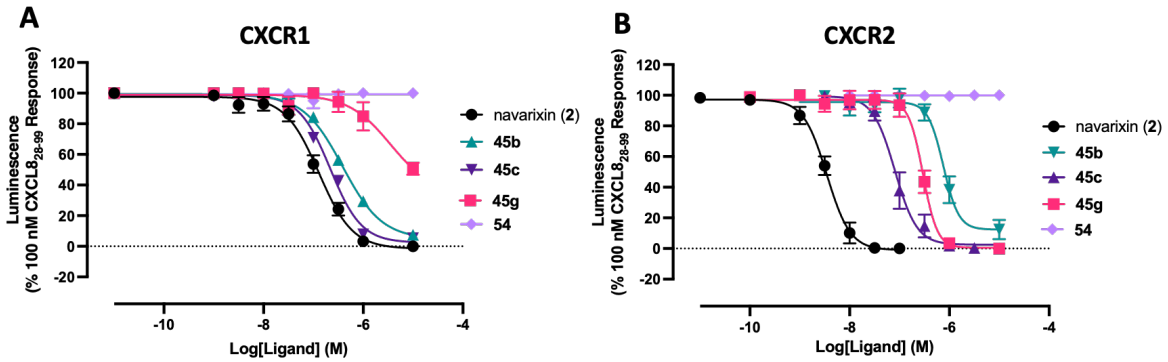

Figure 4-5 Concentration inhibition curves for navarixin (**2**), **45g, 45b, 45c** and **54** demonstrating the effect of NAMs on 10 nM CXCL8$_{28-99}$ stimulated β-arrestin2-SmBit recruitment to CXCR1-LgBiT and CXCR2-LgBiT expressed in HEK293 cell lines. (A) **45g, 45b, 45c** and **54** compared to navarixin (**2**) in the CXCR1 assay. (B) **45g, 45b, 45c** and **54** compared to navarixin (**2**) against in the CXCR2 assay. (C) Data represent pooled data (mean ± SEM), normalised to the control, 10 nM CXCL8$_{28-99}$ response, from n = 3 individual experiments performed in triplicate.

Compound **54,** a by-product from the addition of 3-amino-2-methoxy-*N*,*N*-dimethylbenzamide (**56b**) to diethyl squarate showed no discernible ability to inhibit CXCL8 dependent β-arrestin2 recruitment to either receptor, up to 10 μM. These results suggest that compound **54** is inactive at CXCR1 and was determined not to be relevant for further investigation.

Table 4-6 Functional inhibition of $CXCL8_{28-99}$ mediated β-arresti2-SmBiT recruitment in CXCR1-LgBit and CXCR2-LgBiT for compounds **45b**, **45c**, **45g**, and **54** compared to lead compound, navarixin (**2**). Data shown are mean ± SEM from n = 3 individual experiments.

Compound	CXCR1 pIC_{50}	CXCR2 pIC_{50}	Selectivity IC_{50} (CXCR2/ CXCR1)
navarixin (**2**)	6.96 ± 0.13	8.68 ± 0.13	52
45g	<5.0	6.53 ± 0.19	>33
45b	6.41 ± 0.18	6.14 ± 0.27	0.5
45c	6.66 ± 0.18	7.09 ± 0.27	2.7
54	ND	ND	ND

Compounds **45g, 45b** and **45c** represent a set of navarixin (**2**) analogues featuring modified phenol moieties. **45g**, **45b** and **45c** retained sub 10 μM inhibitory activity in CXCR2, allowing for calculation of pIC_{50} values. **45g** displayed pIC_{50} of 6.53 ± 0.19 in CXCR2 pointing to some retained potency in CXCR2, albeit with a 100-fold reduction compared to potency displayed by the lead, navarixin (**2**). In contrast, **45g** was unable to fully inhibit arrestin recruitment in CXCR1 at concentrations up to 10 μM (<50% inhibition). As such, only a maximum limit for the **45g** CXCR1 pIC_{50} estimate could be provided – suggesting that while much less potent, **45g** retained similar selectivity for CXCR2 over CXCR1 (**Table 4-6**). In CXCR1, inhibition of arrestin recruitment for **45b** and **45c** displayed similar 3–fold reduction compared to navarixin (**2**) with pIC_{50} 6.41 ± 0.18 and 6.66 ± 0.18 respectively. In CXCR2, the analogues showed inhibitory activities in order of potency **45c** > **45g** > **45b** (Table 4-5). The methoxy analogue **45b** displayed the lowest potency in CXCR2, with a 350–fold reduction in potency compared to navarixin (**2**). The reduced activity is comparable to the effect of introducing a methoxy observed by Aki *et al.*[344] In contrast, the introduction of the methyl group in **45b** was well tolerated in CXCR1 with only a 3-fold reduction in potency. Both **45b** and **45c** show reduced CXCR2 selectivity

over CXCR1 from 52-fold displayed by navarixin (**2**) to 0.5 and 2.7-fold reductions respectively. In fact, **45b** demonstrated a 2-fold selectivity for CXCR1 over CXCR2, marking the first compound of this work with significant CXCR1 selectivity, albeit within a 3-fold change. This suggests that the binding interactions of the phenol or the electron-withdrawing effect of the oxygen at position 2 of the benzamide on phenyl ring are crucial for retaining potency in CXCR2, which are not as evident in CXCR1 in this functional assay.

Interestingly the increased steric bulk introduced by the acetate **45c** (pIC_{50} = 7.09 ± 0.27) was better tolerated in CXCR2 than the methoxy **45b** analogue (pIC_{50} = 6.14 ± 0.27), showing a 10-fold higher potency. Although this increase in steric bulk was tolerated in CXCR1, the relative difference in potency was lower with pIC_{50} values of 6.66 ± 0.18 and 6.41 ± 0.18 for the acetate and methoxy analogues **45c** and **45b** respectively. This may suggest that the carbonyl of **45c** could be contributing to hydrogen bonding interactions relating to $K320^{8.49}$ which may not be possible in CXCR1 due to the increased distance of $N311^{8.49}$ to the ligand observed in the models in previous docking studies (**4.2.2**).

Indications that the phenolate anion is important for binding in both receptors can be observed in the comparison of structural isomers **45g** and **45c**. Whilst both contain increased steric bulk in the phenol region, the acetate contains an oxygen atom *ortho* to the benzamide. This suggests that an oxygen atom at this position not only facilitates key binding interactions, but also suggests it has a localised effect on the aromatic ring and the adjacent amide substituents.

4.4.2 Generation of stable cell lines expressing single point mutant CXCR1 and CXCR2 receptors

Site-directed single point mutations were introduced into CXCR1 ($N311A^{8.49}$) and CXCR2 receptors ($K320A^{8.49}$) to provide insights into the properties and roles significant in receptor-ligand binding. Observations from *in silico* receptor modelling in **Chapter 2** identified the singular non-conserved residue within 3 Å of navarixin (**2**) when bound to the IAM binding site of CXCR1 and CXCR2, corresponding to $N311^{8.49}$ in CXCR1 and $K320^{8.49}$ in CXCR2. These mutations served as a secondary strategy to elucidate the contribution of this residue to IAM binding, aiming to analyse the effect of mutating this residue to the amino acid with methyl side chain only (Ala) in each receptor. Stable

transfection of HEK293T cells, already expressing β-arrestin2-SmBiT with DNA constructs containing CXCR1N311A$^{8.49}$ and CXCR2K320A$^{8.49}$-LgBiT receptors was accomplished using lipofectamine 3000 reagent and OptiMEM. Subsequent selection for the mutant receptor expression in geneticin (G418) enriched media, resulted in HEK293T cells stably expressing the desired mutant receptor-LgBiT and arrestin SmBiT sensor for NanoBiT assays as previously described.

4.4.3 CXCR2 K320A$^{8.49}$ and CXCR1 N311A$^{8.49}$ mutations do not alter the potency of CXCL8 $_{28-99}$

The potency of the CXCL8$_{28-99}$ towards β-arrestin2-SmBiT recruitment was assessed using the NanoBiT complementation assay (previously described in **Chapter 3**), to establish whether the introduced mutations had any adverse effect on receptor activation by agonists. **Figure 4-6** displays the CXCL8$_{28-99}$ response curves obtained for CXCR1N311A$^{8.49}$ and CXCR2K320A$^{8.49}$ cell lines. EC_{50} values for both mutants were within 2-fold of the wild type variants **Table 4-7**, indicating that receptor function for CXCL8$_{28-99}$ mediated β-arrestin2 recruitment was retained for the mutant cell lines. The limited change in CXCL8 response after CXCR2K320A$^{8.49}$ mutation is corroborated by literature reports by Salchow *et al*.[134] in a [^{35}S]GTPγS binding assay.[134] For CXCR1 pEC_{80} values of 7.9 ± 0.7 and 8.0 ± 0.3 for the wild type and mutant, respectively. The pEC_{80} values for CXCR2 were determined to be 8.0 ± 0.4 and 8.3 ± 0.4 for the wild type and mutants, respectively. As pEC_{80} values were within 3-fold change from the wild type receptors, 10 nM CXCL8$_{29-99}$ was retained as a comparable stimulus for the mutant receptors in the NanoBiT IC_{50} assay, as described in **Chapter 3** for assessment at wild type CXCR1 and CXC2.

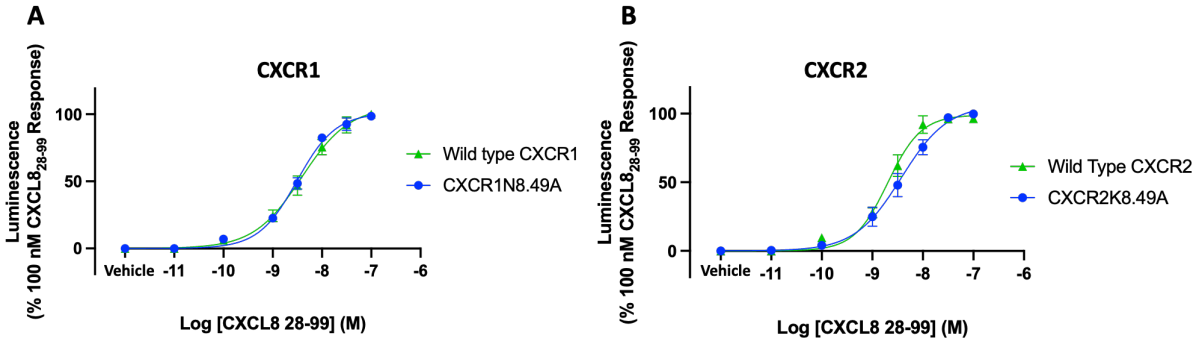

Figure 4-6 CXCL8$_{28-99}$ Concentration dependent response curves for mutant receptor cell lines with wild type data shown for comparison (A) CXCR1N311A$^{8.49}$ and wild type CXCR1 (B) CXCR2K320A$^{8.49}$and wild type CXCR2. Data shown are from pooled individual experiments (mean ± SEM) of n = 5 for both receptors, normalised to the maximal control CXCL8$_{28-99}$ response at each receptor, with each experiment performed in duplicate. Cells were pre-treated with assay buffer for 1 h at 37 °C, followed by stimulation by CXCL8$_{28-99}$ and luminescence from complemented nanoluciferase was measured after 30 min period.

Table 4-7 Effect of CXCR1 and CXCR2 receptor mutations on pEC$_{50}$ on CXCL8$_{28-99}$ dependent recruitment of β-arrestin2. Data shown are mean ± SEM from n = 5 individual experiments.

Receptor	CXCL8$_{28-99}$ pEC$_{50}$ (mean ± SEM)	Wild-type EC$_{50}$: Mutant fold EC$_{50}$ shift	Hillslope
CXCR1 wild type	8.4 ± 0.2		0.9 ± 0.3
CXCR1N311A$^{8.49}$	8.5 ± 0.1	1.2	1.1 ± 0.3
CXCR2 wild type	8.7 ± 0.1		1.3 ± 0.3
CXCR2K320A$^{8.49}$	8.4 ± 0.2	2.0	1.0 ± 0.3

4.4.4 Effect of CXCR2 K320A$^{8.49}$ and CXCR1 N311A$^{8.49}$ mutations on NAM potency

In addition to designing and synthesizing compounds to target this non-conserved residue, the impact of introducing Ala site point mutations (CXCR1N311A$^{8.49}$ and CXCR2K320A$^{8.49}$) in the binding sites of each receptor on CXCL8$_{28-99}$ mediated β-arrestin2 recruitment was investigated. The inhibition response curves for navarixin (**2**), **45a**, **45b**, **45g** and **47** against CXCR1N311A$^{8.49}$ and CXCR2K320A$^{8.49}$ expressing HEK293 cells are displayed in **Figure 4-7** and the pIC$_{50}$ values calculated are summarised in **Table 4-8**. Data were taken from the luminescence response 30 min after 10 nM CXCL8$_{28-99}$ addition, after first pre-treating the cells with the compounds for 30 min.

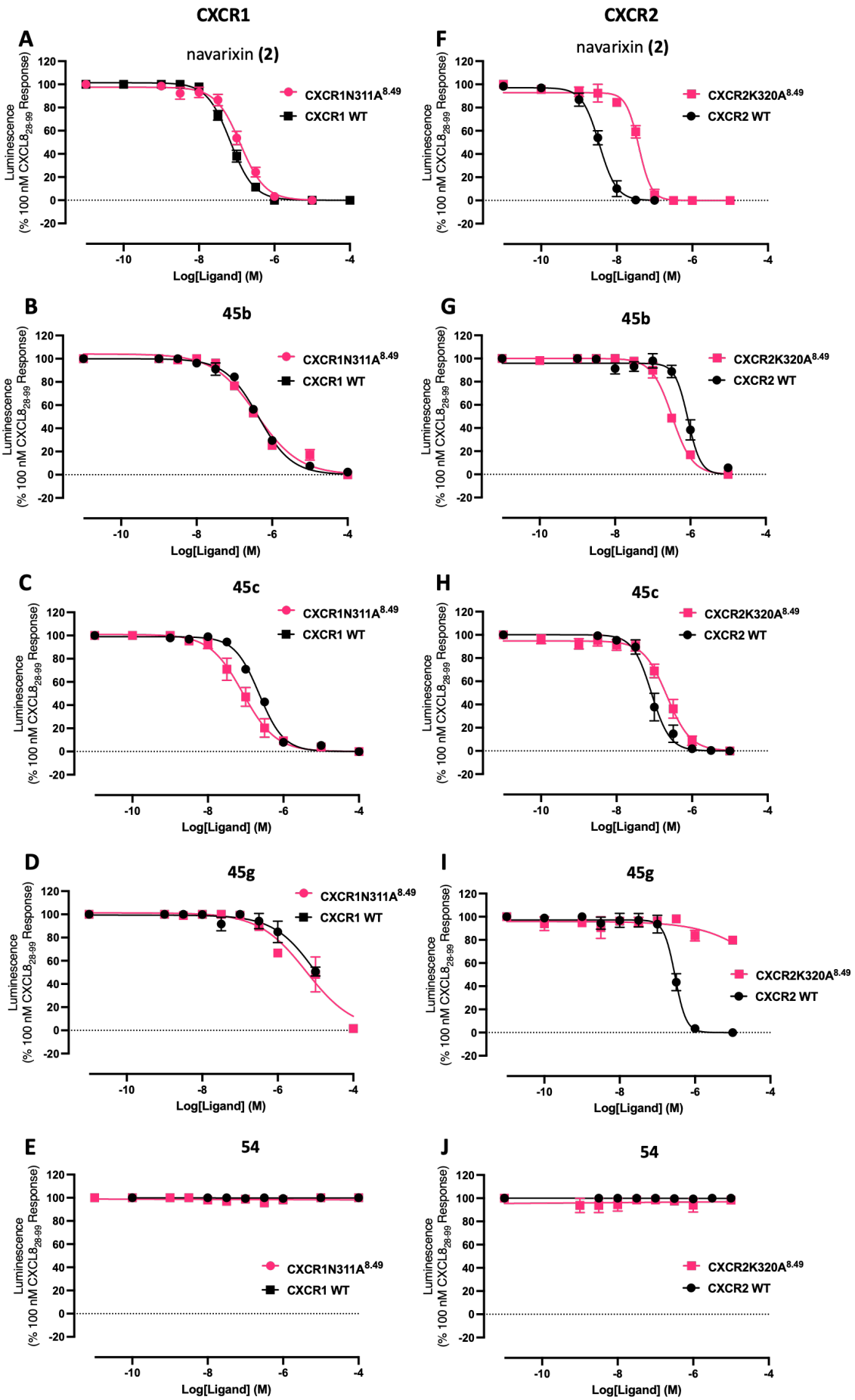
CXCR1
CXCR2
A
navarixin (2)
F
navarixin (2)
B
45b
G
45b
C
45c
H
45c
D
45g
I
45g
E
54
J
54
Luminescence (% 100 nM CXCL8$_{28-99}$ Response)
Log[Ligand] (M)
CXCR1N311A$^{8.49}$
CXCR1 WT
CXCR2K320A$^{8.49}$
CXCR2 WT

Figure 4-7 Concentration inhibition curves depicting the effects of CXCR1 and CXCR2 receptor site point mutations on the potency of navarixin (**2**), **45b**, **45c**, **45g,** and **54**. The curves were generated from inhibition assays of β-arrestin2-SmBit recruitment stimulated by 10 nM $CXCL8_{28-99}$. Mutant data is represented in pink, while wild-type data is depicted in black. Panels (A) to (E) show the effects of navarixin (**2**), **45b**, **45c**, **45g,** and **54**, respectively, in wild-type CXCR1 and CXCR1N311A$^{8.49}$. Panels (F) to (J) display the responses of the same ligands in wild-type CXCR2 and CXCR2N8.49A. The data represents pooled results (mean ± SEM), normalized to the $CXCL8_{28-99}$ control response, obtained from three individual experiments conducted in triplicate (n = 3).

Similarly to the observations in the wild type receptors in cell lines in **Section 4.5.1**, compound **54** failed to show any inhibitory activity at the mutated receptors up to 100 μM in CXCR1, or 10 μM in CXCR2. The potency of navarixin (**2**) was reduced in the CXCR2K320A$^{8.49}$, compared to the wild type expressing cells displaying a 20-fold reduction in pIC_{50} values. Additionally, the selectivity for CXCR2 over CXCR1 displayed by navarixin (**2**) was effectively abolished by the introduction of the 8.49A mutation, as its potency was not adversely affected by the Ala mutation of N311$^{8.49}$ in CXCR1, showing IC_{50} values within 2 – fold potency. These results underscore the crucial role of K320$^{8.49}$ in maintaining the potency of phenol-containing intracellular modulators at CXCR2, such as navarixin (**2**), highlighting its importance compared to N311$^{8.49}$ in CXCR1.

Table 4-8 Functional inhibition of $CXCL8_{28-99}$ mediated β-arrestin2-SmBiT recruitment in $CXCR1N311A^{8.49}$ -LgBit and $CXCR2K320A^{8.49}$-LgBiT for compounds **45b**, **45c**, **45g,** and **54** compared to lead compound, navarixin (**2**). Data shown are mean ± SEM from n = 3 individual experiments.

Compound	$CXCR1N311A^{8.49}$ pIC_{50} ± SEM	$CXCR2K320A^{8.49}$ pIC_{50} ± SEM	Selectivity IC_{50} (CXCR2/CXCR1)
navarixin (**2**)	7.16 ± 0.14	7.41 ± 0.12	1.8
45c	6.59 ± 0.41	6.66 ± 0.22	1.2
45b	6.00 ± 0.32	6.46 ± 0.15	2.9
45g	5.97 ± 1.37	<5.0	>10
54	<5.0	<5.0	X

45b, 45c, and **45g** displayed reduced potency when compared to navarixin (**2**) in the Ala mutated receptors $CXCR1N311A^{8.49}$ and $CXCR2K320A^{8.49}$, shown by the rightward shift exemplified in **Figure 4-7**. In $CXCR1N311A^{8.49}$ the order of potencies was navarixin (**2**) > **45c** > **45b** > **45g**, this is like the order in $CXCR2K320A^{8.49}$, with navarixin (**2**) > **45c** > **45b**. In contrast, 45g was unable to fully inhibit arrestin recruitment at 10 μM in CXCR2, therefore a pIC_{50} limit of <5.0 was assumed. The Ala mutation introduced at both receptors showed no drastic effects on modulators **45b** and **45c**, displaying potency within 3-fold of the potencies observed in wild type CXCR1 and CXCR2 expressing cells. This suggests that whilst $K320^{8.49}$ was crucial for retaining potency in CXCR2 for navarixin (**2**), it is not the case for **45b** and **45c.**

4.5 Comparative Analysis of Computational Predictions and Experimental Findings

As previously mentioned in **Chapter 2** and **Chapter 3**, the models developed in **Chapter 2** are "snapshots" of the receptor, and the molecular docking techniques employed in this project do not address the dynamic nature of the binding pocket. Hence, inherent limitations arise when attempting to analyse the effect of introducing side chain chemical modifications during docking studies. This is because the docking protocols used in this study do not allow residues within the binding site the rotational or translational freedom required to accommodate the chemical alterations made to the lead compound.

This is demonstrated by the inability of the K320$^{8.49}$ residue to adopt a desired conformation during molecular docking for beneficial binding of phenol modified ligands in CXCR2 (**Section 4.2.2**). This resulted in the absence of predicted binding poses for **45c**, or the observation of a "twisted" phenyl pose in the case of **45b** and **45g**, which significantly increased the docking scores of these compounds, compared navarixin (**2**). Given the observed inhibitory activity of these ligands at CXCR2, albeit with a 100-fold reduction compared to navarixin (**2**), it is presumed that the binding pocket would adapt to accommodate the ligand. Such adjustments are not captured through molecular docking where flexible side chain conformations are not considered.

In molecular docking studies, notable differences were observed between the methyl benzoate analogue **45g**, and the phenyl acetate analogue **45c**, in their interactions with CXCR1 and CXCR2 models. **45g** exhibited superior docking scores and more favourable binding interactions when compared to **45c** in CXCR1, indicating a stronger interaction profile within the binding site of this receptor. Additionally, **45g** displayed enhanced docking scores compared to **45c** in CXCR2, suggesting a potentially stronger binding affinity for this compound in the CXCR2 receptor model. Notably, in the CXCR1 model, **45g** was found to establish hydrogen bonding interactions with S72$^{2.37}$ through the ester carbonyl, compensating for the loss of hydrogen bonding from the *para*-oxygen present in **45c** and navarixin (**2**). However, biological testing provided contrasting results. **45g** exhibited poor potency in CXCR2 and a notable 10-fold reduction in inhibition in CXCR1 compared to **45c**. It was proposed that the C2 oxygen substituent on the benzamide ring exhibits an electronic effect on surrounding atoms that may enhance their binding capabilities as well as the compensating interactions established by the ester moieties

during docking. The discrepancy between the molecular docking results and the biological testing outcomes highlights the need for caution when relying solely on computational predictions in drug discovery. This emphasises the importance of experimental validation to elucidate the true activity and selectivity of potential drug candidates.

Using molecular dynamics simulations could provide further insights into the dynamics and flexibility of the binding site. This would allow for a more comprehensive understanding of ligand-receptor interactions. Molecular dynamics simulations could reveal how the binding site of CXCR1 and CXCR2 receptors adapt to different bound ligands and fluctuate over time; in particular, the movement of the polar binding site entrance, notable for CXCR1/CXCR2 selectivity.[293] These studies could potentially reveal additional binding modes and interactions that were not captured by static molecular docking studies. Integrating molecular dynamics simulations with experimental validation may lead to a more accurate prediction of ligand activity and selectivity, guiding the rational design of improved drug candidates targeting CXCR1 and CXCR2.

4.6 Conclusion

The work described in this section adds to the structure activity relationship of squaramide based NAMs targeting an intracellular binding pocket which overlaps with $G\alpha_i$. Investigation of the binding pocket from CXCR1 and CXCR2 models generated in **Chapter 2** pinpointed $K320^{8.49}$ in CXCR2 as a key binding residue that could be heavily implicated in the selectivity towards CXCR2 observed by NAMs, such as navarixin (**2**), through ionic interactions with the phenolate moiety. To investigate this, a series of ligands were designed based on navarixin (**2**) with modifications to the phenolate region. Glide docking of the proposed ligands gave a clear indication that introducing modifications that did not have the capability of forming ionic interactions with $K320^{8.49}$ were better tolerated in CXCR1 compared to CXCR2. Therefore, the ligands displayed an appreciable ability to modulate the selectivity of ligands towards CXCR1/CXCR2 selectivity or a dual antagonism.

The synthesis of NAMs detailed in this chapter covers the challenges faced when modifying the highly electron deficient phenol moiety of 3,4-diaminocyclobut-3-ene-1,2-dione based NAMs such as navarixin (**2**). Despite the challenges faced, three of the proposed ligands, **45b, 45c** and **45g**, were generated and the synthetic route towards these

compounds lays a foundation for further generation of novel analogues of navarixin (**2**) with modified phenol moieties.

Functional screening of the newly synthesised NAMs **45b** and **45c** in wild type CXCR1 and CXCR2 indicated that they possessed dual antagonistic profiles, with potencies in the order of 100 nM to 1μM. Additional functional screening of the compounds, along with navarixin (**2**) in mutant CXCR1 and CXCR2 expressing cell lines, further showed the significance of $K320^{8.49}$ for CXCR2/CXCR1 selectivity. Specifically, the selectivity was nullified upon substitution of this residue with $Ala^{8.49}$. However, no appreciable effect on inhibitor potency was observed for the same site point mutation in CXCR1 for navarixin (**2**), **45b** or **45c**. The functional pIC_{50} data presented in **Section 4.5.4** correlates with CXCR2 model's inability to tolerate modifications to the phenol moiety demonstrated from molecular docking in **Section 4.2.3**. Unfortunately, in the CXCR1 model, the promise shown in the decreased docking scores observed for **45b**, **45c**, and **45g** compared to navarixin (**2**), were not replicated in the whole cell assays. Whilst direct binding measurements would be a more representative comparison to docking score, the potency profiles collected for these ligands imply that the CXCR1 model may be inadequate for discerning the effect of the phenol modifications represented by **45b**, **45c,** and **45g.**

The findings support the inclusion of the phenol ring in the pharmacophore, as well as the established SAR conducted around the phenolic region of 3,4-diaminocyclobut-3-ene-1,2-dione class of NAMs in CXCR2.[344,346,347] However, based on the findings presented in this chapter, it seems that the presence of the phenol is not essential for maintaining potency in CXCR1. Reduced selectivity between CXCR1 and CXCR2 has been observed using the proposed phenol modification, though only a small sample size of three compounds was tested. Notably, **45b** is significant as the first selective CXCR1 NAM identified, showing a 2-fold selectivity for CXCR1 over CXCR2. Although this selectivity is within a 3-fold range, further modifications, such as using ethoxy instead of methoxy or exploring other phenol ether derivatives, are warranted. These changes could help determine if they might further enhance CXCR1 selectivity.

Chapter 5 - Conclusions and Future Work

As evidence is accumulating describing the divergent roles that CXCR1 and CXCR2 play in cancer, there are further questions as to whether these differences could extend to other neutrophil-mediated diseases. Moreover, elucidating the distinct contributions of CXCR1 and CXCR2 in these diseases could inform the development of more tailored and effective therapies. To further explore the distinct signalling pathways of CXCR1 and CXCR2 the generation of selective molecular tools for each receptor such as fluorescent ligands, covalent ligands, and proteolysis-targeting chimeras (PROTACs) may prove beneficial. These tools will enable researchers to further delineate the roles of CXCR1 and CXCR2 in disease models, thereby enhancing our understanding of their involvement in various pathological conditions.

The work presented in this thesis focussed on the design, synthesis and characterisation of intracellular allosteric modulators belonging to 3,4-diaminocyclobut-3-ene-1,2-dione class of CXCR1/2 IAMs with the goal to build upon current understandings of SAR towards rationalising dual CXCR1/2 antagonism or CXCR1 selectivity.

5.1 Generation of theoretical CXCR1 and CXCR2 models

In **Chapter 2**, CXCR1 and CXCR2 models were developed based on the recently published CXCR2 crystal structure in complex with NAM 00767013 (**1**) for use in a CADD program. The generated models were extensively validated to ensure their accuracy and reliability for subsequent studies. Initial assessment utilised an energy-based scoring function, DOPE, to evaluate CXCR1 homology models, although the models were indistinguishable using this metric and faced challenges, where the top performing DOPE models performed poorly during Glide docking of 00767013 (**1**). Inverse docking was employed to address these challenges as an alternative approach to rank the models based on ligand binding. Subsequent virtual screening of known ligands, and decoys using Glide docking protocols demonstrated the efficacy of the proposed CXCR1 homology model and the CXCR2 model in recognizing and generating low binding energy poses for known ligands compared to a set of theoretical decoys generated through DUD-E. Flexible ligand docking significantly improved ligand enrichment compared to rigid docking protocols in both CXCR1 and CXCR2 models, and so would be the preferred docking protocol for following CXCR1 and CXCR2 models throughout the thesis. Subsequent docking of

navarixin (**2**) and 00767013 (**1**) suggested that the CXCR2 model and CXCR1 homology model accurately approximates the binding mode between the receptor and 3,4-diaminocyclobut-3-ene-1,2-dione based antagonists from the experimental crystal structure (PDB ID: 6LFL[54]), retaining the characteristic binding mode and expected ligand-protein interactions. This warranted the use of these models for use in CADD in subsequent chapters.

5.2 Amino acid ester functionalisation of navarixin (2)

Systematic exploration of the binding cavity of the navarixin (**2**)-CXCR1 complex in **Chapter 3** revealed promising insights into potential modifications for enhancing ligand binding and receptor selectivity.

SiteMap analysis of the CXCR1-navarixin (**2**) and CXCR2-navarixin (**2**) complexes identified multiple shallow binding cavities in proximity to the *N,N*-dimethylamide moiety of navarixin (**2**), which did not appear to be crucial for binding. 10 amino acid ester functionalised analogues **30a-j**, containing diverse side chain functionality were designed in attempts exploit the identified binding cavities. Subsequent synthesis and characterisation using NanoBiT complementation assays in CXCR1 and CXCR2 expressing whole cells did not yield the desired CXCR1 selectivity. Addition of amino acid ester functionalities was tolerated in both receptors, albeit with up to 100-fold reduction in CXCR1 and 450-fold reduction in potency towards CXCR2. Modulated inhibitory activity was also observed based on the differing side chains allowing for an SAR to be built around the functionalised analogues, giving evidence that side chains of the amino acid esters were able to exert control on potency.

Initial docking results showed promising improvements in docking scores for most proposed ligands towards both CXCR1 and CXCR2, while indicating that selectivity could be modulated through amino acid ester functionalisation. When comparing docking scores with experimental pIC_{50} values, however, a weak correlation was observed, suggesting that these docking simulations poorly predict the inhibitory activity measured in the functional assays. Whilst the models were indispensable for generating a hypothesis around structural modifications introduced by amino acid ester functionalisation, they are not without limitations inherent to *in silico* predictions. Molecular docking studies can predict binding energies and binding interactions which offer insights into the relationship between predicted binding affinity and experimental activity. However, they are limited by the

variability of functional assays and the simplifications inherent in molecular docking protocols, which may not fully capture the intricacies of binding in a biological context or the dynamic behaviour of receptors.

Compound **30i**, a proline methyl ester functionalised analogue of navarixin (**2**), emerged as the most potent among the tested ligands in the NanoBiT assay, showing equipotency in CXCR1, but a five-fold reduction in potency in CXCR2 compared to navarixin (**2**). It resulted in a reduction in the selectivity profile between CXCR2 and CXCR1 from 52-fold for navarixin (**2**) to 9-fold for **30i**. However, subsequent NanoBRET studies of **30i** in CXCR1 expressing HEK293 membranes revealed that the binding affinity was 15-fold lower in CXCR1 compared to navarixin (**2**). Notably, **30i** was the only tested analogue containing a tertiary amide, resembling navarixin (**2**) more closely compared to the secondary amides found in other analogues. These findings, along with concurrent insights from exploring fluorescent CXCR2 probes within the group, prompted an investigation into *N*-methylation. Synthesis and evaluation of a small series of *N*-methylated analogues suggested that the impact of *N*-methylation may not be as significant in CXCR1, and the importance of the *N*-methyl group may depend on the second substituent on the amide. Further investigation is warranted to develop a more comprehensive understanding given that these findings are only based on four compounds.

5.3 Modifications of phenol moiety

Through investigation of CXCR1 and CXCR2 models in **Chapter 2**, N311$^{8.49}$ in CXCR1 and K320$^{8.49}$ in CXCR2, were identified as binding residues that could potentially be responsible for the selectivity between the two receptors observed by 3,4-diaminocyclobut-3-ene-1,2-dione based NAMs, such as navarixin (**2**). To investigate this further in **Chapter 3**, ligands were designed with modifications to the phenol moiety of lead compound navarixin (**2**), that aimed to target this non-conserved residue between the two receptors to modulate selectivity. Despite challenges in synthesising modified phenol navarixin (**2**) analogues, three novel ligands are synthesized **45b**, **45c,** and **45g**. **45b** (methoxy analogue) and **45c** (acetate analogue) displayed dual antagonistic profiles in wild-type CXCR1 and CXCR2 functional β-arrestin2 recruitment assay, whilst retaining potency towards CXCR1, compared to navarixin (**2**) (pIC_{50} (CXCR1) = 6.96 ± 0.13) with values of 6.41 ± 0.18 (compound **45b**) and 6.66 ± 0.18 (compound **45c**), respectively. Functional screening against mutant receptor expressing HEK293 cell lines further confirmed the significance

of K320$^{8.49}$ for selectivity. Whilst mutating K320$^{8.49}$ to A320$^{8.49}$ had a 20-fold reduction in potency for navarixin (**2**), little-to-no modulation of potency was observed in A311$^{8.49}$ mutant CXCR1 expressing cell lines. Furthermore, compound **45b** and **45c** displayed effectively equipotency between the mutant receptors.

5.4 Future work

5.4.1 Optimisation of purification techniques

A recurring difficulty faced in the synthetic route for all characterised compounds in this thesis was attributed to the purification of the final step, often resulting in low yielding reactions. Access to HPLC purification in the late stages of the thesis showed promising signs at elevating some of these challenges, however time constraints resulted in limited investigations into optimising the LC condition, which may further improve the yields of subsequent reactions. Such optimisation of the purification could be extremely useful for further generation of navarixin (**2**) analogues.

4.4.2 D-amino acid ester functionalisation of navarixin (2)

The work conducted in **Chapter 3** focussed on functionalising navarixin (**2**) with L-amino acid esters, however, did not address the effect that the chiral centre could play on orientating the side chain within the binding pocket, which could have a significant effect on the predicted binding interactions in the binding cavity and experimental characterisation. Further exploration of functionalising navarixin (**2**) with D-amino acid esters is warranted to investigate the effect of the opposite chiral centre.

5.4.3 Molecular dynamics

The models developed in **Chapter 2** were vital for building the hypothesis in subsequent **Chapter 3** and **Chapter 4**, but found limitations in molecular docking studies, when compared to experimental screening *in silico*. Molecular dynamic studies were out of the scope of this thesis, but these simulations could be vital to explore the dynamic behaviour of the receptor-ligand complex over time. By simulating the motions of atoms and molecules, molecular dynamics would provide insights into the flexibility, stability, and

conformational changes of the complex and binding cavity, allowing for delineation of key interactions and binding modes.

5.4.4 Further modifications of the phenol

There is a lot of scope for further investigation of phenol modifications. Compounds **45b** and **45c** showed promising results and effectively reduced CXCR2 selectivity over CXCR1 as the antagonists were equipotent in both receptors and these molecules serve as a starting point for further modification. *In silico* studies conducted in this thesis have indicated the potential for steric bulk introduced around the phenol moiety of navarixin (**2**) to modulate selectivity, therefore compounds could be modified to further increase the size of the modification introduced around this region. The most obvious investigation would be to systematically introduce bulkier alkyl substituents, such as ethoxy instead of methoxy, in **45b**, and propionate instead of acetate in **45c**. This route may also be an alternative route to introducing aromatic ring substitutions in the form of benzyl esters or benzyl ethers to the 2-position of the benzamide, which was originally envisaged when attempting the synthesis of 2'-hydroxy-*N*,*N*-dimethyl-6-nitro-[1,1'-biphenyl]-2-carboxamide (**46a**), but was unsuccessful during this work.

Compound **45g**, a methyl benzoate analogue of navarixin (**2**), was derived from the ring opening 4-nitroisobenzofuran-1,3-dione, which, to our knowledge, was a novel approach to accessing di-substituted benzamides containing an NH at 3-position for ring A of 3,4-diaminocyclo-3-butene1,2-dione IAMs. Whilst the current work only explored the methyl ester analogue, **45g**, this ring opening reaction could be employed to explore more functional modifications around the phenol. Various esters could be explored utilising different alcohols as reagents in the ring opening while the ring opening of 4-nitroisobenzofuran-1,3-dione could be explored with other functionalities, such as amines and ketones, which have been demonstrated previously for phthalic anhydrides.[427-431]

Chapter 6 – Experimental

6.1 Chemistry

6.1.1 Materials and general methods

Chemicals and solvents were purchased from Fischer Scientific UK, Sigma-Aldrich, Merck Millipore and Fluorochem and used without further purification. Unless stated reactions were carried out at ambient temperature. All air-sensitive or moisture-sensitive reactions were conducted in dried glassware (>100 °C) under a nitrogen atmosphere. Dried solvents were used for any moisture sensitive reactions and stored under nitrogen conditions.

Analytical TLC was performed on pre-coated aluminium backed silica gel 200 µm plates (Merck, Kieselgel 60F254). Visualization of TLC plates was accomplished with UV-light (254 and 366 nm), KMnO4, ninhydrin (solution in ethanol), cerium ammonium molybdate, ferric chloride, bromocresol green and *p*-anisaldehyde staining. All organic extracts after aqueous workup procedures were dried over $MgSO_4$ or Na_2SO_4 before gravity filtration and then evaporation to dryness. Organic solvents were evaporated *in vacuo* at $\leq 40^{\circ}C$ (water bath temperature). Flash chromatography purification was conducted on technical grade silica gel columns, 60 Å, 40-63 µm (Supplied from Sigma-Aldrich).

^{1}H and ^{13}C NMR detection was performed using Bruker-AV(III) HD 400 NMR equipped with a 5 mm $BBFO^{+}$ probe [400.25 MHz (^{1}H), 100.66 MHz (^{13}C)]. Where required, ^{13}C NMR detection was performed on Bruker AV 500 MHz. Deuterated solvents for NMR detection were $CDCl_3$, DMSO-d_6, or MeOD-d_4 and purchased from Sigma-Aldrich. Chemical shifts (δ) are given in parts per million (ppm) and referenced against the residual proton or carbon references of the >99 % deuterated solvents as internal standards. Coupling constants (*J*) are given in hertz (Hz). Data are reported as follows: chemical shift, multiplicity (s = singlet, d = doublet, t = triplet, q = quartet, m = multiplet, dd = doublet of doublets, dt = doublet of triplets, br = broad, and combinations of these) coupling constants, and integration. Spectra were assigned using appropriate corelated spectroscopy (COSY), heteronuclear single quantum coherence (HSQC) and heteronuclear multiple-bond coherence (HMBC) techniques. NMR spectra were evaluated using MestReNova 14.0 (Mestrelab Research).

Normal phase flash column chromatography (FCC) was performed on Biotage HPFC SP4 system with UV detection at 254 nm. Solvent systems used for purification are specified for each compound. Reverse phase flash column chromatography (RP-FCC) was performed on an Interchim puriflash 4100 system with UV detection at 254 nm. RP-FCC was performed using MeCN and water with eluent specified for each compound. Preparative layer chromatography (PLC) was performed on Analtech uniplate silica gel PLC plates (200 x 200 x 2 mm). Eluent specified for each compound.

Liquid chromatography-mass spectroscopy (LCMS) was performed on an LCMS/MS system consisting of a Shimadzu Prominence UFLC XR pump, autosample, column compartment, detector (Shimadzu UK Limited), coupled to an Applied Biosystems API2000™ ESI LCMS/MS triple quadrupole MS (Thermo Fischer Scientific Inc.). LCMS was visualised at 254 nm and 220 nm using a Phenomenex Gemini-NX 3 µm-110Å C18 column (50 mm x 2 mm x 3 µm) at 40 °C at a flow rate of 0.5 mL/min. Solvent A was H_2O + 0.1% formic acid (FA) and solvent B acetonitrile (MeCN) + 0.1% FA. The gradient elution consisted of a program of 1 min at 5 % A; 5-98% B over 2 min, 98% B for 2 min, 98-5% over 0.5 min and then 5% B for 1 min. High-resolution mass spectrometry was determined using Bruker Daltonics MicroTOF (ESI-TOFMS).

Purity was confirmed by either LCMS/MS or analytical HPLC and unless stated purity was found to be >95%. LCMS/MS was conducted using a gradient of solvent A and B at a flow rate of 0.5 mL/min. The gradient was initiated by a 1 min isocratic step at 5 % B followed by an increase to 98% B over 11 min, then 98% to 5% over 0.5 min and then 5% B for 1 min. The purity of the final compounds was determined using area under the curve method on the UV trace recorded at a wavelength of 254 nm.

Analytical HPLC was performed on a Shimadzu SCL-40 system controller, LC-40D XR solvent delivery module, SIL-40C XR autosampler, CTO40C column oven and SPD-M40 photodiode array detector, using system 3 to confirm purity. All retention times (t_R) are quoted in minutes.

Preparative HPLC was performed on a HPLC system consisting of Shimadzu CBM-40 controller, LC-20AP pump, SPD-40V detector coupled to a LH-40 auto collector. Separation achieved using system 1 or 2.

System 1: Phenomenex Gemini® reverse phase 5 μm NX-C18 column (250 x 21.2 mm), a flow rate of 10 mL/min and UV detection at 254 nm. Gradient elution method specified for each compound.

System 2: Phenomenex Onyx monolithic reverse phase semi-prep C18 column (100 x 10 mm), a flow rate of 10 mL/min and UV detection at 254 nm. Gradient elution method specified for each compound.

System 3: Phenomenex Onyx Monolithic reverse phase C_{18} column (100 x 4.6 mm), a flow rate of 4.00 mL/min and UV detection at 254 nm. The gradient was initiated by a 1 min isocratic step at 10% solvent B followed by an increase to 95% solvent B over 12 min followed by 1 min at 95%. The purity of the final compounds was determined by area under the curve method on the UV trace recorded at a wavelength of 254 nm.

6.1.2 Synthetic methods

General procedure A: Synthesis of (*R*)-(2-hydroxy-3-((2-((1-(5-methylfuran-2-yl)propyl)amino)-3,4-dicyclobut-1-en-1-yl)amino)benzoyl) methyl L-amino acid esters

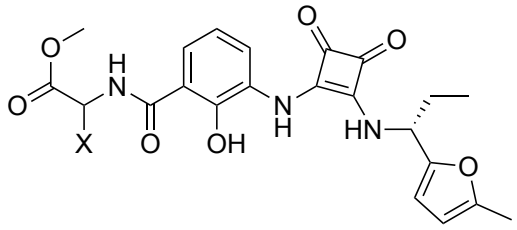

(*R*)-2-Hydroxy-3-((2-((1-(5-methylfuran-2-yl)propyl)amino)-3,4-dioxocyclobut-1-en-1-yl)amino)benzoic acid (**34**) (1 eq); 1-(3-dimethylaminopropyl)3-ethylcarbodiimide hydrochloride (1.2 eq) and 1-hydroxybenzotriazole monohydrate (1.2 eq) were suspended in DMF (15 vol). To the mixture α-substituted amino acid methyl ester or α-substituted amino acid methyl ester hydrochloride (1.1 eq) and triethylamine (TEA) (2.4-3.5 eq) were added and stirred under microwave conditions (90 ℃) for 6-36 min. The reaction mixture was diluted with ice cold water and extracted with EtOAc three times. The combined organic extracts were washed sequentially with ice cold water and brine then dried over $MgSO_4$. The mixture was concentrated under reduced pressure to yield the crude oil, which was purified using preparative thin-layer chromatography (PTLC).

General procedure B: Synthesis of (2-hydroxy-3-nitrobenzoyl) methyl L-amino acid esters

Method A

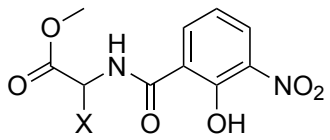

3-Nitrosalicylic acid (**31**) (1 eq) was dissolved in dry DCM (20 vol) and placed under N_2 atmosphere. oxalyl chloride (3 eq) was added to the reaction followed by a catalytic amount of DMF (2 drops) and stirred at ambient temperature for 18-24hr. Reaction mixture monitored by TLC and upon starting material consumption, the reaction was concentrated under reduced pressure, redissolved in dry DCM, and cooled to 0 ℃. To the mixture, α-substituted amino acid methyl ester or α-substituted amino acid methyl ester hydrochloride (1.2 eq) was added, followed by DIPEA (2.4 eq). Upon completion the reaction was concentrated under reduced pressure. The resulting mixture was diluted with water and washed with DCM once. The aqueous layer was then acidified to pH ~2 using 1M $HCl_{(aq)}$ and extracted with DCM three times. The organic extracts were combined then washed sequentially with water and brine. The solvent was removed under reduced pressure to afford the crude product which was purified using FCC.

Method B

3-Nitrosalicylic acid **(31)** (1 eq) was dissolved in DMF (20 vol) to which EDC-$HCl_{(aq)}$ (1.2 eq) added at 0 ℃ and stirred for 15 min. HOBt (1.2 eq) was added and stirred for 15 min followed by the addition of α-substituted amino acid methyl ester or α-substituted amino acid methyl ester hydrochloride (2.0 eq) and DIPEA (2.0 eq). The reaction was stirred at ambient temperature for 18-24 hr and monitored by TLC. Upon completion the reaction was diluted in brine, acidified to pH ~2 using 1M $HCl_{(aq)}$ and then extracted with EtOAc three times. The organic extracts were combined, dried over $MgSO_4$ and then concentrated under reduced pressure affording the crude product which was purified by FCC.

General procedure C: Synthesis of (3-amino-2-hydroxybenzoyl) methyl L-amino acid esters

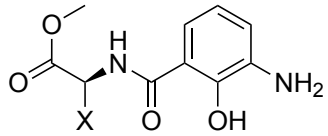

α-Substituted methyl (2-hydroxy-3-nitrobenzoyl-*L*-amino acid ester (1 eq, **35b**, **e**, **f**, and **i**) were dissolved in EtOH (20 vol) and hydrogenated over 10% Pd/C (10% w/w) at ambient temperature and atmospheric pressure for 18 hr. The reaction was monitored by TLC. Upon completion the suspension was filtered through celite and the celite pad was washed with excess EtOH. The resulting filtrate was concentrated under reduced pressure yield the desired product that was used without further purification.

General procedure D: Synthesis of (3-((2-ethoxy-3,4-dioxocyclobut-1-en-1-yl)amino)-2-hydroxybenzoyl) methyl L-amino acid esters

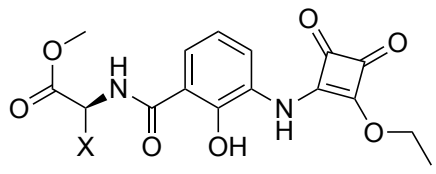

α-Substituted methyl (3-amino-2-hydroxybenzoyl)-*L*-amino acid esters (**36b**, **e**, **f**, and **i**) (1 eq) were dissolved in EtOH (30 vol) to which 3,4-diethoxycyclobut-3-ene-1,2-dione (1.2 eq) was added dropwise at 0 ℃. The reaction was stirred for 48-72 hr and monitored by TLC. Upon completion the reaction mixture was concentrated under reduced pressure, redissolved in water, and then washed with Et_2O three times. The aqueous phase was then acidified to pH ~2 using 1M $HCl_{(aq)}$ followed by the extraction with EtOAc three times. The organic extracts were combined, dried over $MgSO_4$, and concentrated under reduced pressure to yield the crude product, which was used without further purification.

General procedure E: Synthesis of (2-hydroxy-3-((2-(((*R*)-1-(5-methylfuran-2-yl)propyl)amino)-3,4-dioxocyclobut-1-en-1-yl)benzoyl) methyl L-amino acid esters

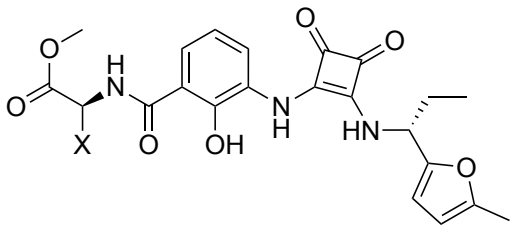

α-Substituted methyl (3-amino-2-hydroxybenzoyl)-*L*-amino acid esters (**37b**, **e**, **f**, and **i**) (1 eq) were dissolved in EtOH (20 vol) to which (*R*)-1-(5-methylfuran-2-yl)propan-1-amine hydrochloride (1.1 eq) and DIPEA (2.1 eq) were added. The reaction mixture was stirred for 48-120 hr and monitored by TLC. Upon completion the reaction was

concentrated under reduced pressure in vacuo, redissolved in DCM, and washed sequentially with 0.5M $HCl_{(aq)}$ three times and brine three times. The mixture was concentrated under reduced pressure to afford the crude product which was purified using PTLC or RP-FCC.

General procedure F: Synthesis of α-substituted methyl *N*-(2-hydroxy-3-nitrobenzoyl)-*N*-methylamino acid methyl esters

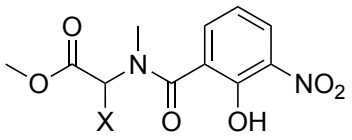

3-Nitrosalicylic acid (**31**) (1 eq) was dissolved in dry DCM (20 vol) and placed under N_2 conditions. Oxalyl chloride (3 eq) was added to the reaction followed by a catalytic amount of DMF (2 drops) and the reaction mixture was stirred at ambient temperature for 18-24hr. The reaction was monitored by TLC. Upon starting material consumption, the reaction was concentrated under reduced pressure, redissolved in dry DCM, and cooled to 0 ℃. To the mixture α-substituted *N*-methyl amino acid methyl ester hydrochloride (1.5 eq) was added, followed by DIPEA (3.5 eq). The reaction was monitored by TLC. Upon completion the reaction was concentrated under reduced pressure diluted with water and washed with DCM three times. The aqueous layer was then acidified to pH ~2 using 1M $HCl_{(aq)}$ and extracted with DCM three times. The DCM extracts were combined then washed sequentially with water and brine. The mixture was concentrated under reduced pressure to afford the crude product which was purified using FCC.

General procedure G: Synthesis of methyl *N*-(3-amino-2-hydroxybenzoyl)-*N*-methyl L-amino acid esters

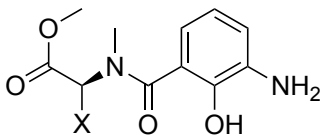

α-Substituted methyl *N*-(2-hydroxy-3-nitrobenzoyl)-*N*-*L*-amino acid ester (1 eq, **40a**, **d**, **g**, and **h**) were dissolved in EtOH (30 vol) and hydrogenated over 10% Pd/C (10% w/w) at ambient temperature and under balloon pressurisation for 18 hr. The suspension was filtered through celite and washed with excess EtOH. The resulting filtrate was concentrated under reduced pressure to yield the product which was used without further purification.

General procedure H: Synthesis of *N*-(3-((2-ethoxy-3,4-dioxocyclobut-1-en-1-yl)amino)-2-hydroxybenzoyl)-*N*-methyl L-amino acid esters

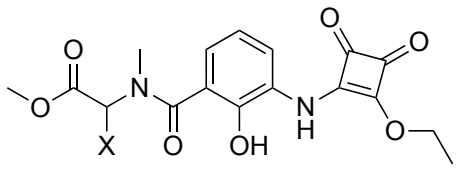

α-Substituted methyl *N*-(3-amino-2-hydroxybenzoyl)-*N*-methyl L-amino acid esters (**41a**, **d**, **g**, and **h**) (1 eq) were dissolved in EtOH (20 vol) to which 3,4-diethoxycyclobut-3-ene-1,2-dione (1.2 eq) was added dropwise at 0 ℃. The reaction was stirred for 96-120 hr. The reaction was monitored by TLC. Upon completion the reaction was concentrated under reduced pressure, redissolved in water, and washed with Et_2O three times. The aqueous was then acidified to pH ~2 using 1M $HCl_{(aq)}$ followed by extraction with EtOAc. The EtOAc extracts were combined, dried over $MgSO_4$, and concentrated under reduced pressure to afford the crude product which was purified by FCC.

General procedure I: Synthesis of *N*-(2-hydroxy-3-((2-(((*R*)-1-(5-methylfuran-2-yl)propyl)amino)-3,4-dioxocyclobut-1-en-1-yl)benzoyl)-*N*-methyl L-amino acid esters

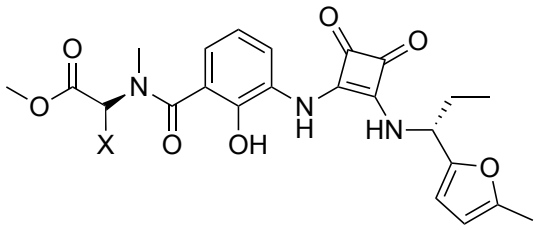

α-Substituted methyl (3-amino-2-hydroxybenzoyl)-*L*-amino acid esters (**42a**, **d**, **g**, and **h**) (1 eq) were dissolved in EtOH (20 vol) to which (*R*)-1-(5-methylfuran-2-yl)propan-1-amine hydrochloride (1.2 eq) and DIPEA (2.2 eq) were added. The reaction was stirred at ambient temperatures for 32-70 hr and monitored by TLC. Upon completion the reaction was concentrated under reduced pressure in vacuo , redissolved in 1:1 DCM:water and extracted with DCM three times. The DCM extracts were combined and washed sequentially with water and brine. The organics were dried over $MgSO_4$ and concentrated under reduced pressure affording crude product which was purified using prep-HPLC.

General procedure J: Nitro reduction of nitrobenzamides

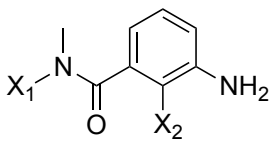

Nitrobenzamides (1 eq, **40k**, **47b**, **47c**, and **47g**) were dissolved in EtOH (30 vol) and hydrogenated over 10% Pd/C (10% w/w) at ambient temperature and under balloon pressurisation for 18 hr. The reaction was monitored by TLC. Upon reaction completion, the suspension was filtered through celite and washed with excess EtOH. The mixture was concentrated under reduced pressure to yield the product which was used without further purification.

General procedure K: Mono-amination of 3,4-Diethoxy-3-cyclobutene-1,2-dione

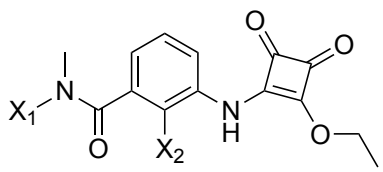

Anilines (**41k**, **48b**, and **48g**) (1 eq) were dissolved in EtOH (20 vol) to which 3,4-diethoxycyclobut-3-ene-1,2-dione (1.2 eq) was added dropwise at 0 ℃. The reaction was stirred for 96-120 hr. The reaction was monitored by TLC. Upon completion the reaction was concentrated under reduced pressure, redissolved in water, and washed with Et_2O three times. The aqueous phase was then acidified to pH ~2 using 1M $HCl_{(aq)}$ followed by extraction with EtOAc. The EtOAc extracts were combined, dried over $MgSO_4$, and concentrated under reduced pressure to afford the crude product, which was purified by FCC or used without further purification.

General procedure L: Amination of squaric acid monoester monoamides

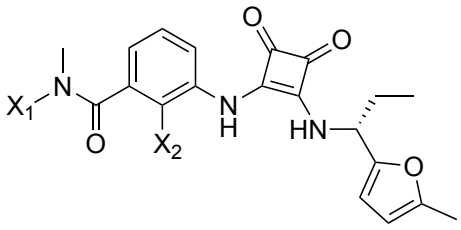

Squaric acid monoester monoamide (**42k**, **49b**, and **49g**) (1 eq) were dissolved in EtOH (40 vol) to which (*R*)-1-(5-methylfuran-2-yl)propan-1-amine hydrochloride (1.2 eq) and DIPEA (2.2 eq) were added. The reaction was stirred for 32-70 hr. The reaction was monitored by TLC. Upon completion, the reaction was concentrated under reduced pressure in vacuo, redissolved in 1:1 DCM:water and extracted with DCM three times. The DCM extracts were combined and washed sequentially with water and brine. The DCM layer was dried over $MgSO_4$, and concentrated under reduced pressure affording the crude product, which was purified using prep-HPLC.

3-Amino-2-hydroxybenzoic acid (32)

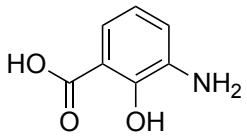

3-Nitrosalicylic acid (**31**) (2.07 g, 11.30 mmol, 1 eq) was dissolved in THF (12 mL) and hydrogenated over 10% Pd/C (208 mg, 10% w/w), at room temperature and under balloon pressurisation. The reaction was monitored by TLC. Upon completion the suspension was filtered through celite and washed with excess MeOH. The filtrate was concentrated under reduced pressure affording a dark green solid (1.12 g, 65%).

^{1}H NMR (DMSO-*d*$_6$) δ 9.56 – 7.25 (m, 3H, N*H*$_2$ and phenol O*H*), 7.05 (dd, *J* = 7.9/7.9 Hz, 1H, Ar-C*H*-6), 6.83 (dd, *J* = 7.7/7.7 Hz, 1H, Ar-C*H*-4), 6.60 (dd, *J* = 7.8/7.8 Hz, 1H, Ar-C*H*-5).

^{13}C NMR (DMSO-*d*$_6$) δ 172.8 (*C*OOH), 149.8 (Ar-*C*OH), 136.2 (Ar-*C*NH$_2$), 118.3 (Ar-*C*), 118.1 (Ar-*C*), 117.5 (Ar-*C*), 113.0 (Ar-*C*COOH).

LCMS t_R: 0.57 min

***m/z*:** LCMS (TOF ES$^+$) $C_7H_7NO_3$ $[M+H]^+$ calcd 154.1; found 154.1

3-((2-Ethoxy-3,4-dioxocyclobut-1-en-1-yl)amino)-2-hydroxybenzoic acid (33)

Method A

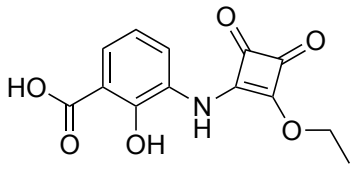

3-Amino-2-hydroxybenzoic acid (**32**) (107 mg, 0.65 mmol, 1 eq) was dissolved in 1,4-dioxane (2.8 mL) to which 3,4-diethoxycyclobut-3-ene-1,2-dione (153 μL, 0.78 mmol, 1.2 eq) was added dropwise at 0 ℃ followed by diisopropylethylamine (DIPEA) (64 μL, 0.65 mmol, 1 eq) and then exposed to microwave irradiation (120 ℃) for 15 min. The reaction was monitored by TLC. Upon completion, 1,4-Dioxane was removed, and the resulting oil was dissolved in 1M $NaOH_{(aq)}$ (15 mL) before washing with Et_2O (3 x 15 mL). The aqueous layer was acidified to pH ~2 using 1M $HCl_{(aq)}$ then extracted with DCM (3 x 15 mL). The combined DCM extracts were dried over Na_2SO_4 and concentrated under reduced pressure before purification by FCC (gradient elution 5 -15% MeOH:DCM) affording a brown oil (42 mg, 22%).

Method B

3-Nitrosalicylic acid (**32**) (603 mg, 3.29 mmol, 1 eq) was dissolved in THF (7 mL) and hydrogenated over 10% Pd/C (61 mg, 10% w/w), at room temperature and under balloon

pressurisation. The reaction was monitored by TLC. Upon completion DMF (5mL) was added and THF removed under reduced pressure. The mixture was cooled to 0 ℃ and 3,4-diethoxycyclobut-3-ene-1,2-dione (585 μL, 3.95 mmol, 1.2 eq) added dropwise followed by DIPEA (574 μL, 3.29 mmol). The reaction mixture was stirred at 65 ℃ overnight and monitored by TLC. Upon completion the mixture was filtered through celite, washing with 20% MeOH:DCM (3 x 20 mL). The filtrate was concentrated under reduced pressure to afford viscous red oil. The oil was dissolved in water (20 mL) and washed with Et_2O (3 x 15 mL). The aqueous layer was acidified to pH ~2 with 1M $HCl_{(aq)}$ then extracted with EtOAc (5 x 20 mL). The combined organic extracts were dried over Na_2SO_2 and concentrated under reduced pressure. The resulting crude was purified by FCC (gradient elution 5 - 15% MeOH:DCM) affording a dark orange solid (612 mg, 67%).

LCMS t_R: 3.11 min

^{1}H NMR (DMSO-*d*$_6$) δ 10.35 (s, 1H, phenol O*H*), 7.67 (dd, *J* = 8.0/1.6 Hz, 1H, Ar-C*H*-6), 7.46 (dd, *J* = 7.8/1.6 Hz, 1H, Ar-C*H*-4), 6.93 (dd, *J* = 7.9/7.9 Hz, 1H, Ar-C*H*-5), 4.67 (q, *J* = 7.1 Hz, 2H, OC*H*$_2$CH$_3$), 1.34 (t, *J* = 7.0 Hz, 3H, OCH$_2$C*H*$_3$).

^{13}C NMR (DMSO-*d*$_6$) δ 184.7 (squaramide *C*=O), 178.7 (benzoic acid *C*=O), 172.5 (*C*OCH$_2$CH$_3$), 171.4 (*C*NH), 155.1 (Ar-*C*OH), 130.6 (Ar-*C*), 127.9 (Ar-*C*), 126.1 (Ar-*C*), 118.8 (Ar-*C*), 113.8 (Ar-*C*COOH), 69.6 (O*C*H$_2$CH$_3$), 16.0 (OCH$_2$*C*H$_3$).

***m/z*:** LCMS (TOF ES$^+$) $C_{13}H_{11}NO_6$ $[M+H]^+$ calcd 278.1; found 278.0

(*R*)-2-Hydroxy-3-((2-((1-(5-methylfuran-2-yl)propyl)amino)-3,4-dioxocyclobut-1-en-1-yl)amino)benzoic acid (34)

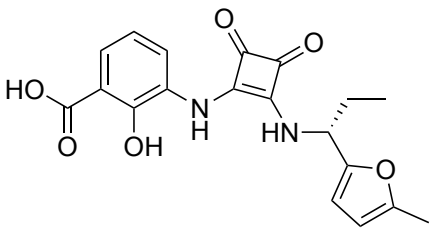

3-((2-Ethoxy-3,4-dioxocyclobut-1-en-1-yl)amino)-hydroxybenzoic acid (**33**) (345 mg, 1.24 mmol, 1 eq) was dissolved in ethanol (5 mL) to which (*R*)-1-(5-methylfuran-2-yl)propan-1-amine hydrochloride (219 mg, 1.25 mmol, 1 eq) was added followed by DIPEA (477 μL, 2.73 mmol, 2.2 eq). The reaction was stirred for 24 hr at ambient temperatures and monitored by TLC. Upon completion the solvent was removed under reduced pressure and the resulting brown oil was dissolved in water (15 mL), acidified to pH ~2 using 1M $HCl_{(aq)}$ followed by extraction using EtOAc (3 x 20 mL). The combined

organic extracts were dried over Na_2SO_4 and concentrated under reduced pressure to afford a dark brown crystalline solid (322 mg, 70%).

LCMS t_R: 3.91 min

^{1}H NMR (DMSO-*d*$_6$) δ 9.38 (s, 1H, phenol O*H*), 8.68 (d, *J* = 9.0 Hz, 1H, N*H*), 8.01 (d, *J* = 8.0 Hz, 1H, Ar-C*H*-6), 7.47 (dd, *J* = 8.0, 1.4 Hz, 1H Ar-C*H*-4), 6.89 (dd, *J* = 8.0/8.0 Hz, 1H, Ar-C*H*-5), 6.27 (d, *J* = 3.1 Hz, 1H, furyl C*H*), 6.05 (dd, *J* = 2.8, 1.5 Hz, 1H, furanyl C*H*), 5.14 (q, *J* = 7.7 Hz, 1H, NHC*H*CH_2CH_3), 2.27 (s, 3H, furanyl CCH_3), 1.91 (ddt, *J* = 39.6, 14.1, 7.1 Hz, 2H, NHCHCH_2CH_3), 0.92 (t, *J* = 7.3 Hz, 3H, NHCHCH$_2$CH_3).

^{13}C NMR (DMSO-*d*$_6$) δ 180.2 (squaramide *C*=O), 172.2 (benzoic acid *C*=O), 168.6 (squaramide *C*=C), 163.2 (squaramide *C*=C), 152.0 (furyl *C*), 151.4 (furyl *C*), 127.6 (Ar-*C*), 124.6 (Ar-*C*H), 123.8 (Ar-*C*H), 118.5 (Ar-*C*H), 113.2 (Ar-*C*H), 107.6 (furyl *C*H), 106.46 (furyl *C*H), 52.8 (NH*C*HCH$_2$CH$_3$), 27.2 (NHCH*C*H$_2$CH$_3$), 13.3 (furyl C*C*H$_3$), 10.3 (NHCHCH$_2$*C*H$_3$).

m/z: LCMS (TOF ES$^+$) $C_{19}H_{18}N_2O_6$ $[M+H]^+$ calcd 371.1; found 371.1

Methyl (*R*)-(2-hydroxy-3-((2-((1-(5-methylfuran-2-yl)propyl)amino)-3,4-dioxocyclobut-1-en-1-yl)amino)benzoyl)glycinate (30h)

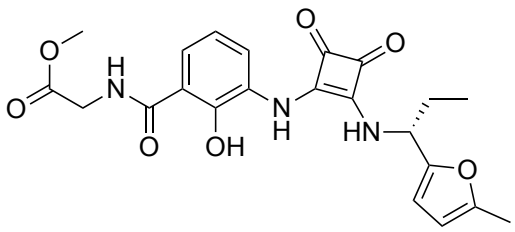

Synthesised following general procedure A using (*R*)-2-hydroxy-3-((2-((1-(5-methylfuran-2-yl)propyl)amino)-3,4-dioxocyclobut-1-en-1-yl)amino)benzoic acid (**34**) (79 mg, 0.21 mmol, 1 eq), 1-(3-dimethylaminopropyl)3-ethylcarbodiimide hydrochloride (50 mg, 0.26 mmol, 1.2 eq), 1-hydroxybenzotriazole (42 mg, 0.26mmol, 1.2 eq) and methyl glycinate hydrochloride (32 mg, 0.24 mmol, 1.1 eq). The resulting crude was purified by PTLC (2.5% MeOH:DCM) to afford a white solid (4.6 mg, 5%).

LCMS t_R: 5.68 min

^{1}H NMR (DMSO-*d*$_6$) ^{1}H NMR (400 MHz, DMSO) δ 13.46 (s, 0.5H, O*H*) *9*.45 (m, 1H, N*H*), 8.84 (m, 1H, Ar-C*H*-6), 7.87 (m, 1H, Ar-C*H*-4), 7.42 (m, 1H, Ar-C*H*-5), 6.23 (d, *J* = 3.1 Hz, 1H, furyl CCH$_3$), 6.04 (d, *J* = 3.1 Hz, 1H, furyl *C*H), 5.14 (q, *J* = 7.8 Hz, 1H,

C*H*CH_2CH_3), 4.07 (d, *J* = 5.2 Hz, 2H, NHC*H*$_2$), 3.65 (s, 3H, COOC*H*$_3$), 2.26 (s, 3H, furyl CC*H*$_3$), 2.05 – 1.73 (m, 2H, CHC*H*$_2$CH$_3$), 0.92 (t, *J* = 7.3 Hz, 3H, CHCH$_2$C*H*$_3$).

^{13}C NMR (DMSO-*d*$_6$) δ 172.5 (squaramide C=O), 163.3 (*C*=O), 152.2 (furyl *C*CH), 151.2 (furyl *C*CH$_3$), 122.6 (Ar-*C*H), 116.7 (Ar-*C*H), 113.2 (Ar-*C*H), 107.6 (furyl *C*H), 106.4 (furyl *C*H), 52.7 (COO*C*H$_3$), 51.7 (*C*CH$_2$CH$_3$), 40.8 (NH*C*H$_2$), 27.1 (CH*C*H$_2$CH$_3$), 13.3 (furyl C*C*H$_3$), 10.3 (ethyl CH$_2$*C*H$_3$).

***m/z*:** HRMS (TOF ES$^+$) $C_{22}H_{23}N_3O_7$ [M+Na]$^+$ calcd 465.1462; found 465.1480

Methyl (2-hydroxy-3-((2-(((R)-1-(5-methylfuran-2-yl)propyl)amino)-3,4-dioxocyclobut-1-en-1-yl)amino)benzoyl)-L-alaninate (30a)

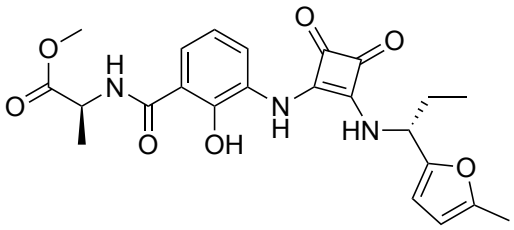

Synthesised following general procedure A using (*R*)-2-hydroxy-3-((2-((1-(5-methylfuran-2-yl)propyl)amino)-3,4-dioxocyclobut-1-en-1-yl)amino)benzoic acid (**34**) (73 mg, 0.20 mmol, 1 eq), 1-(3-dimethylaminopropyl)3-ethylcarbodiimide hydrochloride (48 mg, 0.24 mmol, 1.2 eq), 1-hydroxybenzotriazole (37 mg, 0.26 mmol) and methyl alaninate hydrochloride (56 mg, 0.22 mmol, 1.1 eq). Resulting crude was purified by PTLC purification (5% MeOH:DCM) to afford a white solid 7.2 mg, 8%.

LCMS t_R: 5.96 min

^{1}H NMR (DMSO-*d*$_6$) δ 13.49 (s, 1H, O*H*), 9.36 (s, 1H, N*H*), 9.28 (d, J = 6.8 Hz, 1H, N*H*), 8.70 (d, J = 9.0 Hz, 1H, N*H*), 8.02 (dd, J = 8.1/1.4 Hz, 1H, Ar-C*H*-6), 7.68 (dd, 8.1/1.3 Hz, 1H, Ar-C*H*-4), 6.93 (dd, 8.0/8.0 Hz, 1H, Ar-C*H*-5), 6.27 (d, J = 3.1 Hz, 1H, furyl C*H*), 6.06 (d, J = 3.1 Hz, 1H, furyl C*H*), 5.14 (q, J = 7.8 Hz, NHC*H*CH$_3$), 4.56 (t, J = 7.2 Hz, 1H, C*H*CH$_2$CH$_3$), 3.68 (s, 3H, COOC*H*$_3$), 2.27 (d, J = 1.0 Hz, 3H, NHCHC*H*$_3$), 1.93 (m, 2H, CHC*H*$_2$CH$_3$), 1.45 (d, J = 7.5 Hz, NHCHC*H*$_3$), 0.93 (t, J = 7.3 Hz, 3H, CHCH$_2$C*H*$_3$).

^{13}C NMR (DMSO-*d*$_6$) δ 172.5 (C=O), 163.2 (*C*=O), 152.0 (furyl *C*CH), 151.4 (furyl *C*CH-$_3$), 123.6 (Ar-*C*), 118.3 (Ar-*C*), 113.3 (Ar-*C*H), 107.6 (furyl *C*H), 106.5 (furyl *C*H), 52.8 (COO*C*H$_3$) , 52.1 (*C*HCH$_3$), 48.1 (*C*CH$_2$CH$_3$) , 27.2 (CH*C*H$_2$CH$_3$), 16.4 (CH*C*H$_3$), 13.3 (furyl C*C*H$_3$), 10.3 (ethyl CH$_2$*C*H$_3$).

m/z: HRMS (TOF ES$^+$) $C_{23}H_{25}N_3O_7$ [M+H]$^+$ calcd 456.1726; found 456.1772.

Methyl (2-hydroxy-3-((2-(((*R*)-1-(5-methylfuran-2-yl)propyl)amino)-3,4-dioxocyclobut-1-en-1-yl)amino)benzoyl)-*L*-phenylalaninate (30d)

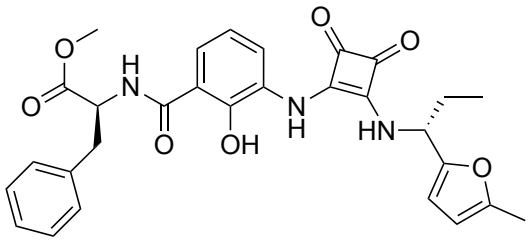

Synthesised following general procedure A using (*R*)-2-hydroxy-3-((2-((1-(5-methylfuran-2-yl)propyl)amino)-3,4-dioxocyclobut-1-en-1-yl)amino)benzoic acid (**34**) (73 mg, 0.11 mmol, 1 eq), 1-(3-dimethylaminopropyl)3-ethylcarbodiimide hydrochloride (48 mg, 0.14 mmol, 1.2 eq), 1-hydroxybenzotriazole (25 mg, 0.16 mmol, 1.5 eq) and methyl phenylalaninate hydrochloride (26 mg, 0.12 mmol, 1 eq). The resulting crude was purified by PTLC (5% MeOH:DCM) to afford an orange oil (18.0 mg, 30%).

LCMS t_R: 6.72 min

^{1}H NMR (DMSO-*d*$_6$) δ 13.26 (s, 1H, O*H*), 9.32 (s, 1H, N*H*) 8.67 (d, J = 8.8 Hz, 1H, N*H*), 7.96 (m, 1H, Ar-C*H*-6), 7.58 (m, 1H, Ar-C*H*-4), 7.26 (m, 5H, Ar-C*H*-5), 6.90 (m, 1H, Ar-C*H*), 6.24 (s, 1H, furan C*H*), 6.03 (dd, 1H, 1.3/3.0 Hz, furan, C*H*), 5.12 (q, 1H, J = 7.8 Hz, NHC*H*CH_2CH_3), 4.72 (m, 1H,C*H*$COOCH_3$), 3.66 (s, 3H, COOC*H*$_3$), 2.25 (d, J = 1.0 Hz, 3H, furan CC*H*$_3$), 1.89 (m, 2H, CHC*H*$_2CH_3$), 0.91 (t, J = 7.3 Hz, 3H, $CHCH_2CH_3$)

^{13}C NMR (DMSO-*d*$_6$) δ 176.4 (squaramide *C*=O) 137.8 (Ar-*C*H), 129.5 (Ar-*C*H), 128.8 (Ar-*C*H), 120.5 (Ar-*C*H), 119.6 (Ar-*C*H), 116.3 (Ar-*C*H), 107.4 (Furan *C*H), 106.9 (Furan *C*H), 54.4 (NH*C*HCH_2CH_3), 53.3 (COO*C*H_3), 52.7 ($CHCH_2(C_6H_5)$ 27.7 (*C*H_2CH_3), 13.8 (Furyl C*C*H_3), 10.74 (CH_2CH_3).

m/z: **HRMS (TOF ES$^+$) $C_{29}H_{29}N_3O_7$ [M+H]$^+$ calcd 532.2039; found 532.2074.**

Methyl (2-hydroxy-3-((2-(((*R*)-1-(5-methylfuran-2-yl)propyl)amino)-3,4-dioxocyclobut-1-en-1-yl)amino)benzoyl)-*L*-histidinate (30j)

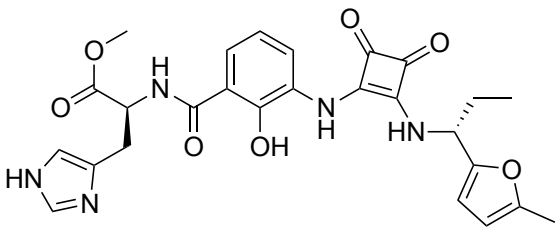

Synthesised following general procedure A using (*R*)-2-hydroxy-3-((2-((1-(5-methylfuran-2-yl)propyl)amino)-3,4-dioxocyclobut-1-en-1-yl)amino)benzoic acid (**34**) (65 mg, 0.18 mmol, 1 eq), 1-(3-dimethylaminopropyl)3-ethylcarbodiimide hydrochloride (42 mg, 0.22 mmol, 1.2 eq), 1-hydroxybenzotriazole (36 mg, 0.23 mmol, 1.2 eq) and methyl histidinate hydrochloride (46 mg, 0.19 mmol, 1 eq). The resulting crude was purified by PTLC (3% MeOH:DCM) to afford a brown solid (4.8 mg, 5%).

LCMS t_R: 4.03 min

^{1}H NMR (DMSO-*d*$_6$) δ 9.43 (s, 1H, N*H*), 8.81 (d, J = 9.0 Hz, 1H, N*H*), 7.91 (m, 1H, Ar-C*H*-6), 7.55 (m, 1H, Ar-C*H*-4), 7.43 (m, 1H, Ar-C*H*-5), 6.85 (s, 1H Ar-C*H*), 6.51 (s, 1H, Ar-C*H*), 6.23 (d, J = 3.1 Hz, 1H, furan C*H*), 6.04 (dd, J = 1.2/3.1 Hz, 1H, furan C*H*), 5.14 (q, J = 7.7 Hz, 1H, C*H*COOCH$_3$), 4.72 (q, J = 6.9 Hz, 1H, C*H*CH$_2$CH$_3$), 3.62 (s, 3H, C(O)OC*H*$_3$), 2.26 (s, 3H, furyl CC*H*$_3$), 1.88 (m, 2H, CHC*H*$_2$CH$_3$), 0.92 (t, J = 7.3 Hz, 3H, CHCH$_2$C*H*$_3$).

^{13}C NMR (DMSO-*d*$_6$) ^{13}C NMR (101 MHz, DMSO) δ 180.5 (squaramide *C*=O), 172.1 (COO*C*H$_3$), 168.4 (NH*C*=O), 163.2 (squaramide C=*C*NH), 152.3 (furan *C*), 151.3 (furan *C*), 134.9 (Ar-*C*OH), 115.7 (Ar-*C*H), 114.5 (Ar-*C*H), 113.4 (Ar-*C*H), 107.4 (furan *C*H), 106.4 (furan *C*H), 52.8 (COO*C*H$_3$), 52.6 (*C*HCH$_2$CH$_3$), 51.9 (CH*C*H$_2$(C$_3$H$_3$N$_2$)), 27.2 (*C*H$_2$CH$_3$), 13.3 (furan C*C*H$_3$), 10.3 (CH$_2$*C*H$_3$).

m/z: HRMS (TOF ES$^+$) $C_{26}H_{27}N_5O_7$ $[M+H]^+$ calcd 522.1944; found 522.1999

Methyl (2-hydroxy-3-((2-(((*R*)-1-(5-methylfuran-2-yl)propyl)amino)-3,4-dioxocyclobut-1-en-1-yl)amino)benzoyl)-*L*-methioninate (30c)

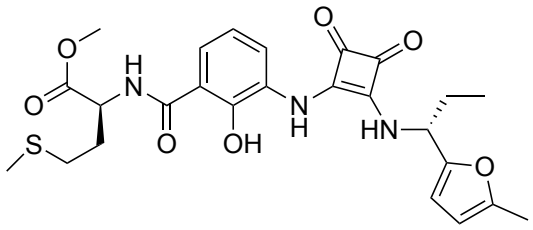

Synthesised following general procedure A using (*R*)-2-hydroxy-3-((2-((1-(5-methylfuran-2-yl)propyl)amino)-3,4-dioxocyclobut-1-en-1-yl)amino)benzoic acid (**34**) (70 mg, 0.19 mmol, 1 eq), 1-(3-dimethylaminopropyl)3-ethylcarbodiimide hydrochloride (46 mg, 0.24 mmol, 1.3 eq), 1-hydroxybenzotriazole (35 mg, 0.23 mmol, 1.2 eq) and methyl histidinate hydrochloride (46 mg, 0.23 mmol, 1.2 eq). The resulting crude was purified by PTLC (3% MeOH:DCM) to afford a yellow oil (7.0 mg, 7%).

LCMS t_R: 6.39 min

^{1}H NMR (DMSO-*d*$_6$) δ 13.39 (s, 0.6H, phenol O*H*) 9.74 – 8.49 (m, 3H, squaramide N*H* and amide N*H*), 7.90 – 7.80 (m, 2H, Ar-C*H*-6 and Ar-C*H*-4), 6.94 (s, 1H, Ar-C*H*-5), 6.26 (s, 1H, furan C*H*), 6.05 (s, 1H, furan C*H*), 5.15 (q, *J* = 7.7 Hz, 1H, C*H*CH$_2$CH$_3$), 4.65 (m, 1H, C*H*CH$_2$CH$_2$SCH$_3$), 3.68 (s, 1H, COOC*H*$_3$), 2.72 – 2.56 (m, 2H, CH$_2$C*H*$_2$SCH$_3$), 2.27 (s, 3H, furan CC*H*$_3$), 2.13 – 2.01 (m, 7H, CHC*H*$_2$CH$_3$ and CHC*H*$_2$CH$_2$SC*H*$_3$), 0.93 (t, *J* = 7.3 Hz, 3H, CHCH$_2$C*H*$_3$).

^{13}C NMR (DMSO-*d*$_6$) δ 172.5 (squaramide C=O), 163.3 (*C*=O), 152.0 (furan *C*CH), 151.4 (furan *C*CH$_3$), 123.5 (Ar-*C*H), 117.2 (Ar-*C*H), 113.2 (Ar-*C*H), 108.5 (furan *C*H), 106.5 (furan *C*H), 52.8 (COO*C*H$_3$), 30.2 (*C*HCH$_2$CH$_2$SCH$_3$) 27.7 (CH*C*H$_2$CH$_3$), 15.0 (SC*H*$_3$) 13.8 (furyl C*C*H$_3$), 10.7 (CH$_2$*C*H$_3$).

m/z: HRMS (TOF ES$^+$) $C_{25}H_{29}N_3O_7S$ $[M+Na]^+$ calcd 539.1624; found 539.1639

Methyl (2-hydroxy-3-((2-(((*R*)-1-(5-methylfuran-2-yl)propyl)amino)-3,4-dioxocyclobut-1-en-1-yl)amino)benzoyl)-*L*-serinate (30g)

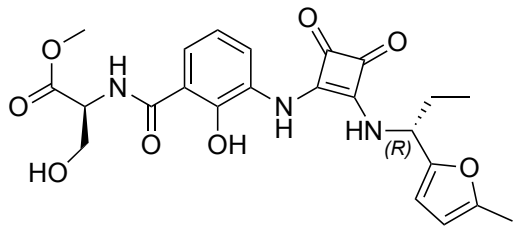

Synthesised following general procedure A using (*R*)-2-hydroxy-3-((2-((1-(5-methylfuran-2-yl)propyl)amino)-3,4-dioxocyclobut-1-en-1-yl)amino)benzoic acid (**34**) (52 mg, 0.14 mmol, 1 eq), 1-(3-dimethylaminopropyl)3-ethylcarbodiimide hydrochloride (32 mg, 0.17 mmol, 1.2 eq), 1-hydroxybenzotriazole (26 mg, 0.17 mmol, 1.2 eq) and methyl histidinate hydrochloride (26 mg, 0.0.15 mmol, 1 eq). The resulting crude was purified by PTLC (4% MeOH:DCM) to afford a yellow powder (5.6 mg, 9%).

LCMS t_R: 5.41 min

^{1}H NMR (DMSO-*d*$_6$) δ 9.45 (s, 1H, squaramide N*H*), 8.84 (m, 1H, squaramide N*H*), 7.87 (m, 1H, Ar-C*H*-6), 7.42 (m, 1H, Ar-C*H*-4), 6.96 (m, 1H, Ar-C*H*-5), 6.23 (d, J = 3.1 Hz, 1H, furan C*H*), 6.04 (d, J = 3.1 Hz, 1H furan C*H*), 5.14 (q, J = 7.8 Hz, 1H C*H*CH$_2$CH$_3$), 4.07 (d, J = 5.2 Hz, 2H, CHC*H*$_2$OH), 3.65 (s, 3H COOC*H*$_3$), 2.26 (d, J = 1.0 Hz, 3H, furan CC*H*$_3$), 1.90 (m, 2H, CHC*H*$_2$CH$_3$), 0.92 (t, J = 7.3 Hz, 3H, CHCH$_2$C*H*$_3$).

^{13}C NMR (DMSO-*d*$_6$) δ 175.2 (squaramide C=O), 163.7 (*C*=O), 153.1 (furan *C*CH), 151.8 (furan *C*CH$_3$), 123.3 (Ar-*C*H), 117.6 (Ar-*C*H), 113.2 (Ar-*C*H), 107.9 (furan *C*H), 106.9 (furan *C*H), 53.3 (COO*C*H$_3$), 52.1 (C*C*H$_2$OH), 27.7 (CH*C*H$_2$CH$_3$), 13.8 (furan C*C*H$_3$), 10.7 (CH$_2$*C*H$_3$).

m/z: HRMS (TOF ES$^+$) $C_{23}H_{25}N_3O_8$ [M+Na]$^+$ calcd 495.1567; found 495.1560

Methyl (2-hydroxy-3-nitrobenzoyl)-*L*-tyrosinate (35e)

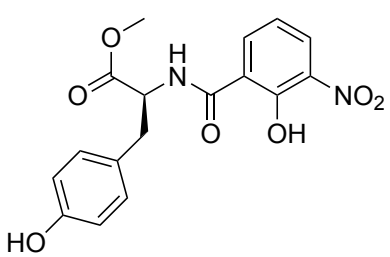

Synthesised according to general procedure B, method B using 3-nitrosalicylic acid (353 mg, 1.93 mmol, 1 eq), oxalyl chloride (496 μL, 5.8 mmol, 3 eq), methyl *L*-tyrosinate (667 mg, 2.9 mmo, 1.5 eql) and DIPEA (550 µL, 3.16 mmol, 1.5 eq). The resulting crude was purified

using FCC (gradient elution: 20 - 80% EtOAc:cyclohexane) affording an orange oil (630 mg, 90%).

LCMS t_R: 2.68 min

^{1}H NMR (DMSO-*d*$_6$) δ 10.51 (s, 1H, phenol O*H*), 9.22 (s, 1H, N*H*), 7.13 – 6.98 (m, 4H, Ar-C*H*), 6.81 – 6.59 (m, 3H, Ar-C*H*), 4.64 (ddd, *J* = 9.0, 7.3, 5.6 Hz, 1H, C*H*CH$_2$(C$_6$OH$_5$)), 3.62 (s, 3H, COOC*H*$_3$), 3.10 – 2.87 (m, 2H, CHC*H*$_2$C$_6$H$_4$O)).

m/z: LCMS (TOF ES$^+$) $C_{17}H_{16}N_2O_7$ $[M+H]^+$ calcd 361.10; found 361.1

Methyl (2-hydroxy-3-nitrobenzoyl)-*L*-leucinate (35b)

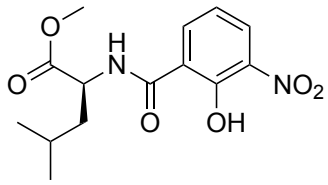

Synthesised according to general procedure B, method B using 3-nitrosalicylic acid (300 mg, 1.63 mmol, 1 eq), oxalyl chloride (420 μL, 4.9 mmol, 3 eq), methyl *L*-leucinate (575 mg, 3.16 mmol, 1.5 eq) and DIPEA (550 µL, 3.16 mmol, 1.5 eq). The resulting crude was purified using FCC (gradient elution: 10 - 50% EtOAc:cyclohexane) to afford an orange oil (420 mg, 82%).

m/z: LCMS (TOF ES$^+$) $C_{14}H_{18}N_2O_6$ $[M+H]^+$ calcd 311.1; found 311.1

Methyl (2-hydroxy-3-nitrobenzoyl)-*L*-threoninate (35f)

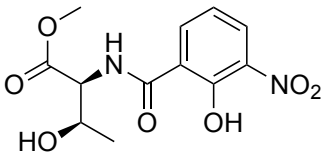

Synthesised according to general procedure B method B using 3-nitrosalicylic acid (310 mg, 1.69 mmol, 1 eq), oxalyl chloride (420 μL, 4.2 mmol, 3 eq), methyl *L*-threoninate (575 mg, 3.30 mmol, 1.5 eq) and DIPEA (555 µL, 3.17 mmol, 1.5 eq). The resulting crude was purified using FCC (gradient elution: 10 - 60% EtOAc:cyclohexane) afforded an orange oil (412 mg, 82%).

LCMS t_R: 2.50 min

m/z: LCMS (TOF ES$^+$) $C_{12}H_{14}N_2O_7$ $[M+H]^+$ calcd 299.1; found 299.1

Methyl (2-hydroxy-3-nitrobenzoyl)-*L*-prolinate (35i)

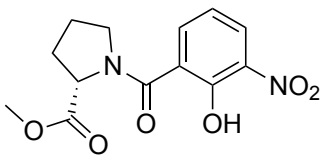

Synthesised according to general procedure B, method B using 3-nitrosalicylic acid (310 mg, 1.69 mmol, 1 eq), oxalyl chloride (440 μL, 5.08 mmol, 3 eq), methyl *L*-threoninate (575 mg, 3.30 mmol, 1.5 eq) and DIPEA (555 µL, 3.17 mmol, 1.5

eq). The resulting crude was purified using FCC (gradient elution: 10 - 60% EtOAc:cyclohexane) to afford an orange oil (382 mg, 77%)

LCMS t_R: 2.67 min

m/z: LCMS (TOF ES$^+$) $C_{13}H_{14}N_2O_6$ $[M+H]^+$ calcd 295.1; found 295.1

Methyl (3-((2-ethoxy-3,4-dioxocyclobut-1-en-1-yl)amino)-2-hydroxybenzoyl)-*L*-tyrosinate (36e)

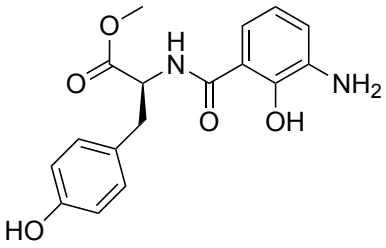

Synthesised according to general procedure C using methyl (2-hydroxy-3-nitrobenzoyl)-*L*-tyrosinate (**35e**) (593 mg, 1.65 mmol, 1 eq) and 10% Pd/C (60 mg, 10% w/w) to afford a dark green oil (480 mg, 88%).

LCMS t_R: 2.50 min

m/z: LCMS (TOF ES$^+$) $C_{17}H_{18}N_2O_5$ $[M+H]^+$ calcd 331.1; found 331.0

Methyl (3-((2-ethoxy-3,4-dioxocyclobut-1-en-1-yl)amino)-2-hydroxybenzoyl)-*L*-leucinate (36b)

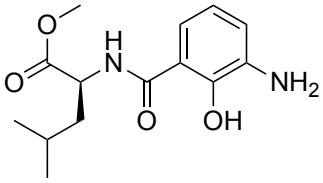

Synthesised according to general procedure C using methyl (2-hydroxy-3-nitrobenzoyl)-*L*-leucinate (**35b**) (405 mg, 1.30 mmol, 1 eq) and 10% Pd/C (42 mg, 10% w/w) to afford a dark green oil (350 mg, 96%).

m/z: LCMS (TOF ES$^+$) $C_{14}H_{20}N_2O_4$ $[M+H]^+$ calcd 281.2; found 281.1

Methyl (3-((2-ethoxy-3,4-dioxocyclobut-1-en-1-yl)amino)-2-hydroxybenzoyl)-*L*-threoninate (36f)

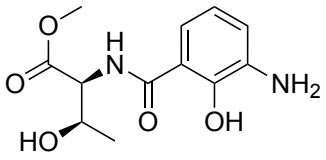

Synthesised according to general procedure C using methyl (2-hydroxy-3-nitrobenzoyl)-*L*-threoninate (**35f**) (299 mg, 1.00 mmol, 1 eq) and 10% Pd/C (31 mg, 10% w/w) to afford a dark green oil (252 mg, 94%).

m/z: LCMS (TOF ES$^+$) $C_{12}H_{16}N_2O_5$ $[M+H]^+$ calcd 269.1; found 269.2

Methyl (3-((2-ethoxy-3,4-dioxocyclobut-1-en-1-yl)amino)-2-hydroxybenzoyl)-*L*-prolinate (36i)

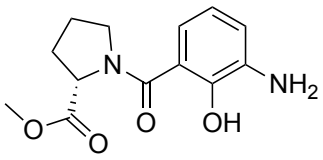

Synthesised according to general procedure C using methyl (2-hydroxy-3-nitrobenzoyl)-*L*-prolinate (**35i**) (359 mg, 1.22 mmol) and 10% Pd/C (37 mg, 10% w/w) to afford a dark green oil (350 mg, 93%).

LCMS t_R: 2.16 min

m/z: LCMS (TOF ES$^+$) $C_{13}H_{16}N_2O_4$ $[M+H]^+$ calcd 265.1; found 265.0

Methyl (3-((2-ethoxy-3,4-dioxocyclobut-1-en-1-yl)amino)-2-hydroxybenzoyl)-*L*-tyrosinate (37e)

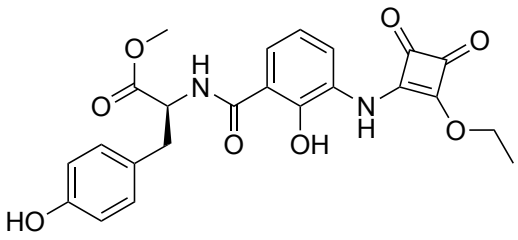

Synthesised according to general procedure D using methyl (3-amino-2-hydroxybenzoyl)-*L*-tyrosinate (**36e**) (208 mg, 0.63 mmol, 1 eq) and 3,4-diethoxycyclobut-3-ene-1,2-dione (111 μL, 0.76 mmol, 1.2 eq) to afford an orange oil as crude which was used without further purification (224 mg).

LCMS t_R: 2.63 min

m/z: LCMS (TOF ES$^+$) $C_{23}H_{22}N_2O_8$ $[M+H]^+$ calcd 455.1; found 455.1

Methyl (3-((2-ethoxy-3,4-dioxocyclobut-1-en-1-yl)amino)-2-hydroxybenzoyl)-*L*-leucinate (37b)

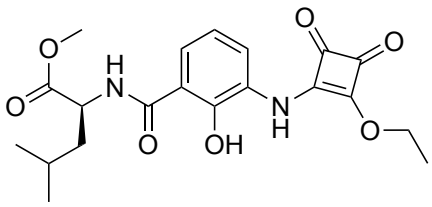

Synthesised according to general procedure D using methyl (3-amino-2-hydroxybenzoyl)-*L*-leucinate (**36b**) (368 mg, 1.34 mmol, 1 eq) and 3,4-diethoxycyclobut-3-ene-1,2-dione (234 μL, 1.51 mmol, 1.2 eq) to afford a viscous brown oil (396 mg) as crude which was used without further purification.

LCMS t_R: 2.85 min

m/z: LCMS (TOF ES$^+$) $C_{20}H_{24}N_2O_7$ $[M+H]^+$ calcd 405.2; found 405.0

Methyl (3-((2-ethoxy-3,4-dioxocyclobut-1-en-1-yl)amino)-2-hydroxybenzoyl)-*L*-threoninate (37f)

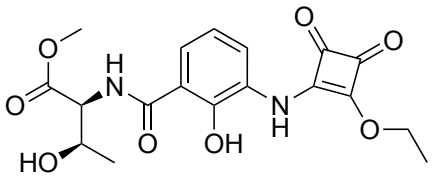

Synthesised according to general procedure D using methyl (3-amino-2-hydroxybenzoyl)-*L*-threoninate (**36f**) (201mg, 0.72 mmol, 1 eq) and 3,4-diethoxycyclobut-3-ene-1,2-dione (133 μL, 0.86 mmol, 1.2 eq) to afford a viscous brown oil as crude (120 mg) which was used without further purification.

LCMS t_R: 2.47 min

m/z: LCMS (TOF ES$^+$) $C_{18}H_{20}N_2O_8$ $[M+H]^+$ calcd 393.1; found 392.9

Methyl (3-((2-ethoxy-3,4-dioxocyclobut-1-en-1-yl)amino)-2-hydroxybenzoyl)-*L*-prolinate (37i)

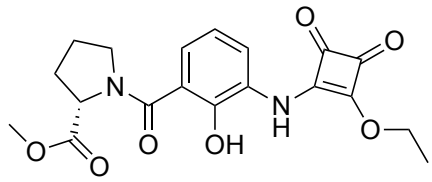

Synthesised according to general procedure D using methyl (3-amino-2-hydroxybenzoyl)-*L*-prolinate (**36i**) (328 mg, 1.24 mmol, 1 eq) and 3,4-diethoxycyclobut-3-ene-1,2-dione (225 μL, 1.50 mmol, 1.2 eq) to afford a viscous brown oil crude (80 mg) which was used without further purification.

m/z: LCMS (TOF ES$^+$) $C_{19}H_{20}N_2O_7$ $[M+H]^+$ calcd 388.1; found 388.0

Methyl (2-hydroxy-3-((2-(((*R*)-1-(5-methylfuran-2-yl)propyl)amino)-3,4-dioxocyclobut-1-en-1-yl)amino)benzoyl)-*L*-tyrosinate (30e)

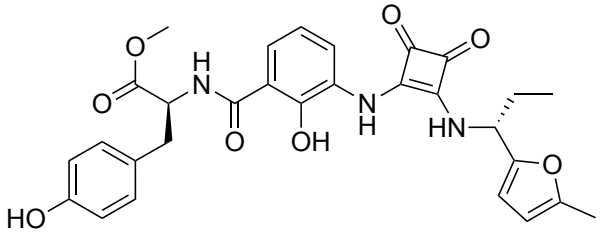

Synthesised according to general procedure E using Methyl (3-((2-ethoxy-3,4-dioxocyclobut-1-en-1-yl)amino)-2-hydroxybenzoyl)-*L*-tyrosinate (**37e**) (80 mg, 0.18 mmol, 1 eq), (*R*)-1-(5-methylfuran-2-yl)propan-1-amine hydrochloride (33 mg, 0.19 mmol, 1.05 eq) and DIPEA (62 μL, 0.35 mmol, 2 eq). The resulting crude was purified by RP-FCC (gradient elution 10-90% MeCN:water) to afford a white solid (1.8 mg, 2%).

LCMS t_R: 6.32 min

^{1}H NMR (DMSO-*d*$_6$) δ 13.26 (s, 1H, O*H*), 9.32 (s, 1H, N*H*) 8.67 (dd, J = 8.8/1.6 Hz, 1H, N*H*), 7.96 (s, 1H, Ar-C*H*-6), 7.58 (dd, J = 8.3/1.4 1H, Ar-C*H*-4), 7.26 (m, 4H, Ar-C*H*), 6.90 (m, 1H, Ar-C*H*-5), 6.24 (s, 1H, furan C*H*), 6.03 (dd, 1H, 1.3/3.0 Hz, furan C*H*), 5.12 (q, 1H, J = 7.8 Hz, C*H*CH_2CH_3), 4.72 (m, 1H, C*H*C(O)OCH_3), 3.66 (s, 3H, C(O)OCH_3), 2.25 (d, J = 1.0 Hz, 3H, furan CCH_3), 1.89 (m, 2H, CHCH_2CH_3), 0.91 (t, J = 7.3 Hz, 3H, $CHCH_2CH_3$)

^{13}C NMR (MeOD) δ 183.8 (squaramide C=O), 181.5 (C=O), 172.1 (C=O), 170.2 (Ar-*C*), 168.9 (Ar-*C*), 163.4 (Ar-*C*), 156.0 (Ar-*C*), 152.0 (squaramide *C*=*C*), 151.8 (squaramide *C*=C) 129.8 (Ar-*C*H), 127.6 (Ar-*C*H), 114.9 (Ar-*C*H), 107.3 (furan *C*H), 105.8 (furan *C*H), 54.4 (*C*H), 53.7 (*C*H), 51.4 (CH_2), 35.9 (CH$CH_2(C_6H_5O)$), 27.3 (CH_2CH_3), 12.0 (furan CCH_3), 9.3 ($CHCH_2CH_3$).

m/z: HRMS (TOF ES$^+$) $C_{29}H_{29}N_3O_8$ $[M+Na]^+$ calcd 547.1852; found 570.1849

Methyl (2-hydroxy-3-((2-(((*R*)-1-(5-methylfuran-2-yl)propyl)amino)-3,4-dioxocyclobut-1-en-1-yl)amino)benzoyl)-*L*-leucinate (30b)

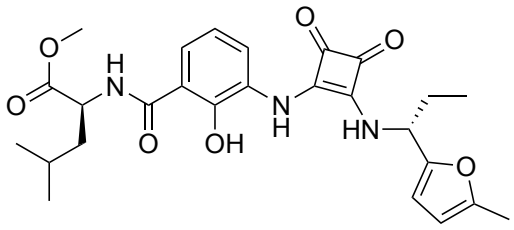

Synthesised according to general procedure E using Methyl (3-((2-ethoxy-3,4-dioxocyclobut-1-en-1-yl)amino)-2-hydroxybenzoyl)-*L*-leucinate (**37b**) (65 mg, 0.17 mmol, 1 eq), (*R*)-1-(5-methylfuran-2-yl)propan-1-amine hydrochloride (32 mg, 0.18 mmol, 1.05 eq) and DIPEA (55 μL, 0.30 mmol, 1.8 eq). The resulting crude was purified by PTLC (3:1:4 EtOAC:IMS:cyclohexane) to afford a white solid (22 mg, 26%).

^{1}H NMR (CD_3OD) δ 8.13 (dd, *J* = 8.0/1.6 Hz, 1H, Ar-C*H*-6), 7.56 (dd, *J* = 8.0/1.4 Hz, 1H, Ar-C*H*-4), 6.88 (dd, *J* = 8.1/8.1 Hz, 1H, Ar-C*H*-5), 6.21 (d, *J* = 3.1 Hz, 1H, furan C*H*), 6.00 – 5.94 (m, 1H, furan C*H*), 5.22 (t, *J* = 7.2 Hz, 1H, C*H*$CH_2CH(CH_3)_2$), 4.71 (dd, *J* = 10.2/4.2 Hz, 1H, NHC*H*CH_2CH_3), 3.75 (s, 3H, COOCH_3), 2.28 (s, 3H, furan CCH_3), 2.14 – 1.65 (m, 5H, CHCH_2CH_3 and CHCH_2C*H*$(CH_3)_2$), 1.06 – 0.92 (m, 9H, $CHCH_2CH(CH_3)_2$ and $CHCH_2CH_3$).

LCMS t_R: 6.17 min

m/z: HRMS (TOF ES$^+$) $C_{26}H_{31}N_3O_7$ [M+Na]$^+$ calcd 520.2060; found 520.2052

Methyl (2-hydroxy-3-((2-(((*R*)-1-(5-methylfuran-2-yl)propyl)amino)-3,4-dioxocyclobut-1-en-1-yl)amino)benzoyl)-*L*-threoninate (30f)

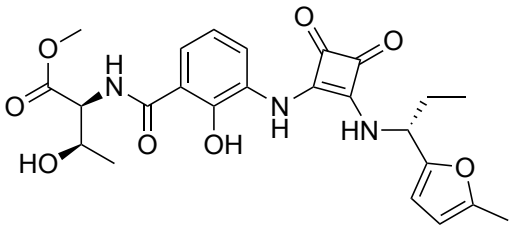

Synthesised according to general procedure E using Methyl (3-((2-ethoxy-3,4-dioxocyclobut-1-en-1-yl)amino)-2-hydroxybenzoyl)-*L*-threoninate (**37f**) (49 mg, 0.14 mmol, 1 eq), (*R*)-1-(5-methylfuran-2-yl)propan-1-amine hydrochloride (26 mg, 0.15 mmol, 1.05 eq) and DIPEA (49 μL, 0.30 mmol, 2 eq). The resulting crude was purified by RP-FCC (gradient elution 10-90% MeCN:water) to afford a yellow oil (1.7 mg, 1%). LCMS t_R: 5.86 min

^{1}H NMR (CD_3OD) δ 8.16 (d, *J* = 8.0 Hz, 1H, Ar-C*H*-6), 7.59 (dd, *J* = 8.1/1.4 Hz, 1H, Ar-C*H*-4), 6.92 (dd, *J* = 8.1/8.1 Hz, 1H, Ar-C*H*-5), 6.22 (d, *J* = 3.1 Hz, 1H, furan C*H*), 5.98 (dd, *J* = 3.1/1.2 Hz, 1H, furan C*H*), 5.24 (t, *J* = 7.2 Hz, 1H, C*H*CH_2CH_3), 4.75 (d, *J* = 3.4 Hz, 1H, C*H*$CHCH_3$(OH)), 4.42 (qd, *J* = 6.4/3.4 Hz, 1H, $CHCHCH_3$(OH)), 3.80 (s, 3H, $COOCH_3$), 2.29 (d, *J* = 1.0 Hz, 3H, furan CCH_3), 2.14 – 1.89 (m, 2H, $CHCH_2CH_3$), 1.26 (d, *J* = 6.5 Hz, 3H, $CHCHCH_3$(OH)), 1.03 (t, *J* = 7.4 Hz, 3H, $CHCH_2CH_3$).

m/z: HRMS (TOF ES$^+$) $C_{24}H_{27}N_3O_8$ [M+H]$^+$ calcd 486.1832; found 486.1856

Methyl (2-hydroxy-3-((2-(((*R*)-1-(5-methylfuran-2-yl)propyl)amino)-3,4-dioxocyclobut-1-en-1-yl)amino)benzoyl)-*L*-prolinate (30i)

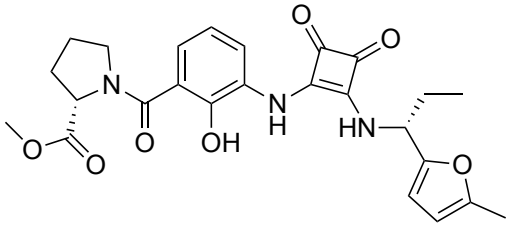

Synthesised according to general procedure E using Methyl (3-((2-ethoxy-3,4-dioxocyclobut-1-en-1-yl)amino)-2-hydroxybenzoyl)-*L*-prolinate (**37i**) (132 mg, 0.34

mmol, 1 eq), (*R*)-1-(5-methylfuran-2-yl)propan-1-amine hydrochloride (63 mg, 0.37 mmol, 1.1 eq) and DIPEA (119 μL, 0.61 mmol, 1.8 eq). The resulting crude was purified by RP-FCC (gradient elution 10-90% MeCN:water) to afford a white solid (5.7 mg, 4%).

^{1}H NMR (400 MHz, MeOD) δ 8.06 (dd, *J* = 8.1/1.5 Hz, 1H, Ar-C*H*-6), 7.29 (dd, *J* = 7.9/1.4 Hz, 1H, Ar-C*H*-4), 6.95 (dd, *J* = 8.0/8.0 Hz, 1H, Ar-C*H*-5), 6.22 (d, *J* = 3.1 Hz, 1H, furan C*H*), 5.98 (dd, *J* = 3.1/1.1 Hz, 1H, furan C*H*), 4.74 - 4.61 (m, *J* = 7.1 Hz, 1H, C*H*COOCH$_3$), 3.89 - 3.66 (m, 4H, COOC*H*$_3$ and NHC*H*CH$_2$CH$_3$), 2.39 (m, *J* = 8.4 Hz, 1H, C*H*), 2.29 (d, *J* = 1.0 Hz, 3H, furyl CC*H*$_3$), 2.12 – 1.90 (m, 6H, C*H*$_2$), 1.03 (t, *J* = 7.4 Hz,3H, NHCHCH$_2$C*H*$_3$).

LCMS t_R: 5.95 min

m/z: HRMS (TOF ES$^+$) $C_{25}H_{27}N_3O_7$ $[M+H]^+$ calcd 482.1883; found 482.1923

Methyl *N*-methyl-*L*-alaninate (39b)

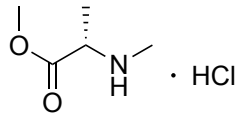

· HCl

N-methyl-*L*-alanine hydrochloride (1.02 g, 9.9 mmol, 1 eq) was dissolved in MeOH (40 mL) to which acetyl chloride (7.05 mL, 99 mmol, 10 eq) was added dropwise at 0 ℃. The reaction was allowed to warm to ambient temperatures and then refluxed for 18 hr. The reaction was monitored by TLC. Upon completion the mixture was concentrated under reduced pressure affording a clear colourless oil (1.08 g, 96%).

^{1}H NMR (CDCl$_3$) δ 3.95 (q, *J* = 6.2 Hz, 1H, C*H*CH$_3$) 3.84 (s, 3H, COOC*H*$_3$), 2.82 – 2.77 (m, *J* = 5.4 Hz, 3H, NHC*H*$_3$), 1.73 (d, *J* = 7.1 Hz, 1H, NHC*H*$_3$).

m/z: LCMS (TOF ES$^+$) $C_5H_{11}NO_2$ $[M+H]^+$ calcd 118.1; found 118.0

Methyl methyl-*L*-phenylalaninate (39d)

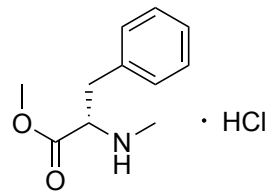

· HCl

Methyl-*L*-phenylalaninate hydrochloride (500 mg, 2.8 mmol, 1 eq) was dissolved in MeOH (20 mL) to which acetyl chloride (2 mL, 28 mmol, 10 eq) was added dropwise at 0 ℃. The reaction was allowed to warm to ambient temperatures and then refluxed for 18 hr. The reaction was monitored by TLC. Upon completion, the mixture was concentrated under reduced pressure affording a clear colourless oil (530 mg, 98%).

^{1}H NMR ($CDCl_3$) δ 7.63 – 7.05 (m, 5H, Ar-C*H*), 4.47 – 4.11 (m, 1H, C*H*), 3.64 (s, 3H, COOCH_3), 3.53 – 3.29 (m, 1H, CHCH_{2a}(C_6H_5)), 3.13 (m, 1H, CHCH_{2b}(C_6H_5)), 2.57 (s, 3H, NHCH_3).

m/z: LCMS (TOF ES$^+$) $C_{11}H_{15}NO_2$ $[M+H]^+$ calcd 194.1; found 194.0

Methyl methyl-*L*-serinate (39g)

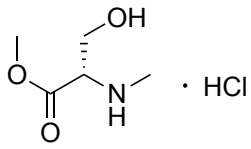

Methyl-*L*-serinate hydrochloride (216 mg, 1.38 mmol, 1 eq) was dissolved in MeOH (5 mL) to which acetyl chloride (1.01 mL, 13.80 mmol, 10 eq) was added dropwise at 0 ℃. The reaction was allowed to warm to ambient temperatures and then refluxed for 18 hr. The reaction was monitored by TLC. Upon completion the mixture was concentrated under reduced pressure. The resulting solid was triturated in Et_2O affording a white solid (196 mg, 84%).

^{1}H NMR (DMSO-*d_6*) δ 9.40 (s, 1H CH_2OH), 5.71 (s, 1H, N*H*CH_3), 4.38 – 4.06 (m, 1H, C*H*CH_2OH), 4.02 – 3.80 (m, 2H, CHCH_2OH), 3.76 (s, 3H, CH_3OCO), 2.57 (s, 1H CHN*H*CH_3).

m/z: LCMS (TOF ES$^+$) $C_5H_{11}NO_3$ $[M+H]^+$ calcd 134.1; found 134.1

Methyl *N*-(2-hydroxy-3-nitrobenzoyl)-*N*-methyl glycinate (40h)

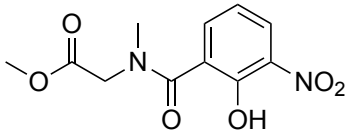

Synthesised according to general procedure F using 3-nitrosalicylic acid (507 mg, 2.77 mmol, 1 eq), oxalyl chloride (720 μL, 8.4 mmol, 3 eq), methyl methyl *L*-glycinate (582 mg, 4.10 mmol, 1.5 eq) and DIPEA (1.7 mL, 9.75 mmol, 1.5 eq). The resulting crude oil was purified using FCC (10 - 80% EtOAc:cyclohexane) affording an orange oil (422 mg, 57%).

^{1}H NMR (DMSO-*d_6*) δ 10.73 (s, 1H, phenol O*H*), 8.14 – 7.83 (m, H, Ar-C*H*-4), 7.48 (dd, *J* = 7.4/7.4 Hz, 1H, Ar-C*H*-6), 7.26 – 6.99 (m, 1H, Ar-C*H*-5), 4.27 (s, 1.4H, CH_{2a}), 4.03 (s, 1H, CH_{2b}), 3.69 (d, *J* = 5.8 Hz, 3H, COOCH_3), 3.08 – 2.77 (m, 3H, NCH_3).

^{13}C NMR (DMSO-*d_6*) δ 170.5 (C=O), 165.7 (C=O), 144.2 (Ar-*C*OH), 136.6 (Ar-*C*H), 134.2 (Ar-*C*H), 129.2 (Ar-*C*H), 127.0 (Ar-*C*H), 126.3 (Ar-*C*H), 62.6 (C_aH_2), 62.3 (C_bH_2), 53.3 (COOC_aH_3) 52.6 (COOC_bH_3), 32.6 (NCH_{3a}), 31.3 (NCH_{3b}).

m/z: LCMS (TOF ES$^+$) $C_{11}H_{12}N_2O_6$ $[M+H]^+$ calcd 269.1; found 269.1

Methyl *N*-(2-hydroxy-3-nitrobenzoyl)-*N*-methyl-*L*-alaninate (40a)

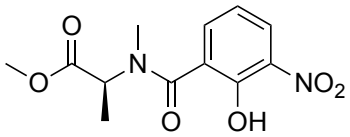

Synthesised according to general procedure F using 3-nitrosalicylic acid (1.02 g, 5.60 mmol, 1 eq), oxalyl chloride (1.4 mL, 16.7 mmol, 3 eq), methyl methyl-*L*-alaninate (**39b**) (1.05 g, 6.70 mmol, 1.5 eq), and DIPEA (3.2 mL, 17.80 mmol, 1.5 eq). The resulting crude was purified using FCC (gradient elution: 20 - 80% EtOAc:cyclohexane) to afford an orange oil (1.01 g, 70%).

^{1}H NMR (DMSO-*d*$_6$) δ 10.69 (s, 1H, phenol O*H*), 8.28 – 7.87 (m, 1H, Ar-C*H*-4), 7.86 – 7.37 (m, 1H, Ar-C*H*-6), 7.33 – 6.81 (m, 1H, Ar-C*H*-5), 5.01 (q, *J* = 7.2 Hz, 0.6H, C$H_{\mathbf{a}}$CH$_3$), 4.39 – 4.20 (m, 0.4H, C$H_{\mathbf{b}}$CH$_3$), 3.80 – 3.55 (m, 3H, COOCH_3), 2.94 – 2.84 (m, 1H, NC$H_{3\mathbf{a}}$), 2.78 (s, 2H, NC$H_{3\mathbf{b}}$), 1.63 – 1.16 (m, 3H, CHCH_3).

^{13}C NMR (DMSO-*d*$_6$) δ 166.5 (C=O), 161.7 (C=O), 144.3 (Ar-*C*OH), 136.7 (Ar-*C*H), 136.3 (Ar-*C*H), 129.7 (Ar-*C*H), 127.0 (Ar-*C*H), 126.3 (Ar-*C*H), 62.6 (*C*$_{\mathbf{a}}$H$_2$), 62.3 (*C*$_{\mathbf{b}}$H$_2$), 53.3 (COO*C*$_{\mathbf{a}}$H$_3$) 52.6 (COO*C*$_{\mathbf{b}}$H$_3$), 32.6 (N*C*$_{\mathbf{a}}$H$_3$**)**, 31.3 (N*C*$_{\mathbf{b}}$H$_3$), 14.4 (CHC$H_{3\mathbf{a}}$), 14.3 (CH*C*H$_{3\mathbf{b}}$).

m/z: LCMS (TOF ES$^+$) $C_{12}H_{14}N_2O_6$ $[M+H]^+$ calcd 283.1; found 283.1

Methyl *N*-(2-hydroxy-3-nitrobenzoyl)-*N*-methyl-*L*-phenylalaninate (40d)

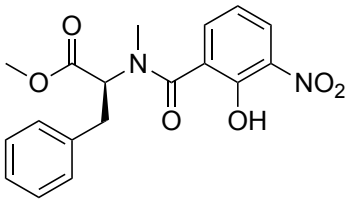

Synthesised according to general procedure F using 3-nitrosalicylic acid (510 mg, 2.79 mmol, 1 eq), oxalyl chloride (717 µL, 8,30 mmol, 3 eq), methyl methyl-*L*-phenylalaninate (**39d**) (645 mg, 2.79 mmol, 1.5 eq), and DIPEA (1.16 mL, 6.60 mmol, 1.5 eq). The resulting crude was purified by FCC gradient (gradient elution: 10% - 50% EtOAc:Cyclohexane) to afford a yellow oil (810 mg, 81%).

^{1}H NMR (DMSO-*d*$_6$) δ 10.31 (s, 0.7H, phenol O*H*), 8.13 – 7.85 (m, 1H, Ar-C*H*-4), 7.50 – 6.43 (m, 7H, Ar-C*H*), 5.17 (dd, *J* = 10.4/5.3 Hz, 0.7H, CH_aCH$_2$(C$_6$H$_5$)), 4.31 (dd, *J* = 9.4/5.6 Hz, 0.3H, C$H_{\mathbf{a}}$CH$_2$(C$_6$H$_5$)), 3.76 – 3.58 (m, 3H, COOCH_3), 3.21 – 2.90 (m, 1H, CHCH_2(C$_6$H$_5$) and NC$H_{3\mathbf{a}}$), 2.63 (s, 2H, NC$H_{3\mathbf{b}}$).

^{13}C NMR (DMSO-*d*$_6$) δ 171.0 (ester C=O), 167.7 (amide C=O), 138.0 (aryl *C*H), 136.7 (aryl *C*H), 134.1 (aryl *C*H), 129.7 (aryl *C*H), 129.6 (aryl *C*H), 128.9 (aryl *C*H), 128.8 (aryl *C*H), 127.0 (aryl *C*H), 126.3 (aryl *C*H), 62.6 (*C*$_{\mathbf{a}}$HCH$_2$(C$_6$H$_5$)), 59.1 (*C*$_{\mathbf{b}}$HCH$_2$(C$_6$H$_5$)), 52.6 (ester COO*C*$_{\mathbf{b}}$) H$_3$), 34.8 (N*C*$_{\mathbf{a}}$H$_{3\mathbf{a}}$**)**, 34.3 (N*C*$_{\mathbf{b}}$H$_3$).

m/z: LCMS (TOF ES$^+$) $C_{18}H_{18}N_2O_6$ [M+H]$^+$ calcd 359.1; found 359.1

Methyl *N*-(2-hydroxy-3-nitrobenzoyl)-*N*-methyl-*L*-serinate (40g)

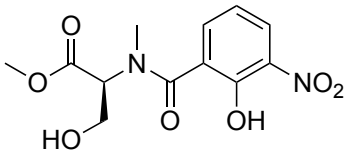

Synthesised according to general procedure F using 3-nitrosalicylic acid (136 mg, 0.73 mmol, 1 eq), oxalyl chloride (191 μL, 2.20 mmol, 3 eq), methyl methyl-*L*-serinate (**39g**) (150 mg, 0.89 mmol, 1.5 eq), and DIPEA (280 μL, 1.60 mmol, 1.5 eq). The resulting crude was purified by FCC (gradient elution: 10% - 70% EtOAc:Cyclohexane) to afford a yellow oil (128 mg, 58%).

^{1}H NMR (DMSO-*d*$_6$) δ 11.05 – 10.21 (m, 1H, phenol O*H*), 8.14 – 7.98 (m, 1H, Ar-C*H*-4), 7.56 – 7.44 (m, 1H, aryl C*H*-6), 7.21 – 6.96 (m, 1H, aryl C*H*-5), 5.81 – 5.70 (m, 1H, CHCH$_2$O*H*), 5.22 – 4.94 (m, 0.7H, C*H*$_\mathbf{a}$CH$_2$OH), 4.18 (t, *J* = 4.3 Hz, 0.3H, C*H*$_\mathbf{b}$CH$_2$OH), 3.96 – 3.57 (m, 5H, COOC*H*$_3$ and CHC*H*$_2$OH), 3.00 (s, 1.2H, NC*H*$_{3\mathbf{a}}$), 2.87 (s, 1.8H, NC*H*$_{3\mathbf{b}}$).

m/z: LCMS (TOF ES$^+$) $C_{12}H_{14}N_2O_7$ [M+H]$^+$ calcd 299.1; found 299.0

Methyl *N*-(3-amino-2-hydroxybenzoyl)-*N*-methyl-glycinate (41h)

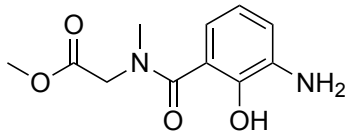

Synthesised according to general procedure G using methyl *N*-(2-hydroxy-3-nitrobenzoyl)-*N*-methyl glycinate (**40h**) (200 mg, 0.75 mmol, 1) and 10% Pd/C (20 mg, 10% w/w) to afford a green oil (165 mg).

^{1}H NMR (DMSO-*d*$_6$) δ 6.67 – 6.53 (m, 2H, Ar-C*H*-6 and Ar-C*H*-4), 6.37 – 6.29 (m, 1H, Ar-C*H*-5), 3.80 – 3.50 (m, 3H, COOC*H*$_3$), 2.97 – 2.66 (m, 3H, NC*H*$_3$).

^{13}C NMR (DMSO-*d*$_6$) δ 172.2 (*C*=O), 170.3 (*C*=O), 138.3 (Ar-*C*OH), 120.7 (Ar-*C*H), 115.8 (Ar-*C*H), 115.2 (Ar-*C*H), 52.8 (COO*C*H$_3$), 52.5 (*C*HCH$_3$), 26.8 (N*C*H$_3$).

m/z: LCMS (TOF ES$^+$) $C_{11}H_{14}N_2O_4$ [M+H]$^+$ calcd 239.1; found 239.1

Methyl *N*-(3-amino-2-hydroxybenzoyl)-*N*-methyl-*L*-alaninate (41a)

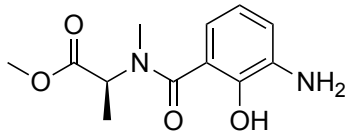

Synthesised according to general procedure G using Methyl *N*-(2-hydroxy-3-nitrobenzoyl)-*N*-methyl alaninate (**40a**) (502 mg, 1.98 mmol, 1 eq) and 10% Pd/C (50 mg, 10% w/w). The resulting crude was purified by FCC (isocratic 20% EtOAc:Cyclohexane + 1% TEA) to afford a green oil (495 mg, 99%).

^{1}H NMR (DMSO-*d*$_6$) δ 6.71 – 6.59 (m, 2H, Ar-C*H*-4 and Ar-C*H*-6), 6.38 – 6.27 (m, 1H, Ar-C*H*-5), 3.82 – 3.53 (m, 3H, COOCH_3), 2.97 – 2.66 (m, 3H, NCH_3), 1.55 – 1.30 (m, 3H, CHCH_3).

^{13}C NMR (DMSO-*d*$_6$) δ 172.2 (*C*=O), 170.3 (*C*=O), 138.3 (Ar-*C*OH), 120.7 (Ar-*C*H), 115.8 (Ar-*C*H), 115.2 (Ar-*C*H), 52.8 (COO*C*H_3), 52.5 (*C*HCH$_3$), 26.8 (N*C*H$_3$), 14.6 (CH*C*H$_3$).

m/z: LCMS (TOF ES$^+$) $C_{12}H_{16}N_2O_4$ $[M+H]^+$ calcd 253.1; found 253.0

Methyl *N*-(3-amino-2-hydroxybenzoyl)-*N*-methyl-*L*-phenylalaninate (41d)

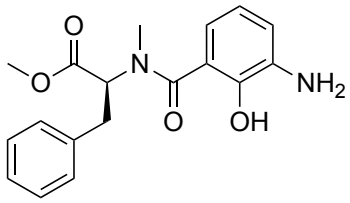

Synthesised as described in General procedure G using Methyl *N*-(2-hydroxy-3-nitrobenzoyl)-*N*-methyl phenylalaninate (**40d**) (720 mg, 2.01 mmol, 1 eq) and 10% Pd/C (75 mg, 10% w/w) to afford a green oil (602 mg, 91%).

^{1}H NMR (DMSO-*d*$_6$) δ 10.31 (s, 0.6H, phenol O*H*), 8.13 – 6.84 (m, 8H, Ar-C*H*), 5.02 (dd, *J* = 10.4/5.3 Hz, 0.7H, C$H_{\mathbf{a}}$CH$_2$(C$_6$H$_5$)), 4.30 (dd, *J* = 9.4/5.6 Hz, 0.3H, C$H_{\mathbf{b}}$CH$_2$(C$_6$H$_5$)), 3.75 – 3.57 (m, 3H, COOCH_3), 3.25 – 2.96 (m, 3H, CHCH_2(C$_6$H$_5$) and NC$H_{3\mathbf{a}}$), 2.63 (s, 2H, NC$H_{3\mathbf{b}}$).

m/z: LCMS (TOF ES$^+$) $C_{18}H_{20}N_2O_4$ $[M+H]^+$ calcd 329.2; found 329.2

Methyl *N*-(3-amino-2-hydroxybenzoyl)-*N*-methyl-*L*-serinate (41g)

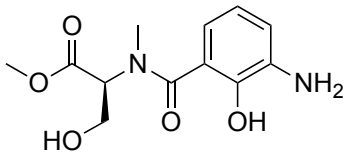

Synthesised according to general procedure G using Methyl *N*-(2-hydroxy-3-nitrobenzoyl)-*N*-methyl serinate (**40g**) (120 mg, 0.40 mmol, 1 eq) and 10% Pd/C (13 mg, 10% w/w) to afford a green oil (109 mg, 98%).

m/z: LCMS (TOF ES$^+$) $C_{12}H_{16}N_2O_5$ $[M+H]^+$ calcd 269.1; found 269.0

Methyl-*N*-(3-((2-ethoxy-3,4-dioxocyclobut-1-en-1-yl)amino)-2-hydroxybenzoyl)-*N*-methylglycinate (42h)

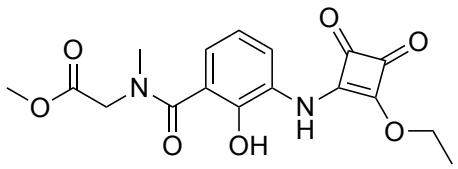

Synthesised according to general procedure H using Methyl *N*-(3-amino-2-hydroxybenzoyl)-*N*-methyl-glycinate (**41h**) (140 mg, 0.58 mmol, 1 eq) and 3,4-diethoxycyclobut-3-ene-1,2-dione (105 µL, 0.71 mmol, 1.2 eq). The crude was purified by RP-FCC (gradient 10% - 80% MeCN:water) to afford a yellow semisolid (125 mg, 59%).

^{1}H NMR (DMSO-*d*$_6$) δ 9.80 (s, 1H, N*H*), 7.23 (d, *J* = 7.2 Hz, 1H, Ar-C*H*-6), 7.12 – 6.81 (m, 2H, Ar-C*H*), 4.65 (q, *J* = 7.0 Hz, 2H, COC*H*$_2$CH$_3$), 4.40 – 4.00 (m, 2H, (NCH$_3$)C*H*$_2$), 3.68 (m, 3H, COOC*H*$_3$), 3.08 – 2.80 (m, 3H, CH$_2$NC*H*$_3$), 1.33 (t, *J* = 7.0 Hz, 3H, COCH$_2$C*H*$_3$).

^{13}C NMR (DMSO-*d*$_6$) δ 184.5 (squaramide C=O), 178.5 (*C*=O), 171.9 (*C*=O), 170.1 (*C*OCH$_2$CH$_3$), 169.2 (Ar-*C*OH), 165.4 (*C*=C), 126.6 (Ar-*C*H), 126.1 (Ar-*C*H), 120.0 (Ar-*C*H), 70.0 (O*C*H$_2$CH$_3$), 52.3 (CH$_3$N*C*H$_2$), 47.6 (COO*C*H$_3$), 35.7 (CH$_3$N*C*H2), 16.1 (OCH$_2$*C*H$_3$).

m/z: LCMS (TOF ES$^+$) $C_{17}H_{18}N_2O_7$ $[M+H]^+$ calcd 363.1; found 363.2

Methyl-*N*-(3-((2-ethoxy-3,4-dioxocyclobut-1-en-1-yl)amino)-2-hydroxybenzoyl)-*N*-methyl-*L*-alaninate (42a)

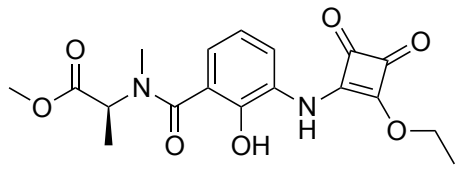

Synthesised according to general procedure H using Methyl *N*-(3-amino-2-hydroxybenzoyl)-*N*-methyl-alaninate (**41a**) (53 mg, 0.21 mmol, 1 eq) and 3,4-diethoxycyclobut-3-ene-1,2-dione (38 µL, 0.25 mmol, 1.2 eq). The crude was purified by RP-FCC (gradient 10% - 80% MeCN:water) to afford a yellow oil (10 mg, 13%)**.**

^{1}H NMR (DMSO-*d*$_6$) δ 7.34 – 7.16 (m, 2H, Ar-C*H*-6 and N*H*), 7.09 – 6.83 (m, 2H, Ar-C*H*-4 and Ar-C*H*-5), 5.00 (m, 0.7H, C*H*$_a$CH$_3$), 4.65 (q, *J* = 7.1 Hz, 1H, ethoxy OC*H*$_2$CH$_3$), 4.10 (m, 1.4H, C*H*$_b$CH$_3$), 3.65 (s, 3H, COOC*H*$_3$), 2.89 – 2.79 (m, 3H, amide NC*H*$_3$), 1.49 – 1.40 (m, 3H, CHC*H*$_3$), 1.33 (t, *J* = 7.0 Hz, 3H, OCH$_2$C*H*$_3$).

^{13}C NMR (DMSO-*d*$_6$) δ 184.5 (C=O), 178.57 (C=O), 171.8 (C=O), 169.0 (C=*C*), 129.6 (C=*C*), 128.6 (Ar-*C*), 126.8 (Ar-*C*), 126.8 (Ar-*C*), 126.0 (Ar-*C*), 125.7 (Ar-*C*), 119.8 (Ar-

*C*H), 69.5 (*C*H$_2$CH$_3$), 64.7 (*C*HCH$_3$), 49.1 (COO*C*H$_3$), 34.4 (N*C*H$_3$), 16.1 (C*H*$_3$), 14.5 (*C*H$_3$).

m/z: LCMS (TOF ES$^+$) $C_{18}H_{20}N_2O_7$ [M+H]$^+$ calcd 377.1; found 377.1

Methyl-*N*-(3-((2-ethoxy-3,4-dioxocyclobut-1-en-1-yl)amino)-2-hydroxybenzoyl)-*N*-methyl-*L*-phenylalannate (42d)

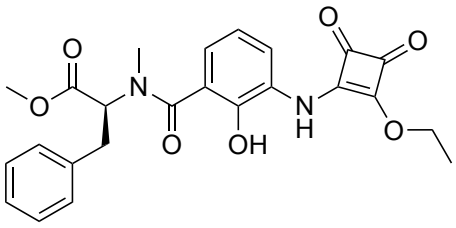

Synthesised according to general procedure H using Methyl *N*-(3-amino-2-hydroxybenzoyl)-*N*-methyl-phenylalaninate (**41d**) (315 mg, 0.96 mmol, 1 eq) and 3,4-diethoxycyclobut-3-ene-1,2-dione (171 µL, 1.06 mmol, 1.2 eq). The crude was purified by RP-FCC (gradient 10% - 80% MeCN:water) to afford a yellow oil (170 mg, 40%).

^{1}H NMR (MeOD) δ 7.60 – 6.60 (m, 8H,Ar-C*H*), 5.49 (s, 1H, 0.8, C*H*CH$_2$), 4.75 (q, *J* = 7.1 Hz, 2H, OC*H*$_2$CH$_3$), 3.78 (s, 3H, COOC*H*$_3$), 3.53 – 2.66 (m, 5H CHC*H*$_2$ and NC*H*$_3$), 1.42 (t, *J* = 7.1 Hz, 3H, OCH$_2$C*H*$_3$).

m/z: LCMS (TOF ES$^+$) $C_{24}H_{24}N_2O_7$ [M+H]$^+$ calcd 453.2; found 453.2

Methyl-*N*-(3-((2-ethoxy-3,4-dioxocyclobut-1-en-1-yl)amino)-2-hydroxybenzoyl)-*N*-methyl-*L*-serinate (42g)

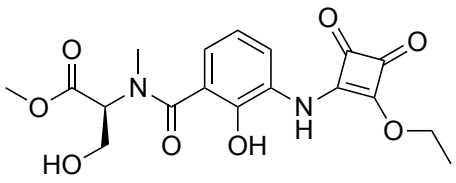

Synthesised according to general procedure H using Methyl *N*-(3-amino-2-hydroxybenzoyl)-*N*-methyl-serinate (**41g**) (109 mg, 0.41 mmol, 1 eq) and 3,4-diethoxycyclobut-3-ene-1,2-dione (72 µL, 0.49 mmol, 1.2 eq). The resulting crude was purified by RP-FCC (gradient 10% - 80% MeCN:water) to afford a yellow oil (8 mg, 7%).

^{1}H NMR (DMSO-*d*$_6$) δ 10.12 (s, 0.9H, O*H*), 9.47 (s, 1H, NH), 7.22 (dd, *J* = 7.8/7.8 Hz, 1H, Ar-C*H*-6), 7.15 – 6.74 (m, 2H, Ar-C*H*-4 and Ar-C*H*-5), 5.01 (s, 1.2H, C*H*$_\mathbf{a}$CH$_2$OH), 4.65 (q, *J* = 7.2 Hz, 2H, COC*H*$_2$CH$_3$), 4.30 (m, 0.8H, C*H*$_\mathbf{b}$CH$_2$OH), 4.03 – 3.52 (m, 5.6H, COOC*H*$_3$ and NCHC*H*$_{2\mathbf{a}}$OH), 3.12 – 2.80 (m, 3.4H, O=CNC*H*$_3$ and NCHC*H*$_{2\mathbf{b}}$OH), 1.33 (t, *J* = 7.0 Hz, 3H, COCH$_2$C*H*$_3$).

^{13}C NMR (DMSO-*d*$_6$) δ 184.6 (*C*=O), 126.5 (Ar-C), 126.1 (Ar-C), 120.0 (Ar-C), 69.6 (CO*C*H$_2$CH$_3$), 59.4 (COO*C*H$_3$), 52.4 (N*C*H$_3$), 16.1 (COCH$_2$*C*H$_3$).

m/z: LCMS (TOF ES$^+$) $C_{18}H_{20}N_2O_8$ [M+H]$^+$ calcd 393.1; found 393.2

Methyl (*R*)-*N*-(2-hydroxy-3-((2-((1-(5-methylfuran-2-yl)propyl)amino)-3,4-dioxocyclobut-1-en-1-yl)amino)benzoyl)-*N*-methylglycinate (43h)

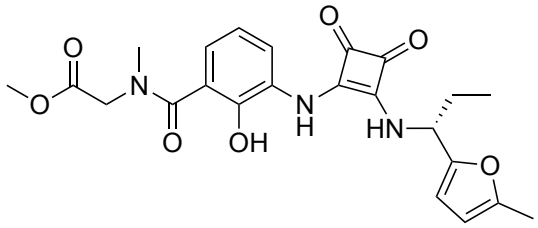

Synthesised according to general procedure I using methyl *N*-(3-((2-ethoxy-3,4-dioxocyclobut-1-en-1-yl)amino)-2-hydroxybenzoyl)-*N*-methyl-*L*-glycinate (**42h**) (113 mg, 0.31 mmol, 1 eq); (*R*)-1-(5-methylfuran-2-yl)propan-1-amine hydrochloride (66 mg, 0.37 mmol, 1.2 eq) and DIPEA (120 μL, 0.68 mmol, 2 eq). The crude was purified by preparative HPLC using system 1 using the following gradient: 40% - 75% MeCN:water (0.1% FA) over 20 min; 75% - 95% (0.1% FA) over 2 min; held at 95% for 2 min. Purification afforded a white solid (18 mg, 13%).

^{1}H NMR (DMSO-*d*$_6$) δ 8.68 (d, *J* = 9.0 Hz, 1H, N*H*), 7.79 (dd, *J* = 8.0/8.0 Hz, 1H, Ar-C*H*-6), 7.03 – 6.70 (m, 2H, Ar-C*H*-4 and Ar-C*H*-5), 6.31 - 6.20 (m, *J* = 3.1 Hz, 1H, Ar-C*H*), 6.04 (d, *J* = 3.1 Hz, 1H, C*H*CCH$_3$), 5.20 – 5.06 (m, 1H, C*H*CH$_2$CH$_3$), 4.32 – 4.02 (m, 2H, N(CH$_3$)C*H*$_2$), 3.67 (s, 3H, COOC*H*$_3$), 3.05 – 2.86 (m, 3H, NC*H*$_3$), 2.28 -2.22 (m, 3H, furan CC*H*$_3$), 2.10 – 1.70 (m, 2H, CHC*H*$_2$CH$_3$), 0.92 (t, *J* = 7.3 Hz, 3H, CHCH$_2$C*H*$_3$).

HPLC t_R: 11.00 min (System 1), 4.78 (System 3)

m/z: HRMS (TOF ES$^+$) $C_{23}H_{25}N_3O_7$ [M+H]$^+$ calcd 478.1590; found 478.1597

Methyl *N*-(2-hydroxy-3-((2-(((*R*)-1-(5-methylfuran-2-yl)propyl)amino)-3,4-dioxocyclobut-1-en-1-yl)amino)benzoyl)-*N*-methyl-*L*-alaninate (43a)

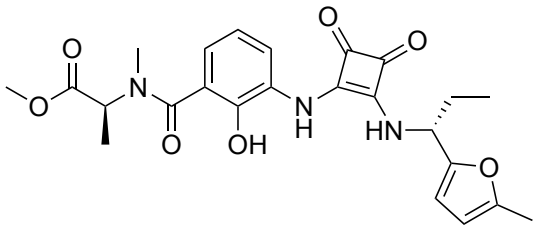

Synthesised according to general procedure I using methyl *N*-(3-((2-ethoxy-3,4-dioxocyclobut-1-en-1-yl)amino)-2-hydroxybenzoyl)-*N*-methyl-*L*-alaninate (10 mg, 0.03 mmol, 1 eq); (*R*)-1-(5-methylfuran-2-yl)propan-1-amine hydrochloride (6 mg, 0.03 mmol, 1 eq) and DIPEA (11 μL, 0.08 mmol, 2.5 eq). The resulting crude was purified by preparative HPLC system 2 using the following gradient: 40% - 50% over 4.5 min; 50% - 90% over 1 min; held at 90% for 1 min. Purification afforded a white solid (1.7 mg, 14%).

HPLC t_R: 3.18 min (system 2),

m/z: HRMS (TOF ES$^+$) $C_{24}H_{27}N_3O_7$ $[M+H]^+$ calcd 470.1883; found 470.1929

Methyl *N*-(2-hydroxy-3-((2-(((*R*)-1-(5-methylfuran-2-yl)propyl)amino)-3,4-dioxocyclobut-1-en-1-yl)amino)benzoyl)-*N*-methyl-*L*-phenylalaninate (43d)

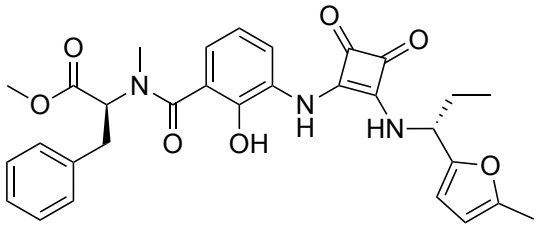

Synthesised according to general procedure I using methyl *N*-(3-((2-ethoxy-3,4-dioxocyclobut-1-en-1-yl)amino)-2-hydroxybenzoyl)-*N*-methyl-*L*-phenylalaninate (**42d**) (151 mg, 0.33 mmol, 1 eq); (*R*)-1-(5-methylfuran-2-yl)propan-1-amine hydrochloride (70 mg, 0.40 mmol, 1.2 eq) and DIPEA (128 μL, 0.73 mmol, 2.2 eq). The resulting crude was purified by preparative HPLC system 1 using the following gradient 10% - 90% over 25 min; held at 90% for 2.5 min. Purification afforded a yellow oil (8.3 mg, 5%).

^{1}H NMR (DMSO-*d*$_6$) δ 8.76 (s, 0.9H, phenol O*H*), 8.37 (s, 0.3H, N*H*), 7.72 (d, *J* = 8.0 Hz, 1H, N*H*), 7.41 – 6.35 (m, 8H, Ar-C*H*), 6.23 (d, *J* = 3.1 Hz, 1H, furyl C*H*), 6.03 (d, *J* = 3.1

Hz, 1H, furyl C*H*), 5.14 (m, 1.63H, C*H*CH_2CH_3 C$H_a$$CH_2(C_6H_5)$, 4.46 (m, 0.28H, C$H_b$$CH_2(C_6H_5)$), 3.64 (m, 3H, CHNC$H_3$), 2.97 (m, 1H, CHCOOC$H_3$), 2.69 (m, 2H, CHCOOC$H_3$), 2.25 (s, 3H, furyl C$H_3$), 1.89 (m, 2H, CHC$H_2$$CH_3$), 0.92 (t, J = 7.3 Hz, 3H, $CHCH_2$CH_3).

^{13}C NMR (DMSO-*d*$_6$) δ 183.9 (C=O) 180.9 (*C*=O), 170.8 (*C*) 168.7 (Ar-*C*), 163.6 (Ar-*C*), 152.2 (furan *C*H), 151.3 (furan *C*H), 129.1 (Ar-*C*), 128.3 (Ar-*C*), 126.5 (Ar-*C*), 107.4 (furan *C*H), 106.4 (furan *C*H), 58.6 (*C*H) 52.8 (COO*C*H_3), 52.0 (*C*H) 34.7 (*C*H_3) 34.0 (*C*H_2) 27.1 (*C*H_2), 13.3 (furan C*C*H_3), 10.2 ($CHCH_2$*C*H_3).

HPLC t_R**:** 22.69 min (System 1), 6.17 min (System 3)

m/z: HRMS (TOF ES$^+$) $C_{30}H_{31}N_3O_7$ $[M+H]^+$ calcd 546.2196; found 546.2210

Methyl *N*-(2-hydroxy-3-((2-(((*R*)-1-(5-methylfuran-2-yl)propyl)amino)-3,4-dioxocyclobut-1-en-1-yl)amino)benzoyl)-*N*-methyl-*L*-serinate (43g)

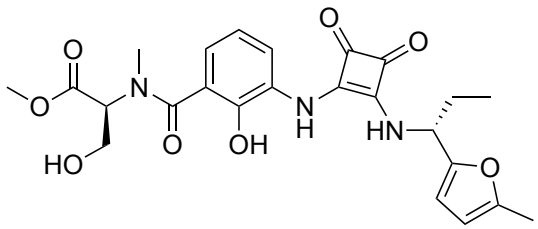

Synthesised according to general procedure I using methyl *N*-(3-((2-ethoxy-3,4-dioxocyclobut-1-en-1-yl)amino)-2-hydroxybenzoyl)-*N*-methyl-*L*-serinate (**42g**) (5 mg, 0.013 mmol, 1 eq); (*R*)-1-(5-methylfuran-2-yl)propan-1-amine hydrochloride (3 mg, 0.017 mmol, 1.3 eq) and DIPEA (3 μL, 0.018 mmol, 1.4 eq). The resulting crude was purified by preparative HPLC system 2 using the following gradient: held at 25%; 25% - 35% over 2 min; 35% - 40% over 4 min; 40% - 90% over 1 min; held at 90% for 1 min. Purification afforded a yellow oil (1.8 mg, 29%).

HPLC t_R: 4.42 min (System 2), 4.36 min (System 3)

m/z: HRMS (TOF ES$^+$) $C_{24}H_{27}N_3O_8$ $[M+H]^+$ calcd 486.1832; found 486.1792

2-Hydroxy-*N*-methyl-3-nitrobenzamide (40k)

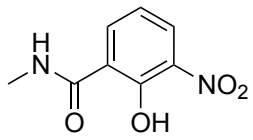

3-Nitrosalicylic acid (510 mg, 2.79 mmol, 1 eq) was suspended in anhydrous DCM (20 mL) to which oxalyl chloride (720 µL, 8.40 mmol, 3 eq) and DMF (2 drops) were added under a nitrogen atmosphere. The reaction was stirred for 18 hr and monitored by TLC. Upon completion the reaction was concentrated under reduced pressure and the resulting oil was redissolved in anhydrous DCM (20 mL). To the solution, 40% methylamine ($MeNH_2$) in water (325 µL, 4.17 mmol, 1.5 eq) was added at 0 ℃ followed by DIPEA (1.3 mL, 7.46 mmol, 2.7 eq). The reaction was stirred for 2 hr and monitored *via* TLC. Upon completion the reaction mixture was concentrated under reduced pressure. The resulting oil was redissolved in DCM (200 mL) and washed with water (3 x 200 mL) and brine (200 mL). The organic extract was dried over $MgSO_4$ and concentrated under reduced pressure yielding an orange oil as the crude product. The crude was purified by FCC (25-75% EtOAc:Cyclohexane) to yield a yellow oil (381 mg, 70%).

^{1}H NMR (DMSO-*d*$_6$) δ 9.26 (s, 1H, N*H*), 8.14 (dd, *J* = 7.9/1.5 Hz, 1H, Ar-C*H*-6), 8.08 (dd, *J* = 8.2/1.6 Hz, 1H, Ar-C*H*-4), 7.07 (d, *J* = 8.0/8.0 Hz, 1H, Ar-C*H*-5), 2.85 (d, *J* = 4.5 Hz, 3H, NHCH_3), 2.66 (d, *J* = 4.9 Hz, 1H, N*H*).

^{13}C NMR (DMSO-*d*$_6$) δ 171.4 (C=O), 161.0 (Ar-C-2), 149.0 (Ar-C-4), 138.1 (Ar-C-3), 118.7 (Ar-C-6), 117.0 (Ar-C-5), 114.0 (Ar-C-1), 26.3 (NH*C*H_3).

m/z: LCMS (TOF ES$^+$) $C_8H_8N_2O_4$ $[M+H]^+$ calcd 197.1; found 197.1

3-Amino-2-hydroxy-*N*-methylbenzamide (41k)

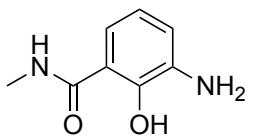

Synthesis according to general procedure J using 2-hydroxy-*N*-methyl-3-nitrobenzamide (**40k**) (180 mg, 0.92 mmol, 1 eq) and 10% Pd/C (19 mg, 10% w/w) affording a brown semisolid (142 mg, 94%).

^{1}H NMR (DMSO-*d*$_6$) : δ 9.12 – 7.99 (m, 1H, N*H*CH_3), 6.99 (dd, *J* = 8.1/1.5 Hz, 1H, Ar-C*H*-6), 6.73 (dd, *J* = 7.7/1.4 Hz, 1H, Ar-C*H*-4), 6.59 (dd, *J* = 7.8/7.8 Hz, 1H, Ar-C*H*-5), 2.79 (d, *J* = 4.5 Hz, 3H, CH_3), 2.66 (d, *J* = 4.9 Hz, 1H, NH_2).

^{13}C NMR (DMSO-*d*$_6$) δ 171.4 (*C*=O), 161.0 (Ar-*C*H-2), 149.0 (Ar-*C*H-3), 138.1 (Ar-*C*H-5), 118.7 (Ar-*C*H-4), 117.0 (Ar-*C*H-6), 113.9 (Ar-*C*H-1), 26.3 (NH*C*H_3).

m/z: LCMS (TOF ES$^+$) $C_8H_{10}N_2O_2$ $[M+H]^+$ calcd 167.1; found 167.1

3-((2-Ethoxy-3,4-dioxocyclobut-1-en-1-yl)amino)-2-hydroxy-*N*-methylbenzamide (42k)

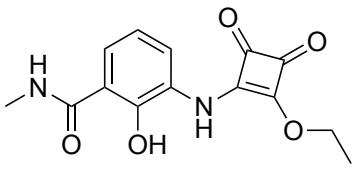

Synthesis according to general procedure K using 3-amino-2-hydroxy-*N*-methylbenzamide (**41k**) (110 mg, 0.66 mmol, 1 eq) and 3,4-diethoxycyclobut-3-ene-1,2-dione (118 μL, 0.80 mmol, 1.2 eq) to afford a yellow oil (105 mg) which was used without further purification.

LCMS t_R: 2.42 min

^{1}H NMR (DMSO-*d*$_6$) δ 13.65 (s, 1H, phenol O*H*), 10.24 (s, 1H, squaramide N*H*), 9.01 (q, *J* = 4.9 Hz, 1H, N*H*CH$_3$), 7.68 (dd, *J* = 8.0/8.0 Hz, 1H, Ar-C*H*-6), 7.37 (dd, *J* = 7.7/1.4 Hz, 1H, C*H*-4) 6.88 (dd, *J* = 7.9/1.3 Hz, 1H, Ar-C*H*-5), 4.67 (q, *J* = 7.1 Hz, 2H, OC*H*$_2$CH$_3$), 2.83 (d, *J* = 4.4 Hz, 3H, NHC*H*$_3$), 1.34 (t, *J* = 7.0 Hz, 3H, OCH$_2$C*H*$_3$).

m/z: LCMS (TOF ES$^+$) $C_{14}H_{14}N_2O_5$ $[M+H]^+$ calcd 291.1; found 291.1

(*R*)-2-Hydroxy-*N*-methyl-3-((2-((1-(5-methylfuran-2-yl)propyl)amino)-3,4-dioxocyclobut-1-en-1-yl)amino)benzamide (43k)

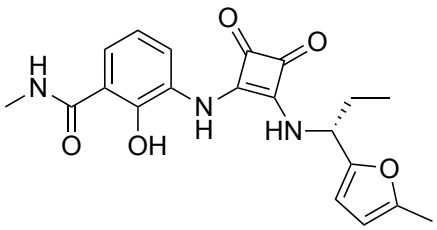

Synthesis according to general procedure L using 3-((2-ethoxy-3,4-dioxocyclobut-1-en-1-yl)amino)-2-hydroxy-*N*-methylbenzamide (**42k**) (97 mg, 0.33 mmol, 1 eq), (*R*)-1-(5-methylfuran-2-yl)propan-1-amine hydrochloride (71.9 mg, 0.41 mmol, 1.2 eq) and DIPEA (70 μL, 0.41 mmol, 1.2 eq). The resulting crude was purified by PTLC (8% MeOH: DCM) to afford a white solid (21 mg, 17%).

^{1}H NMR (DMSO-*d*$_6$) δ 14.04 (s, 1H, O*H*), 9.35 (s, 1H, squaramide N*H*), 9.05 (s, 0.8H, squaramide N*H*), 8.70 (dd, *J* = 9.0 Hz, 1H, N*H*CH$_3$), 7.97 (dd, *J* = 8.0/1.4 Hz, 1H, Ar-C*H*-6), 7.50 (dd, *J* = 8.3/1.5 Hz, 1H, Ar-C*H*-4), 6.86 (dd, *J* = 8.0/8.0 Hz, 1H, Ar-C*H*-5), 6.26 (d, *J* = 3.1 Hz, 1H, furan C*H*), 6.05 (d, *J* = 2.70 Hz, 1H, furan C*H*), 5.13 (td, *J* = 7.9, 7.5

Hz, 1H, C*H*CH_2CH_3), 2.83 (d, *J* = 4.4 Hz, 3H, NHC*H*$_3$), 2.26 (s, 3H, furan CC*H*$_3$), 1.91 (ddq, *J* = 40.2, 14.1, 7.1 Hz, 2H, CHC*H*$_2$CH$_3$), 0.92 (t, *J* = 7.3 Hz, 3H, $CHCH_2CH_3$).

^{13}C NMR (DMSO-*d*$_6$) δ 184.5 (squaramide C=O), 180.7 (C=O), 170.7 (squaramide *C*=C), 169.0 (squaramide *C*=C), 163.7 (Ar-*C*H-2), 152.5 (Furan *C*), 151.9 (Furan *C*), 128.5 (Ar-*C*H-2), 123.4 (Ar-*C*-4), 121.0 (Ar-*C*-6), 114.3 (Ar-*C*-1), 108.0 (Furyl *C*H), 106.9 (Furan *C*H), 53.3 (*C*HCH_2CH_3), 27.7 ($CHCH_2CH_3$), 26.5 (NH*C*H$_3$), 13.8 (Furan C*C*H$_3$), 10.7 ($CHCH_2CH_3$).

HPLC t_R: 4.23 (System 3)

m/z: HRMS (TOF ES$^+$) $C_{20}H_{21}N_3O_5$ $[M+H]^+$ calcd 384.1515; found 384.1527

2-(Methoxycarbonyl)-3-nitrobenzoic acid (58)

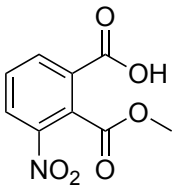

4-Nitroisobenzofuran-1,3-dione (5.01 g, 25.9 mmol, 1 eq) was dissolved in MeOH (33 mL) and refluxed for 18 hr. The reaction was monitored *via* LCMS. Upon completion the reaction mixture was concentrated under reduced pressure to give a clear oil as crude. The crude oil was recrystallised from water to afford a white solid (4.53 g, 78%).

^{1}H NMR (DMSO-*d*$_6$) δ 8.41 (dd, *J* = 8.3/1.1 Hz, 1H, Ar-C*H*-4), 8.32 (dd, *J* = 7.8/1.1 Hz, 1H, Ar-C*H*-6), 7.87 (dd, 8.0/8.0 Hz, 1H, Ar-C*H*-5), 3.85 (s, 3H, COOC*H*$_3$).

^{13}C NMR (DMSO-*d*$_6$) δ 165.4 (C=O), 165.3 (C=O), 146.1 (Ar-*C*-3), 135.7 (Ar-*C*-1), 131.4 (Ar-*C*-2), 131.2 (Ar-*C*-4), 129.4 (Ar-*C*-5), 128.3 (Ar- *C*-6), 53.2 (COO*C*H$_3$).

m/z: LCMS (TOF ES$^+$) $C_9H_7NO_6$ $[M+H]^+$ calcd 226.1; found 226.1

Methyl 2-(dimethylcarbamoyl)-6-nitrobenzoate (47g)

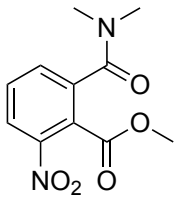

2-(Methoxycarbonyl)-3-nitrobenzoic acid (**58**) (2.00 g, 8.88 mmol, 1 eq) was suspended in anhydrous DCM (40 mL) to which oxalyl chloride (2.30 mL, 26.8 mmol, 3 eq) and DMF (3 drops) were added under a nitrogen atmosphere. The reaction was stirred at ambient temperatures for 18 hr and monitored *via* TLC. Upon completion the reaction was concentrated under reduced pressure and the resulting oil was redissolved in anhydrous DCM (40 mL). To the solution 2M dimethylamide in THF (570 µL, 10.6 mmol, 1.2) was added at 0 ℃ followed by DIPEA (1.85 mL, 19.6 mmol, 2.2 eq). The reaction was stirred for 2 hr and monitored *via* TLC. Upon completion, the reaction mixture was concentrated under reduced pressure. The

resulting oil was redissolved in DCM (200 mL) and washed with water (3 x 200 mL) and brine (200 mL). The organic layer was dried over $MgSO_4$ and then concentrated under reduced pressure to afford an orange oil as crude. The crude was purified by FCC (25-75% EtOAc:Cyclohexane) to yield a yellow solid (1.48 g, 66%).

^{1}H NMR (DMSO-*d*$_6$) δ 8.27 – 8.11 (m, 1H, Ar-C*H*-3), 7.93 – 7.78 (m, 2H, Ar-C*H*-5 and Ar-C4-*H*), 3.78 (s, 3H, COOCH_3), 2.98 (s, 3H, CONCH_3), 2.84 (s, 3H, CONCH_3).

^{13}C NMR (DMSO-*d*$_6$) δ 166.6 (*C*=O), 164.7 (*C*=O), 147.4 (Ar-*C*-3), 137.8 ((Ar-*C*-1), 132.0 (Ar-*C*-3), 131.9 (Ar-*C*-6), 125.8 (Ar-*C*-1), 124.8 (Ar-*C*-4), 53.3 (COO*C*H$_3$), 38.5 (N*C*H$_3$), 34.5 (N*C*H$_3$).

m/z: LCMS (TOF ES$^+$) $C_{11}H_{12}N_2O_5$ $[M+H]^+$ calcd 253.1; found 253.2

Methyl 2-amino-6-(dimethylcarbamoyl)benzoate (48g)

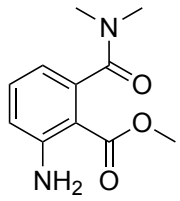

Synthesised according to general procedure J using methyl 2-(dimethylcarbamoyl)-6-nitrobenzoate (**47g**) (252 mg, 1.00 mmol, 1 eq) and 10% Pd/C (26 mg, 10% w/w) to afford a yellow powder (212 mg, 96%).

^{1}H NMR (DMSO-*d*$_6$) : δ 7.22 (dd, *J* = 7.2 Hz, 1H, Ar-C*H*-4), 6.78 (dd, *J* = 8.4, 1.1 Hz, Ar-*C*H-5), 6.49 (s, 2H, N*H*$_2$), 6.31 (dd, *J* = 7.2/1.1 Hz, 1H, Ar-C*H*-3), 3.70 (s, 3H, COOC*H*$_3$), 2.92 (s, 3H, NC*H*$_3$), 2.73 (s, 3H, NC*H*$_3$).

^{13}C NMR (DMSO-*d*$_6$) δ 170.9 (C=O), 167.3 (C=O), 150.7 (Ar-*C*-3), 140.3 (Ar-*C*-1), 132.9 (Ar-*C*-2), 116.6 (Ar-*C*-5), 113.3 (Ar-*C*-4), 107.2 (Ar-*C*-6), 51.8 (COO*C*H$_3$), 38.0 (N*C*H$_3$), 34.0 (N*C*H$_3$).

m/z: LCMS (TOF ES$^+$) $C_{11}H_{14}N_2O_3$ $[M+H]^+$ calcd 223.1; found 223.1

Methyl 2-(dimethylcarbamoyl)-6-((2-ethoxy-3,4-dioxocyclobut-1-en-1-yl)amino)benzoate (49g)

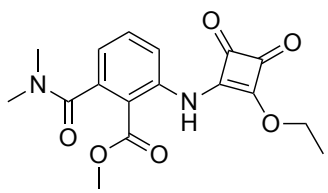

2-Amino-6-(dimethylcarbamoyl)phenyl (**48g**) (102 mg, 0.46 mmol, 1 eq) was dissolved in EtOH (10 mL) to which 3,4-diethoxycyclobut-3-ene-1,2-dione (82 µL, 0.55 mmol, 1.2 eq) and $Zn(OTf)_2$ (86 mg, 0.23 mmol, 0.5 eq) were added. The reaction was refluxed for 48 hr and monitored *via* LCMS. Upon completion the reaction was concentrated under reduced pressure, redissolved in water (20 mL) and

extracted into EtOAc (3 x 20 mL). The organic extracts were combined, washed sequentially with water (3 x 10 mL) and brine (20 mL). The organic layer was then dried over $MgSO_4$ and concentrated under reduced pressure to yield the crude product. The crude was purified by RP-FCC (gradient 15-70% MeCN:water) to afford a yellow oil (55 mg, 35%).

^{1}H NMR (DMSO-*d*$_6$) δ 10.60 (s, 1H, N*H*), 7.60 (dd, *J* = 7.9/7.9 Hz, 1H, Ar-C*H*-4), 7.46 (dd, *J* = 8.2/1.4 Hz, 1H, Ar-C*H*-5), 7.14 (dd, *J* = 7.5/1.4 Hz, 1H, Ar-C*H*-3), 4.72 (q, *J* = 7.1 Hz, 2H, OC*H*$_2$CH$_3$), 3.74 (s, 3H, COOC*H*$_3$), 2.97 (s, 3H, NC*H*$_3$), 2.80 (s, 3H, NC*H*$_3$), 1.38 (t, *J* = 7.1 Hz, 3H, OCH$_2$C*H*$_3$).

^{13}C NMR (DMSO-*d*$_6$) δ 184.8 (C=O), 179.2 (C=O), 170.3 (C=O), 169.5 (C=*C*), 166.4 (C=*C*), 139.7 (Ar-*C*-1), 137.1 (Ar-*C*-3), 132.5 (Ar-*C*-5), 124.3 (Ar-*C*-6), 123.4 (Ar-*C*-4), 70.2 (O*C*H$_2$CH$_3$), 53.1 (COO*C*H$_3$), 38.8 (N*C*H$_3$), 34.7 (N*C*H$_3$), 16.0 (OCH$_2$*C*H$_3$).

m/z: LCMS (TOF ES$^+$) $C_{17}H_{18}N_2O_6$ $[M+H]^+$ calcd 347.1; found 347.2

Methyl (*R*)-2-(dimethylcarbamoyl)-6-((2-((1-(5-methylfuran-2-yl)propyl)amino)-3,4-dioxocyclobut-1-en-1-yl)amino)benzoate (45g)

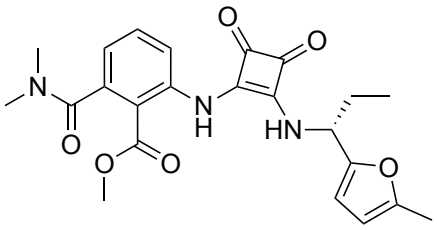

Synthesised according to general procedure L using 2-(dimethylcarbamoyl)-6-((2-ethoxy-3,4-dioxocyclobut-1-en-1-yl)amino)phenyl acetate (**49g**) (46 mg, 0.13 mmol, 1 eq), (*R*)-1-(5-methylfuran-2-yl)propan-1-amine hydrochloride (30 mg, 0.16 mmol, 1.2 eq) and DIPEA (50 μL, 0.29 mmol, 2.2 eq). The crude was purified by preparative HPLC system 2 using the following gradient: 30% - 60% over 5 min; 60% - 90% over 1 min; held at 90% for 1 min. Afforded a white solid (12 mg, 22%).

^{1}H NMR (DMSO-*d*$_6$) : δ 9.57 (s, 1H, N*H*), 8.83 (m, 1H, N*H*), 7.55 (dd, *J* = 7.9/7.9 Hz, 1H, Ar-C*H*-4), 7.44 (dd, *J* = 8.4/1.3 Hz, 1H, Ar-C*H*-5), 7.03 (dd, *J* = 7.5/1.5 Hz, 1H, Ar-C*H*-3), 6.27 (d, *J* = 3.1 Hz, 1H, furan C*H*), 6.06 (d, *J* = 3.0 Hz, 1H, furan C*H*), 5.15 (m, 1H, C*H*CH$_2$CH$_3$), 3.77 (s, 1H, COOC*H*$_3$), 2.97 (s, 3H, NC*H*$_3$), 2.83 (s, 3H, NC*H*$_3$), 2.26

(s, 3H, CHCHCCH_3), 2.04 – 1.74 (m, 2H, CHCH_2CH$_3$), 0.92 (t, J = 7.3 Hz, 3H, CHCH$_2$CH_3).

^{13}C NMR (DMSO-*d*$_6$) : δ 107.7 (furan *C*), 106.5 (furyl *C*), 52.9 (COO*C*H$_3$), 38.4 (*C*H$_3$), 34.3 (CH_3), 27.1 (CHCH_2CH$_3$), 13.4 (furan *C*H$_3$), 10.4 (CH$_2$*C*H$_3$).

HPLC t_R**:** 2.34 (System 2), 4.23 (System 3).

m/z: HRMS (TOF ES$^+$) $C_{23}H_{25}N_3O_6$ [M+Na]$^+$ calcd 462.1614; found 462.1641

2-Hydroxy-*N*,*N*-dimethyl-3-nitrobenzamide (53)

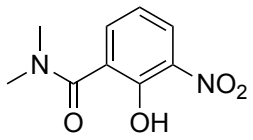

3-nitrosalicylic acid (2.00 g, 8.88 mmol, 1 eq) was suspended in anhydrous DCM (40 mL) to which oxalyl chloride (2.30 mL, 26.8 mmol, 3 eq) and DMF (3 drops) were added under a nitrogen atmosphere. The reaction was stirred for 18 hr and monitored *via* TLC. Upon completion the reaction was concentrated under reduced pressure, and the resulting oil was redissolved in anhydrous DCM (40 mL). To the solution 2M dimethylamide in THF (570 µL, 10.6 mmol, 1.2 eq) was added at 0 ℃ followed by DIPEA (1.85 mL, 19.6 mmol, 2.2 eq). The reaction mixture was stirred for 2 hr and allowed to warm to ambient temperature. The reaction mixture was then concentrated under reduced pressure. The resulting oil was redissolved in DCM (200 mL) and washed sequentially with water (3 x 200 mL) and brine (200 mL). The organic extracts were combined, dried over $MgSO_4$ and concentrated under reduced pressure to yield an orange oil as crude. The crude was purified by FCC (gradient 25-75% EtOAc:cyclohexane) to yield a yellow solid (1.48 g, 66%).

^{1}H NMR (DMSO-*d*$_6$) δ 10.68 (s, 1H, O*H*), 8.01 (dd, J = 8.3/1.4 Hz, 1H, Ar-C*H*-6), 7.54 (dd, J = 7.4/1.3 Hz, 1H, Ar-C*H*-5), 7.41 – 6.79 (m, 1H, Ar-C*H*-4), 3.15 – 2.69 (m, 6H, benzamide N(CH_3)$_2$).

^{13}C NMR (DMSO-*d*$_6$) δ 166.3 (*C*=O), 148.8 (Ar-*C*-2), 136.3 (Ar-*C*-3), 134.2 (Ar-*C*-1), 129.4 (Ar-*C*-5), 125.6 (Ar-*C*-6), 119.7 (Ar-*C*-4).

m/z: LCMS (TOF ES$^+$) $C_9H_{10}N_2O_4$ [M+H]$^+$ calcd 211.1; found 211.0

2-(Dimethylcarbamoyl)-6-nitrophenyl acetate (47c)

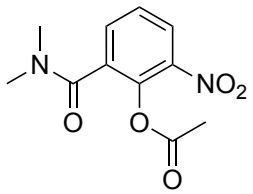

2-Hydroxy-*N*,*N*-dimethyl-3-nitrobenzamide (**53**) (507 mg, 2.41 mmol, 1 eq) was dissolved in DCM (5 mL) to which acetic anhydride (345 μL, 3.61 mmol, 1.5 eq) and TEA (340 μL, 2.41 mmol, 1 eq) were added followed by 4-dimethylaminopyridine (29.5 mg, 0.24 mmol, 0.1 eq). The reaction was stirred at ambient temperature for 18 hr and monitored by TLC. Upon completion the reaction was quenched with 0.5 M sodium bicarbonate $NaHCO_3$ (10 mL) and then extracted into DCM (3 x 15 mL). The DCM extracts were combined and washed sequentially with water (3 x 30 mL) and brine (30 mL), then dried over $MgSO_4$ and concentrated under reduced pressure to yield a yellow oil (420 mg, 77%).

^{1}H NMR (DMSO-*d*$_6$) δ 8.20 (dd, *J* = 8.2/1.2 Hz, 1H, Ar-C*H*-5), 7.80 (dd, *J* = 7.6/1.3 Hz, 1H, Ar-C*H*-4), 7.61 (dd, *J* = 8.0/8.0 Hz, 1H, Ar-C*H*-3), 3.00 (s, 3H, CONCH_3), 2.78 (d, 3H, CONCH_3), 2.29 (s, 3H, OCOCH_3).

^{13}C NMR (DMSO-*d*$_6$) δ 168.4 (*C*=O), 165.0 (*C*=O), 142.5 (Ar-*C*-1), 139.8 136.3 (Ar-*C*-2), 133.9 (Ar-*C*-5), 133.5, 127.9 (Ar-*C*-3), 126.6 (Ar-*C*-6), 119.7 (Ar-*C*-4), 38.5 (N*C*H_3), 34.8 (N*C*H_3), 20.7 (OCO*C*H_3).

m/z: LCMS (TOF ES$^+$) $C_{11}H_{12}N_2O_5$ $[M+H]^+$ calcd 253.1; found 253.1

2-Amino-6-(dimethylcarbamoyl)phenyl acetate (48c)

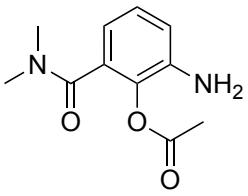

Synthesised according to general procedure J using 2-(dimethylcarbamoyl)-6-nitrophenyl acetate (**47c**) (250 mg, 0.99 mmol, 1 eq) and 10% Pd/C (27 mg, 10% w/w) to afford a brown solid (216 mg, 98%).

^{1}H NMR (DMSO-*d*$_6$) δ 9.94 (s, 1H, N*H*), 7.39 (dd, *J* = 7.9/1.5 Hz, 1H, Ar-C*H*-5), 6.93 (dd, *J* = 7.6/1.6 Hz, 1H, Ar-C*H*-4), 6.83 (dd, *J* = 7.7/7.7 Hz, 1H, Ar-C*H*-3), 3.05 – 2.77 (m, 6H, N(CH_3)$_2$), 2.13 (s, 3H, COOCH_3).

^{13}C NMR (DMSO-*d*$_6$) δ 170.2 (C=O), 168.3 (C=O)), 127.0 (Ar-*C*), 126.6 (Ar-*C*), 124.0 (Ar-*C*), 123.5 (Ar-*C*), 119.2 (Ar-*C*), 23.2 (COO*C*H$_3$).

m/z: LCMS (TOF ES$^+$) $C_{11}H_{14}N_2O_3$ $[M+H]^+$ calcd 223.1; found 223.0

3-Amino-2-hydroxy-*N*,*N*-dimethylbenzamide (62)

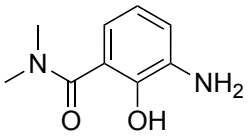

Synthesis according to general procedure J using 2-hydroxy-*N*,*N*-dimethyl-3-nitrobenzamide (**53**) (505 mg, 2.40 mmol, 1 eq) and 10% Pd/C (51 mg, 10% w/w) affording a green solid (426 mg, 98%).

m/z: LCMS (TOF ES$^+$) $C_9H_{12}N_2O_2$ $[M+H]^+$ calcd 181.1; found 181.0

3-((2-Ethoxy-3,4-dioxocyclobut-1-en-1-yl)amino)-2-hydroxy-*N*,*N*-dimethylbenzamide (56)

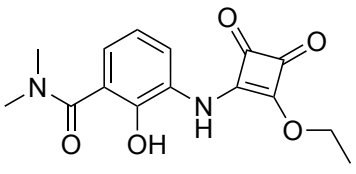

Synthesis according to general procedure K using 3-amino-2-hydroxy-*N*,*N*-dimethylbenzamide (**62**) (415 mg, 2.31 mmol, 1 eq) and 3,4-diethoxycyclobut-3-ene-1,2-dione (410 μL, 2.77 mmol, 1.2 eq) and DIPEA (480 μL, 2.77 mmol, 1.2 eq) afforded a yellow oil (344 mg, 49%) which was used without further purification.

^{1}H NMR (DMSO-*d*$_6$) δ 10.28 (s, 1H, phenol O*H*), 7.64 (dd, *J* = 8.0/1.6 Hz, 1H, Ar-C*H*-6), 7.41 (dd, *J* = 7.8/1.6 Hz, 1H, Ar-C*H*-4), 6.91 (dd, *J* = 7.9/7.9 Hz, 1H, Ar-C*H*-5), 4.67 (q, *J* = 7.1 Hz, 2H, CH_2CH$_3$), 1.33 (t, *J* = 7.0 Hz, 3H, CH$_2$CH_3).

^{13}C NMR (DMSO-*d*$_6$) δ 185.5 (*C*=O), 184.6 (*C*=O), 181.5 (C=O), 128.0 (Ar-*C*), 125.4 (Ar-*C*), 124.3 (Ar-*C*), 119.3 (Ar-*C*), 113.2 (Ar-*C*), 52.3 (COO*C*H$_3$), 40.2 (N*C*H$_3$), 36.5 (N*C*H$_3$), 10.7 (CH$_2$*C*H$_3$).

m/z: LCMS (TOF ES$^+$) $C_{15}H_{16}N_2O_5$ $[M+H]^+$ calcd 305.1; found 305.0

(*R*)-2-Hydroxy-*N*,*N*-dimethyl-3-((2-((1-(5-methylfuran-2-yl)propyl)amino)-3,4-dioxocyclobut-1-en-1-yl)amino)benzamide (navarixin (2))

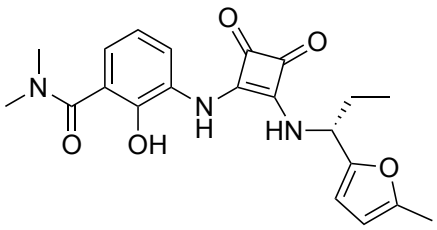

Synthesis according to general procedure L using 3-((2-ethoxy-3,4-dioxocyclobut-1-en-1-yl)amino)-2-hydroxy-*N*,*N*-dimethylbenzamide (**56**) (74 mg, 0.25 mmol, 1 eq), (*R*)-1-(5-methylfuran-2-yl)propan-1-amine hydrochloride (49 mL, 0.27 mmol, 1.1 eq) and DIPEA (49 μL, 0.27 mmol, 1.1 eq). The resulting crude was purified by prep-TLC (4% MeOH:DCM) to afford a white solid (18 mg, 18%).

^{1}H NMR (DMSO-*d*$_6$) δ 8.68 (dd, *J* = 9.1/2.3 Hz, 1H, Ar-C*H*-6), 7.79 (dd, *J* = 7.3/2.6 Hz, 1H, Ar-C*H*-4), 7.19 – 6.68 (m, 2H, Ar-C*H*-5 and squaramide N*H*), 6.25 (d, *J* = 3.1 Hz, 1H, furan C*H*), 6.04 (d, *J* = 3.1 Hz, 1H, furan C*H*), 5.14 (dd, *J* = 21.2/7.8 Hz, 1H,C*H*CH$_2$CH$_3$), 2.93 (s, 6H, NC*H*$_3$), 2.26 (s, 3H, CHCHCC*H*$_3$), 1.98 – 1.79 (m, 2H, CHC*H*$_2$CH$_3$), 0.92 (t, *J* = 7.3 Hz, 3H, CHCH$_2$C*H*$_3$).

^{13}C NMR (DMSO-*d*$_6$) δ 185.7 (squaramide *C*=O) 184.3 (squaramide C=O), 169.0 (squaramide *C*=C), 168.6 (squaramide *C*=C), 163.9 (amide C=O), 152.4 (furan *C*), 151.9 (furan *C*), 143.7 (Ar-*C*H), 129.1 (Ar-*C*H), 124.9 (Ar-*C*H), 122.6 (Ar-*C*H), 121.2 (Ar-*C*), 120.2 (Ar-*C*), 108.0 (furan *C*H), 106.9 (furan *C*H), 53.2 (N*C*H$_3$), 27.6 (*C*H$_2$CH$_3$), 13.8 (furan *C*H$_3$), 10.7 (CH$_2$*C*H$_3$).

m/z: LCMS (TOF ES$^+$) $C_{21}H_{23}N_3O_5$ $[M+H]^+$ calcd 398.2; found 398.0

(*R*)-2-(Dimethylcarbamoyl)-6-((2-((1-(5-methylfuran-2-yl)propyl)amino)-3,4-dioxocyclobut-1-en-1-yl)amino)phenyl acetate (45c)

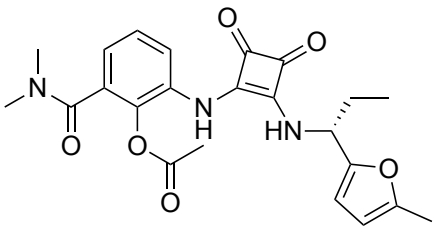

(*R*)-2-Hydroxy-*N*,*N*-dimethyl-3-((2-((1-(5-methylfuran-2-yl)propyl)amino)-3,4-dioxocyclobut-1-en-1-yl)amino)benzamide (navarixin(**2**)) (10 mg, 0.025 mmol, 1 eq) was dissolved in dry DCM (2 mL) to which acetic anhydride (3.6 µL, 0.038 mmol, 1.5 eq) TEA (3.6 µL, 0.026 mmol, 1.05 eq) were added, followed by DMAP (1.0 mg, 0.008 mmol, 0.3 eq). The reaction was stirred at ambient temperature for 16 hr and monitored by TLC. Upon completion the reaction was diluted with DCM (5 mL) and washed sequentially with $NaHCO_3$ (3 x 5 mL), 0.5M $HCl_{(aq)}$ (3 x 5 mL) and brine (5 mL). The organic layer was dried over $MgSO_4$ and concentrated under reduced pressure yielding the crude as an off-white oil. The crude was purified by preparative HPLC system 1 using the following gradient: 40% - 90% for 6 min; held at 90% MeCN:water (0.1% FA) for 3 min. The purification afforded a white solid (3 mg, 27%).

^{1}H NMR (DMSO-*d*$_6$) δ 8.46 (s, 0.25H, squaramide N*H*), 8.08 (s, 1H, squaramide N*H*), 7.82 (dd, *J* = 4.8 Hz, 1H Ar-C*H*-5), 7.67-7.35 (m, 2H, Ar-C*H*-4 and Ar-C*H*-3), 6.25 (s, 1H, furan C*H*), 6.04 (d, *J* = 3.1 Hz, 1H, furan C*H*), 5.23 (q, *J* = 7.9 Hz, 1H, C*H*CH_2CH_3), 2.95 (s, 3H, N(CH_3)$_{2a}$), 2.76 (s, 3H, N(CH_3)$_{2b}$), 2.23 (s, 3H, OCOC*H*$_3$), 2.10 – 1.80 (m, 5H, CC*H*$_3$ and CHC*H*$_2$CH$_3$), 1.13 – 0.84 (m, 3H, CHCH$_2$C*H*$_3$).

^{13}C NMR (DMSO-*d*$_6$) δ 184.6 (squaramide C=O) 166.0 (Ar-*C*H), 132.1 (Ar *C*H), 131.6 (Ar-*C*H), 127.5 (Ar-*C*H), 108.0 (furan *C*H), 106.9 (furan *C*H), 38.4 (N*C*H$_{3a}$), 34.7(amide N*C*H$_{3b}$), 22.5 (OCO*C*H$_3$), 13.8 (furan-C*H*$_3$), 10.9 (CHCH$_2$*C*H$_3$).

HPLC t_R: 6.68 min (System 1), 5.11 min (System 3)

m/z: HRMS (TOF ES$^+$) $C_{23}H_{25}N_3O_6$ $[M+H]^+$ calcd 440.1777; found 440.1734

2-Methoxy-*N*,*N*-dimethyl-3-nitrobenzamide (47b)

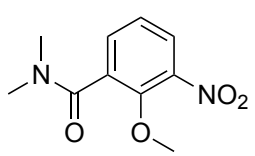

2-Hydroxy-*N*,*N*-dimethyl-3-nitrobenzamide (**53**) **(**218 mg, 1.03 mmol, 1 eq) was suspended in acetone (20 mL) to which potassium carbonate (K_2CO_3) (725 mg, 5.19 mmol, 5 eq) and iodomethane (130 µL, 2.07 mmol, 2 eq).The reaction was then refluxed for 12 hr and monitored by TLC. Upon completion the reaction was diluted in water (50 mL) and extracted into EtOAc (3 x 50 mL). The organic extracts were washed with brine (30 mL), dried over $MgSO_4$ and concentration under reduced pressure afforded a white solid (198 mg, 83%).

^{1}H NMR (DMSO-*d*$_6$) : δ 7.96 (dd, *J* = 8.1/1.3 Hz, 1H, C*H*-4), 7.58 (dd, *J* = 7.6/1.3 Hz, 1H, C*H*-6), 7.37 (dd, *J* = 7.9/7.9 Hz, 1H, C*H*-5), 3.81 (s, *J* = 0.9 Hz, 3H, OCH_3), 3.03 (s, *J* = 0.9 Hz, 3H, NC$H_{3\mathbf{a}}$), 2.80 (s, *J* = 0.9 Hz, 3H, NC$H_{3\mathbf{b}}$).

^{13}C NMR (DMSO-*d*$_6$) δ 169.0 (*C*=O), 152.7 (Ar-*C*OH), 143.6 (Ar-*C*), 131.1 (Ar-*C*), 124.75 (Ar-*C*), 115.8 (Ar-*C*), 114.4 (O*C*H$_3$), 61.0 (N*C*H$_{3\mathbf{a}}$), 36.2 (N*C*H$_{3\mathbf{b}}$).

m/z: LCMS (TOF ES$^+$) $C_{10}H_{12}N_2O_4$ $[M+H]^+$ calcd 225.1; found 225.1

3-Amino-2-methoxy-*N*,*N*-dimethylbenzamide (48b)

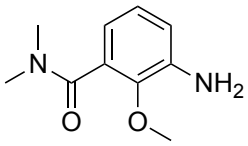

Synthesis according to general procedure using 2-methoxy-*N*,*N*-dimethyl-3-nitrobenzamide (**47b**) (175 mg, 0.93 mmol, 1 eq) and 10% Pd/C (18 mg, 10% w/w) to afford a brown semisolid (146 mg, 99%)

^{1}H NMR (DMSO-*d*$_6$) δ 6.83 (dd, *J* = 7.7/7.7 Hz, 1H, Ar-C*H*-6), 6.70 (dd, *J* = 8.0/1.5 Hz, 1H, Ar-C*H*-4), 6.30 (dd, *J* = 7.4/1.5, 1H, Ar-C*H*-5), 5.02 (s, 2H, CNH_2), 3.60 (s, *J* = 0.9 Hz, 3H, OCH_3), 2.97 (s, 3H, NC$H_{3\mathbf{a}}$), 2.77 (s, 3H, NC$H_{3\mathbf{b}}$).

^{13}C NMR (DMSO-*d*$_6$) δ 169.0 (*C*=O), 142.3 (Ar-*C*-2), 142.0 (Ar-*C*-3, 131.2 (Ar-*C*-5), 124.8 (Ar-*C*-6), 115.8 (Ar-*C*-4), 114.4 (O*C*H$_3$), 60.2 (N*C*H$_3$a), 34.5 (N*C*H$_{3\mathbf{b}}$).

m/z: LCMS (TOF ES$^+$) $C_{10}H_{14}N_2O_2$ $[M+H]^+$ calcd 195.1; found 195.1

3-((2-Ethoxy-3,4-dioxocyclobut-1-en-1-yl)amino)-2-methoxy-*N*,*N*-dimethylbenzamide (49b)

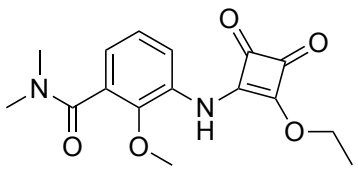

Synthesis according to general procedure K using 3-amino-2-methoxy-*N*,*N*-dimethylbenzamide (**48b**) (141 mg, 0.73 mmol, 1 eq) and 3,4-diethoxycyclobut-3-ene-1,2-dione (130 μL, 0.87 mmol, 1.2 eq). The resulting crude was used without further purification.

^{1}H NMR (DMSO-*d*$_6$) δ 7.29 (dd, *J* = 7.6/7.6 Hz, 1H, Ar-C*H*-6), 7.14 (dd, *J* = 7.7/1.4 Hz, 1H, Ar-C*H*-4), 7.05 (dd, *J* = 7.6/1.4 Hz, 1H, Ar-C*H*-5), 4.67 (q, *J* = 7.0 Hz, 2H, OCH_2CH$_3$), 3.65 (s, 3H, OCH_3), 3.00 (s, 3H, NC$H_{3\mathbf{a}}$), 2.81 (s, 1H, NC$H_{3\mathbf{b}}$), 1.34 (t, *J* = 7.0 Hz, 3H OCH$_2$CH_3).

m/z: LCMS (TOF ES$^+$) $C_{16}H_{18}N_2O_5$ $[M+H]^+$ calcd 319.1; found 319.1

3,3'-((3,4-Dioxocyclobut-1-ene-1,2-diyl)bis(azanediyl))bis(2-methoxy-*N*,*N*-dimethylbenzamide) (54)

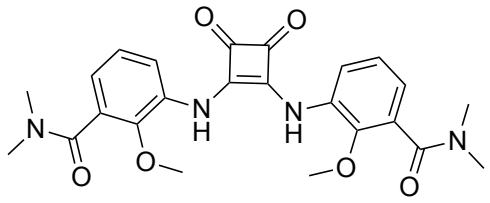

3-((2-Ethoxy-3,4-dioxocyclobut-1-en-1-yl)amino)-2-methoxy-*N*,*N*-dimethylbenzamide (**55b**) (141 mg, 0.726 mmol, 1 eq) was dissolved in EtOH (12 mL) to which 3,4-Diethoxy-3-cyclobutene-1,2-dione (130 μL, 0.87 mmol, 1.2 eq) was added dropwise at 0 ℃. The reaction was allowed to warm to ambient temperatures and stirred for 24 hr. The reaction was monitored by TLC and upon completion the mixture was concentrated under reduced pressure. The resulting oil was triturated with Et$_2$O to give crude oil. The oil was purified by preparative HPLC system 1 using the following gradient: 30% - 50% over 9 min; 50% - 90% over 2 min; held at 90% for 2 min. The purification afforded a yellow oil (10 mg, 3%).

^{1}H NMR (DMSO-*d*$_6$) δ 10.14 (s, 2H, Squaramide N*H*), 7.75 (dd, *J* = 8.1/1.4 Hz, 2H, Ar-C*H*-6), 7.18 (dd, *J* = 7.8/7.8 Hz, 2H, Ar-C*H*-5), 6.96 (dd, *J* = 7.6/1.6 Hz, 2H, Ar-C*H*-4), 3.76 (s, 6H, OCH_3), 3.03 (s, 6H, NC$H_{3\mathbf{a}}$), 2.84 (s, 6H, NC$H_{3\mathbf{b}}$).

^{13}C NMR (DMSO-*d*$_6$) : δ 182.8 (squaramide *C*=O), 167.9 (C=O), 166.5 (squaramide *C*=*C*), 146.4 (Ar-*C*-2), 131.8 (Ar-*C*-3), 131.2 (Ar-*C*-1), 124.7 (Ar-*C*-4), 123.3 (Ar-*C*-6), 122.6 (Ar-*C*-5) , 61.7 (O*C*H$_3$), 38.5 (N*C*H$_{3\mathbf{a}}$), 34.7 (N*C*H$_{3\mathbf{b}}$).

HPLC t_R**:** 6.19 (System 1), 2.57 (System 3)

m/z: HRMS (TOF ES$^+$) $C_{24}H_{26}N_4O_6$ [M+Na]$^+$ calcd 489.1750; found 489.1747

(*R*)-2-Methoxy-*N*,*N*-dimethyl-3-((2-((1-(5-methylfuran-2-yl)propyl)amino)-3,4-dioxocyclobut-1-en-1-yl)amino)benzamide (45b).

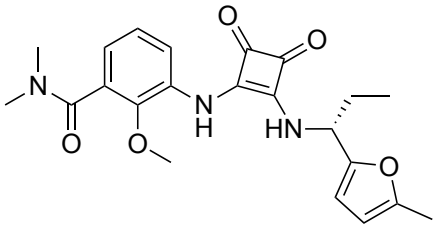

Synthesis according to general procedure L using 3-((2-ethoxy-3,4-dioxocyclobut-1-en-1-yl)amino)-2-methoxy-*N*,*N*-dimethylbenzamide (**58b**) (33 mg, 0.10 mmol, 1 eq), (*R*)-1-(5-methylfuran-2-yl)propan-1-amine hydrochloride (21.9 mg, 0.12 mmol, 1.2 eq) and DIPEA (22 µL, 0.12 mmol, 1.2 eq). The crude was purified by preparative HPLC system 2 using the following gradient: 10% - 50% over 5 min; 50% - 90% over 6 min; held at 1 min. The purification afforded a yellow solid (6 mg, 14%).

^{1}H NMR (DMSO-*d*$_6$) δ 9.39 (s, 1H, squaramide N*H*), 8.73 (dd, *J* = 8.9/1.5 Hz, 1H, squaramide N*H*), 7.92 (d, *J* = 8.2/2.1 Hz, 1H, Ar-C*H*-6), 7.13 (dd, *J* = 7.9/7.9 Hz, 1H, Ar-C*H*-4), 6.87 (d, *J* = 7.6 Hz, 1H, Ar-C*H*-5), 6.28 (d, *J* = 3.2 Hz, 1H, furan C*H*), 6.06 (d, *J* = 3.0 Hz, 1H, furan C*H*), 5.28 – 5.07 (m, *J* = 7.7 Hz, 1H, C*H*CH$_2$CH$_3$), 3.72 (s, 3H, OC*H*$_3$), 3.01 (s, 3H, NC*H*$_{3}$***a***), 2.81 (s, 3H, NC*H*$_{3}$***b***), 2.26 (s, 3H, furyl CC*H*$_3$), 2.06 – 1.71 (m, 2H, CHC*H*$_2$CH$_3$), 0.92 (t, *J* = 7.3 Hz, 3H, CH$_2$C*H*$_3$).

HPLC t_R: 4.68 min (System 2), 4.13 min (System 3).

m/z: HRMS (TOF ES$^+$) $C_{22}H_{25}N_3O_5$ [M+Na]$^+$ calcd 434.1692; found 434.1692

6.2 Pharmacology

6.2.1 Compounds and Assay Reagents

Unlabelled CXCL8 (28-99) (CXCL8) obtained from Sino Biological (Eschborn, Germany) and stored in 10 μM aqueous aliquots at -20 ˚C. Navarixin (**2**) and the fluorescent-navarixin CXCR1 / CXCR2 probe (**44**) were synthesised in-house and supplied by Dr. Bianca Casella (University of Nottingham, UK).[138] Test compound top stocks (10 mM) were made in DMSO and stored at -20 ˚C in 5μL experimental aliquots. The NanoGlo furimazine for nanobit complementation assay was purchased from Promega (UK). Bovine Serum Albumin (BSA) was purchased from Sigma Aldrich.

6.2.2 Generation of CXCR1 and CXCR2 constructs

cDNA expression vectors for wild type CXCR1 and CXCR2 were provided by Dr Desislava Nesheva and Dr James Farmer (University of Nottingham, UK) Human CXCR1 (GenBank: NM_000634.3) and CXCR2 (GenBank NM_001557.3) receptor cDNA sequences, without start codon, were cloned (EcoR1 / XhoI) downstream of an N terminal signal sequence and SNAP-tag between KpnI and BamH1 (New England Biolabs, Hitchin, UK), in the vector pcDNA3.1neo(+) (Invitrogen, Paisley, UK). In other versions of the vector, C terminal fusions of SNAP-CXCR1 or SNAP-CXCR2 was encoded using receptor cDNA lacking the stop codon, and insertion of cDNA in frame between XhoI / XbaI for the LgBiT fragment or thermostable Nanoluciferase (tsNanoLuc; Hoare *et al*.[395]). This generated p3.1neo-SNAP-CXCR1/2-LgBiT (for NanoBiT complementation) or p3.1neo-SNAP-CXCR1/2-tsNanoLuc for fluorescent ligand NanoBRET .

The receptor alanine mutants CXCR1N311A$^{8.49}$ and CXCR2K320A$^{8.49}$ were generated by James Farmer (University of Nottingham). Briefly, mutagenesis was performed according to the quickchange mutagenesis methodology (Agilent, United States). For each receptor cDNA, forward and reverse mutagenic primers were designed with the nucleotide changes needed for alanine substitution central (**Table 6-1**; Sigma-Aldrich). These primers were used in PCR to amplify P3.1neo-CXCR1-LgBiT and p3.1neo-CXCR2-LgBiT plasmids, followed by digestion with the enzyme DpnI. DpnI selectively digests the template (and wild type) methylated DNA, leaving the mutated PCR vector products intact. The PCR

products were then purified, transformed into Escherichia Coli Top10F' cells, and plated onto LB agar plates containing 75 ug/ml ampicillin to select for pcDNA3.1 containing bacteria. Positive colonies were maxiprepped to prepare the p3.1neo-CXCR1N8.49A-LgBiT and p3.1neo-CXCR2N311A$^{8.49}$-LgBiT cDNAs, and the presence of the mutation was confirmed by double stranded sequencing. Relevant sections of the coding region in each mutated plasid are shown in for CXCR1 **Figure 6-1** and CXCR2 **Figure 6-2** below.

Table 6-1 Primer design for CXCR1N311A$^{8.49}$ and CXCR2K320A$^{8.49}$

Receptor	Type	Sequence (5' to 3')
CXCR1N311A$^{8.49}$	Forward	TACGCCTTCATCGGCCAAGCTTTTCGCCATGGATTCCT
	Reverse	AGGAATCCATGGCGAAAACGTTGGCCGATGAAGGCGTA
CXCR2K320A$^{8.49}$	Forward	TACGCCTTCATTGGCCAGGCGTTTCGCCATGGACTCCT
	Reverse	AGGAGTCCATGGCGAAACGCCTGGCCAATGAAGGCGTA

```
CXCR1_WT    MSNITDPQMWDFDDLNFTGMPPADEDYSPCMLETETLNKYVVIIAYALVFLLSLLGNSLV
CXCR1N8.49A MSNITDPQMWDFDDLNFTGMPPADEDYSPCMLETETLNKYVVIIAYALVFLLSLLGNSLV

CXCR1_WT    MLVILYSRVGRSVTDVYLLNLALADLLFALTLPIWAASKVNGWIFGTFLCKVVSLLKEVN
CXCR1N8.49A MLVILYSRVGRSVTDVYLLNLALADLLFALTLPIWAASKVNGWIFGTFLCKVVSLLKEVN

CXCR1_WT    FYSGILLLACISVDRYLAIVHATRTLTQKRHLVKFVCLGCWGLSMNLSLPFFLFRQAYHP
CXCR1N8.49A FYSGILLLACISVDRYLAIVHATRTLTQKRHLVKFVCLGCWGLSMNLSLPFFLFRQAYHP

CXCR1_WT    NNSSPVCYEVLGNDTAKWRMVLRILPHTFGFIVPLFVMLFCYGFTLRTLFKAHMGQKHRA
CXCR1N8.49A NNSSPVCYEVLGNDTAKWRMVLRILPHTFGFIVPLFVMLFCYGFTLRTLFKAHMGQKHRA

CXCR1_WT    MRVIFAVVLIFLLCWLPYNLVLLADTLMRTQVIQESCERRNNIGRALDATEILGFLHSCL
CXCR1N8.49A MRVIFAVVLIFLLCWLPYNLVLLADTLMRTQVIQESCERRNNIGRALDATEILGFLHSCL

CXCR1_WT    NPIIYAFIGQNFRHGFLKILAMHGLVSKEFLARHRVTSYTSSSVNVSSNL
CXCR1N8.49A NPIIYAFIGQAFRHGFLKILAMHGLVSKEFLARHRVTSYTSSSVNVSSNL
```

Figure 6-1 Multiple sequence alignment of wild CXCR1 (Uniprot accession P25024), shown as CXCR1_WT, and CXCR1N311A$^{8.49}$ mutant construct. Mutant highlighted in red showing N311$^{8.49}$ site point mutation to Ala$^{8.49}$.

```
CXCR2_WT      MEDFNMESDSFEDFWKGEDLSNYSYSSTLPPFLLDAAPCEPESLEINKYFVVIIYALVFL
CXCR2K8.49A   MEDFNMESDSFEDFWKGEDLSNYSYSSTLPPFLLDAAPCEPESLEINKYFVVIIYALVFL

CXCR2_WT      LSLLGNSLVMLVILYSRVGRSVTDVYLLNLALADLLFALTLPIWAASKVNGWIFGTFLCK
CXCR2K8.49A   LSLLGNSLVMLVILYSRVGRSVTDVYLLNLALADLLFALTLPIWAASKVNGWIFGTFLCK

CXCR2_WT      VVSLLKEVNFYSGILLLACISVDRYLAIVHATRTLTQKRYLVKFICLSIWGLSLLLALPV
CXCR2K8.49A   VVSLLKEVNFYSGILLLACISVDRYLAIVHATRTLTQKRYLVKFICLSIWGLSLLLALPV

CXCR2_WT      LLFRRTVYSSNVSPACYEDMGNNTANWRMLLRILPQSFGFIVPLLIMLFCYGFTLRTLFK
CXCR2K8.49A   LLFRRTVYSSNVSPACYEDMGNNTANWRMLLRILPQSFGFIVPLLIMLFCYGFTLRTLFK

CXCR2_WT      AHMGQKHRAMRVIFAVVLIFLLCWLPYNLVLLADTLMRTQVIQETCERRNHIDRALDATE
CXCR2K8.49A   AHMGQKHRAMRVIFAVVLIFLLCWLPYNLVLLADTLMRTQVIQETCERRNHIDRALDATE

CXCR2_WT      ILGILHSCLNPLIYAFIGQKFRHGLLKILAIHGLISKDSLPKDSRPSFVGSSSGHTSTTL
CXCR2K8.49A   ILGILHSCLNPLIYAFIGQAFRHGLLKILAIHGLISKDSLPKDSRPSFVGSSSGHTSTTL
```

Figure 6-2 Multiple sequence alignment of wild CXCR2 (Uniprot accession P25025), shown as CXCR2_WT, and CXCR2K320A$^{8.49}$ mutant construct. Mutant highlighted in red showing K320$^{8.49}$ site point mutation to Ala$^{8.49}$.

6.2.3 Transfection and cell culture

The cell line for all cell-based assays, as well as the preparation of membranes for binding assays were human embryonic kidney (HEK293T). For NanoBiT assays, zeocin resistant SmBiT-β-arrestin2 expressing HEK293 cells were stably transfected with pcDNA3.1 SNAP-CXCR1/2-LgBiT cDNA for NanoBiT complementation. HEK293T cells only were transfected with pcDNA3.1neo-SNAP-CXCR1/2-tsNanoLuc for NanoBRET binding assays using Lipofectamine™ 3000 transfection reagent in Opti-MEM media (Invitrogen). A pooled stable population of transfected NanoBiT cells were selected using a combination of geneticin (0.8 mg/mL) and zeocin (200µg/mL) for 7-10 days, while CXCR1-tsNluc / CCXCR2-tsNluc cells were generated in the same way *via* geneticin resistance only (Casella *et al.*[138]). Cell lines stocks were stored in liquid nitrogen when not in use and passage numbers <30 was used for experiments.

For routine culture, cell lines were maintained in in Dulbecco's modified Eagle's medium (DMEM) supplemented with 10% (v/v) foetal bovine serum (FBS) (Sigma-Aldrich) with the addition of G418 (0.2 mg / ml) and zeocin (50µg / ml; NanoBiT lines only) at 37 ˚C in an atmosphere of 5% CO_2. Cells were passaged *via* trypsination at 70 – 90% confluency with split ratios varying between 1:3 and 1:20, depending on requirements. For NanoBiT

assays, cells were seeded 18 h prior to experiment on poly-D-lysine coated white F-bottom 96-well plates (Greiner Bio-One, Stonehouse, UK) at 32,000 cells in 100 ml per well.

6.2.4 NanoBiT complementation assay

The NanoBiT complementation assay measures receptor activation *via* recruitment of a downstream effector (β-arrestin2) using split nanoluciferase technology (LgBiT / SmBiT) to measure protein-protein interactions.[375 442] HEK293T cells were stably transfected with SNAP tagged receptor with C terminal tagged LgBiT and N-terminally tagged SmBiT-β-arrestin2. The receptors investigated were wild type human CXCR1; wild type human CXCR2; CXCR1N311A$^{8.49}$ and CXCR2K320A$^{8.49}$.

Assays were performed in HEPES-balanced salt solution (HBSS; 25 mM HEPES, 10 mM glucose, 146 mM NaCl, 5mM KCl, 1mM $MgSO_4$, 2mM sodium pyruvate, and 1.3 mM $CaCl_2$, pH 7.45) + 0.1% Bovine serum albumin (HBSS + 0.1% BSA solution). 1 in 3 serial compound dilutions were prepared from DMSO stocks using HBSS + 0.1% BSA buffer solution described above for addition to HEK 293 cells. NanoBiT cell lines seeded in 96 well plates (**Section 6.2.3**) were washed with HBSS / 0.1% BSA buffer and compound / vehicle pre-treatments (100 mM – 0.01 nM, maximum 1 % DMSO final concentration) was performed in 40 ml assay buffer for 1 hour at 37 ˚C, 0 % CO_2 . 10 µL furimazine solution (5 µL manufacturer's stock in 1.1 mL HBSS / 0.1% BSA) was then added to each well and incubated for 5 min at room temperature in the dark. Baseline luminescence was then recorded over 1.5 min using a PHERAstar FS plate reader (BMG Labtech, Germany) at 37 ˚C. 10 µL CXCL8 (28-99) agonist was then added at 6 x final concentration in assay buffer (for IC_{50} determinations, assay concentration was 10 nM CXCL8. The plate was returned to the Pherastar and incubated at 37°C, with luminescence response readings being taken every 24 s for a further 35 min.

NanoBiT experiments were performed in triplicate and concentration response / inhibition data analysed in Graphpad Prism 10 (GraphPad Prism Software, San Diego, California)[432]. Data were normalised to vehicle (0%) and to the response for the reference concentration of CXCL8 (28-99) (e.g. 10 nM in IC_{50} determinations) in the absence of compound pretreatment (100 %). CXCL8 (28-99) concentration response curves were fitted to pooled data by nonlinear regression[432].

$$Response = Basal + \ Rmax. \frac{[CXCL8]}{[CXCL8] + EC_{50}}$$

where Rmax is the maximum CXCL8 reponse, and EC_{50} represents the concentration of CXCL8 to produce 50 % of the maximal response.

For compound IC_{50} determinations the following equation was used for fitting:

$$Response = Top. \frac{IC_{50}}{IC_{50} + [Compound]} + Bottom$$

where Top is the response to 10 nM CXCL8 in the absence of inhibitor and Bottom is the maximal compound inhibition observed. The IC_{50} value represents the concentration of compound to produce 50 % maximal inhibition. For both concentration-response and concentration dependent inhibition curves, a unit Hill slope (3 parameter fitting) was assumed.

6.2.5 NanoBRET CXCR1 binding assay

The NanoBRET assay utilised previously reported fluorescent probe (**44**) (Casella *et al.*[138]) and HEK293 SNAP-CXCR1-tsNanoluc membranes prepared by Dr Bianca Casella and Dr James Farmer (as described in Casella *et al.*[138]). Binding Click or tap here to enter text.assays were carried out in OptiPlate-384 white well microplates (PerkinElmer, Beaconsfield, UK), using 40 ml final volume in an assay buffer comprising 25 mM HEPES, 1% DMSO, 0.1 mg/ml saponin, 0.02 % pluronic acid F_{127}, 1mM $MgCl_2$ and 0.1 % BSA (pH 7.4). For competition studies 100 nM of fluorescent ligand (**44**) was prepared in each well, with vehicle (defining total binding or varying concentrations of competing antagonists under investigation. Non-specific binding (NSB) was defined using 10 μM navarixin (**2**). To initiate binding, 1 μg / well HEK293 SNAP-CXCR1-NanoLuc cell membranes were added for 30 min at 37 ˚C, followed by furimazine (1/660 dilution from manufacturer's stock). BRET measurements were made for up to 60 min at 37 ˚C post furimazine addition, of nanoluciferase donor output (450 nm) and BODIPY 630-650 fluorescent ligand acceptor emission (630 nm) to generate the BRET ratio (630 nm/ 450 nm). For the purposes of competition analysis, the endpoint read representing 90 min incubation between the ligands and membranes was used.

NanoBRET Competition binding experiments were performed in triplicate and data analysed in GraphPad Prism 10[432 506]. Specific binding was defined by subtraction of the NSB values. The data were normalised to specific probe binding in the absence of competing ligand (100 %) and NSB (0%). Competition binding curves were fitted to pooled data by three parameter nonlinear regression, assuming a unit Hill slope[432 506]. Competing ligand IC_{50} values (concentration of inhibitor producing 50 % inhibition) were determined using:

$$Specific\ Binding = Basal + Total\ Specific\ Binding.\frac{IC_{50}}{[ligand] + IC_{50}}$$

The mode of action of novel inhibitors was assumed to be competitive and reversible with the fluorescent probe at CXCR1 intracellular allosteric site. This allowed estimate of the unlabelled inhibitor dissociation constants (K_i) to be calculated from IC_{50} values using the binding form of the Cheng-Prusoff[433] equation:

$$K_i = \frac{IC_{50}}{1 + \frac{[\boldsymbol{X}]}{K_{\boldsymbol{X}}}}$$

Where $K_{\mathbf{X}}$ and [**44**] represent the dissociation constant and concentration (100 nM of fluorescent probe **44** respectively. $K_{\mathbf{X}}$ was determined to be 101 ± 21 nM from CXCR1 saturation binding experiments conducted by Bianca Casella.[138]

6.3 Molecular Modelling

6.3.1 Glide docking flexible ligand protocol

Protein models were imported into Maestro in PDB format along with the template CXCR2-00767013 (**1**) complex model (PDB ID: 6LFL).[54] The proteins were prepared using the protein preparation wizard in Maestro[289] which sequentially removed waters, protonated optimised H-bonds using PROPKA at pH 7.0 and performed restrained energy minimization using OPLS4 force field. Glide grids were produced for the target receptor using the position of 00767013 (**1**) in the template after superimposition of all proteins. The centroid for the grid was determined from 0076703 (**1**). The grid had an inner box of 5 Å^3 inner box and 17 Å^3 outer box around the centroid. Ligands to be docked were drawn using Maestro 2D sketcher and prepared in Maestro[289] using LigPrep[434] with chiralities being determined from 3D structure to ensure only desired chiral isomers were generated.

Protonation states of the ligands were produced between 7.4 and 9.0 pH using Epik. Glide ligand docking was performed with standard precision and flexible ligand sampling enabled. Extended sampling of ligands poses was enabled and for each ligand 100 poses were minimised post docking with a maximum of 5 poses were generated. All other setting were set to default and included no binding or volume constraints. In each case the binding pose which best reflected the crystallographic pose was reported unless otherwise stated along with the corresponding Glide docking score. Images were generated using PyMol visualisation software.[435]

References

(1) Murdoch, C.; Finn, A. Chemokine receptors and their role in inflammation and infectious diseases. *Blood.* **2000**, *15* (95(10)), 3032-3034.

(2) Hughes, C. E.; Nibbs, R. J. B. A guide to chemokines and their receptors. *FEBS J.* **2018**, *285* (16), 2944-2944.

(3) Miller, M. C.; Mayo, K. H. Chemokines from a Structural Perspective. *Int. J. Mol. Sci.* **2017**, *18* (10).

(4) Zlotnik, A.; Yoshie, O. Chemokines: a new classification system and their role in immunity. *Immunity.* **2000**, *12* (2), 121-127.

(5) Baggiolini, M. Chemokines and leukocyte traffic. *Nature.* **1998**, *392*, 565-568.

(6) Strieter, R. M.; Polverini, P. J.; Kunkel, S. L.; Arenberg, D. A.; Burdick, M. D.; Kasper, J.; Dzuiba, J.; Van Damme, J.; Walz, A.; Marriott, D.; Chan, S. Y.; Roczniak, S.; Shanafelt, A. B. The Functional Role of the ELR Motif in CXC Chemokine-mediated Angiogenesis. *J. Biol. Chem.* **1995**, *270* (45), 27348-27357.

(7) Giuliano, S.; Guyot, M.; Grépin, R.; Pagès, G. The ELR+CXCL chemokines and their receptors CXCR1/CXCR2: A signaling axis and new target for the treatment of renal cell carcinoma. *Oncoimmunology.* **2014**, *3* (4).

(8) Oppenheim, J. J.; Zachariae, C. O. C.; Mukaida, N.; Matsushima, K. Properties of the novel proinflammatory supergene "intercrine" cytokine family. *Annu. Rev. Immunol.* **1991**, *9* (1), 617-648.

(9) Yoshimura, T. Discovery of IL-8/CXCL8 (The Story from Frederick). *Front. immunol.* **2015**, *6* (Jun).

(10) Ha, H.; Debnath, B.; Neamati, N. Role of the CXCL8-CXCR1/2 Axis in Cancer and Inflammatory Diseases. *Theranostics.* **2017**, *7* (6), 1543-1588.

(11) Tigner, A.; Ibrahim, S. A.; Murray, I. V. Histology, White Blood Cell. *StatPearls.* **2022**.

(12) Rosales, C. Neutrophil: A Cell with Many Roles in Inflammation or Several Cell Types? *Front. Physiol.* **2018**, *9* (Feb), 113.

(13) Mishra, A.; Suman, K. H.; Nair, N.; Majeed, J.; Tripathi, V. An updated review on the role of the CXCL8-CXCR1/2 axis in the progression and metastasis of breast cancer. *Mol. Biol. Rep.* **2021**, *48* (9), 6551-6561.

(14) Barnes, P. J. Targeting cytokines to treat asthma and chronic obstructive pulmonary disease. *Nature Reviews Immunology* **2018**, *18* (7), 454-466.

(15) Sitaru, S.; Budke, A.; Bertini, R.; Sperandio, M. Therapeutic inhibition of CXCR1/2: where do we stand? *Int. Emerg. Med.* **2023**, *18* (6), 1647-1664.

(16) Kaplan, M. J.; Radic, M. Neutrophil extracellular traps (NETs): Double-edged swords of innate immunity. *J. Immunol.* **2012**, *189* (6), 2689.

(17) Vorobjeva, N. V.; Chernyak, B. V. NETosis: Molecular Mechanisms, Role in Physiology and Pathology. *Biochemistry.* **2020**, *85* (10), 1178.

(18) Kennedy, A. D.; Deleo, F. R. Neutrophil apoptosis and the resolution of infection. *Immunol. Res.* **2009**, *43* (1-3), 25-61.

(19) Cambier, S.; Gouwy, M.; Proost, P. The chemokines CXCL8 and CXCL12: molecular and functional properties, role in disease and efforts towards pharmacological intervention. *Cell. Mol. Immunol.* **2023**, *20* (3), 217-251.

(20) Viola, A.; Luster, A. D. Chemokines and their receptors: Drug targets in immunity and inflammation. *Annu. Rev. Pharmacol. Toxicol.* **2008**, *48*, 171-197.

(21) Vandercappellen, J.; Van Damme, J.; Struyf, S. The role of CXC chemokines and their receptors in cancer. *Cancer Lett.* **2008**, *267*, 226-244.

(22) Magić, Z. The nobel prize in physiology or medicine 2009. *Vojnosanitetski Pregled.* **2009**, *66*, 861-861.

(23) Wei, S.; Episkopou, V.; Piantedosi, R.; Gottesman, M. E.; Robertson, E. J.; Blaner, W. S. Studies on the Metabolism of Retinol and Retinol-Binding Protein (RBP) in Transthyretin-Lacking Mice Produced by Homologous Recombination. 1994; p 245.

(24) Ross, E. M.; Gilman, A. G. Reconstitution of catecholamine-sensitive adenylate cyclase activity: interaction of solubilized components with receptor-replete membranes. *Proc. Natl. Acad. Sci.* **1977**, *74* (9), 3715-3719.

(25) Sunahara, R. K.; Insel, P. A. The molecular pharmacology of G protein signaling then and now: A tribute to alfred G. Gilman. *Mol. Pharmacol.* **2016**, *89* (5), 585-592.

(26) Sriram, K.; Insel, P. A. G protein-coupled receptors as targets for approved drugs: how many targets and how many drugs? *Mol. Pharmacol.* **2018**, *93* (4), 251-258.

(27) Hauser, A. S.; Attwood, M. M.; Rask-Andersen, M.; Schiöth, H. B.; Gloriam, D. E. Trends in GPCR drug discovery: new agents, targets and indications. *Nat. Rev. Drug Discov.* **2017**, *16* (12), 829-842.

(28) Addis, P.; Bali, U.; Baron, F.; Campbell, A.; Harborne, S.; Jagger, L.; Milne, G.; Pearce, M.; Rosethorne, E. M.; Satchell, R.; Swift, D.; Young, B.; Unitt, J. F. Key aspects of modern GPCR drug discovery. *SLAS Discov.* **2024**, *29* (1), 1-22.

(29) Peterson, S. M.; Hutchings, C. J.; Hu, C. F.; Mathur, M.; Salameh, J. W.; Axelrod, F.; Sato, A. K. Discovery and design of G protein-coupled receptor targeting antibodies. *Expert Opin. Drug Discov.* **2023**, *18* (4), 417-428.

(30) Hutchings, C. J.; Koglin, M.; Marshall, F. H. Therapeutic antibodies directed at G protein-coupled receptors. *MAbs.* **2010**, *2* (6), 594-594.

(31) Hutchings, C. J. Mini-review: antibody therapeutics targeting G protein-coupled receptors and ion channels. *Antib. Ther.* **2020**, *3* (4), 257-257.

(32) Pándy-Szekeres, G.; Munk, C.; Tsonkov, T. M.; Mordalski, S.; Harpsøe, K.; Hauser, A. S.; Bojarski, A. J.; Gloriam, D. E. GPCRdb in 2018: adding GPCR structure models and ligands. *Nucleic acids res.* **2018**, *46* (D1), D440-D446.

(33) Kolakowski, L. F. GCRDb: A G-protein-coupled receptor database. *Recept Channels.* **1994**, *2* (1), 1-7.

(34) Munk, C.; Isberg, V.; Mordalski, S.; Harpsøe, K.; Rataj, K.; Hauser, A. S.; Kolb, P.; Bojarski, A. J.; Vriend, G.; Gloriam, D. E. GPCRdb: the G protein-coupled receptor database – an introduction. *Br. J. Pharmacol.* **2016**, 2195-2207.

(35) Schiöth, H. B.; Fredriksson, R. The GRAFS classification system of G-protein coupled receptors in comparative perspective. *Gen. Comp. Endicronol.* **2005**, *142* (1-2), 94-101.

(36) Dijkman, P. M.; Muñoz-García, J. C.; Lavington, S. R.; Kumagai, P. S.; dos Reis, R. I.; Yin, D.; Stansfeld, P. J.; Costa-Filho, A. J.; Watts, A. Conformational dynamics of a G protein-coupled receptor helix 8 in lipid membranes. *Sci. Adv* **2020**, *6* (33).

(37) Kobilka, B. K. G protein coupled receptor structure and activation. *Biochim. biophys. acta. - Biomembr.* **2007**, *1768* (4), 794-807.

(38) Jastrzebska, B.; Park, P. S. H. *GPCRs : Structure, Function, and Drug Discovery*; Elsevier Science & Technology, 2019.

(39) Tikhonova, I. G.; Costanzi, S. Unraveling the structure and function of G protein-coupled receptors through NMR spectroscopy. *Curr. Pharm. Des.* **2009**, *15* (35), 4003-4003.

(40) Ballesteros, J. A.; Weinstein, H. Integrated methods for the construction of three-dimensional models and computational probing of structure-function relations in G protein-coupled receptors. *J. Neurosci. Methods.* **1995**, *25* (C), 366-428.

(41) Isberg, V.; de Graaf, C.; Bortolato, A.; Cherezov, V.; Katritch, V.; Marshall, F. H.; Mordalski, S.; Pin, J. P.; Stevens, R. C.; Vriend, G.; Gloriam, D. E. Generic GPCR residue numbers - aligning topology maps while minding the gaps. *Trends. Pharmacol. Sci.* **2014**, *36* (1), 22-31.

(42) Erlandson, S. C.; McMahon, C.; Kruse, A. C. Structural Basis for G Protein-Coupled Receptor Signaling. *Ann. Rev. Biophys.* **2018**, *47* (1), 1-18.

(43) Kamato, D.; Thach, L.; Bernard, R.; Chan, V.; Zheng, W.; Kaur, H.; Brimble, M.; Osman, N.; Little, P. J. Structure, Function, Pharmacology, and Therapeutic Potential of the G Protein, Gα/q,11. *Front. Cardiovasc. Med.* **2015**, *2*, 24-24.

(44) Cabrera-Vera, T. M.; Vanhauwe, J.; Thomas, T. O.; Medkova, M.; Preininger, A.; Mazzoni, M. R.; Hamm, H. E. Insights into G Protein Structure, Function, and Regulation. *Endocr. Rev.* **2003**, *24* (6), 765-781.

(45) Du, Y.; Duc, N. M.; Rasmussen, S. G. F.; Hilger, D.; Kubiak, X.; Wang, L.; Bohon, J.; Kim, H. R.; Wegrecki, M.; Asuru, A.; Jeong, K. M.; Lee, J.; Chance, M. R.; Lodowski, D. T.; Kobilka, B. K.; Chung, K. Y. Assembly of a GPCR-G Protein Complex. *Cell.* **2019**, *177* (5), 1232-1242.

(46) Latorraca, N. R.; Venkatakrishnan, A. J.; Dror, R. O. GPCR dynamics: Structures in motion. *Chem. Rev.* **2017**, *117* (1), 139-155.

(47) Huang, S. K.; Prosser, R. S. Dynamics and mechanistic underpinnings to pharmacology of class A GPCRs: an NMR perspective. *Am. J. Physiol. Cell Physiol.* **2022**, *322* (4), C739-C753.

(48) Egyed, A.; Kiss, D. J.; Keserű, G. M. The Impact of the Secondary Binding Pocket on the Pharmacology of Class A GPCRs. *Front. Pharmacol.* **2022**, *13*.

(49) Wu, C.; Xu, Y.; He, Q.; Li, D.; Duan, J.; Li, C.; You, C.; Chen, H.; Fan, W.; Jiang, Y.; Eric Xu, H. Ligand-induced activation and G protein coupling of prostaglandin F2α receptor. *Nat. Commun.* **2023**, *14* (1).

(50) Shi, L.; Javitch, J. A. The second extracellular loop of the dopamine D2 receptor lines the binding-site crevice. *Proc. Natl. Acad. Sci.* **2004**, *101* (2), 440-445.

(51) Kruse, A. C.; Kobilka, B. K.; Gautam, D.; Sexton, P. M.; Christopoulos, A.; Wess, J. Muscarinic acetylcholine receptors: novel opportunities for drug development. *Nat. Rev. Drug Discov.* **2014**, *13* (7), 549-549.

(52) Wu, Y.; Zeng, L.; Zhao, S. Ligands of adrenergic receptors: A structural point of view. *Biomolecules.* **2021**, *11* (7).

(53) Wacker, D.; Stevens, R. C.; Roth, B. L. How ligands illuminate GPCR molecular pharmacology. *Cell.* **2017**, *170* (3), 414-414.

(54) Liu, K.; Wu, L.; Yuan, S.; Wu, M.; Xu, Y.; Sun, Q.; Li, S.; Zhao, S.; Hua, T.; Liu, Z. J. Structural basis of CXC chemokine receptor 2 activation and signalling. *Nature.* **2020**, *585* (7823), 135-140.

(55) Ishimoto, N.; Park, J. H.; Kawakami, K.; Tajiri, M.; Mizutani, K.; Akashi, S.; Tame, J. R. H.; Inoue, A.; Park, S. Y. Structural basis of CXC chemokine receptor 1 ligand binding and activation. *Nat. Commun.* **2023**, *14* (1), 1-11.

(56) Scholten, D. J.; Canals, M.; Maussang, D.; Roumen, L.; Smit, M. J.; Wijtmans, M.; De Graaf, C.; Vischer, H. F.; Leurs, R.; Leurs, R.; Amsterdam, L.; Graaf, C. D.; Vischer, H. F.; Leurs, R. Pharmacological modulation of chemokine receptor function. *Br. J. Pharmacol.* **2012**, *165* (6), 1617-1643.

(57) Sanchez, J.; Huma, Z. e.; Robert Lane, J.; Liu, X.; Bridgford, J. L.; Payne, R. J.; Canals, M.; Stone, M. J. Evaluation and extension of the two-site, two-step model for binding and activation of the chemokine receptor CCR1. *J. bio. chem.* **2019**, *294* (10), 3464-3475.

(58) Zhou, Q.; Yang, D.; Wu, M.; Guo, Y.; Guo, W.; Zhong, L.; Cai, X.; Dai, A.; Shakhnovich, E.; Liu, Z.-J.; Stevens, R. C.; Madan, M.; Wang, M.-W.; Zhao, S.; Babu, M. Universal activation mechanism of class A GPCRs. *eLife.* **2019**, *8* (e50279).

(59) Dror, R. O.; Mildorf, T. J.; Hilger, D.; Manglik, A.; Borhani, D. W.; Arlow, D. H.; Philippsen, A.; Villanueva, N.; Yang, Z.; Lerch, M. T.; Hubbell, W. L.; Kobilka, B. K.; Sunahara, R. K.; Shaw, D. E. Structural basis for nucleotide exchange in heterotrimeric G proteins. *Science.* **2015**, *348* (6241), 1361-1365.

(60) Papasergi-Scott, M. M.; Pérez-Hernández, G.; Batebi, H.; Gao, Y.; Eskici, G.; Seven, A. B.; Panova, O.; Hilger, D.; Casiraghi, M.; He, F.; Maul, L.; Gmeiner, P.; Kobilka, B. K.; Hildebrand, P. W.; Skiniotis, G. Time-resolved cryo-EM of G-protein activation by a GPCR. *Nature.* **2024**, 1-10.

(61) Rasmussen, S. G. F.; Devree, B. T.; Zou, Y.; Kruse, A. C.; Chung, K. Y.; Kobilka, T. S.; Thian, F. S.; Chae, P. S.; Pardon, E.; Calinski, D.; Mathiesen, J. M.; Shah, S. T. A.; Lyons, J. A.; Caffrey, M.; Gellman, S. H.; Steyaert, J.; Skiniotis, G.; Weis, W. I.; Sunahara, R. K.; Kobilka, B. K. Crystal structure of the β 2 adrenergic receptor-Gs protein complex. *Nature.* **2011**, *477* (7366), 549-557.

(62) Oldham, W. M.; Van Eps, N.; Preininger, A. M.; Hubbell, W. L.; Hamm, H. E. Mechanism of the receptor-catalyzed activation of heterotrimeric G proteins. *Nat. Struct. Mol. Bio.* **2006**, *13* (9), 772-777.

(63) Van Eps, N.; Preininger, A. M.; Alexander, N.; Kaya, A. I.; Meier, S.; Meiler, J.; Hamm, H. E.; Hubbell, W. L. Interaction of a G protein with an activated receptor opens

the interdomain interface in the alpha subunit. *Proc. Natl. Acad. Sci.* **2011**, *108* (23), 9420-9424.

(64) Sayar, K.; Uğur, Ö.; Liu, T.; Hilser, V. J.; Onaran, O. Exploring allosteric coupling in the α-subunit of Heterotrimeric G proteins using evolutionary and ensemble-based approaches. *BMC Struct. Bio.* **2008**, *8*, 1-14.

(65) Stadtmann, A.; Zarbock, A. CXCR2: From Bench to Bedside. *Front. immunol.* **2012**, *3* (263).

(66) Brandolini, L.; Cristiano, L.; Fidoamore, A.; Pizzol, M. D.; Giacomo, E. D.; Florio, T. M.; Confalone, G.; Galante, A.; Cinque, B.; Benedetti, E.; Ruffini, P. A.; Cifone, M. G.; Giordano, A.; Alecci, M.; Allegretti, M.; Cimini, A. Targeting CXCR1 on breast cancer stem cells: Signaling pathways and clinical application modelling. *Oncotarget.* **2015**, *6* (41), 43375-43394.

(67) Dhayni, K.; Zibara, K.; Issa, H.; Kamel, S.; Bennis, Y. Targeting CXCR1 and CXCR2 receptors in cardiovascular diseases. *Pharmacol. Ther.* **2022**, *237*, 108257-108257.

(68) Nguyen, G. T.; Green, E. R.; Mecsas, J. Neutrophils to the ROScue: Mechanisms of NADPH oxidase activation and bacterial resistance. *Front. Cell. Infect. Microbiol.* **2017**, *7* (373), 264679-264679.

(69) Winterbourn, C. C.; Kettle, A. J.; Hampton, M. B. Reactive Oxygen Species and Neutrophil Function. *Ann. Rev. Biochem.* **2016**, *85*, 765-792.

(70) Immler, R.; Simon, S. I.; Sperandio, M. Calcium signaling and related ion channels in neutrophil recruitment and function. *Eur. J. Clin. Invest.* **2018**, *48* (Suppl 2), 12964-12964.

(71) Korbecki, J.; Kupnicka, P.; Chlubek, M.; Gor, J.; Acy; Gutowska, I.; Baranowska-Bosiacka, I. CXCR2 Receptor: Regulation of Expression, Signal Transduction, and Involvement in Cancer. *Int. J. Mol. Sci.* **2022**, *23* (4), 2168.

(72) Allen, S. J.; Crown, S. E.; Handel, T. M. Chemokine:Receptor Structure, Interactions, and Antagonism. *Annu. Rev. Immunol.* **2007**, *25*, 787-820.

(73) Poeta, V. M.; Massara, M.; Capucetti, A.; Bonecchi, R. Chemokines and chemokine receptors: New targets for cancer immunotherapy. *Front. immunol.* **2019**, *10*, 438073-438073.

(74) Boon, K.; Vanalken, N.; Szpakowska, M.; Chevigné, A.; Schols, D.; Van Loy, T. Systematic assessment of chemokine ligand bias at the human chemokine receptor CXCR2 indicates G protein bias over β-arrestin recruitment and receptor internalization. *Cell Commun. Signal.* **2024**, *22* (1), 1-12.

(75) Rajagopal, S.; Bassoni, D. L.; Campbell, J. J.; Gerard, N. P.; Gerard, C.; Wehrman, T. S. Biased Agonism as a Mechanism for Differential Signaling by Chemokine Receptors. *J. bio. chem.* **2013**, *288* (49), 35039-35039.

(76) Smith, J. S.; Lefkowitz, R. J.; Rajagopal, S. Biased signalling: From simple switches to allosteric microprocessors. *Nat. Rev. Drug Discov.* **2018**, *17* (4), 243-260.

(77) Kenakin, T. P.; Kenakin, T. Biased signalling and allosteric machines: new vistas and challenges for drug discovery. *Br. J. Pharmacol.* **2012**, *165* (6), 1659-1669.

(78) Yoshie, O. CCR4 as a Therapeutic Target for Cancer Immunotherapy. *Cancers* **2021**, *13* (21), 5542-5542.

(79) Waugh, D. J. J.; Wilson, C. The Interleukin-8 Pathway in Cancer. *Clin. Cancer Res.* **2008**, *14* (21), 6735-6741.

(80) Sassone-Corsi, P. The Cyclic AMP Pathway. *Cold Spring Harb. Perspect. Biol.* **2012**, *4* (12), 1-3.

(81) Ishikawa, Y.; Homcy, C. J. The adenylyl cyclases as integrators of transmembrane signal transduction. *Circ. Res.* **1997**, *80* (3), 297-304.

(82) Hawkins, P. T.; Stephens, L. R. PI3K signalling in inflammation. *Biochim. Biophys. Acta. Mol. Cell Biol. Lipids* **2015**, *1851* (6), 882-897.

(83) Wang, J.; Zhang, C.; Xu, P.; Yang, Z. W.; Weng, C. Z.; Lai, Y. X. Phosphoinositide 3-kinase/protein kinase B regulates inflammation severity via signaling of Toll-like receptor 4 in severe acute pancreatitis. *Mol. Med. Rep.* **2018**, *17* (6), 7835-7844.

(84) Molczyk, C.; Singh, R. K. CXCR1: A Cancer Stem Cell Marker and Therapeutic Target in Solid Tumors. *Biomedicines* **2023**, *11* (2).

(85) Qin, H.; Zhuang, W.; Liu, X.; Wu, J.; Li, S.; Wang, Y.; Liu, X.; Chen, C.; Zhang, H. Targeting CXCR1 alleviates hyperoxia-induced lung injury through promoting glutamine metabolism. *Cell rep.* **2023**, *42* (7).

(86) Nasser, M. W.; Raghuwanshi, S. K.; Malloy, K. M.; Gangavarapu, P.; Shim, J.-Y.; Rajarathnam, K.; Richardson, R. M. CXCR1 and CXCR2 activation and regulation. Role of aspartate 199 of the second extracellular loop of CXCR2 in CXCL8-mediated rapid receptor internalization. *J. bio. chem.* **2007**, *282* (9), 6906-6915.

(87) Van Koppen, C. J.; Jakobs, K. H. Arrestin-independent internalization of G protein-coupled receptors. *Mol. Pharmacol.* **2004**, *66* (3), 365-367.

(88) Gurevich, V. V.; Gurevich, E. V. The structural basis of arrestin-mediated regulation of G-protein-coupled receptors. *Pharmacol. Ther.* **2006**, *110* (3), 465-502.

(89) Barlic, J.; Khandaker, M. H.; Mahon, E.; Andrews, J.; Devries, M. E.; Mitchell, G. B.; Rahimpour, R.; Tan, C. M.; Ferguson, S. S. G. G.; Kelvin, D. J.; Ontario, J. P. b-Arrestins Regulate Interleukin-8-induced CXCR1 Internalization. *J. Biol. Chem.* **1999**, *274* (23), 16287-16294.

(90) Jean-Charles, P. Y.; Kaur, S.; Shenoy, S. K. GPCR signaling via β-arrestin-dependent mechanisms. *J. Cardiovasc. Pharmacol.* **2017**, *70* (3), 142-142.

(91) Neel, N. F.; Schutyser, E.; Sai, J.; Fan, G. H.; Richmond, A. Chemokine receptor internalization and intracellular trafficking. *Cytokine Growth Fact. Rev.* **2005**, *16* (6), 637-658.

(92) Richardson, R. M.; Snyderman, R.; Marjoram, R. J.; Barak, L. S. Role of the cytoplasmic tails of CXCR1 and CXCR2 in mediating leukocyte migration, activation, and regulation. *J. Ummunol. Ref.* **2003**, *170* (6), 2904-2911.

(93) Nasser, M. W.; Raghuwanshi, S. K.; Grant, D. J.; Jala, V. R.; Rajarathnam, K.; Richardson, R. M. Differential Activation and Regulation of CXCR1 and CXCR2 by CXCL8 Monomer and Dimer. *J. Immunol.* **2009**, *183* (5), 3425-3432.

(94) Rajarathnam, K.; Schnoor, M.; Richardson, R. M.; Rajagopal, S. How do chemokines navigate neutrophils to the target site: Dissecting the structural mechanisms and signaling pathways. *Cell. Signal.* **2019**, *54*, 69-80.

(95) Raghuwanshi, S. K.; Su, Y.; Singh, V.; Haynes, K.; Richmond, A.; Richardson, R. M.; Hayes, K.; Richmond, A.; Richardson, R. M. The Chemokine Receptors CXCR1 and CXCR2 Couple to Distinct G Protein-Coupled Receptor Kinases To Mediate and Regulate Leukocyte Functions. *J. Immunol.* **2012**, *189* (6), 2824-2832.

(96) Wold, E. A.; Chen, J.; Cunningham, K. A.; Zhou, J. Allosteric Modulation of Class A GPCRs: Targets, Agents, and Emerging Concepts. *J. Med. Chem.* **2019**, *62* (1), 88-127.

(97) Langmead, C. J.; Christopoulos, A. Functional and structural perspectives on allosteric modulation of GPCRs. *Curr. Opin. Cell Biol.* **2014**, *27* (1), 94-101.

(98) Ortiz Zacarías, N. V.; Lenselink, E. B.; Ijzerman, A. P.; Handel, T. M.; Heitman, L. H. Intracellular Receptor Modulation: Novel Approach to Target GPCRs. *Trends Pharmacol. Sci.* **2018**, *39* (6), 547-559.

(99) Koelink, P. J.; Overbeek, S. A.; Braber, S.; De Kruijf, P.; Folkerts, G.; Smit, M. J.; Kraneveld, A. D. Targeting chemokine receptors in chronic inflammatory diseases: an extensive review. *Pharmacol. Ther.* **2012**, *133* (1), 1-18.

(100) Shen, S.; Zhao, C.; Wu, C.; Sun, S.; Li, Z.; Yan, W.; Shao, Z. Allosteric modulation of G protein-coupled receptor signaling. *Front. Endocrinol.* **2023**, *14*.

(101) Morales, P.; Scharf, M. M.; Johnson, C. P.; Di Pizio, A.; Hilger, D. Editorial: New approaches for the discovery of GPCR ligands. *Front. Endocrinol.* **2023**, *14*.

(102) Allegretti, M.; Cesta, M. C.; Locati, M. Allosteric modulation of chemoattractant receptors. *Front. immunol.* **2016**, *7* (170), 191578-191578.

(103) Melancon, B. J.; Hopkins, C. R.; Wood, M. R.; Emmitte, K. A.; Niswender, C. M.; Christopoulos, A.; Conn, P. J.; Lindsley, C. W. Allosteric modulation of seven transmembrane spanning receptors: theory, practice, and opportunities for central nervous system drug discovery. *J. Med. Chem.* **2012**, *55* (4), 1445-1464.

(104) Zhang, M.; Lan, X.; Li, X.; Lu, S. Pharmacologically targeting intracellular allosteric sites of GPCRs for drug discovery. *Drug Discov. Today* **2023**, *28* (12), 103803-103803.

(105) Keov, P.; Sexton, P. M.; Christopoulos, A. Allosteric modulation of G protein-coupled receptors: A pharmacological perspective. *Neuropharmacology* **2011**, *60* (1), 24-35.

(106) Han, B.; Salituro, F. G.; Blanco, M. J. Impact of Allosteric Modulation in Drug Discovery: Innovation in Emerging Chemical Modalities. *ACS Med. Chem. Lett.* **2020**, *11* (10), 1810-1810.

(107) Nesheva, D. N. Examining the Mechanism of Action of Small-molecule Negative Allosteric Modulators of the Human Chemokine Receptor CXCR2. University of Nottingham, 2022.

(108) Bradley, M.; Bond, M.; Manini, J.; Brown, Z.; Charlton, S. SB265610 is an allosteric, inverse agonist at the human CXCR2 receptor. *Br. J. Pharmacol.* **2009**, *158* (1), 328-338.

(109) Jeffrey Conn, P.; Christopoulos, A.; Lindsley, C. W. Allosteric modulators of GPCRs: A novel approach for the treatment of CNS disorders. *Nat. Rev. Drug Discov.* **2009**, *8* (1), 41-54.

(110) Bachelerie, F.; Ben-Baruch, A.; Burkhardt, A. M.; Charo, I. F.; Combadiere, C.; Förster, R.; Farber, J. M.; Graham, G. J.; Hills, R.; Horuk, R.; Locati, M.; Luster, A. D.;

Mantovani, A.; Matsushima, K.; Monaghan, A. E.; Moschovakis, G. L.; Murphy, P. M.; Nibbs, R. J. B.; Nomiyama, H.; Oppenheim, J. J.; Power, C. A.; Proudfoot, A. E. I.; Rosenkilde, M. M.; Rot, A.; Sozzani, S.; Sparre-Ulrich, A. H.; Thelen, M.; Uddin, M.; Yoshie, O.; Zlotnik, A. Chemokine receptors *IUPHAR/BPS Guide to Pharmacology* **2020**, *2020-5* (5), 1-33.

(111) Nussinov, R.; Tsai, C.-J. The Different Ways through Which Specificity Works in Orthosteric and Allosteric Drugs. *Curr. Pharm. Des.* **2012**, *18* (9), 1311-1311.

(112) Christopoulos, A.; Kenakin, T. G protein-coupled receptor allosterism and complexing. *Pharmacol. Rev.* **2002**, *54* (2), 323-374.

(113) Johnstone, S.; Albert, J. S. Pharmacological property optimization for allosteric ligands: A medicinal chemistry perspective. *Bioorg. Med. Chem. Lett.* **2017**, *27* (11), 2239-2258.

(114) Bernat, V.; Admas, T. H.; Brox, R.; Heinemann, F. W.; Tschammer, N. Boronic acids as probes for investigation of allosteric modulation of the chemokine receptor CXCR3. *ACS Chem. Biol.* **2014**, *9* (11), 2664-2677.

(115) Valant, C.; Felder, C. C.; Sexton, P. M.; Christopoulos, A. Probe dependence in the allosteric modulation of a G protein-coupled receptor: implications for detection and validation of allosteric ligand effects. *Mol. Pharmacol.* **2012**, *81* (1), 41-52.

(116) Kenakin, T. Functional selectivity in GPCR modulator screening. *Comb. Chem. High T. Scr.* **2008**, *11* (5), 337-343.

(117) Nussinov, R.; Tsai, C. J. Allostery in disease and in drug discovery. *Cell.* **2013**, *153* (2), 293-305.

(118) Woollard, S. M.; Kanmogne, G. D. Maraviroc: a review of its use in HIV infection and beyond. *Drug Des. Dev. Ther.* **2015**, *9*, 5447-5447.

(119) van Westen, G. J. P.; Gaulton, A.; Overington, J. P. Chemical, Target, and Bioactive Properties of Allosteric Modulation. *PLoS Comput. Biol.* **2014**, *10* (4), 1003559-1003559.

(120) Shen, Q.; Wang, G.; Li, S.; Liu, X.; Lu, S.; Chen, Z.; Song, K.; Yan, J.; Geng, L.; Huang, Z.; Huang, W.; Chen, G.; Zhang, J. ASD v3.0: unraveling allosteric regulation with structural mechanisms and biological networks. *Nucleic acids res.* **2016**, *44* (D1), D527-D535.

(121) Huang, W.; Wang, G.; Shen, Q.; Liu, X.; Lu, S.; Geng, L.; Huang, Z.; Zhang, J. ASBench: benchmarking sets for allosteric discovery. *Bioinformatics* **2015**, *31* (15), 2598-2600.

(122) Yueh, C.; Rettenmaier, J.; Xia, B.; Hall, D. R.; Alekseenko, A.; Porter, K. A.; Barkovich, K.; Keseru, G.; Whitty, A.; Wells, J. A.; Vajda, S.; Kozakov, D. Kinase Atlas: Druggability Analysis of Potential Allosteric Sites in Kinases. *J. Med. Chem.* **2019**, *62* (14), 6512-6524.

(123) Huang, W.; Lu, S.; Huang, Z.; Liu, X.; Mou, L.; Luo, Y.; Zhao, Y.; Liu, Y.; Chen, Z.; Hou, T.; Zhang, J. Allosite: a method for predicting allosteric sites. *Bioinformatics* **2013**, *29* (18), 2357-2359.

(124) Huang, M.; Song, K.; Liu, X.; Lu, S.; Shen, Q.; Wang, R.; Gao, J.; Hong, Y.; Li, Q.; Ni, D.; Xu, J.; Chen, G.; Zhang, J. AlloFinder: a strategy for allosteric modulator discovery and allosterome analyses. *Nucleic acids res.* **2018**, *46* (W1), W451-W458.

(125) Ni, D.; Chai, Z.; Wang, Y.; Li, M.; Yu, Z.; Liu, Y.; Lu, S.; Zhang, J. Along the allostery stream: Recent advances in computational methods for allosteric drug discovery. *WIREs Comput. Mol. Sci.* **2022**, *12*.

(126) Amamuddy, O. S.; Veldman, W.; Manyumwa, C.; Khairallah, A.; Agajanian, S.; Oluyemi, O.; Verkhivker, G. M.; Bishop, Ö. T. Integrated Computational Approaches and Tools for Allosteric Drug Discovery. *Int. J. Mol. Sci.* **2020**, *21* (3).

(127) Wagner, J. R.; Lee, C. T.; Durrant, J. D.; Malmstrom, R. D.; Feher, V. A.; Amaro, R. E. Emerging Computational Methods for the Rational Discovery of Allosteric Drugs. *Chem. Rev.* **2016**, *116* (11), 6370-6390.

(128) Congreve, M.; Langmead, C. J.; Mason, J. S.; Marshall, F. H. Progress in Structure Based Drug Design for G Protein-Coupled Receptors. *J. Med. Chem* **2011**, *54*, 4283-4311.

(129) Oswald, C.; Rappas, M.; Kean, J.; Doré, A. S.; Errey, J. C.; Bennett, K.; Deflorian, F.; Christopher, J. A.; Jazayeri, A.; Mason, J. S.; Congreve, M.; Cooke, R. M.; Marshall, F. H. Intracellular allosteric antagonism of the CCR9 receptor. *Nature.* **2016**, *540* (7633), 462-465.

(130) Zheng, Y.; Qin, L.; Zacarías, N. V. O.; De Vries, H.; Han, G. W.; Gustavsson, M.; Dabros, M.; Zhao, C.; Cherney, R. J.; Carter, P.; Stamos, D.; Abagyan, R.; Cherezov, V.; Stevens, R. C.; Ijzerman, A. P.; Heitman, L. H.; Tebben, A.; Kufareva, I.; Handel, T. M. Structure of CC chemokine receptor 2 with orthosteric and allosteric antagonists. *Nature.* **2016**, *540* (7633), 458-461.

(131) Tan, Q.; Zhu, Y.; Li, J.; Chen, Z.; Han, G. W.; Kufareva, I.; Li, T.; Ma, L.; Fenalti, G.; Li, J.; Zhang, W.; Xie, X.; Yang, H.; Jiang, H.; Cherezov, V.; Liu, H.; Stevens, R. C.; Zhao, Q.; Wu, B. Structure of the CCR5 chemokine receptor-HIV entry inhibitor maraviroc complex. *Science.* **2013**, *341* (6152), 1387-1390.

(132) Jaeger, K.; Bruenle, S.; Weinert, T.; Guba, W.; Muehle, J.; Miyazaki, T.; Weber, M.; Furrer, A.; Haenggi, N.; Tetaz, T.; Huang, C. Y.; Mattle, D.; Vonach, J. M.; Gast, A.; Kuglstatter, A.; Rudolph, M. G.; Nogly, P.; Benz, J.; Dawson, R. J. P.; Standfuss, J. Structural Basis for Allosteric Ligand Recognition in the Human CC Chemokine Receptor 7. *Cell.* **2019**, *178* (5), 1222-1230.e1210.

(133) Saha, S.; Shukla, A. K. The Inside Story: Crystal Structure of the Chemokine Receptor CCR7 with an Intracellular Allosteric Antagonist. *Biochemistry.* **2019**, *51* (1), 12-14.

(134) Salchow, K.; Bond, M.; Evans, S.; Press, N.; Charlton, S.; Hunt, P.; Bradley, M. A common intracellular allosteric binding site for antagonists of the CXCR2 receptor: Research paper. *Br. J. Pharmacol.* **2010**, *159* (7), 1429-1439.

(135) Bertini, R.; Barcelos, L. S.; Beccari, A. R.; Cavalieri, B.; Moriconi, A.; Bizzarri, C.; Di Benedetto, P.; Di Giacinto, C.; Gloaguen, I.; Galliera, E.; Corsi, M. M.; Russo, R. C.; Andrade, S. P.; Cesta, M. C.; Nano, G.; Aramini, A.; Cutrin, J. C.; Locati, M.; Allegretti, M.; Teixeira, M. M. Receptor binding mode and pharmacological characterization of a potent and selective dual CXCR1/CXCR2 non-competitive allosteric inhibitor. *Br. J. Pharmacol.* **2012**, *165* (2), 436-454.

(136) Nicholls, D. J.; Tomkinson, N. P.; Wiley, K. E.; Brammall, A.; Bowers, L.; Grahames, C.; Gaw, A.; Meghani, P.; Shelton, P.; Wright, T. J.; Mallinder, P. R. Identification of a Putative Intracellular Allosteric Antagonist Binding-Site in the CXC Chemokine Receptors 1 and 2. *Mol. Pharmacol.* **2008**, *74* (5), 1193-1202.

(137) Bertini, R.; Allegretti, M.; Bizzarri, C.; Moriconi, A.; Locati, M.; Zampella, G.; Cervellera, M. N.; Di Cioccio, V.; Cesta, M. C.; Galliera, E.; Martinez, F. O.; Di Bitondo, R.; Troiani, G.; Sabbatini, V.; D'Anniballe, G.; Anacardio, R.; Cutrin, J. C.; Cavalieri, B.; Mainiero, F.; Strippoli, R.; Villa, P.; Di Girolamo, M.; Martin, F.; Gentile, M.; Santoni, A.; Corda, D.; Poli, G.; Mantovani, A.; Ghezzi, P.; Colotta, F. Noncompetitive allosteric inhibitors of the inflammatory chemokine receptors CXCR1 and CXCR2: Prevention of reperfusion injury. *Proc. Natl. Acad. Sci.* **2004**, *101* (32), 11791-11796.

(138) Casella, B. M.; Farmer, J. P.; Nesheva, D. N.; Williams, H. E. L.; Charlton, S. J.; Holliday, N. D.; Laughton, C. A.; Mistry, S. N. Design, Synthesis, and Application of Fluorescent Ligands Targeting the Intracellular Allosteric Binding Site of the CXC Chemokine Receptor 2. *J. Med. Chem.* **2023**, *66* (18), 12911-12930.

(139) Shukla, S. D.; Vanka, K. S.; Chavelier, A.; Shastri, M. D.; Tambuwala, M. M.; Bakshi, H. A.; Pabreja, K.; Mahmood, M. Q.; O'Toole, R. F. Chronic respiratory diseases: An introduction and need for novel drug delivery approaches. *Targeting Chronic Inflammatory Lung Diseases Using Advanced Drug Delivery Systems* **2020**, 1-1.

(140) Hansen, G. Chronic respiratory diseases. *Monatsschrift Kinderheilkunde* **2013**, *161* (5), 389-389.

(141) Keatings, V. M.; Collins, P. D.; Scott, D. M.; Barnes, P. J. Differences in interleukin-8 and tumor necrosis factor-alpha in induced sputum from patients with chronic obstructive pulmonary disease or asthma. *Am. J. Respir. Crit. Care Med.* **1996**, *153* (2), 530-534.

(142) Qiu, Y.; Zhu, J.; Bandi, V.; Atmar, R. L.; Hattotuwa, K.; Guntupalli, K. K.; Jeffery, P. K. Biopsy neutrophilia, neutrophil chemokine and receptor gene expression in severe exacerbations of chronic obstructive pulmonary disease. *Am. J. Respir. Crit. Care Med.* **2003**, *168* (8), 968-975.

(143) Donnelly, L. E.; Barnes, P. J. Chemokine receptors as therapeutic targets in chronic obstructive pulmonary disease. *Trends Pharmacol. Sci.* **2006**, *27* (10), 546-553.

(144) Qiu, Y.; Zhu, J.; Bandi, V.; Guntupalli, K. K.; Jeffery, P. K. Bronchial mucosal inflammation and upregulation of CXC chemoattractants and receptors in severe exacerbations of asthma. *Thorax* **2007**, *62* (6), 475-475.

(145) Hoenderdos, K.; Condliffe, A. The neutrophil in chronic obstructive pulmonary disease: Too little, too late or too much, too soon? *Am. J. Respir. Cell Mol. Biol.* **2013**, *48*, 531-539.

(146) Planagumà, A.; Domènech, T.; Pont, M.; Calama, E.; García-González, V.; López, R.; Aulí, M.; López, M.; Fonquerna, S.; Ramos, I.; de Alba, J.; Nueda, A.; Prats, N.; Segarra, V.; Miralpeix, M.; Lehner, M. D. Combined anti CXC receptors 1 and 2 therapy is a promising anti-inflammatory treatment for respiratory diseases by reducing neutrophil migration and activation. *Pulm. Pharmacol. Ther* **2015**, *34*, 37-45.

(147) Rennard, S. I.; Dale, D. C.; Donohue, J. F.; Kanniess, F.; Magnussen, H.; Sutherland, E. R.; Watz, H.; Lu, S.; Stryszak, P.; Rosenberg, E.; Staudinger, H. CXCR2 Antagonist MK-7123. A Phase 2 Proof-of-Concept Trial for Chronic Obstructive Pulmonary Disease. *Am. J. Respir. Crit. Care Med.* **2015**, *191* (9), 1001-1011.

(148) Kirsten, A. M.; Förster, K.; Radeczky, E.; Linnhoff, A.; Balint, B.; Watz, H.; Wray, H.; Salkeld, L.; Cullberg, M.; Larsson, B. The safety and tolerability of oral AZD5069, a selective CXCR2 antagonist, in patients with moderate-to-severe COPD. *Pulm. Pharmacol. Ther.* **2015**, *31*, 36-41.

(149) Lazaar, A. L.; Miller, B. E.; Tabberer, M.; Yonchuk, J.; Leidy, N.; Ambery, C.; Bloomer, J.; Watz, H.; Tal-Singer, R. Effect of the CXCR2 antagonist danirixin on symptoms and health status in COPD. *Eur. Clin. Respir. J.* **2018**, *52*.

(150) Busch-Petersen, J.; Carpenter, D. C.; Burman, M.; Foley, J.; Hunsberger, G. E.; Kilian, D. J.; Salmon, M.; Mayer, R. J.; Yonchuk, J. G.; Tal-Singer, R. Danirixin: A reversible and selective antagonist of the CXC chemokine receptor 2. *J. Pharmcol. Exp. Ther.* **2017**, *362* (2), 338-346.

(151) Miller, B. E.; Mistry, S.; Smart, K.; Connolly, P.; Carpenter, D. C.; Cooray, H.; Bloomer, J. C.; Tal-Singer, R.; Lazaar, A. L. The pharmacokinetics and pharmacodynamics of danirixin (GSK1325756) - a selective CXCR2 antagonist - in healthy adult subjects. *BMC Pharmcol. Toxicol.* **2015**, *16* (1).

(152) Pignatti, P.; Moscato, G.; Casarini, S.; Delmastro, M.; Poppa, M.; Brunetti, G.; Pisati, P.; Balbi, B. Downmodulation of CXCL8/IL-8 receptors on neutrophils after recruitment in the airways. *J. Allergy Clin. Immunol.* **2005**, *115* (1), 88-94.

(153) Liu, C.; Zhang, X.; Xiang, Y.; Qu, X.; Liu, H.; Liu, C.; Tan, M.; Jiang, J.; Qin, X. Role of epithelial chemokines in the pathogenesis of airway inflammation in asthma (Review). *Mol. Med. Rep.* **2018**, *17* (5), 6935-6941.

(154) Yuliani, F. S.; Chen, J. Y.; Cheng, W. H.; Wen, H. C.; Chen, B. C.; Lin, C. H. Thrombin induces IL-8/CXCL8 expression by DCLK1-dependent RhoA and YAP activation in human lung epithelial cells. *J. Biomed. Sci.* **2022**, *29* (1), 1-22.

(155) Kurashima, K.; Mukaida, N.; Fujimura, M.; Schröder, J. M.; Matsuda, T.; Matsushima, K. Increase of chemokine levels in sputum precedes exacerbation of acute asthma attacks. *J. leukoc. biol.* **1996**, *59* (3), 313-316.

(156) Yan, Q.; Zhang, X.; Xie, Y.; Yang, J.; Liu, C.; Zhang, M.; Zheng, W.; Lin, X.; Huang, H. T.; Liu, X.; Jiang, Y.; Zhan, S. F.; Huang, X. Bronchial epithelial transcriptomics and experimental validation reveal asthma severity-related neutrophilc signatures and potential treatments. *Communications Biology 2024 7:1* **2024**, *7* (1), 1-19.

(157) Zhu, L. m.; Zeng, D.; Lei, X. c.; Huang, J.; Deng, Y. f.; Ji, Y. b.; Liu, J.; Dai, F. f.; Li, Y. z.; Shi, D. d.; Zhu, Y. q.; Dai, A. g.; Wang, Z. KLF2 regulates neutrophil migration by modulating CXCR1 and CXCR2 in asthma. *Biochim. Biophys. Acta, Mol. Basis Dis.* **2020**, *1866* (12), 165920-165920.

(158) Mattos, M. S.; Ferrero, M. R.; Kraemer, L.; Lopes, G. A. O.; Reis, D. C.; Cassali, G. D.; Oliveira, F. M. S.; Brandolini, L.; Allegretti, M.; Garcia, C. C.; Martins, M. A.; Teixeira, M. M.; Russo, R. C. CXCR1 and CXCR2 Inhibition by Ladarixin Improves Neutrophil-Dependent Airway Inflammation in Mice. *Front. immunol.* **2020**, *11*.

(159) Cukic, V.; Lovre, V.; Dragisic, D.; Ustamujic, A. Asthma and Chronic Obstructive Pulmonary Disease (COPD) – Differences and Similarities. *Materia. Socio-Medica.* **2012**, *24* (2), 100-100.

(160) O'Byrne, P. M.; Metev, H.; Puu, M.; Richter, K.; Keen, C.; Uddin, M.; Larsson, B.; Cullberg, M.; Nair, P. Efficacy and safety of a CXCR2 antagonist, AZD5069, in patients with uncontrolled persistent asthma: a randomised, double-blind, placebo-controlled trial. *The Lancet. Respiratory medicine* **2016**, *4* (10), 797-806.

(161) *Efficacy and Safety of Navarixin (SCH 527123) in Participants With Allergen-Induced Asthma (P05363)*. 2008.

https://clinicaltrials.gov/ct2/show/NCT00688467?term=navarixin&recrs=abcdefghijklm&draw=2&rank=3 (accessed 2024 Mar).

(162) Nair, P.; Gaga, M.; Zervas, E.; Alagha, K.; Hargreave, F. E.; O'Byrne, P. M.; Stryszak, P.; Gann, L.; Sadeh, J.; Chanez, P. Safety and efficacy of a CXCR2 antagonist in patients with severe asthma and sputum neutrophils: a randomized, placebo-controlled clinical trial. *Clinical and experimental allergy : journal of the British Society for Allergy and Clinical Immunology* **2012**, *42* (7), 1097-1103.

(163) Kulke, R.; Bornscheuer, E.; Schluter, C.; Bartels, J.; Rowert, J.; Sticherling, M.; Christophers, E. The CXC receptor 2 is overexpressed in psoriatic epidermis. *J. Invest. Dermatol.* **1998**, *110*, 90-94.

(164) Lemster, B. H.; Carroll, P. B.; Rilo, H. R.; Johnson, N.; Nikaein, A.; Thomson, A. W. IL-8/IL-8 receptor expression in psoriasis and the response to systemic tacrolimus (FK506) therapy. *Clin. Exp. Immunol.* **2008**, *99* (2), 148-154.

(165) Kondo, S.; Yoneta, A.; Yazawa, H.; Kamada, A.; Jimbow, K. Downregulation of CXCR-2 but not CXCR-1 expression by human keratinocytes by UVB. *J. Cell. Physiol.* **2000**, *182* (3), 366-370.

(166) Tang, L.; Yu, Y.; Chen, J.; Li, Q.; Yan, M.; Guo, Z. The inhibitory effect of VitD3 on proliferation of keratinocyte cell line HACAT is mediated by down-regulation of CXCR2 expression. *Clin. Exp. Dermatol.* **2003**, *28* (4), 416-419.

(167) Sumida, H.; Yanagida, K.; Kita, Y.; Abe, J.; Matsushima, K.; Nakamura, M.; Ishii, S.; Sato, S.; Shimizu, T. Interplay between CXCR2 and BLT1 facilitates neutrophil infiltration and resultant keratinocyte activation in a murine model of imiquimod-induced psoriasis. *J. Immunol.* **2014**, *192* (9), 4361-4369.

(168) Jacquelot, N.; Duong, C. P. M.; Belz, G. T.; Zitvogel, L. Targeting Chemokines and Chemokine Receptors in Melanoma and Other Cancers. *Front. immunol.* **2018**, *9*, 2480-2480.

(169) Sarvaiya, P. J.; Guo, D.; Ulasov, I.; Gabikian, P.; Lesniak, M. S. Chemokines in tumor progression and metastasis. *Oncotarget.* **2013**, *4* (12), 2171-2171.

(170) Che, J.; Song, R.; Chen, B.; Dong, X. Targeting CXCR1/2: The medicinal potential as cancer immunotherapy agents, antagonists research highlights and challenges ahead. *Eur. J. Med. Chem.* **2020**, *185*, 111853-111853.

(171) De Larco, J. E.; Wuertz, B. R. K.; Furcht, L. T. The potential role of neutrophils in promoting the metastatic phenotype of tumors releasing interleukin-8. *Clin. Cancer Res.* **2004**, *10* (15), 4895-4900.

(172) Zhu, Y. M.; Webster, S. J.; Flower, D.; Woll, P. J. Interleukin-8/CXCL8 is a growth factor for human lung cancer cells. *Br. J. Cancer* **2004**, *91* (11), 1970-1970.

(173) Luppi, F.; Longo, A. M.; de Boer, W. I.; Rabe, K. F.; Hiemstra, P. S. Interleukin-8 stimulates cell proliferation in non-small cell lung cancer through epidermal growth factor receptor transactivation. *Lung Cancer* **2007**, *56* (1), 25-33.

(174) Kunz, M.; Hartmann, A.; Flory, E.; Toksoy, A.; Koczan, D.; Thiesen, H. J.; Mukaida, N.; Neumann, M.; Rapp, U. R.; Bröcker, E. B.; Gillitzer, R. Anoxia-Induced Up-Regulation of Interleukin-8 in Human Malignant Melanoma: A Potential Mechanism for High Tumor Aggressiveness. *Am. J. Physiol.* **1999**, *155* (3), 753-763.

(175) Sharma, B.; Singh, S.; Varney, M. L.; Singh, R. K. Targeting CXCR1/CXCR2 receptor antagonism in malignant melanoma. *Expert Opin. Ther. Targets* **2010**, *14* (4), 435-435.

(176) Singh, S.; Singh, A. P.; Sharma, B.; Owen, L. B.; Singh, R. K. CXCL8 and its cognate receptors in melanoma progression and metastasis. *Future Oncol.* **2010**, *6* (1), 111-111.

(177) Xiong, X.; Liao, X.; Qiu, S.; Xu, H.; Zhang, S.; Wang, S.; Ai, J.; Yang, L. CXCL8 in Tumor Biology and Its Implications for Clinical Translation. *Front. Mol. Biosci.* **2022**, *9*.

(178) Alfaro, C.; Teijeira, A.; Oñate, C.; Perez, G.; Sanmamed, M. F.; Andueza, M. P.; Alignani, D.; Labiano, S.; Azpilikueta, A.; Rodriguez-Paulete, A.; Garasa, S.; Fusco, J. P.; Aznar, A.; Inoges, S.; De Pizzol, M.; Allegretti, M.; Medina-Echeverz, J.; Berraondo, P.; Perez-Gracia, J. L.; Melero, I. Tumor-Produced Interleukin-8 Attracts Human Myeloid-Derived Suppressor Cells and Elicits Extrusion of Neutrophil Extracellular Traps (NETs). *Clin. Cancer Res.* **2016**, *22* (15), 3924-3936.

(179) Pausch, T. M.; Aue, E.; Wirsik, N. M.; Freire Valls, A.; Shen, Y.; Radhakrishnan, P.; Hackert, T.; Schneider, M.; Schmidt, T. Metastasis-associated fibroblasts promote angiogenesis in metastasized pancreatic cancer via the CXCL8 and the CCL2 axes. *Sci. Rep.* **2020**, *10* (1).

(180) Litman-Zawadzka, A.; Łukaszewicz-Zajac, M.; Gryko, M.; Kulczyńska-Przybik, A.; Mroczko, B. Serum chemokine CXCL8 as a better biomarker for diagnosis and prediction of pancreatic cancer than its specific receptor CXCR2, C-reactive protein, and classic tumor markers CA 19-9 and CEA. *Pol. Arch. Intern. Med.* **2018**, *128* (9), 524-531.

(181) Benoy, I. H.; Salgado, R.; Van Dam, P.; Geboers, K.; Van Marck, E.; Scharpé, S.; Vermeulen, P. B.; Dirix, L. Y. Increased Serum Interleukin-8 in Patients with Early and Metastatic Breast Cancer Correlates with Early Dissemination and Survival. *Clin. Cancer Res.* **2004**, *10* (21), 7157-7162.

(182) Kamalakar, A.; Bendre, M. S.; Washam, C. L.; Fowler, T. W.; Carver, A.; Dilley, J. D.; Bracey, J. W.; Akel, N. S.; Margulies, A. G.; Skinner, R. A.; Swain, F. L.; Hogue, W. R.; Montgomery, C. O.; Lahiji, P.; Maher, J. J.; Leitzel, K. E.; Ali, S. M.; Lipton, A.; Nicholas, R. W.; Gaddy, D.; Suva, L. J. Circulating interleukin-8 levels explain breast cancer osteolysis in mice and humans. *Bone* **2014**, *61*, 176-185.

(183) Liu, Q.; Li, A.; Tian, Y.; Wu, J. D.; Liu, Y.; Li, T.; Chen, Y.; Han, X.; Wu, K. The CXCL8-CXCR1/2 pathways in cancer. *Cytokine Growth Fact. Rev.* **2016**, *31*, 61-71.

(184) Han, Z. J.; Li, Y. B.; Yang, L. X.; Cheng, H. J.; Liu, X.; Chen, H. Roles of the CXCL8-CXCR1/2 Axis in the Tumor Microenvironment and Immunotherapy. *Molecules* **2022**, *27* (1), 61-71.

(185) Xue, M. Q.; Liu, J.; Sang, J. F.; Su, L.; Yao, Y. Z. Expression characteristic of CXCR1 in different breast tissues and the relevance between its expression and efficacy of neo-adjuvant chemotherapy in breast cancer. *Oncotarget.* **2017**, *8* (30), 48930-48930.

(186) Shiravand, Y.; Khodadadi, F.; Kashani, S. M. A.; Hosseini-Fard, S. R.; Hosseini, S.; Sadeghirad, H.; Ladwa, R.; O'byrne, K.; Kulasinghe, A. Immune Checkpoint Inhibitors in Cancer Therapy. *Curr. Oncol.* **2022**, *29* (5), 3044-3044.

(187) Harel, M.; Lahav, C.; Jacob, E.; Dahan, N.; Sela, I.; Elon, Y.; Raveh Shoval, S.; Yahalom, G.; Kamer, I.; Zer, A.; Sharon, O.; Carbone, D. P.; Dicker, A. P.; Bar, J.; Shaked, Y. Original research: Longitudinal plasma proteomic profiling of patients with non-small cell lung cancer undergoing immune checkpoint blockade. *J. Immunother. Cancer* **2022**, *10* (6), 4582-4582.

(188) David, J. M.; Dominguez, C.; Hamilton, D. H.; Palena, C. The IL-8/IL-8R Axis: A Double Agent in Tumor Immune Resistance. *Vaccines* **2016**, *4* (3).

(189) Wang, J.; Hu, W.; Wang, K.; Yu, J.; Luo, B.; Luo, G.; Wang, W.; Wang, H.; Li, J.; Wen, J. Repertaxin, an inhibitor of the chemokine receptors CXCR1 and CXCR2, inhibits malignant behavior of human gastric cancer MKN45 cells in vitro and in vivo and enhances efficacy of 5-fluorouracil. *Int. J. Oncol.* **2016**, *48* (4), 1341-1352.

(190) Henrot, P.; Prevel, R.; Berger, P.; Dupin, I. Chemokines in COPD: From Implication to Therapeutic Use. *Int. J. Mol. Sci.* **2019**, *20* (11).

(191) Cheng, Y.; Ma, X. l.; Wei, Y. q.; Wei, X. W. Potential roles and targeted therapy of the CXCLs/CXCR2 axis in cancer and inflammatory diseases. *Biochim. Biophys. Acta Rev. Cancer* **2019**, *1871* (2), 289-312.

(192) Medema, J. P. Cancer stem cells: the challenges ahead. *Nat. Cell Biol.* **2013**, *15* (4), 338-344.

(193) Chen, L.; Fan, J.; Chen, H.; Meng, Z.; Chen, Z.; Wang, P.; Liu, L. The IL-8/CXCR1 axis is associated with cancer stem cell-like properties and correlates with clinical prognosis in human pancreatic cancer cases. *Sci. Rep.* **2014**, *4* (1), 1-7.

(194) Charafe-Jauffret, E.; Ginestier, C.; Iovino, F.; Wicinski, J.; Cervera, N.; Finetti, P.; Hur, M. H.; Diebel, M. E.; Monville, F.; Dutcher, J.; Brown, M.; Viens, P.; Xerri, L.; Bertucci, F.; Stassi, G.; Dontu, G.; Birnbaum, D.; Wicha, M. S. Breast cancer cell lines contain functional cancer stem sells with metastatic capacity and a distinct molecular signature. *Cance Res.* **2009**, *69* (4), 1302-1313.

(195) Clark, D. W.; Palle, K. Aldehyde dehydrogenases in cancer stem cells: potential as therapeutic targets. *Ann. Transl. Med.* **2016**, *4* (24).

(196) Goldstein, L. J.; Perez, R. P.; Yardley, D.; Han, L. K.; Reuben, J. M.; Gao, H.; McCanna, S.; Butler, B.; Ruffini, P. A.; Liu, Y.; Rosato, R. R.; Chang, J. C. A window-of-opportunity trial of the CXCR1/2 inhibitor reparixin in operable HER-2-negative breast cancer. *Breast Cancer Res.* **2020**, *22* (1), 4-4.

(197) Hastrup, N.; Khalilieh, S.; Dale, D. C.; Hanson, L. G.; Magnusson, P.; Tzontcheva, A.; Tseng, J.; Huyck, S.; Rosenberg, E.; Krogsgaard, K. The effects of the CXCR2 antagonist, MK-7123, on bone marrow functions in healthy subjects. *Cytokine* **2015**, *72* (2), 197-203.

(198) Jurcevic, S.; Humfrey, C.; Uddin, M.; Warrington, S.; Larsson, B.; Keen, C. The effect of a selective CXCR2 antagonist (AZD5069) on human blood neutrophil count and innate immune functions. *Br. J. Clin. Pharmacol.* **2015**, *80* (6), 1324-1336.

(199) Goldstein, L. J.; Mansutti, M.; Levy, C.; Chang, J. C.; Henry, S.; Fernandez-Perez, I.; Prausovà, J.; Staroslawska, E.; Viale, G.; Butler, B.; McCanna, S.; Ruffini, P. A.; Wicha, M. S.; Schott, A. F.; Alvarez, R. H.; Abu-Khalaf, M.; Ibrahim, N.; Daniel, B.; Meshad, M.; Kanamori, D.; Zelnak, A.; Graham, M.; Comer, J.; Huizing, M.; Duhoux, F.; Richard, V.; Verhoeven, D.; Smakal, M.; Krasenska, M.; Kohoutek, M.; Zimovjanova, M.; Kubala, E.;

Campone, M.; Ferrero, J. M.; Goncalves, A.; Venat-Bouvet, L.; Medioni, J.; Biganzoli, L.; Parra, H. S.; Pedrazzoli, P.; Colleoni, M.; Moroni, M.; Amadori, D.; Morandi, P.; Cinieri, S.; Tomczak, P.; Sarosiek, T.; Wojtukiewicz, M.; Mruk, A.; Kukielka-Budny, B.; Novoa, S. A.; Alonso, E. V.; Jimenez, M. M. A randomized, placebo-controlled phase 2 study of paclitaxel in combination with reparixin compared to paclitaxel alone as front-line therapy for metastatic triple-negative breast cancer (fRida). *Breast cancer res. treat.* **2021**, *190* (2), 265-275.

(200) Sharma, I.; Singh, A.; Siraj, F.; Saxena, S. IL-8/CXCR1/2 signalling promotes tumor cell proliferation, invasion and vascular mimicry in glioblastoma. *J. Biomed. Sci.* **2018**, *25* (1).

(201) Zhang, B.; Shi, L.; Lu, S.; Sun, X.; Liu, Y.; Li, H.; Wang, X.; Zhao, C.; Zhang, H.; Wang, Y. Autocrine IL-8 promotes F-actin polymerization and mediate mesenchymal transition via ELMO1-NF-κB-Snail signaling in glioma. *Cancer Biol. Ther.* **2015**, *16* (6), 898-898.

(202) Ramjeesingh, R.; Leung, R.; Siu, C. H. Interleukin-8 secreted by endothelial cells induces Chemotaxis of melanoma cells through the chemokine receptor CXCR1. *FASEB J.* **2003**, *17* (10), 1292-1294.

(203) Widdowson, K. L.; Gleason, J. G. Il-8 receptor antagonists. WO1998005328A1, 1997.

(204) Widdowson, K. L.; Gleason, J. G. Il-8 receptor antagonists. WO1998005329A1, 1998.

(205) Thompson, S. K.; Halbert, S. M.; Widdowson, K. L. Carboxylic acid indole inhibitors of chemokines. WO1997035572A1, 1997.

(206) Widdowson, K., L. . Il-8 receptor antagonists. WO1997049400A1, 1997.

(207) Bryan, D. L.; Gleason, J. G.; Widdowson, K. L. Il-8 receptor antagonists. WO1998006397A1, 1998.

(208) Xiang, J.-N. Il-8 receptor antagonists. WO1998007418A1, 1998.

(209) Widdowson, K. L.; Hong, N.; Melvin, C. R. J. Il-8 receptor antagonists. WO1998032438A1, 1998.

(210) Giovannini, R.; Hamprecht, D.; Kistler, B.; Lingard, I. Bicyclic ring system substituted amide functionalised phenols as medicaments. WO2012080456, 2012.

(211) White, J. R.; Lee, J. M.; Young, P. R.; Hertzberg, R. P.; Jurewicz, A. J.; Chaikin, M. A.; Widdowson, K.; Foley, J. J.; Martin, L. D.; Griswold, D. E.; Sarau, H. M. Identification of a potent, selective non-peptide CXCR2 antagonist that inhibits interleukin-8-induced neutrophil migration. *J. bio. chem.* **1998**, *273* (17), 10095-10098.

(212) Lazaar, A. L.; Sweeney, L. E.; Macdonald, A. J.; Alexis, N. E.; Chen, C.; Tal-Singer, R. SB-656933, a novel CXCR2 selective antagonist, inhibits ex vivo neutrophil activation and ozone-induced airway inflammation in humans. *Br. J. Clin. Pharmacol.* **2011**, *72* (2), 282-293.

(213) Jin, Q.; McCleland, B. W.; Palovich, M. R.; Widdowson, K. L. Hydroxy diphenyl urea sulfonamides as IL-8 receptor antagonists. US6500863B1, 1998.

(214) Jin, Q.; Mccleland, B. W.; Palovich, M. R.; Widdowson, K. L. Hydroxy diphenyl urea sulfonamides as il-8 receptor antagonists. WO2009039091A1, 2009.

(215) Moss, R. B.; Mistry, S. J.; Konstan, M. W.; Pilewski, J. M.; Kerem, E.; Tal-Singer, R.; Lazaar, A. L. Safety and early treatment effects of the CXCR2 antagonist SB-656933 in patients with cystic fibrosis. *J. Cyst. Fibros.* **2013**, *12* (3), 241-248.

(216) Lazaar, A. L.; Miller, B. E.; Donald, A. C.; Keeley, T.; Ambery, C.; Russell, J.; Watz, H.; Tal-Singer, R. CXCR2 antagonist for patients with chronic obstructive pulmonary disease with chronic mucus hypersecretion: A phase 2b trial. *Resp. Res.* **2020**, *21* (1), 1-10.

(217) de Boer, W. I. Potential new drugs for therapy of chronic obstructive pulmonary disease. *Expert Opin. Investig. Drugs* **2003**, *12* (7), 1067-1086.

(218) Milatovic, S.; Nanney, L. B.; Yu, Y.; White, J. R.; Richmond, A. Impaired healing of nitrogen mustard wounds in CXCR2 null mice. *Wound Repair Regen.* **2003**, *11* (3), 213-219.

(219) Biffis, A.; Centomo, P.; Del Zotto, A.; Zecca, M. Pd Metal Catalysts for Cross-Couplings and Related Reactions in the 21st Century: A Critical Review. *Chem. Rev.* **2018**, *118* (4), 2249-2295.

(220) Roger, B.; Peter, C.; Fraser, H.; Lain, W.; Paul, W. Pyrimidine compounds and their use as modulators of chemokine receptor activity. WO2001058902A1, 2001.

(221) Roger, B.; Fraser, H.; Paul, W. Pyrimidine compounds and their use as modulators of chemokine receptor activity. WO2001058906A1, 2001.

(222) Baxter, A.; Cooper, A.; Kinchin, E.; Moakes, K.; Unitt, J.; Wallace, A. Hit-to-Lead studies: the discovery of potent, orally bioavailable thiazolopyrimidine CXCR2 receptor antagonists. *Bioorg. Med. Chem. Lett.* **2006**, *16* (4), 960-963.

(223) Walters, I.; Austin, C.; Austin, R.; Bonnert, R.; Cage, P.; Christie, M.; Ebden, M.; Gardiner, S.; Grahames, C.; Hill, S.; Hunt, F.; Jewell, R.; Lewis, S.; Martin, I.; Nicholls, D.; Robinson, D. Evaluation of a series of bicyclic CXCR2 antagonists. *Bioorg. Med. Chem. Lett.* **2008**, *18* (2), 798-803.

(224) Leaker, B. R.; Barnes, P. J.; O'Connor, B. Inhibition of LPS-induced airway neutrophilic inflammation in healthy volunteers with an oral CXCR2 antagonist. *Resp. Res.* **2013**, *14* (1).

(225) Virtala, R.; Ekman, A. K.; Jansson, L.; Westin, U.; Cardell, L. O. Airway inflammation evaluated in a human nasal lipopolysaccharide challenge model by investigating the effect of a CXCR2 inhibitor. *Clin. Exp. Allergy* **2012**, *42* (4), 590-596.

(226) Dwyer, M. P.; Yu, Y. CXCR2 modulators: a patent review (2009 - 2013). *Expert Opin. Ther. Pat.* **2014**, *24* (5), 519-534.

(227) Premji, M.; James, R. A.; Paul, S. J. Pyrimidyl sulfonaminde derivative and its use for the treatment of chemokine mediated diseases. WO2010007427A1, 2010.

(228) Nicholls, D. J.; Wiley, K.; Dainty, I.; MacIntosh, F.; Phillips, C.; Gaw, A.; Mårdh, C. K. Pharmacological characterization of AZD5069, a slowly reversible CXC Chemokine Receptor 2 antagonist. *J. Pharmcol. Exp. Ther.* **2015**, *353* (2), 340-350.

(229) Watz, H.; Uddin, M.; Pedersen, F.; Kirsten, A.; Goldmann, T.; Stellmacher, F.; Groth, E.; Larsson, B.; Böttcher, G.; Malmgren, A.; Kraan, M.; Rabe, K. F. Effects of the CXCR2 antagonist AZD5069 on lung neutrophil recruitment in asthma. *Pulm. Pharmacol. Ther.* **2017**, *45*, 121-123.

(230) De Soyza, A.; Pavord, I.; Elborn, J. S.; Smith, D.; Wray, H.; Puu, M.; Larsson, B.; Stockley, R. A randomised, placebo-controlled study of the CXCR2 antagonist AZD5069 in bronchiectasis. *Eur. Clin. Respir. J.* **2015**, *46* (4), 1021-1032.

(231) Bissonnette, R.; Maari, C.; Tsianakas, A.; Reid, D. A.; McCutchan, S.; Baumgartner, S.; Mackay, J.; Bhakta, N. A Randomized, Double-Blind, Placebo-Controlled, Phase 2a Study to Evaluate the Efficacy and Safety of RIST4721 in Subjects with Palmoplantar Pustulosis. *Dermatol. Ther.* **2021**, *11* (6), 2179-2179.

(232) Szymczak, K.; Pelletier, M. G. H.; Mackay, J. M.; Reid, D. A.; Gaines, P. C. W. CXCR2 Antagonist RIST4721 Acts as a Potent Chemotaxis Inhibitor of Mature Neutrophils Derived from Ex Vivo-Cultured Mouse Bone Marrow. *Biomedicines* **2023**, *11* (2).

(233) Riccardo;, B.; Vilma;, B. C. S.; Marcello;, C. G. A.; Candida;, C. M.; Carmelo;, G.; Marco;, M.; Francesco;, C.; Stefano, P. N - (2 - aryl - propionyl) - sulfonamides and pharmaceutical preparations containing them. US2003216392, 2003.

(234) Allegretti, M.; Aramini, A.; Bianchini, G.; Cesta, M. C. 2-aryl-propionic acids and derivatives and pharmaceutical compositions containing them. WO2010031835A2, 2009.

(235) Mazaleuskaya, L. L.; Theken, K. N.; Gong, L.; Thorn, C. F.; Fitzgerald, G. A.; Altman, R. B.; Klein, T. E. PharmGKB summary: ibuprofen pathways. *Pharmacogenet. Genom.* **2015**, *25* (2), 96-96.

(236) Bushra, R.; Aslam, N. An Overview of Clinical Pharmacology of Ibuprofen. *Oman Med. J.* **2010**, *25* (3), 155-155.

(237) Allegretti, M.; Bertini, R.; Cesta, M. C.; Bizzarri, C.; Di Bitondo, R.; Di Cioccio, V.; Galliera, E.; Berdini, V.; Topai, A.; Zampella, G.; Russo, V.; Di Bello, N.; Nano, G.; Nicolini, L.; Locati, M.; Fantucci, P.; Florio, S.; Colotta, F. 2-Arylpropionic CXC chemokine receptor 1 (CXCR1) ligands as novel noncompetitive CXCL8 inhibitors. *J. Med. Chem.* **2005**, *48* (13), 4312-4331.

(238) Moriconi, A.; Cesta, M. C.; Cervellera, M. N.; Aramini, A.; Coniglio, S.; Colagioia, S.; Beccari, A. R.; Bizzarri, C.; Cavicchia, M. R.; Locati, M.; Galliera, E.; Di Benedetto, P.; Vigilante, P.; Bertini, R.; Allegretti, M. Design of noncompetitive interleukin-8 inhibitors acting on CXCR1 and CXCR2. *J. Med. Chem.* **2007**, *50* (17), 3984-4002.

(239) Allegretti, M.; Cesta, M. C.; Garin, A.; Proudfoot, A. E. I. Current status of chemokine receptor inhibitors in development. *Immunol. Lett.* **2012**, *145* (1-2), 68-78.

(240) Witkowski, P.; Wijkstrom, M.; Bachul, P. J.; Morgan, K. A.; Levy, M.; Onaca, N.; Chaidarun, S. S.; Gardner, T.; Shapiro, A. M. J.; Posselt, A.; Ahmad, S. A.; Daffonchio, L.; Ruffini, P. A.; Bellin, M. D. Targeting CXCR1/2 in the first multicenter, double-blinded, randomized trial in autologous islet transplant recipients. *Am. J. Transplant.* **2021**, *21* (11), 3714-3724.

(241) Citro, A.; Cantarelli, E.; Maffi, P.; Nano, R.; Melzi, R.; Mercalli, A.; Dugnani, E.; Sordi, V.; Magistretti, P.; Daffonchio, L.; Ruffini, P. A.; Allegretti, M.; Secchi, A.; Bonifacio, E.; Piemonti, L. CXCR1/2 inhibition enhances pancreatic islet survival after transplantation. *J. Clin. Invest.* **2012**, *122* (10), 3647-3647.

(242) Pawlick, R. L.; Wink, J.; Pepper, A. R.; Bruni, A.; Abualhassen, N.; Rafiei, Y.; Gala-Lopez, B.; Bral, M.; Shapiro, A. M. J. Reparixin, a CXCR1/2 inhibitor in islet allotransplantation. *Islets* **2016**, *8* (5), 115-124.

(243) Singh, J. K.; Farnie, G.; Bundred, N. J.; Simões, B. M.; Shergill, A.; Landberg, G.; Howell, S. J.; Clarke, R. B. Targeting CXCR1/2 Significantly Reduces Breast Cancer Stem Cell Activity and Increases the Efficacy of Inhibiting HER2 via HER2-dependent and -independent Mechanisms. *Clin. Cancer Res.* **2013**, *19* (3), 643-643.

(244) Emanuele, B.; Paolo, P.; Francesco, G.; Efisio, C.; Thomas, L.; Ludger, R.; Vart Keymeulen, Sr.; Pieter, G.; Luisa, D.; Pier a, R.; Marcello, A.; Lorenzo, P. 249-OR: A Randomized, Double-Blind Phase 2 Trial of the CXCR1/2 Inhibitor Ladarixin in Adult Patients with New-Onset Type 1 Diabetes. *Diabetes* **2020**, *69* ((Supplement_1)).

(245) Brandolini, L.; Aramini, A.; Bianchini, G.; Ruocco, A.; Bertini, R.; Novelli, R.; Angelico, P.; Valsecchi, A. E.; Russo, R.; Castelli, V.; Cimini, A.; Allegretti, M. Inflammation-Independent Antinociceptive Effects of DF2755A, a CXCR1/2 Selective Inhibitor: A New Potential Therapeutic Treatment for Peripheral Neuropathy Associated to Non-Ulcerative Interstitial Cystitis/Bladder Pain Syndrome. *Front. Pharmacol.* **2022**, *13*.

(246) Merritt, J. R.; Rokosz, L. L.; Nelson, K. H.; Kaiser, B.; Wang, W.; Stauffer, T. M.; Ozgur, L. E.; Schilling, A.; Li, G.; Baldwin, J. J.; Taveras, A. G.; Dwyer, M. P.; Chao, J. Synthesis and structure-activity relationships of 3,4-diaminocyclobut-3-ene-1,2-dione CXCR2 antagonists. *Bioorganic and Medicinal Chemistry Letters* **2006**, *16* (15), 4107-4110.

(247) Widdowson, K. L.; Gleason, J. G. Il-8 receptor antagonists. WO1998005317A1, 1997.

(248) Dwyer, M. P.; Yu, Y.; Chao, J. J. J.; Aki, C.; Biju, P.; Girijavallabhan, V.; Rindgen, D.; Bond, R.; Mayer-Ezel, R.; Jakway, J.; Hipkin, R. W.; Fossetta, J.; Gonsiorek, W.; Bian, H.; Fan, X.; Terminelli, C.; Fine, J.; Lundell, D.; Merritt, J. R.; Rokosz, L. L.; Kaiser, B.; Li, G.; Wang, W.; Stauffer, T.; Ozgur, L.; Baldwin, J.; Taveras, A. G. Discovery of 2-hydroxy-N,N-dimethyl-3-{2-[[(R)-1-(5-methylfuran-2-yl)propyl]amino]-3,4-dioxocyclobut-1-enylamino}benzamide (SCH 527123): a potent, orally bioavailable CXCR2/CXCR1 receptor antagonist. *J. Med. Chem.* **2006**, *49* (26), 7603-7606.

(249) Yu, Y.; Dwyer, M. P.; Chao, J. J.; Aki, C.; Chao, J. J.; Purakkattle, B.; Rindgen, D.; Bond, R.; Mayer-Ezel, R.; Jakway, J.; Qiu, H.; Hipkin, R. W.; Fossetta, J.; Gonsiorek, W.; Bian, H.; Fan, X.; Terminelli, C.; Fine, J.; Lundell, D.; Merritt, J. R.; He, Z.; Lai, G.; Wu, M.; Taveras, A. Synthesis and structure-activity relationships of heteroaryl substituted-3,4-diamino-3-cyclobut-3-ene-1,2-dione CXCR2/CXCR1 receptor antagonists. *Bioorganic and Medicinal Chemistry Letters* **2008**, *18* (4), 1318-1322.

(250) Chao, J.; Taveras, A. G.; Chao, J.; Aki, C.; Dwyer, M.; Yu, Y.; Purakkattle, B.; Rindgen, D.; Jakway, J.; Hipkin, W.; Fosetta, J.; Fan, X.; Lundell, D.; Fine, J.; Minnicozzi, M.; Phillips, J.; Merritt, J. R. C(4)-alkyl substituted furanyl cyclobutenediones as potent, orally bioavailable CXCR2 and CXCR1 receptor antagonists. *Bioorg. Med. Chem. Lett.* **2007**, *17* (13), 3778-3783.

(251) Lai, G.; Merritt, J. R.; He, Z.; Feng, D.; Chao, J.; Czarniecki, M. F.; Rokosz, L. L.; Stauffer, T. M.; Rindgen, D.; Taveras, A. G. Synthesis and structure-activity relationships of new disubstituted phenyl-containing 3,4-diamino-3-cyclobutene-1,2-diones as CXCR2 receptor antagonists. *Bioorganic and Medicinal Chemistry Letters* **2008**, *18* (6), 1864-1868.

(252) Gonsiorek, W.; Fan, X.; Hesk, D.; Fossetta, J.; Qiu, H.; Jakway, J.; Billah, M.; Dwyer, M.; Chao, J.; Deno, G.; Taveras, A.; Lundell, D. J.; Hipkin, R. W. Pharmacological

characterization of Sch527123, a potent allosteric CXCR1/CXCR2 antagonist. *J. Pharmcol. Exp. Ther.* **2007**, *322* (2), 477-485.

(253) Chapman, R. W.; Minnicozzi, M.; Celly, C. S.; Phillips, J. E.; Kung, T. T.; Hipkin, R. W.; Fan, X.; Rindgen, D.; Deno, G.; Bond, R.; Gonsiorek, W.; Billah, M. M.; Fine, J. S.; Hey, J. A. A novel, orally active CXCR1/2 receptor antagonist, Sch527123, inhibits neutrophil recruitment, mucus production, and goblet cell hyperplasia in animal models of pulmonary inflammation. *J. Pharmcol. Exp. Ther.* **2007**, *322* (2), 486-493.

(254) Holz, O.; Khalilieh, S.; Ludwig-Sengpiel, A.; Watz, H.; Stryszak, P.; Soni, P.; Tsai, M.; Sadeh, J.; Magnussen, H. SCH527123, a novel CXCR2 antagonist, inhibits ozone-induced neutrophilia in healthy subjects. *Eur. Clin. Respir. J.* **2010**, *35* (3), 564-570.

(255) Singh, S.; Sadanandam, A.; Nannuru, K. C.; Varney, M. L.; Mayer-Ezell, R.; Bond, R.; Singh, R. K. Small-molecule antagonists for CXCR2 and CXCR1 inhibit human melanoma growth by decreasing tumor cell proliferation, survival, and angiogenesis. *Clin. Cancer Res.* **2009**, *15* (7), 2380-2386.

(256) Varney, M. L.; Singh, S.; Li, A.; Mayer-Ezell, R.; Bond, R.; Singh, R. K. Small Molecule Antagonists for CXCR2 and CXCR1 Inhibit Human Colon Cancer Liver Metastases. *Cancer Lett.* **2011**, *300* (2), 180-180.

(257) Chen, S.-H.; Wu, H.; Dong, J.; Liu, S.; Niu, Y. Novel hydrazino-cyclobut-s-ene-i, 2-dione derivatives as CXCR2 antagonists. WO2010091543, 2010.

(258) Zebala, J. A.; Maeda, D. Y.; Schuler, A. D. Method for treating cancer using chemokine antagonists. WO2010015613A1, 2008.

(259) Ambarkhane, A. V.; Mauler, A.; Timpe, C.; Baettig, U. Choline salt of an anti - inflammatory substituted cyclobutenedione compound. WO2013030803A1, 2013.

(260) Aciro, C.; Bagal, S. K.; Harvey, J. W.; Jones, L. H.; Mowbray, C. E.; Owen, R. M.; Sabnis, Y. A.; Storer, R. I.; Yeap, S. K. Cyclobutenedione derivatives. WO2010131145A1, 2010.

(261) Aubert, J.; Boiteau, J., G.; Clary, L.; Musicki, B.; Rossio, P.; Schuppli-Nollet, M. Novel disubstituted 3,4-diamino-3-cyclobutene-1,2-dione compounds for use in the treatment of chemokine-mediated diseases. WO2013061004A8, 2014.

(262) Branislav, M.; Jerome, A.; Jean-Guy, B.; Laurence, C.; Patricia, R.; Marlene, S., N. Disubstituted 3,4-diamino-3-cyclobutene-1,2-dione compounds for use in the treatment of chemokine-mediated pathologies. WO2013061005A1, 2014.

(263) Branislav, M.; Jerome, A.; Jean-Guy, B.; Laurence, C.; Patricia, R.; Marlene, S., N. Novel disubstituted 3,4-diamino-3-cyclobutene-1,2-dione compounds for use in the treatment of chemokine-mediated diseases. WO2013061002A1, 2013.

(264) Branislav, M.; Jerome, A.; Jean-Guy, B.; Laurence, C.; Patricia, R.; Marlene, S., N. . Disubstituted 3,4-Diamino-3-Cyclobutene-1,2-Dione Compounds for Use in the Treatment of Chemokine-Mediated Diseases. US20150374708A1, 2015.

(265) Tabet, S.; Rodeville, N.; Mathieu, A.; Raffin, C.; Millois-Barbuis, C.; Musicki, B.; Muller, F.; Gerfaud, T.; Boiteau, J. G.; Cardinaud, I. Early Development Scale-Up of a Novel CXCR Antagonist: Focus on Racemic and Stereoselective Routes of a Key Intermediate. *Org. Process Res. Dev.* **2017**, *21* (12), 2032-2044.

(266) Sliwoski, G.; Kothiwale, S.; Meiler, J.; Lowe, E. W. Computational methods in drug discovery. *Pharmacol. Rev.* **2014**, *66* (1), 334-395.

(267) Hartenfeller, M.; Schneider, G. Enabling future drug discovery by de novo design. *WIREs Comput. Mol. Sci.* **2011**, *1* (5), 742-759.

(268) Lionta, E.; Spyrou, G.; Vassilatis, D. K.; Cournia, Z. Structure-Based Virtual Screening for Drug Discovery: Principles, Applications and Recent Advances. *Curr. Top. Med. Chem.* **2014**, *14* (16), 1923-1923.

(269) Waszkowycz, B.; Clark, D. E.; Gancia, E. Outstanding challenges in protein–ligand docking and structure-based virtual screening. *WIREs Comput. Mol. Sci.* **2011**, *1* (2), 229-259.

(270) García-Nafría, J.; Tate, C. G. Structure determination of GPCRs: cryo-EM compared with X-ray crystallography. *Biochem. Soc. Trans.* **2021**, *49* (5), 2345-2345.

(271) Waltenspühl, Y.; Ehrenmann, J.; Klenk, C.; Plückthun, A. Engineering of Challenging G Protein-Coupled Receptors for Structure Determination and Biophysical Studies. *Molecules* **2021**, *26* (5).

(272) Basith, S.; Cui, M.; Macalino, S. J. Y.; Park, J.; Clavio, N. A. B.; Kang, S.; Choi, S. Exploring G protein-coupled receptors (GPCRs) ligand space via cheminformatics approaches: Impact on rational drug design. *Front. Pharmacol.* **2018**, *9* (MAR), 338587-338587.

(273) Yang, D.; Zhou, Q.; Labroska, V.; Qin, S.; Darbalaei, S.; Wu, Y.; Yuliantie, E.; Xie, L.; Tao, H.; Cheng, J.; Liu, Q.; Zhao, S.; Shui, W.; Jiang, Y.; Wang, M. W. G protein-coupled receptors: structure- and function-based drug discovery. *Nat. Commun.* **2021**, *6*.

(274) Kolb, P.; Klebe, G. The Golden Age of GPCR Structural Biology: Any Impact on Drug Design? *Angew. Chem. Int. Ed.* **2011**, *50* (49), 11573-11575.

(275) Zardecki, C. A.-O.; Dutta, S.; Goodsell, D. A.-O.; Lowe, R.; Voigt, M.; Burley, S. A.-O. PDB-101: Educational resources supporting molecular explorations through biology and medicine. *Prot. Sci.* **2021**, *31* (1), 129-140.

(276) Cheng, L.; Xia, F.; Li, Z.; Shen, C.; Yang, Z.; Hou, H.; Sun, S.; Feng, Y.; Yong, X.; Tian, X.; Qin, H.; Yan, W.; Shao, Z. Structure, function and drug discovery of GPCR signaling. *Mol. Biomed.* **2023**, *4* (1), 1-39.

(277) Datta, S.; Grant, D. J. W. Crystal structures of drugs: Advances in determination, prediction and engineering. *Nat. Rev. Drug Discov.* **2004**, *3* (1), 42-57.

(278) Batool, M.; Ahmad, B.; Choi, S. A Structure-Based Drug Discovery Paradigm. *Int. J. Mol. Sci.* **2019**, *20* (11).

(279) Wu, M.; Lander, G. C. How low can we go? Structure determination of small biological complexes using single-particle cryo-EM. *Curr. Opin. Struct. Biol.* **2020**, *64*, 9-9.

(280) Liu, Y.; Huynh, D. T.; Yeates, T. O. A 3.8 Å resolution cryo-EM structure of a small protein bound to an imaging scaffold. *Nat. Commun.* **2019**, *10* (1), 1-7.

(281) Wu, B.; Chien, E. Y. T.; Mol, C. D.; Fenalti, G.; Liu, W.; Katritch, V.; Abagyan, R.; Brooun, A.; Wells, P.; Bi, F. C.; Hamel, D. J.; Kuhn, P.; Handel, T. M.; Cherezov, V.; Stevens, R. C. Structures of the CXCR4 chemokine GPCR with small-molecule and cyclic peptide antagonists. *Science.* **2010**, *330* (6007), 1066-1071.

(282) Shao, Z.; Tan, Y.; Shen, Q.; Hou, L.; Yao, B.; Qin, J.; Xu, P.; Mao, C.; Chen, L. N.; Zhang, H.; Shen, D. D.; Zhang, C.; Li, W.; Du, X.; Li, F.; Chen, Z. H.; Jiang, Y.; Xu, H. E.; Ying, S.; Ma, H.; Zhang, Y.; Shen, H. Molecular insights into ligand recognition and activation of chemokine receptors CCR2 and CCR3. *Cell Discov.* **2022**, *8* (1).

(283) Qin, L.; Kufareva, I.; Holden, L. G.; Wang, C.; Zheng, Y.; Zhao, C.; Fenalti, G.; Wu, H.; Han, G. W.; Cherezov, V.; Abagyan, R.; Stevens, R. C.; Handel, T. M. Crystal structure of the chemokine receptor CXCR4 in complex with a viral chemokine. *Science.* **2015**, *347* (6226), 1117-1122.

(284) Zheng, Y.; Han, G. W.; Abagyan, R.; Wu, B.; Stevens, R. C.; Cherezov, V.; Kufareva, I.; Handel, T. M. Structure of CC Chemokine Receptor 5 with a Potent Chemokine Antagonist Reveals Mechanisms of Chemokine Recognition and Molecular Mimicry by HIV. *Immunity.* **2017**, *46* (6), 1005-1017.

(285) Lu, M.; Zhao, W.; Han, S.; Lin, X.; Xu, T.; Tan, Q.; Wang, M.; Yi, C.; Chu, X.; Yang, W.; Zhu, Y.; Wu, B.; Zhao, Q. Activation of the human chemokine receptor CX3CR1 regulated by cholesterol. *Sci. Adv* **2022**, *8* (26).

(286) Wasilko, D. J.; Johnson, Z. L.; Ammirati, M.; Che, Y.; Griffor, M. C.; Han, S.; Wu, H. Structural basis for chemokine receptor CCR6 activation by the endogenous protein ligand CCL20. *Nat. Commun.* **2020**, *11* (1).

(287) Zhang, H.; Chen, K.; Tan, Q.; Shao, Q.; Han, S.; Zhang, C.; Yi, C.; Chu, X.; Zhu, Y.; Xu, Y.; Zhao, Q.; Wu, B. Structural basis for chemokine recognition and receptor activation of chemokine receptor CCR5. *Nat. Commun.* **2021**, *12* (1), 1-12.

(288) Isaikina, P.; Tsai, C. J.; Dietz, N.; Pamula, F.; Grahl, A.; Goldie, K. N.; Guixà-González, R.; Branco, C.; Paolini-Bertrand, M.; Calo, N.; Cerini, F.; Schertler, G. F. X.; Hartley, O.; Stahlberg, H.; Maier, T.; Deupi, X.; Grzesiek, S. Structural basis of the activation of the CC chemokine receptor 5 by a chemokine agonist. *Sci. Adv* **2021**, *7* (25), 8685-8701.

(289) Schrödinger. Schrödinger Release 2023-4. PIPER: New York, 2023.

(290) González, A.; Perez-Acle, T.; Pardo, L.; Deupi, X. Molecular basis of ligand dissociation in β-adrenergic receptors. *PloS one* **2011**, *6* (9).

(291) Selvam, B.; Wereszczynski, J.; Tikhonova, I. G. Comparison of Dynamics of Extracellular Accesses to the b 1 and b 2 Adrenoceptors Binding Sites Uncovers the Potential of Kinetic Basis of Antagonist Selectivity. *Chem. Biol. Drug Des.* **2012**, *80*, 215-226.

(292) Emtage, A. L.; Mistry, S. N.; Fischer, P. M.; Kellam, B.; Laughton, C. A. GPCRs through the keyhole: the role of protein flexibility in ligand binding to β-adrenoceptors. *J. Biomol. Struct. Dyn.* **2017**, *35* (12), 2604-2619.

(293) Yang, H.; Shen, Z.; Luo, L.; Gao, J.; Chen, S.; Che, J.; Xu, L.; Wu, M.; Dong, X. Molecular dynamics insights into the selectivity toward CXCR1 and CXCR2 antagonists. *Chem. Phys. Lett.* **2022**, *795*, 139539-139539.

(294) Park, S. H.; Das, B. B.; Casagrande, F.; Tian, Y.; Nothnagel, H. J.; Chu, M.; Kiefer, H.; Maier, K.; De Angelis, A. A.; Marassi, F. M.; Opella, S. J. Structure of the chemokine receptor CXCR1 in phospholipid bilayers. *Nature.* **2012**, *491* (7426), 779-783.

(295) Harner, M. J.; Mueller, L.; Robbins, K. J.; Reily, M. D. NMR in drug design. *Arch. Biochem. Biophys.* **2017**, *628*, 132-147.

(296) Huang, S.-Y.; Zou, X. Efficient molecular docking of NMR structures: Application to HIV-1 protease. *Prot. Sci.* **2007**, *16* (1), 43-43.

(297) Stark, J. L.; Powers, R. Application of NMR and Molecular Docking in Structure-based Drug Discovery. *Top. Curr. Chem.* **2012**, *326*, 1-1.

(298) Dwyer, M. P.; Biju, P. Discovery of 3,4-Diaminocyclobut-3-ene-1,2-dione-Based CXCR2 Receptor Antagonists for the Treatment of Inflammatory Disorders. *Curr. Top. Med. Chem.* **2010**, *10* (13), 1339-1350.

(299) Bateman, A.; Martin, M. J.; Orchard, S.; Magrane, M.; Ahmad, S.; Alpi, E.; Bowler-Barnett, E. H.; Britto, R.; Bye-A-Jee, H.; Cukura, A.; Denny, P.; Dogan, T.; Ebenezer, T. G.; Fan, J.; Garmiri, P.; da Costa Gonzales, L. J.; Hatton-Ellis, E.; Hussein, A.; Ignatchenko, A.; Insana, G.; Ishtiaq, R.; Joshi, V.; Jyothi, D.; Kandasaamy, S.; Lock, A.; Luciani, A.; Lugaric, M.; Luo, J.; Lussi, Y.; MacDougall, A.; Madeira, F.; Mahmoudy, M.; Mishra, A.; Moulang, K.; Nightingale, A.; Pundir, S.; Qi, G.; Raj, S.; Raposo, P.; Rice, D. L.; Saidi, R.; Santos, R.; Speretta, E.; Stephenson, J.; Totoo, P.; Turner, E.; Tyagi, N.; Vasudev, P.; Warner, K.; Watkins, X.; Zaru, R.; Zellner, H.; Bridge, A. J.; Aimo, L.; Argoud-Puy, G.; Auchincloss, A. H.; Axelsen, K. B.; Bansal, P.; Baratin, D.; Batista Neto, T. M.; Blatter, M. C.; Bolleman, J. T.; Boutet, E.; Breuza, L.; Gil, B. C.; Casals-Casas, C.; Echioukh, K. C.; Coudert, E.; Cuche, B.; de Castro, E.; Estreicher, A.; Famiglietti, M. L.; Feuermann, M.; Gasteiger, E.; Gaudet, P.; Gehant, S.; Gerritsen, V.; Gos, A.; Gruaz, N.; Hulo, C.; Hyka-Nouspikel, N.; Jungo, F.; Kerhornou, A.; Le Mercier, P.; Lieberherr, D.; Masson, P.; Morgat, A.; Muthukrishnan, V.; Paesano, S.; Pedruzzi, I.; Pilbout, S.; Pourcel, L.; Poux, S.; Pozzato, M.; Pruess, M.; Redaschi, N.; Rivoire, C.; Sigrist, C. J. A.; Sonesson, K.; Sundaram, S.; Wu, C. H.; Arighi, C. N.; Arminski, L.; Chen, C.; Chen, Y.; Huang, H.; Laiho, K.; McGarvey, P.; Natale, D. A.; Ross, K.; Vinayaka, C. R.; Wang, Q.; Wang, Y.; Zhang, J. UniProt: the Universal Protein Knowledgebase in 2023. *Nucleic acids res.* **2023**, *51* (D1), D523-D531.

(300) Altschul, S. F.; Gish, W.; Miller, W.; Myers, E. W.; Lipman, D. J. Basic local alignment search tool. *J. Mol. Biol.* **1990**, *215* (3), 403-410.

(301) Berman, H. M.; Westbrook, J.; Feng, Z.; Gilliland, G.; Bhat, T. N.; Weissig, H.; Shindyalov, I. N.; Bourne, P. E. The Protein Data Bank. *Nucleic acids res.* **2000**, *28* (1), 235-242.

(302) Jacobson, M. P.; Pincus, D. L.; Rapp, C. S.; Day, T. J. F.; Honig, B.; Shaw, D. E.; Friesner, R. A. A hierarchical approach to all-atom protein loop prediction. *Proteins* **2004**, *55* (2), 351-367.

(303) Papadopoulos, J. S.; Agarwala, R. COBALT: Constraint-based alignment tool for multiple protein sequences. *Bioinformatics* **2007**, *23* (9), 1073-1079.

(304) Webb, B.; Sali, A. Comparative Protein Structure Modeling Using Modeller. *Curr. Protoc. Bioinformatics* **2016**, *20* (54), 1-37.

(305) Shen, M.-Y.; Sali, A. Statistical potential for assessment and prediction of protein structures. *Prot. Sci.* **2006**, *15* (11), 2507–2524.

(306) Laskowski, R. A.; MacArthur, M. W.; Moss, D. S.; Thornton, J. M. PROCHECK: a program to check the stereochemical quality of protein structures. *J. Appl. Crystallogr.* **1993**, *26* (2), 283-291.

(307) Williams, C. J.; Headd, J. J.; Moriarty, N. W.; Prisant, M. G.; Videau, L. L.; Deis, L. N.; Verma, V.; Keedy, D. A.; Hintze, B. J.; Chen, V. B.; Jain, S.; Lewis, S. M.; Arendall,

W. B.; Snoeyink, J.; Adams, P. D.; Lovell, S. C.; Richardson, J. S.; Richardson, D. C. MolProbity: More and better reference data for improved all-atom structure validation. *Prot. Sci.* **2018**, *27* (1), 293-315.

(308) Daina, A.; Michielin, O.; Zoete, V. SwissADME: a free web tool to evaluate pharmacokinetics, drug-likeness and medicinal chemistry friendliness of small molecules. *Sci. Rep.* **2017**, *7*, 42717.

(309) Kulleperuma, K.; Smith, S. M. E.; Morgan, D.; Musset, B.; Holyoake, J.; Chakrabarti, N.; Cherny, V. V.; DeCoursey, T. E.; Pomès, R. Construction and validation of a homology model of the human voltage-gated proton channel hHV1. *J. Gen. Physiol.* **2013**, *141* (4), 445-445.

(310) Haddad, Y.; Adam, V.; Heger, Z. Ten quick tips for homology modeling of high-resolution protein 3D structures. *PLoS Comput. Biol.* **2020**, *16* (4).

(311) Schrödinger, L. L. C. The PyMOL Molecular Graphics System, Version~1.8. 2015.

(312) Chan, W. K. B.; Zhang, H.; Yang, J.; Brender, J. R.; Hur, J.; Ozgur, A.; Zhang, Y. GLASS: a comprehensive database for experimentally validated GPCR-ligand associations. *Bioinformatics* **2015**, *31* (18), 3035-3035.

(313) Mysinger, M. M.; Carchia, M.; Irwin, J. J.; Shoichet, B. K. Directory of useful decoys, enhanced (DUD-E): Better ligands and decoys for better benchmarking. *J. Med. Chem.* **2012**, *55* (14), 6582-6594.

(314) Irwin, J. J.; Sterling, T.; Mysinger, M. M.; Bolstad, E. S.; Coleman, R. G. ZINC: A free tool to discover chemistry for biology. *J. Chem. Inf. Model.* **2012**, *52* (7), 1757-1768.

(315) Stein, R. M.; Yang, Y.; Balius, T. E.; O'Meara, M. J.; Lyu, J.; Young, J.; Tang, K.; Shoichet, B. K.; Irwin, J. J. Property-Unmatched Decoys in Docking Benchmarks. *J. Chem. Inf. Model.* **2021**, *61* (2), 699-714.

(316) Bajusz, D.; Rácz, A.; Héberger, K. Why is Tanimoto index an appropriate choice for fingerprint-based similarity calculations? *J. Cheminf.* **2015**, *7* (1), 1-13.

(317) Muegge, I.; Mukherjee, P. An overview of molecular fingerprint similarity search in virtual screening. *Expert Opin. Drug Discov.* **2016**, *11* (2), 137-148.

(318) Cereto-Massagué, A.; Ojeda, M. J.; Valls, C.; Mulero, M.; Garcia-Vallvé, S.; Pujadas, G. Molecular fingerprint similarity search in virtual screening. *Methods* **2015**, *71* (C), 58-63.

(319) Kooistra, A. J.; Mordalski, S.; Pándy-Szekeres, G.; Esguerra, M.; Mamyrbekov, A.; Munk, C.; Keserű, G. M.; Gloriam, D. E. GPCRdb in 2021: integrating GPCR sequence, structure and function. *Nucleic acids res.* **2021**, *49* (D1), D335-D343.

(320) Kooistra, A. J.; Munk, C.; Hauser, A. S.; Gloriam, D. E. An online GPCR structure analysis platform. *Nature Structural & Molecular Biology 2021 28:11* **2021**, *28* (11), 875-878.

(321) Wink, L. H.; Baker, D. L.; Cole, J. A.; Parrill, A. L. A Benchmark Study of Loop Modeling Methods Applied to G Protein-Coupled Receptors. *J. Comput. Aided Mol. Des.* **2019**, *33* (6), 573-573.

(322) Kmiecik, S.; Jamroz, M.; Kolinski, M. Structure Prediction of the Second Extracellular Loop in G-Protein-Coupled Receptors. *Biophys. J.* **2014**, *106* (11), 2408-2408.

(323) Nicoli, A.; Dunkel, A.; Giorgino, T.; De Graaf, C.; Di Pizio, A. Classification Model for the Second Extracellular Loop of Class A GPCRs. *J. Chem. Inf. Model.* **2022**, *62* (3), 511-522.

(324) Emtage, A. L. Structural exploration of beta1-adrenoceptor selectivity University of Nottingham UK. University of Nottingham, UK, 2013.

(325) Khoddami, M.; Nadri, H.; Moradi, A.; Sakhteman, A. Homology modeling, molecular dynamic simulation, and docking based binding site analysis of human dopamine (D4) receptor. *J. Mol. Model.* **2015**, *21* (2), 1-10.

(326) Iman, M.; Davood, A. Homology modeling of lanosterol 14α-demethylase of Candida albicans and insights into azole binding. *Med. Chem. Res.* **2014**, *23* (6), 2890-2899.

(327) Sasidharan, S.; Saudagar, P. Prediction, validation, and analysis of protein structures: A beginner's guide. *Adv. Prot. Mol. Struct. Biol. Methods* **2022**, 373-385.

(328) Kuntz, I. D. Structure-Based Strategies for Drug Design and Discovery. *Science.* **1992**, *257* (5073), 1078-1082.

(329) Chen, Y. Z.; Zhi, D. G. Ligand-Protein Inverse Docking and Its Potential Use in the Computer Search of Protein Targets of a Small Molecule. *Proteins* **2001**, *43*, 217-226.

(330) Grinter, S. Z.; Liang, Y.; Huang, S. Y.; Hyder, S. M.; Zou, X. An inverse docking approach for identifying new potential anti-cancer targets. *J. Mol. Graph. Mod.* **2011**, *29* (6), 795-795.

(331) Huang, H.; Zhang, G.; Zhou, Y.; Lin, C.; Chen, S.; Lin, Y.; Mai, S.; Huang, Z. Reverse screening methods to search for the protein targets of chemopreventive compounds. *Front. Chem.* **2018**, *6* (138), 361885-361885.

(332) Furlan, V.; Konc, J.; Bren, U. Inverse Molecular Docking as a Novel Approach to Study Anticarcinogenic and Anti-Neuroinflammatory Effects of Curcumin. *Molecules* **2018**, *23* (12), 3351.

(333) Halgren, T. A.; Murphy, R. B.; Friesner, R. A.; Beard, H. S.; Frye, L. L.; Pollard, W. T.; Banks, J. L. Glide: a new approach for rapid, accurate docking and scoring. 2. Enrichment factors in database screening. *J. Med. Chem.* **2004**, *47* (7), 1750-1759.

(334) Waterhouse, A.; Bertoni, M.; Bienert, S.; Studer, G.; Tauriello, G.; Gumienny, R.; Heer, F. T.; De Beer, T. A. P.; Rempfer, C.; Bordoli, L.; Lepore, R.; Schwede, T. SWISS-MODEL: Homology modelling of protein structures and complexes. *Nucleic acids res.* **2018**, *46* (W1), W296-W303.

(335) Chen, V. B.; Arendall, W. B.; Headd, J. J.; Keedy, D. A.; Immormino, R. M.; Kapral, G. J.; Murray, L. W.; Richardson, J. S.; Richardson, D. C. MolProbity: all-atom structure validation for macromolecular crystallography. *Acta Crystallogr. D Biol. Crystallogr.* **2010**, *66* (Pt 1), 12-12.

(336) Costanzi, S.; Cohen, A.; Danfora, A.; Dolatmoradi, M. Influence of the Structural Accuracy of Homology Models on Their Applicability to Docking-Based Virtual Screening: The β2 Adrenergic Receptor as a Case Study. *J. Chem. Inf. Model.* **2019**, *59* (7), 3177-3190.

(337) Costanzi, S. Homology modeling of class a G protein-coupled receptors. *Methods Mol. Biol.* **2012**, *857*, 259-279.

(338) *Long-Term Study of the Effects of Navarixin (SCH 527123, MK-7123) in Participants With Moderate to Severe COPD (MK-7123-019)*. https://clinicaltrials.gov/ct2/show/NCT01006616 (accessed 2024 Mar).

(339) Armstrong, A. J.; Geva, R.; Chung, H. C.; Lemech, C.; Miller, W. H.; Hansen, A. R.; Lee, J. S.; Tsai, F.; Solomon, B. J.; Kim, T. M.; Rolfo, C.; Giranda, V.; Ren, Y.; Liu, F.; Kandala, B.; Freshwater, T.; Wang, J. S. CXCR2 antagonist navarixin in combination with pembrolizumab in select advanced solid tumors: a phase 2 randomized trial. *Inv. New Drugs* **2024**, *42* (1).

(340) Evans, T. R. J.; Basu, B.; Hubner, R.; Ma, Y. T.; Meyer, T.; Palmer, D. H.; Pinato, D. J. J.; Plummer, E. R.; Ross, P. J.; Samson, A.; Sarker, D.; Kendall, T.; Bellamy, C.; Reeves, H. L.; Thomson, F.; Lawless, C. A.; Stobo, J.; Sansom, O. J.; Mann, D. A.; Bird, T. G. A phase I/II study of the CXCR2 inhibitor, AZD5069, in combination with durvalumab, in patients (pts) with advanced hepatocellular carcinoma (HCC). *Am. Soc. Clin. Oncol.* **2023**, *41*, 631.

(341) Piemonti, L.; Landoni, G.; Voza, A.; Puoti, M.; Gentile, I.; Coppola, N.; Nava, S.; Mattei, A.; Marinangeli, F.; Marchetti, G.; Bonfanti, P.; Mastroianni, C. M.; Bassetti, M.; Crisafulli, E.; Grossi, P. A.; Zangrillo, A.; Desai, A.; Merli, M.; Foggia, M.; Carpano, M.; Schiavoni, L.; D'Arminio Monforte, A.; Bisi, L.; Russo, G.; Busti, F.; Rovelli, C.; Perrotta, E.; Goisis, G.; Gavioli, E. M.; Toya, S.; De Pizzol, M.; Mantelli, F.; Allegretti, M.; Minnella, E. M. Efficacy and Safety of Reparixin in Patients with Severe COVID-19 Pneumonia: A Phase 3, Randomized, Double-Blind Placebo-Controlled Study. *Infect. Dis. Ther.* **2023**, *12* (10), 2437-2456.

(342) Liotti, F.; de Pizzol, M.; Allegretti, M.; Prevete, N.; Melillo, R. M. Multiple anti-tumor effects of Reparixin on thyroid cancer. *Oncotarget.* **2017**, *8* (22), 35946-35946.

(343) Ruffini, P. A. The CXCL8-CXCR1/2 Axis as a Therapeutic Target in Breast Cancer Stem-Like Cells. *Front. Oncol.* **2019**, *9*, 40.

(344) Aki, C.; Chao, J.; Ferreira, J. A.; Dwyer, M. P.; Yu, Y.; Chao, J.; Merritt, R. J.; Lai, G.; Wu, M.; Hipkin, R. W.; Fan, X.; Gonsiorek, W.; Fosseta, J.; Rindgen, D.; Fine, J.; Lundell, D.; Taveras, A. G.; Biju, P. Diaminocyclobutenediones as potent and orally bioavailable CXCR2 receptor antagonists: SAR in the phenolic amide region. *Bioorganic and Medicinal Chemistry Letters* **2009**, *19* (15), 4446-4449.

(345) Xue, D.; Chen, W.; Neamati, N. Discovery, structure-activity relationship study and biological evaluation of 2-thioureidothiophene-3-carboxylates as a novel class of C-X-C chemokine receptor 2 (CXCR2) antagonists. *Eur. J. Med. Chem.* **2020**, *204*, 112387-112387.

(346) Ha, H.; Debnath, B.; Odde, S.; Bensman, T.; Ho, H.; Beringer, P. M.; Neamati, N. Discovery of Novel CXCR2 Inhibitors Using Ligand-Based Pharmacophore Models. *J. Chem. Inf. Model.* **2015**, *55* (8), 1720-1738.

(347) Che, J.; Wang, Z.; Sheng, H.; Huang, F.; Dong, X.; Hu, Y.; Xie, X.; Hu, Y. Ligand-based pharmacophore model for the discovery of novel CXCR2 antagonists as anti-cancer metastatic agents. *Roy. Soc. Open. Sci.* **2018**, *5* (7).

(348) Biju, P.; Taveras, A. G.; Dwyer, M. P.; Yu, Y.; Chao, J.; Hipkin, R. W.; Fan, X.; Rindgen, D.; Fine, J.; Lundell, D. Fluoroalkyl α side chain containing 3,4-diamino-cyclobutenediones as potent and orally bioavailable CXCR2-CXCR1 dual antagonists. *Bioorganic and Medicinal Chemistry Letters* **2009**, *19* (5), 1431-1433.

(349) Huber, M. E.; Wurnig, S.; Toy, L.; Weiler, C.; Merten, N.; Kostenis, E.; Hansen, F. K.; Schiedel, M. Fluorescent Ligands Enable Target Engagement Studies for the Intracellular Allosteric Binding Site of the Chemokine Receptor CXCR2. *J. Med. Chem.* **2023**, *66* (14), 9916-9933.

(350) Chen, X.; Dragoli, D. R.; FAN, J.; Kalisiak, J.; Leleti, M. R.; Malathong, V.; McMahon, J.; Tanaka, H.; Yang, J.; Yu, C.; Zhang, P.; Mali, V. Inhibitors of CXCR2. US10370363B2, 2018.

(351) Halgren, T. A. Identifying and characterizing binding sites and assessing druggability. *J. Chem. Inf. Model.* **2009**, *49* (2), 377-389.

(352) Lanka, G.; Bathula, R.; Bhargavi, M.; Potlapally, S. R. Homology modeling and molecular docking studies for the identification of novel potential therapeutics against human PHD3 as a drug target for type 2 diabetes mellitus. *J. Drug Del. Ther.* **2019**, *9* (4), 265-273.

(353) Michaelides, I. N.; Collie, G. W.; Börjesson, U.; Vasalou, C.; Alkhatib, O.; Barlind, L.; Cheung, T.; Dale, I. L.; Embrey, K. J.; Hennessy, E. J.; Khurana, P.; Koh, C. M.; Lamb, M. L.; Liu, J.; Moss, T. A.; O'Neill, D. J.; Phillips, C.; Shaw, J.; Snijder, A.; Storer, R. I.; Stubbs, C. J.; Han, F.; Li, C.; Qiao, J.; Sun, D. Q.; Wang, J.; Wang, P.; Yang, W. Discovery and Optimization of the First ATP Competitive Type-III c-MET Inhibitor. *J. Med. Chem.* **2023**, *66* (13), 8782-8807.

(354) Pillaiyar, T.; Wozniak, M.; Abboud, D.; Rasch, A.; Liebing, A. D.; Poso, A.; Kronenberger, T.; Stäubert, C.; Laufer, S. A.; Hanson, J. Development of Ligands for the Super Conserved Orphan G Protein-Coupled Receptor GPR27 with Improved Efficacy and Potency. *J. Med. Chem.* **2023**, *66*, 17118-17137.

(355) Kueffer, L. E.; Lin, D. Y.-w.; Amatya, N.; Serrenho, J.; Joseph, R. E.; Courtney, A. H.; Andreotti, A. H. Screening and Characterization of Allosteric Small Molecules Targeting Bruton's Tyrosine Kinase. *Biochemistry.* **2023**, *63*, 94-106.

(356) Zheng, X.; Gan, L.; Wang, E.; Wang, J. Pocket-Based Drug Design: Exploring Pocket Space. *AAPS J.* **2013**, *15* (1), 228-228.

(357) Xu, Q.; Deng, H.; Li, X.; Quan, Z. S. Application of Amino Acids in the Structural Modification of Natural Products: A Review. *Front. Chem.* **2021**, *9*, 650569-650569.

(358) Vale, N.; Ferreira, A.; Matos, J.; Fresco, P.; Gouveia, M. J. molecules Amino Acids in the Development of Prodrugs. *Molecules* **2018**, *23* (9), 2318.

(359) Liu, A.; Han, J.; Nakano, A.; Konno, H.; Moriwaki, H.; Abe, H.; Izawa, K.; Soloshonok, V. A. New pharmaceuticals approved by FDA in 2020: Small-molecule drugs derived from amino acids and related compounds. *Chirality* **2022**, *34* (1), 86-103.

(360) Mishra, S.; Kaur, M.; Chander, S.; Murugesan, S.; Nim, L.; Arora, D. S.; Singh, P. Rational modification of a lead molecule: Improving the antifungal activity of indole – triazole – amino acid conjugates. *Eur. J. Med. Chem.* **2018**, *155*, 658-669.

(361) Chevalier, A.; Zhang, Y.; Khdour, O. M.; Hecht, S. M. Selective Functionalization of Antimycin A Through an N-Transacylation Reaction. *Org. Lett.* **2016**, *18* (10), 2395-2398.

(362) Branislav, M.; Jerome, A.; Jean-Guy, B.; Laurence, C.; Patricia, R.; Marlene, S.-N. Disubstituted 3,4-diamino-3-cyclobutene-1,2-dione compounds for use in the treatment of chemokine-mediated diseases. US9120772B2, 2015.

(363) Halliday, J. D.; Allan Symons, E.; Bindner Can J Chen, P. E. The chemistry of N,N′-dimethylformamidine. III. Tautomerism and hindered rotation. *Can. J. Chem.* **1978**, *56* (11), 1470-1476.

(364) Gottlieb, H. E.; Kotlyar, V.; Nudelman, A. NMR Chemical Shifts of Common Laboratory Solvents as Trace Impurities. *J. Org. Chem.* **1997**, *62* (21), 7512–7515.

(365) Rösch, A. T.; Söntjens, S. H. M.; Robben, J.; Palmans, A. R. A.; Schnitzer, T. Rotational Isomerism of an Amide Substituted Squaraine Dye: A Combined Spectroscopic and Computational Study. *J. Org. Chem.* **2021**, *86* (18), 13100-13103.

(366) Kim, Y. J.; Park, Y.; Park, K. K. Rotational Isomers of N-Alkyl-N-(o-acylphenyl)acetamides. *J. Mol. Struct.* **2006**, *783* (1-3), 61-65.

(367) McMahon, J.; Gallagher, J. F.; Anderson, F. P.; Lough, A. J. A structural systematic study of four isomers of difluoro-N-(3-pyridyl)benzamide. *Acta crystallogr. C, Cryst. Struct. Commun.* **2009**, *65* (7).

(368) Huggins, M. T.; Kesharwani, T.; Buttrick, J.; Nicholson, C. Variable Temperature NMR Experiment Studying Restricted Bond Rotation. *J. Chem. Ed.* **2020**, *97* (5), 1425-1429.

(369) Krishnan, V. V.; Thompson, W. B.; Maitra, K.; Maitra, S. Modulations in restricted amide rotation by steric induced conformational trapping. *Chem. Phys. Lett.* **2012**, *523* (27), 124-127.

(370) Thomsen, W.; Frazer, J.; Unett, D. Functional assays for screening GPCR targets. *Curr. Opin. Biotech.* **2005**, *16* (6), 655-665.

(371) Zhang, R.; Xie, X. Tools for GPCR drug discovery. *Acta Pharmacol. Sin.* **2012**, *33* (3), 372-384.

(372) Yasi, E. A.; Kruyer, N. S.; Peralta-Yahya, P. Advances in G Protein-Coupled Receptor High-throughput Screening. *Curr. Opin. Biotech.* **2020**, *64*, 210-210.

(373) Hoare, S. R. J.; Tewson, P. H.; Quinn, A. M.; Hughes, T. E.; Bridge, L. J. Analyzing kinetic signaling data for G-protein-coupled receptors. *Sci. Rep.* **2020**, *10* (1), 1-23.

(374) Sykes, D. A.; Moore, H.; Stott, L.; Holliday, N.; Javitch, J. A.; Lane, J. R.; Charlton, S. J. Extrapyramidal side effects of antipsychotics are linked to their association kinetics at dopamine D 2 receptors. *Nat. Commun.* **2017**, *8* (763).

(375) Dixon, A. S.; Schwinn, M. K.; Hall, M. P.; Zimmerman, K.; Otto, P.; Lubben, T. H.; Butler, B. L.; Binkowski, B. F.; MacHleidt, T.; Kirkland, T. A.; Wood, M. G.; Eggers, C. T.; Encell, L. P.; Wood, K. V. NanoLuc Complementation Reporter Optimized for Accurate Measurement of Protein Interactions in Cells. *ACS Chem. Biol.* **2016**, *11* (2), 400-408.

(376) England, C. G.; Ehlerding, E. B.; Cai, W. NanoLuc: A Small Luciferase is Brightening up the Field of Bioluminescence. *Bioconjug. Chem.* **2016**, *27* (5), 1175-1175.

(377) Hall, M. P.; Unch, J.; Binkowski, B. F.; Valley, M. P.; Butler, B. L.; Wood, M. G.; Otto, P.; Zimmerman, K.; Vidugiris, G.; MacHleidt, T.; Robers, M. B.; Benink, H. A.; Eggers, C. T.; Slater, M. R.; Meisenheimer, P. L.; Klaubert, D. H.; Fan, F.; Encell, L. P.; Wood, K. V. Engineered luciferase reporter from a deep sea shrimp utilizing a novel imidazopyrazinone substrate. *ACS Chem. Biol.* **2012**, *7* (11), 1848-1857.

(378) Rozbeh, R.; Forchhammer, K. Split NanoLuc technology allows quantitation of interactions between PII protein and its receptors with unprecedented sensitivity and reveals transient interactions. *Sci. Rep.* **2021**, *11* (1), 1-13.

(379) Mortier, A.; Berghmans, N.; Ronsse, I.; Grauwen, K.; Stegen, S.; van Damme, J.; Proost, P. Biological Activity of CXCL8 Forms Generated by Alternative Cleavage of the Signal Peptide or by Aminopeptidase-Mediated Truncation. *PLoS one* **2011**, *6* (8).

(380) Che, J.; Wang, Z.; Shen, Z.; Zhuang, W.; Ying, H.; Hu, Y.; Hu, Y.; Xie, X.; Dong, X. Discovery of 1,5-Dihydro-4H-imidazol-4-one Derivatives as Potent, Selective Antagonists of CXC Chemokine Receptor 2. *Cite This: ACS Med. Chem. Lett. 2021* **2021**, *12*, 845-845.

(381) Paul, O.; John, P. N.; Carsten, S.; James, W. S. Heterocyclic compounds as inhibitors of CXCR2. WO2009106539A1, 2009.

(382) Jerome, A. Use of squaramide in the prevention and/or treatment of rosacea. US20130231393A1, 2010.

(383) Taveras, A. G.; Aki, C. J.; Bond, R. W.; Chao, J.; Dwyer, M.; Ferreira, J. A.; Chao, J.; Younong, Y.; Baldwin, J. J.; Kaiser, B.; Li, G.; Merritt, R. J.; Nelson, K. H.; Rokosz, L. L. 3,4-DI-substituted cyclobutene-1,2-diones as CXC-chemokine receptor ligands. WO2004011418A1, 2002.

(384) Biju, P.; Taveras, A.; Yu, Y.; Zheng, J.; Chao, J.; Rindgen, D.; Jakway, J.; Hipkin, R. W.; Fossetta, J.; Fan, X.; Fine, J.; Qiu, H.; Merritt, J. R.; Baldwin, J. J. 3,4-Diamino-2,5-thiadiazole-1-oxides as potent CXCR2/CXCR1 antagonists. *Bioorganic and Medicinal Chemistry Letters* **2008**, *18* (1), 228-231.

(385) Briddon, S. J.; Kellam, B.; Hill, S. J. Design and use of fluorescent ligands to study ligand-receptor interactions in single living cells. *Methods Mol. Biol.* **2011**, *746*, 211-236.

(386) Soave, M.; Briddon, S. J.; Hill, S. J.; Stoddart, L. A. Fluorescent ligands: Bringing light to emerging GPCR paradigms. *Br. J. Pharmacol.* **2020**, *177* (5), 978-991.

(387) Bouzo-Lorenzo, M.; Stoddart, L. A.; Xia, L.; Ijzerman, A. P.; Heitman, L. H.; Briddon, S. J.; Hill, S. J. A live cell NanoBRET binding assay allows the study of ligand-binding kinetics to the adenosine A3 receptor. *Purinergic signalling* **2019**, *15* (2), 139-153.

(388) Stoddart, L. A.; White, C. W.; Nguyen, K.; Hill, S. J.; Pfleger, K. D. G. Fluorescence- and bioluminescence-based approaches to study GPCR ligand binding. *Br. J. Pharmacol.* **2016**, *173* (20), 3028-3037.

(389) Stoddart, L. A.; Johnstone, E. K. M.; Wheal, A. J.; Goulding, J.; Robers, M. B.; MacHleidt, T.; Wood, K. V.; Hill, S. J.; Pfleger, K. D. G. Application of BRET to monitor ligand binding to GPCRs. *Nature methods* **2015**, *12* (7), 661-663.

(390) Stoddart, L. A.; Kilpatrick, L. E.; Hill, S. J. NanoBRET Approaches to Study Ligand Binding to GPCRs and RTKs. *Trends Pharmacol. Sci.* **2018**, *39* (2), 136-147.

(391) Stoddart, L. A.; Kilpatrick, L. E.; Briddon, S. J.; Hill, S. J. Probing the pharmacology of G protein-coupled receptors with fluorescent ligands. *Neuropharmacology* **2015**, *98*, 48-57.

(392) Dale, N. C.; Johnstone, E. K. M.; White, C. W.; Pfleger, K. D. G. NanoBRET: The bright future of proximity-based assays. *Front. Bioeng. Biotech.* **2019**, *7*, 446459-446459.

(393) Dragulescu-Andrasi, A.; Chan, C. T.; De, A.; Massoud, T. F.; Gambhir, S. S. Bioluminescence resonance energy transfer (BRET) imaging of protein-protein interactions within deep tissues of living subjects. *Proc. Natl. Acad. Sci.* **2011**, *108* (29), 12060-12065.

(394) Bernetti, M.; Masetti, M.; Rocchia, W.; Cavalli, A. Kinetics of Drug Binding and Residence Time. *Annu. Rev. Phys. Chem* **2019**, *70*, 143-171.

(395) Hoare, B. L.; Tippett, D. N.; Kaur, A.; Cullum, S. A.; Miljuš, T.; Koers, E. J.; Harwood, C. R.; Dijon, N.; Holliday, N. D.; Sykes, D. A.; Veprintsev, D. B. ThermoBRET: A Ligand-Engagement Nanoscale Thermostability Assay Applied to GPCRs. *Chembiochem* **2024**, *25* (2).

(396) Chan, D. S. H.; Kavanagh, M. E.; McLean, K. J.; Munro, A. W.; Matak-Vinković, D.; Coyne, A. G.; Abell, C. Effect of DMSO on Protein Structure and Interactions Assessed by Collision-Induced Dissociation and Unfolding. *Anal. Chem.* **2017**, *89* (18), 9976-9983.

(397) Verheijen, M.; Lienhard, M.; Schrooders, Y.; Clayton, O.; Nudischer, R.; Boerno, S.; Timmermann, B.; Selevsek, N.; Schlapbach, R.; Gmuender, H.; Gotta, S.; Geraedts, J.; Herwig, R.; Kleinjans, J.; Caiment, F. DMSO induces drastic changes in human cellular processes and epigenetic landscape in vitro. *Sci. Rep.* **2019**, *9* (1), 1-12.

(398) Timm, M.; Saaby, L.; Moesby, L.; Hansen, E. W. Considerations regarding use of solvents in in vitro cell based assays. *Cytotechnology* **2013**, *65* (5), 887-887.

(399) Che, J. X.; Wang, Z. L.; Dong, X. W.; Hu, Y. H.; Xie, X.; Hu, Y. Z. Bicyclo[2.2.1]heptane containing: N, N ′-diarylsquaramide CXCR2 selective antagonists as anti-cancer metastasis agents. *RSC Adv.* **2018**, *8* (20), 11061-11069.

(400) Xie, F.; Zhao, H.; Li, D.; Chen, H.; Quan, H.; Shi, X.; Lou, L.; Hu, Y. Synthesis and biological evaluation of 2,4,5-substituted pyrimidines as a new class of tubulin polymerization inhibitors. *J. Med. Chem.* **2011**, *54* (9), 3200-3205.

(401) Walsh, C. J.; Mandal, B. K. A new class of aromatic dianhydrides for chermostable polyimides. *Chem. Mat.* **2001**, *13* (8), 2472-2475.

(402) D'Alterio, M. C.; Casals-Cruañas, È.; Tzouras, N. V.; Talarico, G.; Nolan, S. P.; Poater, A. Mechanistic Aspects of the Palladium-Catalyzed Suzuki-Miyaura Cross-Coupling Reaction. *Chem. Eur.* **2021**, *27* (54), 13481-13493.

(403) Miyaura, N.; Suzuki, A. Palladium-Catalyzed Cross-Coupling Reactions of Organoboron Compounds. *Chem. Rev.* **1995**, *95* (7), 2457-2483.

(404) Lagoda, N. A.; Larina, E. V.; Vidyaeva, E. V.; Kurokhtina, A. A.; Schmidt, A. F. Activation of Aryl Chlorides in the Suzuki-Miyaura Reaction by "ligand-Free" Pd Species through a Homogeneous Catalytic Mechanism: Distinguishing between Homogeneous and Heterogeneous Catalytic Mechanisms. *Org. Process Res. Dev.* **2021**, *25* (4), 916-925.

(405) Schmidt, A. F.; Kurokhtina, A. A.; Larina, E. V.; Lagoda, N. A.; Babenko, T. A. Homogeneous Catalysis of The Suzuki–Miyaura Reaction with Aryl Chlorides. *Rus. J. Phys. Chem.* **2022**, *16* (3), 407-410.

(406) Li, J. H.; Serdyuk, L.; Ferraris, D. V.; Xiao, G.; Tays, K. L.; Kletzly, P. W.; Li, W.; Lautar, S.; Zhang, J.; Kalish, V. J. Synthesis of substituted 5[H]phenanthridin-6-ones as potent poly(ADP-ribose)polymerase-1 (PARP1) inhibitors. *Bioorg. Med. Chem. Lett.* **2001**, *11* (13), 1687-1690.

(407) Li, Y.; Ding, Y. J.; Wang, J. Y.; Su, Y. M.; Wang, X. S. Pd-catalyzed C-H lactonization for expedient synthesis of biaryl lactones and total synthesis of cannabinol. *Org. Lett.* **2013**, *15* (11), 2574-2577.

(408) Mortlock, A. A.; Bath, C.; Butlin, R. J.; Heys, C.; Hunt, S. J.; Reid, A. C.; Sumner, N. F.; Tang, E. K.; Whiting, E.; Wilson, C.; Wright, N. D. N-Methyl-2-[4-(2-methylpropyl)phenyl]-3-(3-methoxy-5-methylpyrazin-2-ylsulfamoyl)benzamide; one of a class of novel benzenesulphonamides which are orally-active, ETA-selective endothelin antagonists. *Bioorg. Med. Chem. Lett.* **1997**, *7* (11), 1399-1402.

(409) Li, Y.; Pan, B.; He, X.; Xia, W.; Zhang, Y.; Liang, H.; Subba Reddy, C. V.; Cao, R.; Qiu, L. Pd-catalyzed asymmetric Suzuki–Miyaura coupling reactions for the synthesis of chiral biaryl compounds with a large steric substituent at the 2-position. *Beilstein J. Org. Chem.* **2020**, *16* (1), 966-973.

(410) Pi, J. J.; Lu, X. Y.; Liu, J. H.; Lu, X.; Xiao, B.; Fu, Y.; Guimond, N. Exploration of Biaryl Carboxylic Acids as Proton Shuttles for the Selective Functionalization of Indole C-H Bonds. *J. Org. Chem.* **2018**, *83* (10), 5791-5800.

(411) Kahnt, M.; Heller, L. F. N.; Al-Harrasi, A.; Csuk, R. Ethylenediamine Derived Carboxamides of Betulinic and Ursolic Acid as Potential Cytotoxic Agents. *Molecules* **2018**, *23* (10), 2558-2558.

(412) Chen, W.; Wu, X.; McManus, J. B.; Bida, G. T.; Li, K. P.; Wu, Z.; Nicewicz, D. A.; Li, Z. Direct C-H Radiocyanation of Arenes via Organic Photoredox Catalysis. *Org. Lett.* **2022**, *24* (50), 9316-9321.

(413) Gaisina, I. N.; Gallier, F.; Ougolkov, A. V.; Kim, K. H.; Kurome, T.; Guo, S.; Holzle, D.; Luchini, D. N.; Blond, S. Y.; Billadeau, D. D.; Kozikowski, A. P. From a natural product lead to the identification of potent and selective benzofuran-3-yl-(indol-3-yl)maleimides as glycogen synthase kinase 3βinhibitors that suppress proliferation and survival of pancreatic cancer cells. *J. Med. Chem.* **2009**, *52* (7), 1853-1863.

(414) Xie, Y. F.; Lake, K.; Ligsay, K.; Komandla, M.; Sircar, I.; Nagarajan, G.; Li, J.; Xu, K.; Parise, J.; Schneider, L.; Huang, D.; Liu, J.; Dines, K.; Sakurai, N.; Barbosa, M.; Jack, R. Structure–activity relationships of novel, highly potent, selective, and orally active CCR1 antagonists. *Bioorg. Med. Chem. Lett.* **2007**, *17* (12), 3367-3372.

(415) Mamari, H. H. A.; Mamari, H. H. A. Developments and Uses of Lewis Acids: From Conventional Catalysts to Modern Green Catalysts. *Electrophile and Lewis Acid* **2023**.

(416) Corma, A.; García, H. Lewis acids: From conventional homogeneous to green homogeneous and heterogeneous catalysis. *Chem. Rev.* **2003**, *103* (11), 4307-4365.

(417) Zhu, X.; Ganesan, A. Regioselective synthesis of 3-alkylindoles mediated by zinc triflate. *J. Org. Chem.* **2002**, *67* (8), 2705-2708.

(418) Liang, K.; Shao, Q.; Xia, G.; Wang, Y.; Jiang, L.; Hong, L.; Wang, H. Tuning solid state emission of semisquaraines via trimming central-ring structures. *Dyes Pig.* **2020**, *173*, 107926-107926.

(419) Zhang, T.; Hong, X. Q.; Zhi, H. T.; Hu, J.; Chen, W. H. Synthesis and mechanism of biological action of morpholinyl-bearing arylsquaramides as small-molecule lysosomal pH modulators. *RSC Adv.* **2022**, *12* (35), 22748-22759.

(420) Rostami, A.; Ebrahimi, A.; Husband, J.; Anwar, M. U.; Csuk, R.; Al-Harrasi, A. Squaramide–Quaternary Ammonium Salt as an Effective Binary Organocatalytic System

for Oxazolidinone Synthesis from Isocyanates and Epoxides. *Eur. J. Org. Chem.* **2020**, *2020* (12), 1881-1895.

(421) Stanetty, P.; Rodler, I.; Krumpak, B. Synthese neuer N, N,1,1-Tetramethyl-isobenzofuranamine. *J. prakt. Chem.* **1993**, *335* (1), 17-22.

(422) Funk, P.; Motyka, K.; Džubák, P.; Znojek, P.; Gurská, S.; Kusz, J.; McMaster, C.; Hajdúch, M.; Soural, M. Preparation of 2-phenyl-3-hydroxyquinoline-4(1H)-one-5-carboxamides as potential anticancer and fluorescence agents. *RSC Adv.* **2015**, *5* (60), 48861-48867.

(423) Ho, T. L.; Ho, M. F. A stereoselective synthesis of platyphyllide. *J. Chem. Soc. Perk. Trans. I* **1999**, (13), 1823-1826.

(424) Ballatore, C.; Gay, B.; Huang, L.; Robinson, K. H.; James, M. J.; Trojanowski, J. Q.; Lee, V. M. Y.; Brunden, K. R.; Smith, A. B. Evaluation of the cyclopentane-1,2-dione as a potential bio-isostere of the carboxylic acid functional group. *Bioorg. Med. Chem. Lett.* **2014**, *24* (17), 4171-4175.

(425) Amor-Coarasa, A.; Kelly, J. M.; Singh, P. K.; Ponnala, S.; Nikolopoulou, A.; Williams, C.; Vedvyas, Y.; Jin, M. M.; David Warren, J.; Babich, J. W. [18F]Fluoroethyltriazolyl Monocyclam Derivatives as Imaging Probes for the Chemokine Receptor CXCR4. *Molecules 2019, Vol. 24, Page 1612* **2019**, *24* (8), 1612-1612.

(426) Engl, O. D.; Fritz, S. P.; Käslin, A.; Wennemers, H. Organocatalytic route to dihydrocoumarins and dihydroquinolinones in all stereochemical configurations. *Org. Lett.* **2014**, *16* (20), 5454-5457.

(427) Zhang, J.; Zhou, Y.; Ma, S.; Zhou, F. Reprocessing of cross-linked polyamide networks via catalyst-free methods under moderate conditions. *Green Chem.* **2024**, *26* (6), 3368-3377.

(428) Aziz, F.; Reddy, K.; Fernandez Vega, V.; Dey, R.; Hicks, K. A.; Rao, S.; Jordan, L. O.; Smith, E.; Shumate, J.; Scampavia, L.; Carpino, N.; Spicer, T. P.; French, J. B. Rebamipide and Derivatives are Potent, Selective Inhibitors of Histidine Phosphatase Activity of the Suppressor of T Cell Receptor Signaling Proteins. *J. Med. Chem.* **2024**, *67* (3), 1949-1960.

(429) Tiruveedhula, V. V. N. P. B.; Witzigmann, C. M.; Verma, R.; Kabir, M. S.; Rott, M.; Schwan, W. R.; Medina-Bielski, S.; Lane, M.; Close, W.; Polanowski, R. L.; Sherman, D.; Monte, A.; Deschamps, J. R.; Cook, J. M. Design and synthesis of novel antimicrobials with activity against Gram-positive bacteria and mycobacterial species, including M. tuberculosis. *Bioorg. Med. Chem.* **2013**, *21* (24), 7830-7840.

(430) Chamoli, T.; Rawat, M. S. M.; Jacob, M. Studies on synthetic and structural characterization of new fluorine substituted phthalides of pharmaceutical interest. *J. Enzyme Inhib. Med. Chem.* **2012**, *27* (5), 748-757.

(431) Ye, J.; Chu, A. J.; Harper, R.; Chan, S. T.; Shek, T. L.; Zhang, Y.; Ip, M.; Sambir, M.; Artsimovitch, I.; Zuo, Z.; Yang, X.; Ma, C. Discovery of Antibacterials That Inhibit Bacterial RNA Polymerase Interactions with Sigma Factors. *J. Med. Chem.* **2020**, *63* (14), 7695-7720.

(432) Non-Linear Regression Analysis, Graphpad Prism 10.0.0 for Mac, GraphPad Software, Boston, Massachusetts USA, www.graphpad.com.

(433) Yung-Chi, C.; Prusoff, W. H. Relationship between the inhibition constant (K1) and the concentration of inhibitor which causes 50 per cent inhibition (I50) of an enzymatic reaction. *Biochem. Pharmacol.* **1973**, *22* (23), 3099-3108.

(434) Schrodinger, L. L. C. Schrodinger Release 2024-1: LigPrep. Schrodinger LLC: 2021.

(435) Schrödinger, L. L. C. The AxPyMOL Molecular Graphics Plugin for Microsoft PowerPoint, Version~1.8. 2015.

Appendix

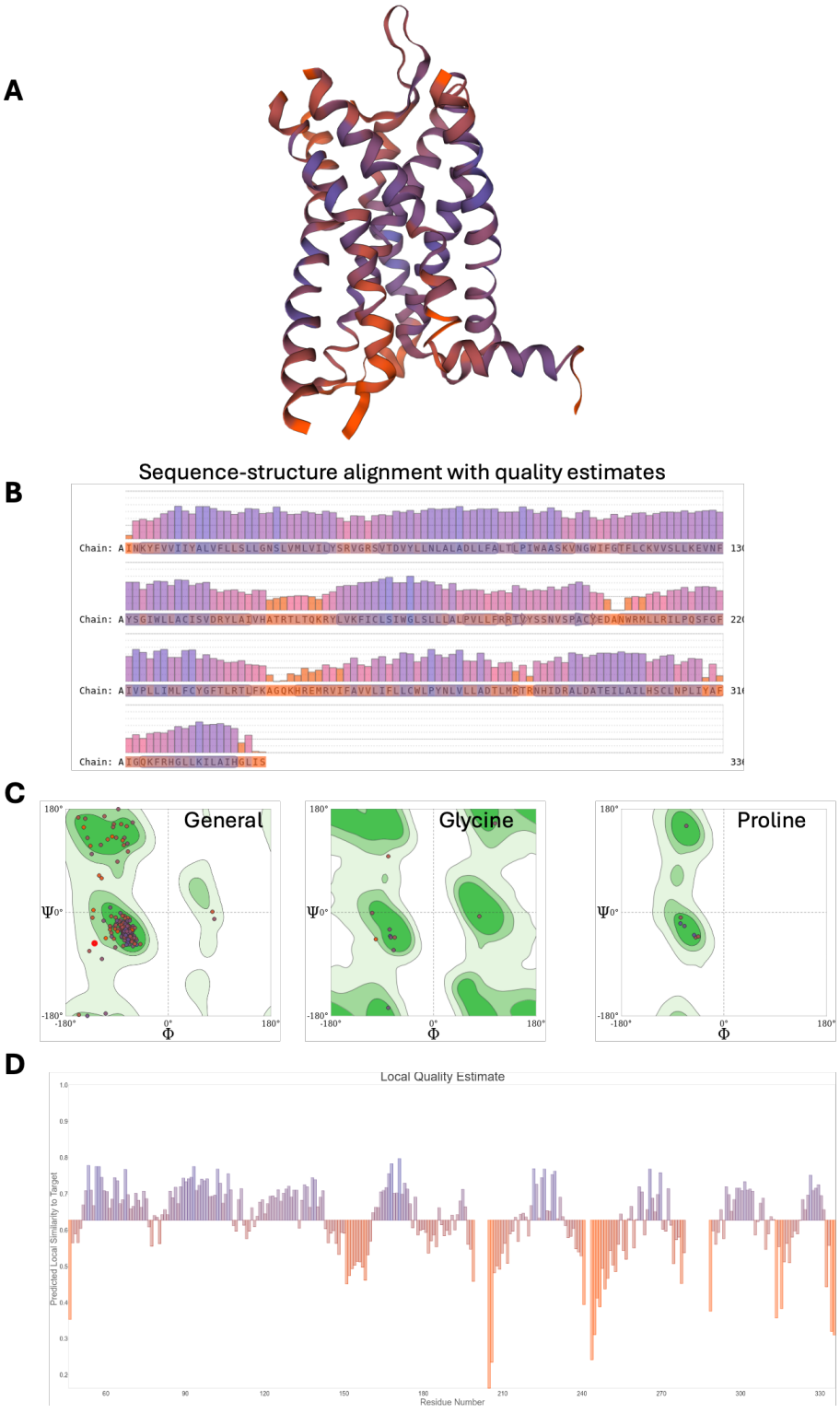

Appendix 1 Structural validation of truncated CXCR2 crystal structure (PDB ID: 6LFL). (A) Crystal structure prepared in protein preparation wizard in Schrödinger[289] before structural validation QMEAN local estimates are shown in coloured cartoon representation

(worst in orange to best in blue). (B) Sequence-structure alignment of CXCR2 crystal structure l (Chain: A) TM helices shown as circled regions. QMEAN estimates across the alignment shown (orange worst to best in blue). (C) Ramachandran plots for general, glycine and proline residues. The Ramachandran plots show the values of dihedral angles Φ and Ψ for residues while green contours display optimal expected values. (D) Local QMEAN estimates (orange worst to best in blue) worst regions correspond to relatively disordered and non-conserved loop regions compared to the CXCR2 template. Data generated in Swissmodelassess.[334]

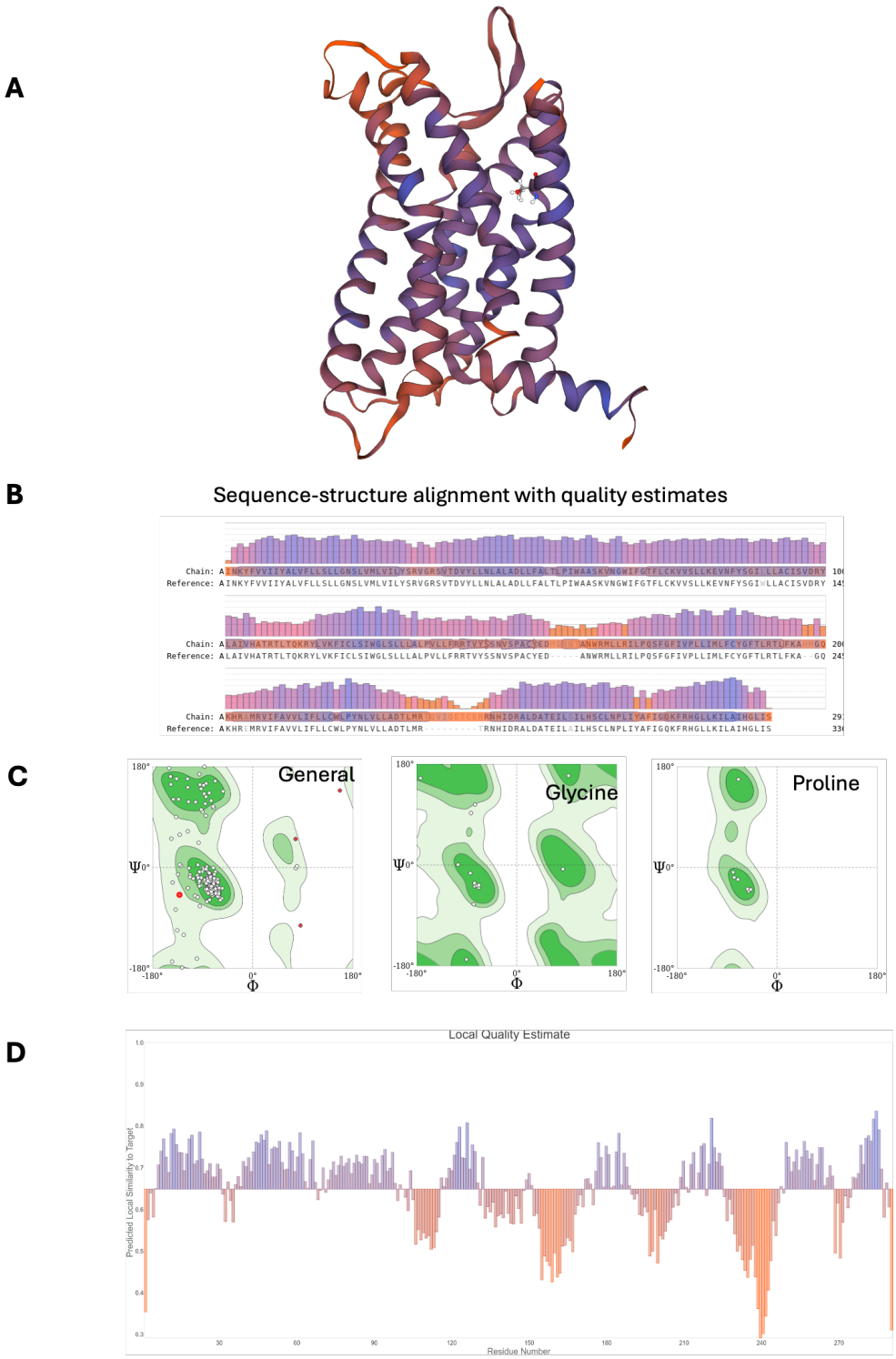

Appendix 2 Structural validation of CXCR2 model. (A) CXCR2 model based on CXCR2 crystal structure (PDB ID 6LFL) modified and refined to represent the canonical protein sequence. QMEAN local estimates are shown in coloured cartoon representation (worst in orange to best in blue). (B) Sequence-structure alignment of refined CXCR2 model (Chain:

A) and the original CXCR2 crystal structure (reference) TM helices shown as circled regions. QMEAN estimates across the alignment shown (orange worst to best in blue). (C) Ramachandran plots for general, glycine and proline residues. The Ramachandran plots show the values of dihedral angles Φ and Ψ for residues while green contours display optimal expected values. (D) Local QMEAN estimates (orange worst to best in blue) worst regions correspond to relatively disordered and non-conserved loop regions compared to the CXCR2 template. Data generated in Swissmodelassess.[334]

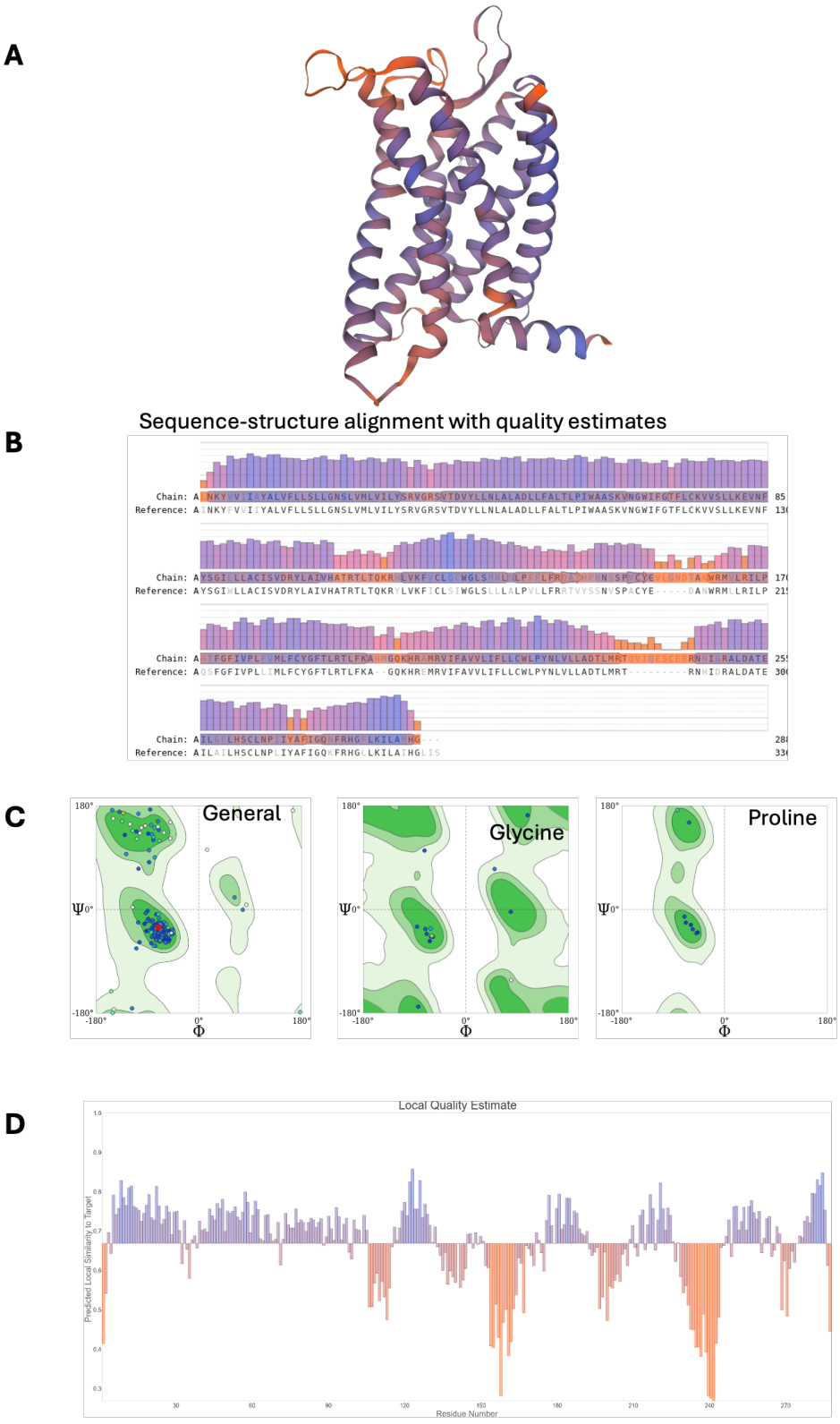

Appendix 3 Structural validation of initial unrefined CXCR1 homology model. (A) CXCR1 homology model built in modeller based on CXCR2 crystal structure (PDB ID 6LFL) QMEAN local estimates are shown in coloured cartoon representation (worst in orange to best in blue). (B) Sequence-structure alignment of initial CXCR1 homology

model (Chain: A) and the CXCR2 template, TM helices shown as circled regions. QMEAN estimates across the alignment shown (orange worst to best in blue). (C) Ramachandran plots for general, glycine and proline residues. The Ramachandran plots show the values of dihedral angles Φ and Ψ for residues while green contours display optimal expected values. (D) Local QMEAN estimates (orange worst to best in blue) worst regions correspond to relatively disordered and non-conserved loop regions compared to the CXCR2 template. Data generated in Swissmodelassess.[334]

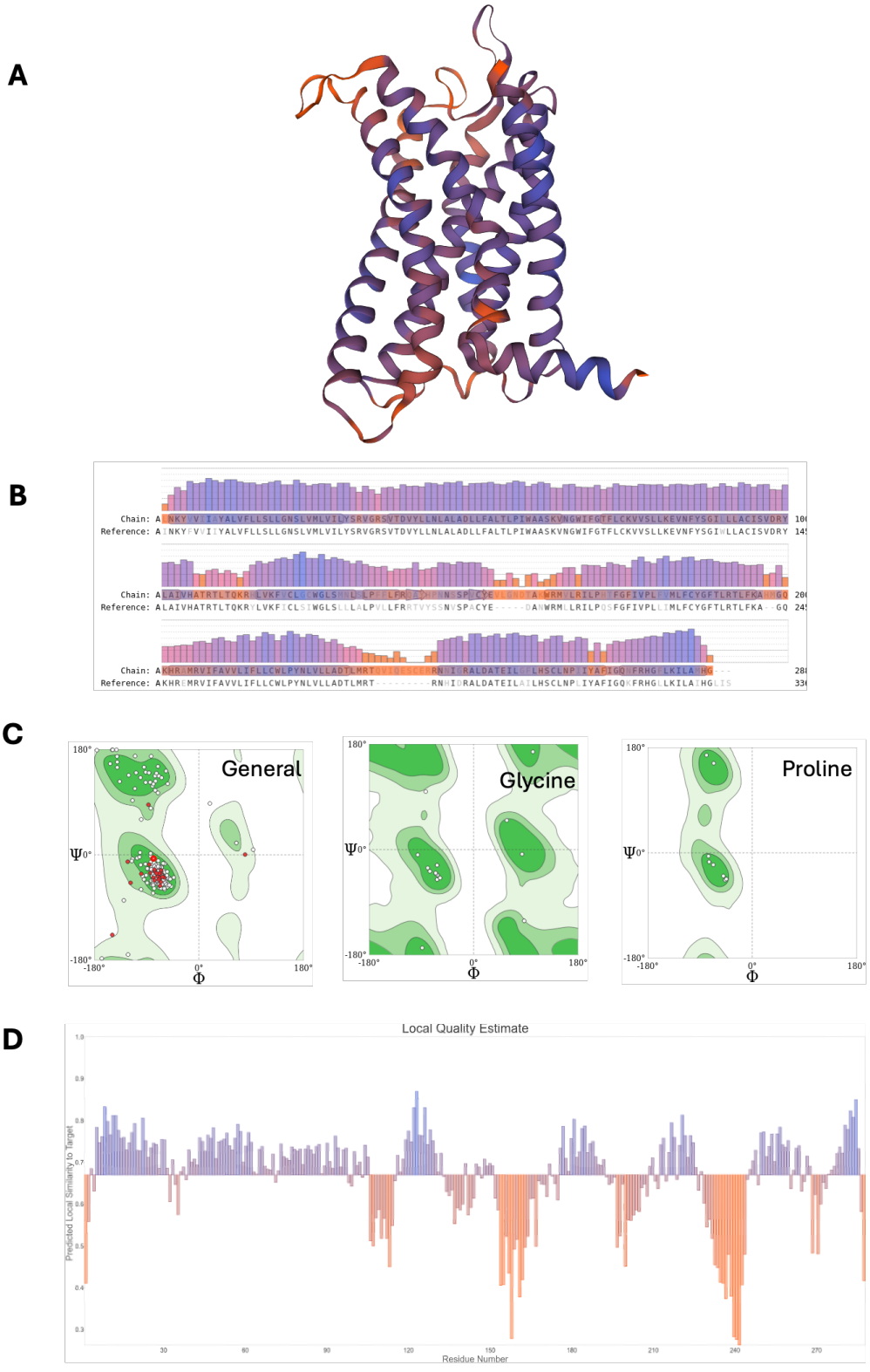

Appendix 4 Structural validation of refined CXCR1 homology model. (A) CXCR1 homology model built in modeller based on CXCR2 crystal structure (PDB ID 6LFL) and then refined by iterative manual rotamer changes and restrained minimisation. QMEAN local estimates are shown in coloured cartoon representation (worst in orange to best in

blue). (B) Sequence-structure alignment of refined CXCR1 homology model (Chain: A) and the CXCR2 template (reference), TM helices shown as circled regions. QMEAN estimates across the alignment shown (orange worst to best in blue). (C) Ramachandran plots for general, glycine and proline residues. The Ramachandran plots show the values of dihedral angles Φ and Ψ for residues while green contours display optimal expected values. (D) Local QMEAN estimates (orange worst to best in blue) worst regions correspond to relatively disordered and non-conserved loop regions compared to the CXCR2 template. Data generated in Swissmodelassess.[334]